Universidad Nacional Autónoma de México

Programa de Posgrado en Astrofísica

Instituto de Astronomía

Metal content of highly accreting quasars at $z \approx 2$

TESIS

que para optar por el grado de:

Maestro en ciencias (Astrofísica)

presenta:

Karla Garnica Luna

Asesorada por:

Dra. Paola Marziani (OAPD-INAF)
Dra. Castalia Alenka Negrete Peñaloza (IA-CU)

Ciudad Universitaria, CDMX,
Febrero 2022

Universidad Nacional Autónoma de México

Programa de Posgrado en Astrofísica

Instituto de Astronomía

Metal content of highly accreting quasars at $z \approx 2$

T E S I S

que para obtener el grado de:

Maestro en ciencias (Astrofísica)

presenta:

Karla Garnica Luna

Asesorada por:

Dra. Paola Marziani (OAPD-INAF)
Dra. Castalia Alenka Negrete Peñaloza (IA-CU)

Ciudad Universitaria, CDMX,
Febrero 2022

A Mariel, Tito y César

Resumen

Presentamos un análisis de espectros UV de cuasares con corrimiento al rojo intermedio que se cree que pertenecen a la Población A extrema (xA), con el objetivo de estimar las abundancias químicas del gas que emite las líneas anchas. Seguimos el enfoque descrito en Śniegowska et al. (2021) ampliando su muestra de 13 a 42 fuentes. Nuestro objetivo es probar la robustez del análisis realizado por Śniegowska et al. (2021), así como confirmar los dos resultados más importantes de esta investigación: la evidencia de valores de metalicidad muy superiores a la metalicidad solar ($10Z_\odot < Z < 50\ Z_\odot$) y la desviación de la abundancia relativa de elementos con respecto a la solar. La base de nuestro análisis son ajustes multi-componentes en tres regiones espectrales centradas en 1900, 1550 y 1400 Å con el fin de separar las componentes anchas de AlIIIλ1860, CIII]λ1909, CIVλ1549, HeIIλ1640, y SiIVλ1397 + OIV]λ1402 y sus excesos de flujo en el ala azul del perfil de emisión. Al comparar los cocientes de flujo observados de estos componentes con las mismos cocientes de flujo predichos por el código de fotoionización `CLOUDY`, encontramos que el gas virializado (componentes ancha) presenta una metalicidad superior a $10Z_\odot$. Para las nubes no virializadas, derivamos un límite inferior a la metalicidad alrededor de $5Z_\odot$ bajo la suposición de composición química proporcional a la solar, lo que confirma los resultados anteriores obtenidos por Śniegowska et al. (2021). Nos enfocamos especialmente en las relaciones entre las líneas de metales y HeIIλ1640. Esto nos permitió confirmar diferencias sistemáticas en la metalicidad a escala solar derivada de las líneas de Aluminio y Silicio, y de Carbono, siendo el primero un factor ≈ 2 más alto. Para los cuásares luminosos con alta tasa de acreción, es probable que los valores de Z sean elevados, pero que los valores escalados de Z se vean afectados por la posible contaminación debida al gas altamente enriquecido asociado con la formación de estrellas circumnucleares. Los valores altos de Z sugieren un proceso complejo que involucra la formación de estrellas en las regiones nucleares y circumnucleares, la interacción entre los objetos compactos nucleares y el disco de acreción, posiblemente con la formación de estrellas inducida por acreción.

Abstract

We present an analysis of UV spectra of quasars at intermediate redshifts believed to belong to the extreme Population A (xA), aimed to estimate the chemical abundances of the broad line emitting gas. We follow the approach described in Śniegowska et al. (2021) extending their sample from 13 to 42 sources. Our aim is to test the robustness of the analysis carried out by Śniegowska et al. (2021), as well as to confirm the two most intriguing results of this investigation: evidence of metallicity values much superior than the solar metallicity ($10Z_{\odot} < Z < 50\ Z_{\odot}$), and deviation of the relative abundance of elements with respect to solar. The basis of our analysis are multi-component fits in three regions of the spectra centered at 1900, 1550 and 1400 Å in order to deblend the broad components of AlIIIλ1860, CIII]λ1909, CIVλ1549, HeIIλ1640, and SiIVλ1397 + OIV]λ1402 and their blue excess. By comparing the observed flux ratios of these components with the same ratios predicted by photoionization code `CLOUDY` we found that the virialized gas (broad components) presents a metallicity higher than $10Z_{\odot}$. For non-virialized clouds we derive a lower limit to the metallicity around $\sim 5Z_{\odot}$ under the assumption of chemical composition proportional to the solar one, confirming the previous results obtained by Śniegowska et al. (2021). We relay especially on the ratios between metal lines and HeIIλ1640. This allowed us to confirm systematic differences in the solar-scaled metallicity derived from the lines of Aluminium and Silicon, and of Carbon, with

the first being a factor ≈ 2 higher. For luminous quasars accreting at high rate, high Z values are likely, but that Z scaled-values are affected by the possible pollution due to highly-enriched gas associated with the circumnuclear star formation. The high-Z values suggest a complex process involving nuclear and circumnuclear star formation, interaction between nuclear compact objects and accretion disk, possibly with the formation of accretion-modified stars.

Contents

Resumen **II**

Abstract **IV**

1 Introduction **1**

1.1 Active Galactic Nuclei 4

1.1.1 Seyfert Galaxies 8

1.1.2 Radiogalaxies 8

1.1.3 Quasars 10

1.1.4 Blazars 11

1.2 Classification 12

1.2.1 Spectral classification 13

1.2.2 Unified model 13

1.3 Photoionization of the broad line region 16

1.3.1 Emission line flux ratios 17

1.3.2 Photoionization models 18

1.4 Eigenvector 1 19

1.4.1 Population A and B 21

1.4.2 Extreme accretors in the context of 4DE1 23

1.5 Star formation in the circumnuclear region of AGN 25

1.6 Outline of this thesis 27

2 The Sample **29**

2.1 Sloan Digital Sky Survey 29

2.1.1 Apache Point Observatory 30
2.2 Sample Definition 31
2.2.1 Sample Processing 34
2.2.2 Additional redshift correction 35
2.2.3 Sample properties 37

3 Methods 40

3.1 Line interpretation and diagnostic ratios 41
3.1.1 Broad component 41
3.1.2 BLUE component 42
3.2 Multi-component fitting procedure 43
3.3 Regions of interest 46
3.3.1 1900 Å region 46
3.3.2 1550 Å region 49
3.3.3 1400 Å region 52
3.4 Error estimation on line fluxes 53
3.5 Measurements of profile normalized intensities 58
3.6 Estimate of physical parameters 59
3.6.1 Bolometric Luminosity 59
3.6.2 Black Hole Mass 60
3.6.3 Mass and Luminosity dependent parameters 61
3.6.3.1 Eddington Luminosity 61
3.6.3.2 Virial Luminosity 62
3.7 Metal content estimates 65
3.7.1 BLR photoionization models 65

4 Results 67

4.1 Immediate Results 68
4.1.1 `Specfit` measurements. 68
4.1.2 Normalized intensities measurements 74
4.2 Intensity ratios 77
4.2.1 BC intensity ratios 77

    4.2.2 BLUE intensity ratios 81
  4.3 Identification of xA sources and "intruders" 83
  4.4 Correlation between diagnostic ratios and physical parameters 84
  4.5 Metallicity inferences 86
    4.5.1 Estimates of Z distributions at fixed (U, n_{H}) 86
    4.5.2 Estimates of Z relaxing the constraints on U and n_{H} 94

5 Discussion **99**
  5.1 Fitting methods 99
    5.1.1 `specfit` vs profile ratios 99
    5.1.2 Comparison with the results of S21 101
    5.1.3 Analysis of Z distributions at fixed (U, n_{H}) for specfit and profile ratio measurements 103
  5.2 Correlation between diagnostic ratios and AGN physical properties: CIV full profile measurements 106
  5.3 Elemental pollution 108
    5.3.1 Highly-supersolar abundances 108
    5.3.2 Metal segregation 110
    5.3.3 Abundance pollution 111

6 Conclusions and Future Work **113**
  6.1 Metal content 114
  6.2 Sample correlations 115
  6.3 Future Work 116

Bibliography **117**

A Rest-frame spectra and fits **123**

B Tables **145**

List of Figures **153**

List of Tables **155**

Chapter 1

Introduction

Galaxies are systems of stars, gas, dust and dark matter held together by gravity (Carroll & Ostlie, 2007). By studying the galaxy we live in, the Milky Way, we can understand some of its elements and get an idea of how the other galaxies are alike. However, the fact that we are within the Milky Way drive to not fully understand aspects due to the difficulties of observation caused by extinction, among other factors. Therefore, the study of the other galaxies in the Universe becomes relevant because it helps us to figure out the structure, morphology and large-scale behavior of the other galaxies and hence of the Milky Way.

In addition, it has been detected a massive point source in the center of our galaxy, through the orbital motion of the stars closest to the center, with a mass close to $3 \times 10^6\ M_\odot$ (solar mass = $M_\odot$) (Schödel et al., 2002; Melia & Falcke, 2001; Kormendy & Richstone, 1995). This radio-emitting source is known as Sgr A* and match the galactic center. Although the data collected does not allow a totally unequivocal interpretation of this mass concentration, there is no plausible alternative to the conclusion that the center of the Milky Way harbors a supermassive black hole (Schneider, 2006). Black holes (BH) are compact massive sources predicted by the theory of general relativity, we can describe them as a singularity because density and gravity become infinite in a single point and space-time curves infinitely avoiding light to escape. This boundary is known as the "event horizon" and is

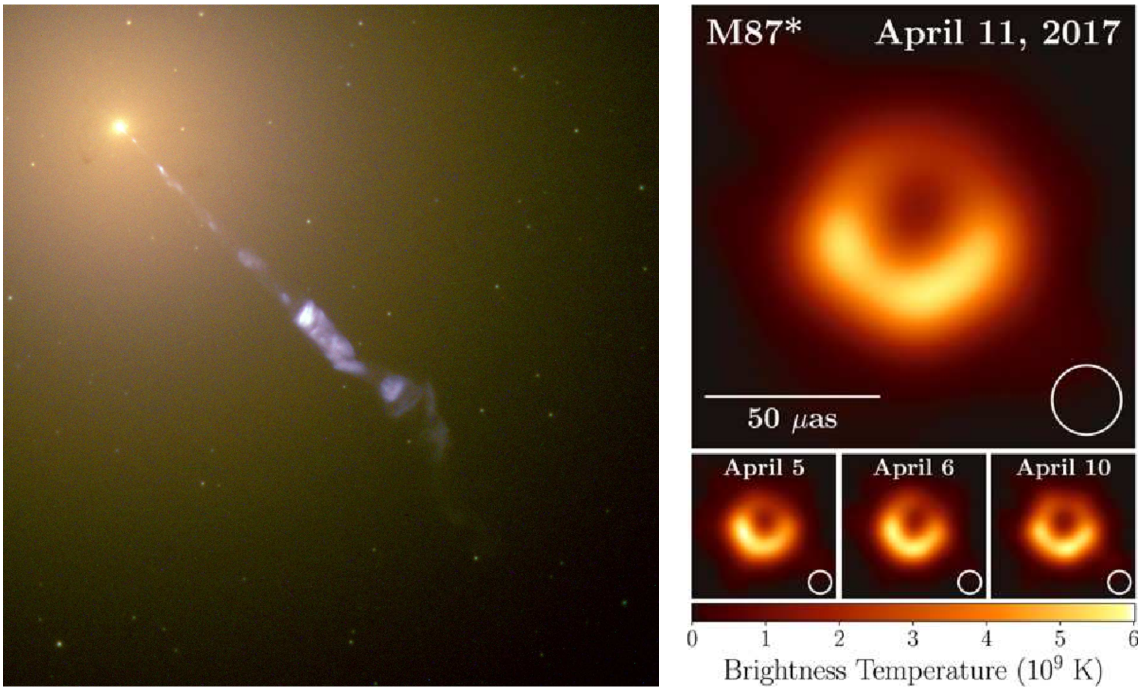

(a) **(b)**

Figure 1.1: (a). Composite image of M87 from Hubble Space Telescope observations. The bright spots in the image are globular clusters, in blue the relativistic jet is seen emerging from the galaxy. Figure taken from https://www.nasa.gov. (b). Image of M87* with observations from April 11, 2017 obtained by the Event Horizon Telescope. The image is the average of three different image methods after convolving each with a circular Gaussian kernel to give matched resolutions. The largest of the three kernels (20 μas FWHM) is shown in the lower right. The image is shown in units of brightness temperature, $T_b = S\lambda^2/2k_B\Omega$, where S is the flux density, λ is the observing wavelength, k_B is the Boltzmann constant, and Ω is the solid angle of the resolution element. Bottom: similar images taken over different days showing the stability of the basic image structure and the equivalence among different days. North is up and east is to the left. Figure and description taken from Event Horizon Telescope Collaboration et al. (2019a).

represented by the Schwarzschild radius

$$R_s = \frac{2GM}{c^2},$$

where G is the gravitational constant, M is the mass of the source (black hole mass) and c the speed of light.

Nowadays there is an international collaboration called *Event Horizon Telescope* (EHT) whose aims to directly observe the immediate surroundings of a black hole with angular resolution comparable to the event horizon (for Sgr A* the event horizon is comparable to 10 μas), currently they are working under a ~ 25 μas of angular resolution in the 1.3 mm wavelength band. (Event Horizon Telescope Collaboration et al., 2019b). On April 10^{th}, 2017, this collaboration published the first photograph of a supermassive black hole which corresponds to M87, an active elliptical galaxy known for its characteristic relativistic jet visible in the optical (see Fig. 1.1a). Image 1.1b was obtained using a very long baseline global interferometry (VLBI) array at short wavelengths. This required the use of various radio telescopes around the world, including the Alfonso Serrano Large Millimeter Telescope in Puebla, Mexico, which consists of a 50 m antenna.

> “Obtaining the first image of the shadow of the event horizon gives the guideline to direct studies of the event horizon shadow of supermassive black hole candidates via electromagnetic waves, thus transforming this elusive boundary from a mathematical concept to a physical entity that can be studied and tested via repeated astronomical observations.”
>
> Event Horizon Telescope Collaboration et al. (2019a)

According to observational evidence, supermassive black holes can be found at the core of most massive galaxies (Kormendy & Richstone, 1995; Richstone et al., 1998; Event Horizon Telescope Collaboration et al., 2019a). In some cases the luminosity of the galaxy’s nuclear region is exceptionally high, variable and shows signs of the existence of very energetic processes related to a compact central zone or nucleus, as is the case of M87. This is called an active galaxy nucleus or *AGN* by its acronym.

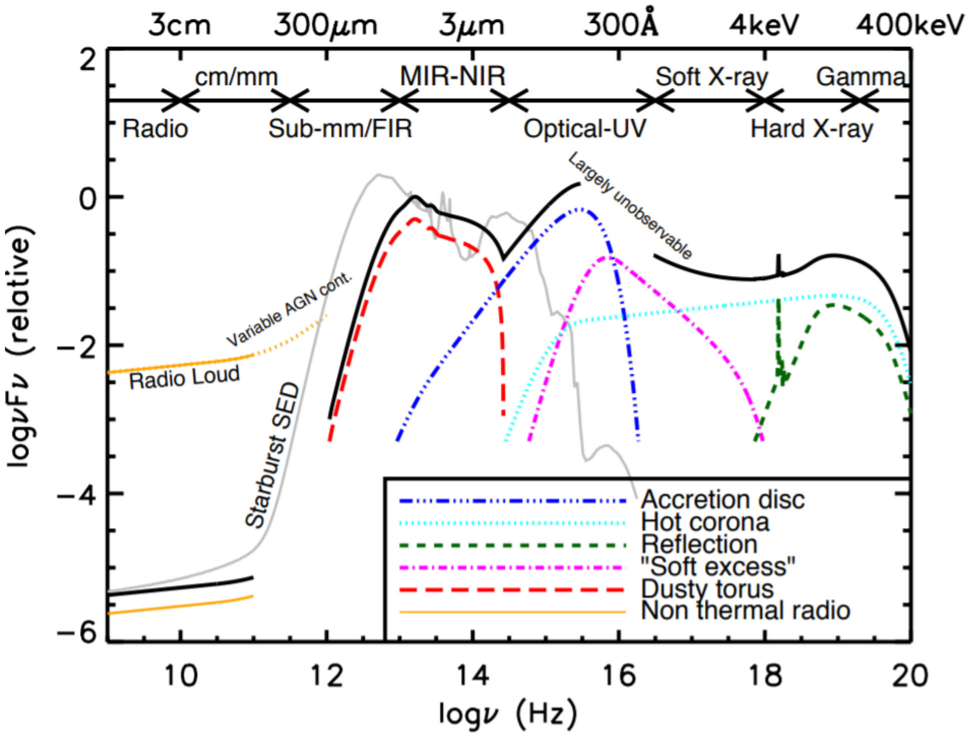

Figure 1.2: Schematic representation of the spectral energy distribution of an unobscured AGN (black curve), separated into the main physical components (as indicated by the colored curves) and compared to the SED of a star-forming galaxy (light grey curve). Figure and description taken from Hickox & Alexander (2018).

1.1 Active Galactic Nuclei

The term AGN refers to the existence of energetic phenomena in the nucleus or central regions of galaxies that cannot be attributed directly or clearly to the stars (Peterson, 1997). That is, the energy that we are detecting is being generated by non-thermal processes such as synchrotron and Compton emissions (see Fig. 1.2). The mechanism responsible for generating this energy focuses on the existence of a supermassive black hole located in the nucleus of the galaxy with a mass of $\log(M_{\rm BH}) \gtrsim 6$ $\rm M_{\odot}$ (Padovani et al., 2017), which accretes surrounding gas to generate luminosity. This accretion forms an optically thick disk of material that thermally emits due to its viscosity. The gas within this accretion disk has a temperature range that produces emission covering the UV and optical spectral ranges (with temperature as an inverse function of distance to the supermassive black hole) (Hickox & Alexander, 2018).

The *Spectral Energy Distribution* (SED) is a distribution of energy as a function of different wavelengths/frequencies and are usefull in astrophysical sources to identify its processes. Figure 1.2 show us a general view of the SED for unobscured AGN and the mechanisms that compose it, upper abscissa corresponds to the wavelength in units of Å, lower abscissa corresponds to the frecuency in units of Hertz (Hz) and ordinate flux density. The black solid curve represents the total SED for radio-quiet AGN and the various coloured curves (with an arbitrary offset) represent the individual components. The primary emission from the AGN accretion disk peaks in the UV region. Radio-loud AGN have radio emission that can be several orders of magnitude higher than radio-quiet AGN (shown with the labelled orange line). The grey curve shows an example radio-UV SED of a starburst galaxy (M82) (Harrison, 2014).

The first observational clues of AGN were made in 1908 by Edward A. Fath, detecting prominent emission lines in what he called the "spiral nebula", now galaxy NGC 1068, at the Lick Observatory. In 1943, Carl K. Seyfert observed galaxies with emission lines of high ionization potential that had broadening of $\Delta v \sim 8500 \text{ km s}^{-1}$. These galaxies also showed bright central regions similar to stellar nuclei in optical images that Seyfert distinguished, they are known as $Seyfert\ Galaxies$.

In 1959, Lodewijk Woltjer argued that the distance from the central source to the region where the observable lines are emitted (r) within the nuclei of the Seyfert galaxies, could not extend beyond $r \lesssim 100$ pc because they appeared as point-like objects in optical images. On the other hand, at $r \lesssim 100$ pc and a typical line width of $v \backsim 1000$ km s^{-1} implies a huge mass concentration at the center of these galaxies. With these two parameters, it was determined that the mass of the central region was close to $M \backsim 10^{10}$ M $_{\odot}$, or that r was much smaller than the estimated upper limit, which implies an enormous energy density within the AGN.

An important milestone in the history of AGNs was made with the 3C and 3CR radio catalogs of the University of Cambridge in England, which were completed around 1960. In 1963, Thomas Matthews and Allan Sandage proved that 3C48 was a point source ("stellar type") with a visual magnitude $m_v = 16\, mag$, whose complex optical spectrum consisted of a blue continuum and intense and wide emission lines

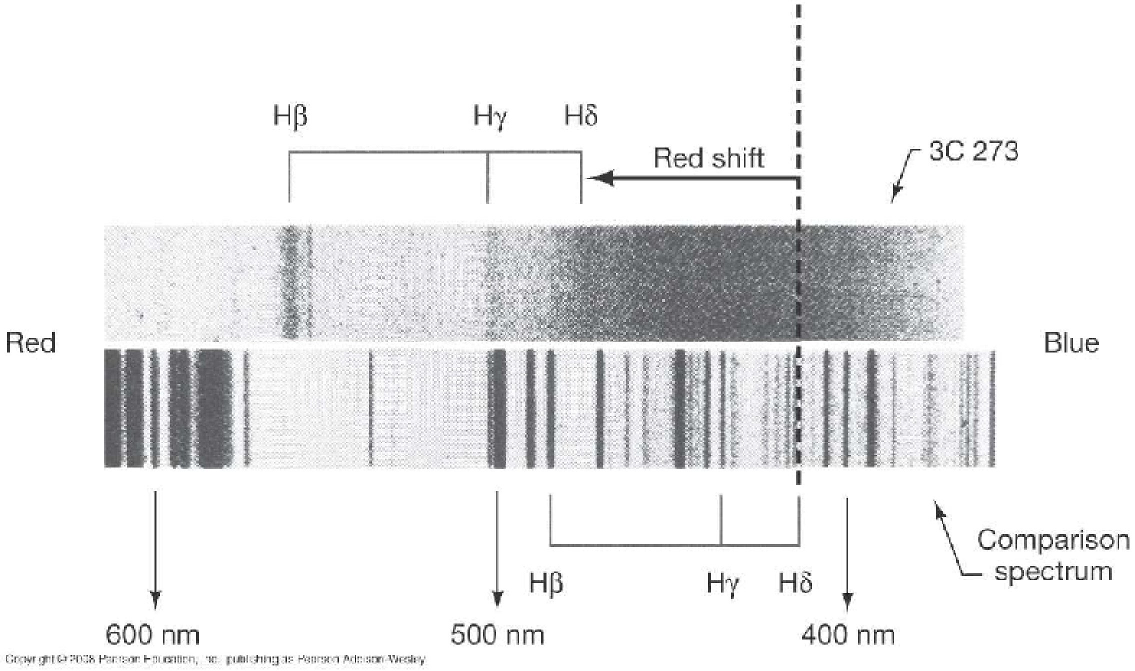

Figure 1.3: Identification of redshifted spectral lines. *Above.* Optical spectrum of quasar 3C273 showing redshifted lines of the Balmer series. *Bottom.* Rest frame spectrum. Figure taken from https://www.lindahall.org/maarten-schmidt/.

that could not be assigned to any atomic transitions and therefore could not be identified.

In the same year, Maarten Schmidt was able to identify the 3C273 radio source with an optical point source that also showed strong and broad emission lines at unusual wavelengths. This was achieved through a lunar occultation: the Moon passed in front of the radio source and hid it. From the measurement of the exact time that the radio emission was blocked and became visible again, the position of the radio source was precisely fixed. Schmidt noted that the source emission lines could be identified with those of the Balmer hydrogen series but with a redshift of $z = 0.158$, extremely high for the time. Figure 1.3 exemplifies the shift in spectral lines with redshift compared to a spectrum at the restframe. From this moment it became clear that these objects were highly luminous and therefore could be observed at great distances. These objects were named quasi-stellar radio sources (quasi-stellar objects - QSO) or simply, quasars.

As mentioned in the previous paragraphs, AGN have properties that distinguish them from other galaxies and astrophysical objects, some of these properties are:

(1) high bolometric luminosities up to L$_{bol}$ $\approx 10^{48} erg\ s^{-1}$, which makes them the strongest non-explosive sources in the entire Universe, around 100 times more than other galaxies, and therefore detectable at high redshifts $z \backsim 7$ (e.g. Bañados et al., 2019; Yang et al., 2021); (2) a compact region responsible for the emission in practically all wavelengths which implies high energy densities; (3) marked evolution of its luminosity functions; (4) detectable emission throughout the entire range of the electromagnetic spectrum (Padovani et al., 2017).

Currently, a wide range of sources has been classified as quasars, radio galaxies, Seyfert galaxies, blazars and subclassifications of these sources, encompassing various characteristics of AGN. Some are the most luminous cases, others have collimated jets of charged particles detectable at certain wavelengths. What all these sources have in common is a strong non-thermal emission from a compact central area of the host galaxy.

One of the first classifications was to divide the AGN zoo into strong radio objects (Radio Loud - RL) and radio quiet (RQ). A useful criterion to carefully distinguish between RL and RQ objects is the radio-to-optical relationship of specific fluxes at 6 cm (5 GHz) and in B band at 4400 Å (680 THz) proposed by Kellermann et al. in 1989:

$$R_K = log \frac{f_{radio}}{f_B}. \tag{1.1}$$

According to this relationship, a source is RQ when $R_K < 1$ and RL for $R_K > 10$, therefore an object that is RQ is not necessarily " radio-quiet ": it can still display a certain amount radio emission. Of the entire range of different AGN, only 10% are strong radio emitters (Urry & Padovani, 1996).

Given this, the classification of galaxies with an active nucleus has been a fundamental part for a better understanding of their properties. The main classes of AGN are described below.

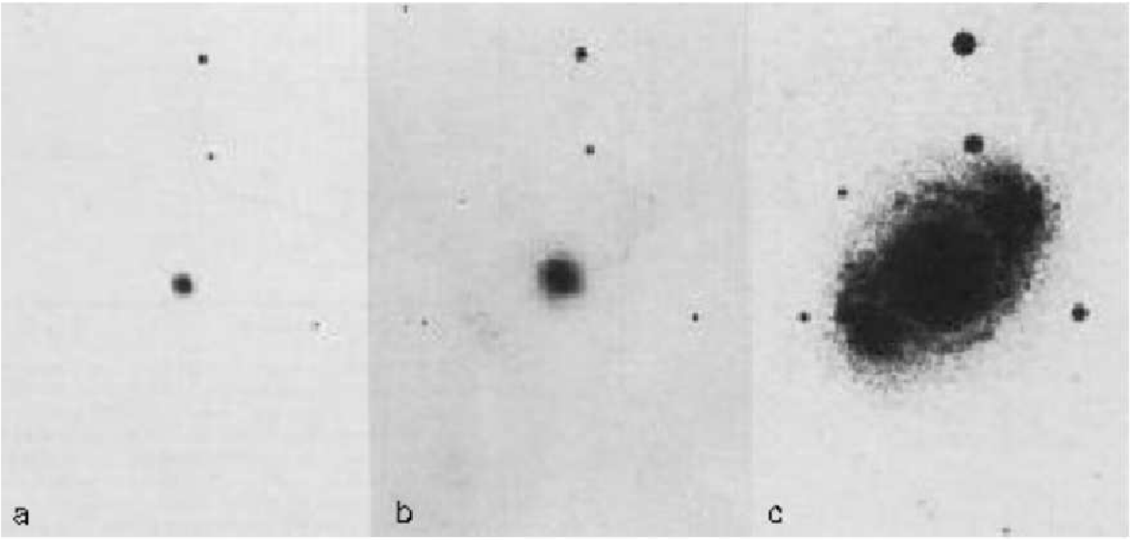

Figure 1.4: Images of the Seyfert galaxy NGC 4151. The exposure time increases from (a) to (c). In short exposures the source appears to be point-like, with long exposures it is possible to observe the host galaxy. Figure taken from Schneider (2006).

1.1.1 Seyfert Galaxies

These galaxies are named after Carl Seyfert who studied them in 1943 noting the differences they had with respect to other galaxies. In optical images they are identified as spiral galaxies with a bright and point-like nucleus (see Figure 1.4) accompanied by a spectrum that shows prominent emission lines.

These galaxies are subclassified into Seyfert Type 1 (Sy 1) and Seyfert Type 2 (Sy 2). We can distinguish these subclasses of galaxies by their spectrum. Seyfert 1 galaxies show both wide and narrow lines in their spectrum while Seyfert 2 show only narrow lines. Subsequently, intermediate types of Seyfert galaxies with broad lines less prominent than those in Seyfert 1 were discovered, leaving their spectrum in a transition between type 1 and type 2. The typical luminosities of their nucleus are 10^{43-45} erg s^{-1}(Netzer, 2013; Peterson, 1997).

1.1.2 Radiogalaxies

Radio galaxies are generally elliptical galaxies that host an active nucleus. They are the first sources that were identified with an optical counterpart, one of their main characteristics is their strong radio emission accompanied by relativistic jets. Jets are structures made up of collimated particles accelerated by a magnetic field

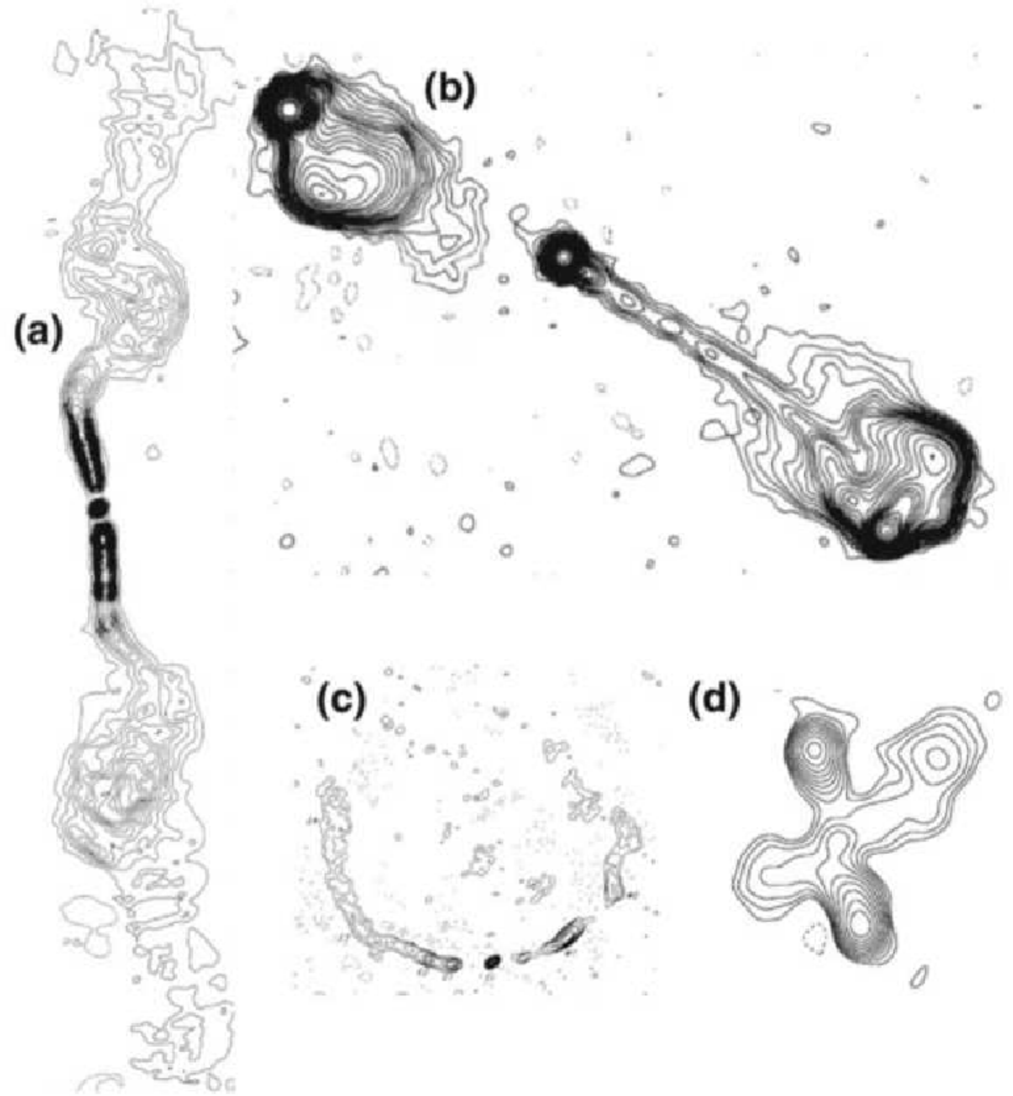

Figure 1.5: Examples of morphology in radio galaxies. The lines represent the contours in radius. a) 3C 499, a FR I radio galaxy with a concentration of luminosity close to the nucleus. b) 3C 175, a FR II radiogalaxy with concentration of luminosity in the lobes. c) 3C 83, a radio galaxy with wide angle in the tail, its main characteristic is the curvature of its lobes. d) 3C 223.1, an X-shaped radio galaxy. The apparent shape of these galaxies is obtained from the lobes which can become curved in the presence of a dense medium. Figure taken from Padovani et al. (2017).

that move close to the speed of light. These structures connect the active nucleus with radio lobes and extend through the interstellar medium, sometimes reaching distances greater than 1 Mpc (Andernach et al., 2021).

Radio galaxies can be subclassified in two ways. The first of them is by distinguishing their spectra, in turn, it divides them into two groups:

- Broad-line radio galaxies (BLRG)
- Narrow-line radio galaxies (NLRG)

The second way to classify them was proposed in 1974 by Fanaroff and Riley, differentiating radio galaxies into two classes according to their radio morphology. They named Fanaroff-Riley I (FR I) to the objects that are characterized by having a concentration of luminosity near the nucleus, which decreases towards the lobes as can be seen in Figure 1.5a. The typical luminosity of these galaxies is $L_\nu(1.4\ \text{GHz}) \lesssim 10^{32}$ erg s^{-1}. The Fanaroff-Riley II (FR II), are defined as radio galaxies in which the concentration of luminosity is in the lobes and decreases towards the nucleus as in Figure 1.5 b. These are galaxies with typical luminosity L_ν (1.4 GHz) $\gtrsim 10^{32}$ erg s^{-1}.

Currently, radio galaxies have been found that show a radius morphology different from that proposed by Fanaroff-Riley. These have lobes with a "bent" appearance (see Figure 1.5c) that occurs due to the environment they are in. Some examples of these are radio galaxies with a wide/narrow tail angle and radio galaxies with an X shape are shown in Figure 1.5d.

1.1.3 Quasars

A quasar is a source that when observed, the morphology of the host galaxy cannot be resolved and optically appears almost punctual. Its name is an abbreviation for quasi-stellar radio source, and some astronomers prefer to use the designation QSO (quasi stellar object), since not all quasars emit in radio. According to Schmidt (1969), quasars have the following properties:

- Stellar source identified in 10 % of cases with a radio counterpart.
- Time-varying continuum flux.
- UV excess flux.
- Broad emission lines.
- High redshift.

Quasars are observable at optical ranges wit ground-based telescopes, if their z>1.4 quasar spectra are dominated by spectral lines with a restframe in the ultraviolet regime. The first observed quasar redshifts were at $z = 0.16$ and 0.37. In subsequent searches larger and larger redshifts have continued to appear, currently there are records of $z \sim 7$ (e.g. Bañados et al., 2019; Yang et al., 2021). The large distances inferred from the Quasars mean that their luminosities have to be extremely large, typical values are within the range of 10^{45-48} erg s^{-1} which characterizes them as the most luminous objects in the AGN range.

1.1.4 Blazars

Blazars are defined primarily by their strong polarization and high variability. These sources are prominent emitters at wavelengths from radio to γ rays. Two types of blazars are differentiated according to their spectroscopic properties; flat-spectrum radio quasars (FSRQ) and BL Lac objects.

BL Lac objects owe their name to the most studied object of their class, BL Lacertae, located in the constellation of the Lizard. These objects are characterized by their rapid variability, on time scales from minutes to years. They are also spectroscopically characterized by a strongly polarized power law continuum (30-40% linear polarization) where no emission lines are observed. There are two subclasses of BL Lac objects defined by the relationship between X-ray and radio fluxes, which is anticorrelated with the wavelength at the maximum peak of their synchrotron emission:

- High-frequency peaked (HFP).
- Low-frequency peaked (LFP).

The spectra of flat-spectrum radio quasars have strong broad and emitting lines. These sources are subclassified into optical violent variable sources (Optical Violent Variables - OVV) and highly polarized quasars (Highly Polarized Quasars - HPQ).

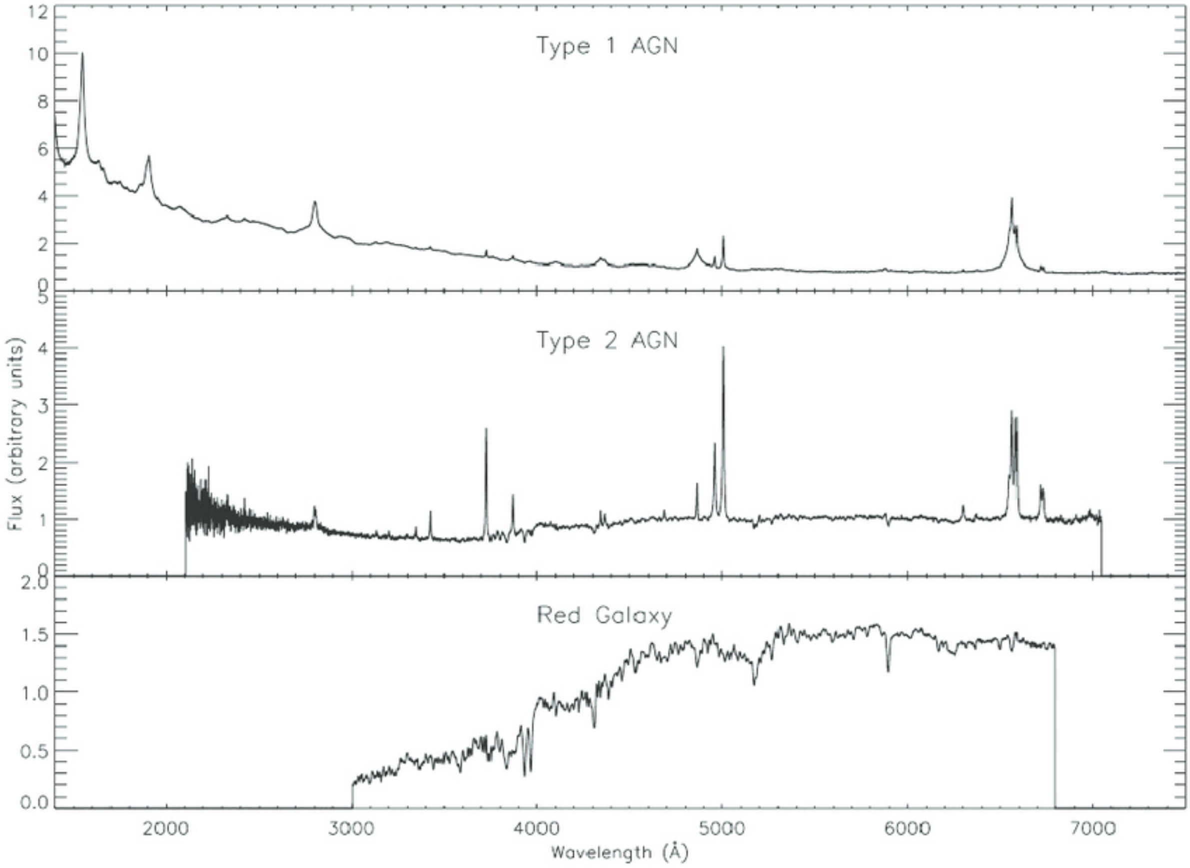

Figure 1.6: Main types of galactic spectra. *Top.* Spectrum of a type 1 AGN, in which the presence of both wide and narrow lines can be observed. *Middle.* Spectrum of a type 2 AGN, in which we can only observe the presence of narrow lines. *Bottom.* Spectrum of a *not active* galaxy. Spectra of normal galaxies consist of the sum of the stars from the galaxy. Figure taken from Mickaelian (2015).

1.2 Classification

There are several ways to classify AGN, either by their morphology or the type of lines in their spectrum. Since there is a wide variety of AGN sources, their classification has been a fundamental part for the better understanding of galaxies. Two basic ways to classify AGN are presented below: (1) by their spectroscopic characteristics and (2) a model that unifies all classes of AGN according to the orientation of the observer.

1.2.1 Spectral classification

A spectral line is like a fingerprint that helps us to identify elements and components present in a star, galaxy, or interstellar gas. Spectral lines provide us useful information about the observed source, we can know what is its chemical composition as well as if the source is moving away or closer to us or even if the source is rotating. There are two types of spectral lines: emission lines and absorption lines.

The spectral characteristics of an AGN refer to the type of emission lines that these sources present in their spectrum. The simplest way to distinguish an active galaxy from a normal one, is by comparing its spectrum. As we have mentioned previously, in an active galaxy the nucleus is responsible for releasing energy so powerful that in some cases opaque the star emission in the galaxy. On the other hand, when we are observing a normal galaxy, we detect a spectrum composed of all the stars in the galaxy, an overlap of stellar spectra (black bodies) that cover a temperature range according to the stars from the galaxy.

The emission lines that we find in the spectra are useful for classifying the AGN into three large groups. The main types of spectra that we observe in AGN are:

- Type 2: spectra with only narrow emission lines with full width at half maximum (FWHM) in a range of $100 \lesssim \mathrm{FWHM} \lesssim 500\ \mathrm{km\ \ s}^{-1}$.
- Type 1: spectra with broad lines with $\mathrm{FWHM} \gtrsim 1000\ \mathrm{km\ \ s}^{-1}$ and thin lines.
- Type 0: unusual spectra, there is an absence of emission lines.

This classification can be used for objects within the AGN zoo, as can be seen with the Seyfert 1 and 2 galaxies as well as the NLRG and BLRG radio galaxies.

1.2.2 Unified model

The enormous amount of energy coming from a compact central zone leads us to a model governed by a supermassive black hole, which attracts the surrounding gas by its gravitational force and releases gravitational energy as radiation. This, together with the characteristics shown by AGN, helped astronomers to consolidate a model

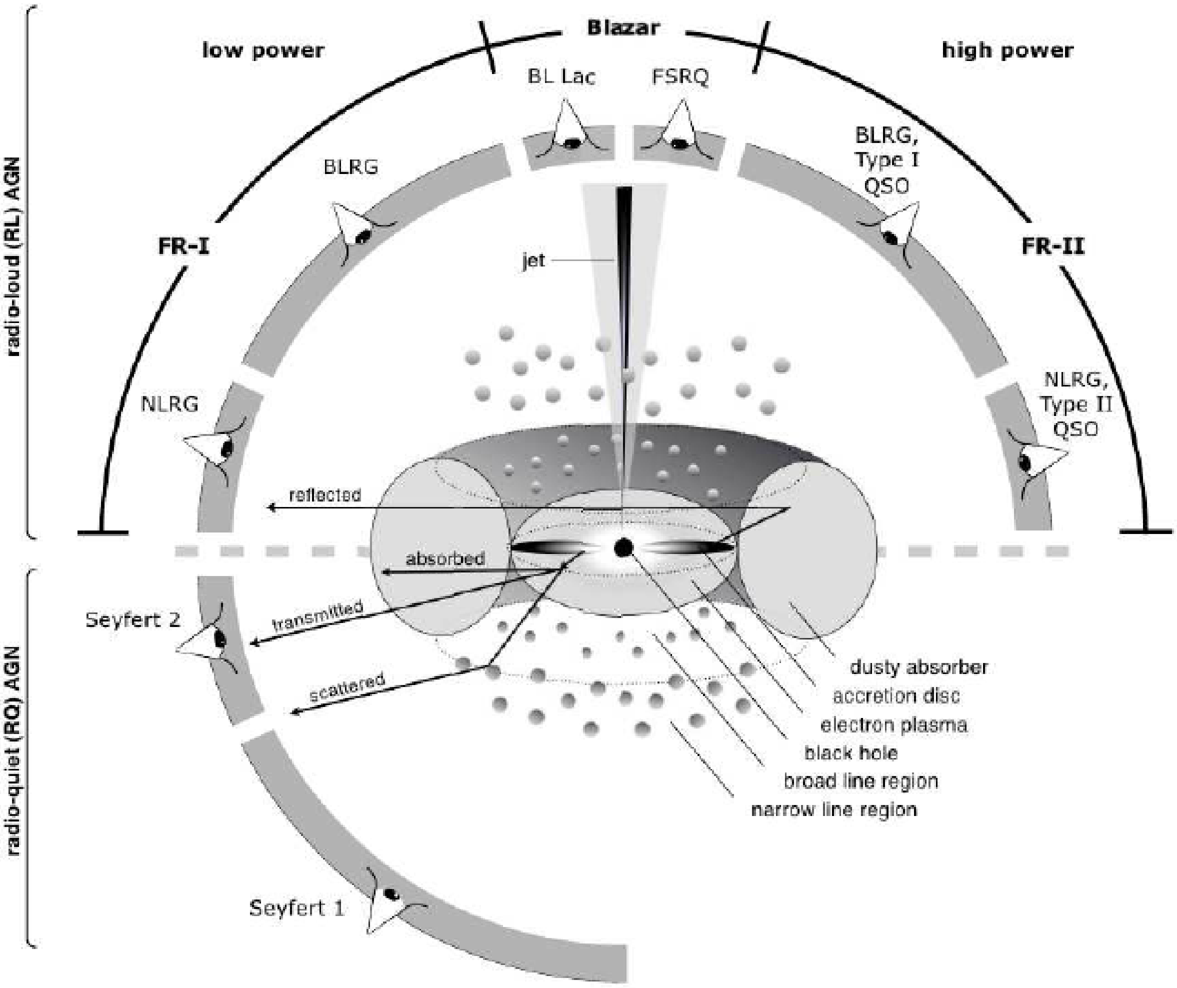

Figure 1.7: Schematic representation of the AGN in the unified model. The type of object we see depends on our viewing angle, regardless of whether the AGN produces significant jet emission and how powerful the central machinery is. The upper part shows how a RL AGN can be unified using this model. The bottom part shows the unification for the RQ AGN. Figure taken from Beckmann & Shrader (2012).

that may explain the possible unification of the various sources called AGN. The first descriptions of this model were introduced by Antonucci (1993) and Urry & Padovani (1996).

The unified model involves:

- Supermassive black hole. Located in the nucleus of the galaxy with a mass of $10^{6-9}M_{\odot}$ with an upper limit of $10^{10}M_{\odot}$. These are the most compact objects that can exist with a given mass M.

- Accretion disk. This is formed due to the gravitational potential of the black hole causing gas to accumulate around it which settles in a rotating disk. Substructures such as the corona are linked to this, which plays an important role in producing the hard X-ray continuum.

- Toroid. This is an optically thick gas and dust *donut* with structure that can be smooth or clumpy, that surrounds the accretion disk and obscures the view to the center of the AGN, with a radius of 1-100 pc.

- Jets. A pair of collimated plasma jets emerging from the galactic nucleus. In a typical case, jets are perpendicular to the structure of the accretion disk and the torus. Its size can range from a few kpc to Mpc.

- Broad line region (BLR). This is a section of dense clouds ($n_e \sim 10^{9-13}$ cm $^{-3}$) close to the black hole, partially ionized by emission from the accretion disk and orbiting around it. The speed of these clouds corresponds to the width of the lines generated in this region.

- Narrow Line Region (NLR). This is a section of less dense clouds ($n_e \sim 10^3\mathrm{cm}^{-3}$) far from the black hole that extend $\sim$ 100 pc with a spherical or conical geometry above and below the torus.

This AGN model predicts that differences in appearance are only a function of different viewing angles with respect to the observer. This causes various absorption effects intrinsic to the innermost regions of the AGN, as well as geometric effects with respect to the transmission of the emission.

The evidence that AGNs can be unified under a model according to Peterson (1997) are:

- The main difference between Seyferts and quasars is the luminosity of the central source.

- Seyfert 1 and Seyfert 2 galaxies are inherently the same sources. The difference is that in the case of the Seyfert 2 galaxies, we cannot see the nuclear source directly because of our unfavorable line of sight, which is intercepted by hidden material. A similar relationship holds between NLRG and BLRG.

Table 1.1: Main AGN classifications according to their optical and radio spectroscopic properties.

	Type 2	Type 1	Type 0
Radio Quiet	Sy 2 QSO	Sy 1 QSO	
Radio Loud	NLRG Cuasar	BLRG Cuasar	BL Lac FSRQ

Table based on Tadhunter (2008) and Schneider (2006).

- Blazars are apparently strong radio sources in which our line of sight is close to the axis of the jet.

This model only considers absorption and emission, which is not enough to understand why some sources are strong radio emitters and others are not. In other words, what makes the central machinery produce a jet.

1.3 Photoionization of the broad line region

The broad line region, one of the closest regions to the black hole, can provide us with information about the kinematics and structure of the central zone. This region is characterized by having an electron density high enough to produce forbidden lines, such as [O III]$\lambda\lambda$4959,5007, wich is collisionally suppressed.

Photoionization by radiation from the central source continuum is the most likely cause of excitation for emission lines in AGN gas. The number of photons emitted by the central source per second that can ionize hydrogen is given by

$$Q(H) = \int_{\nu_1}^{\infty} \frac{L_\nu}{h\nu} d\nu, \tag{1.2}$$

where L_ν is the specific luminosity of the central source, ν_1 is the lower limit of the ionization frequency, h is the Planck constant and the integral is over all ionizing photons of hydrogen.

From this, the *ionization parameter* (U) is defined as the ratio between the number of ionizing photons and the number of particles

$$U = \frac{Q(H)}{4\pi r^2 c\, n_H}, \tag{1.3}$$

where r is the radius of the cloud (the distance from the central ionization source to the clouds emitting the lines), c is the speed of light, n_H is the hydrogen density. This is a dimensionless parameter that describes the balance between the ionization rate caused by the incident photon flux and the recombination rate, which is directly dependent on hydrogen density.

1.3.1 Emission line flux ratios

Emission lines are useful tools to deduce physical properties of the emitting gas. For example, the temperature of the BLR gas (which is typically $T \sim 20\,000\ K$) can be determined from the ionization stages of the elements (Osterbrock & Ferland, 2006).

For a transition to occur, specific physical conditions are needed, since some spectral lines are only emitted under a certain density or temperature. Considering this logic, we can use emission lines flux ratios as indicators of the medium in which they were emitted. The line ratios

- Al III λ1869/ CIVλ1549
- Si IV + O IV]λ1400/ CIVλ1549
- N V λ1240/ He II λ1640
- N V λ1240/ CIVλ1549

are used as metallicity indicators as they are sensitive to the content of metals in AGN, since the energy levels in the ground state and excited state of these ions are very similar. This implies that the dependence on the shape of the continuum and the line ratios electronic temperature with these characteristics is small (Negrete et al., 2012b). Detailed photoionization models for BLR are very successful and can reproduce very well the details of line ratios (Schneider, 2006). In this way, photoionization models can be compared with observational data and their derived metallicity.

1.3.2 Photoionization models

The broad line region cannot be resolved using direct imaging techniques even with the closest sources (Negrete et al., 2013). Therefore, in this thesis, photoionization models are used to study it. These models simulate the physical conditions of a BLR cloud using a set of initial parameters and as a result they predict the spectral lines that can be emitted in that region and the intensity at which they are emitted. Photoionization models are computed following a description of parameters such as:

- the shape of the ionizing continuum
- the abundance of elements or metallicity (Z)
- the density of particles in the cloud (n_H)
- the columnar density of the cloud (N_c)
- the ionization parameter (U)
- the filling factor (η)
- dust, among others.

Photoionization models predict what a region looks like as a function of independent variables. Using them together with observational data help us to interpret the emitting region and by making use of model sets we can define the ideal parameters under which the spectral lines are emitted. A tool to carry out this type of simulation is the Cloudy photoionization code, developed by Ferland et al. (2017).

1.4 Eigenvector 1

Boroson & Green (1992a) identified a series of correlations based on a principal component analysis (PCA) of the spectral properties of type 1 AGN. From the two sets of derived correlations, the first correlation space or the first eigenvector (E1), highlights a relationship between the ratio of the equivalent widths (W) of W(FeII)/ W($H\beta_{\rm BC}$) and the luminosity of [O III]λ5007. "This tool gave for the first time a powerful systematic description for the spectral diversity of quasars" (Marziani et al., 2006).

Later in Sulentic et al. (2000b) this correlation space was modified by eliminating the narrow lines of the sample as parameters (e.g. [OIII]λ5007) and adding the excess of soft X-rays as a parameter to the E1. Figure 1.8 shows the two-dimensional projections of this E1 stage.

Finally, in Sulentic et al. (2007a) this space was expanded by adding the parameter of CIV asymmetry index in the UV, and hence generating the now known as the four-dimensional Eigenvector 1 (4DE1). The 4DE1 involves observational parameters that define its four dimensions:

1) FWHM($H\beta_{\rm BC}$);

2) $R_{\rm Fe_{II}}$= I(FeIIλ4570)/I($H\beta_{\rm BC}$), the intensity ratio of Fe_{II} and the broad component (BC) of $H\beta_{\rm BC}$;

3) Γ_{soft}, the soft X-ray photometric index;

4) the centroid at mid-height c(1/2) of CIVλ1549.

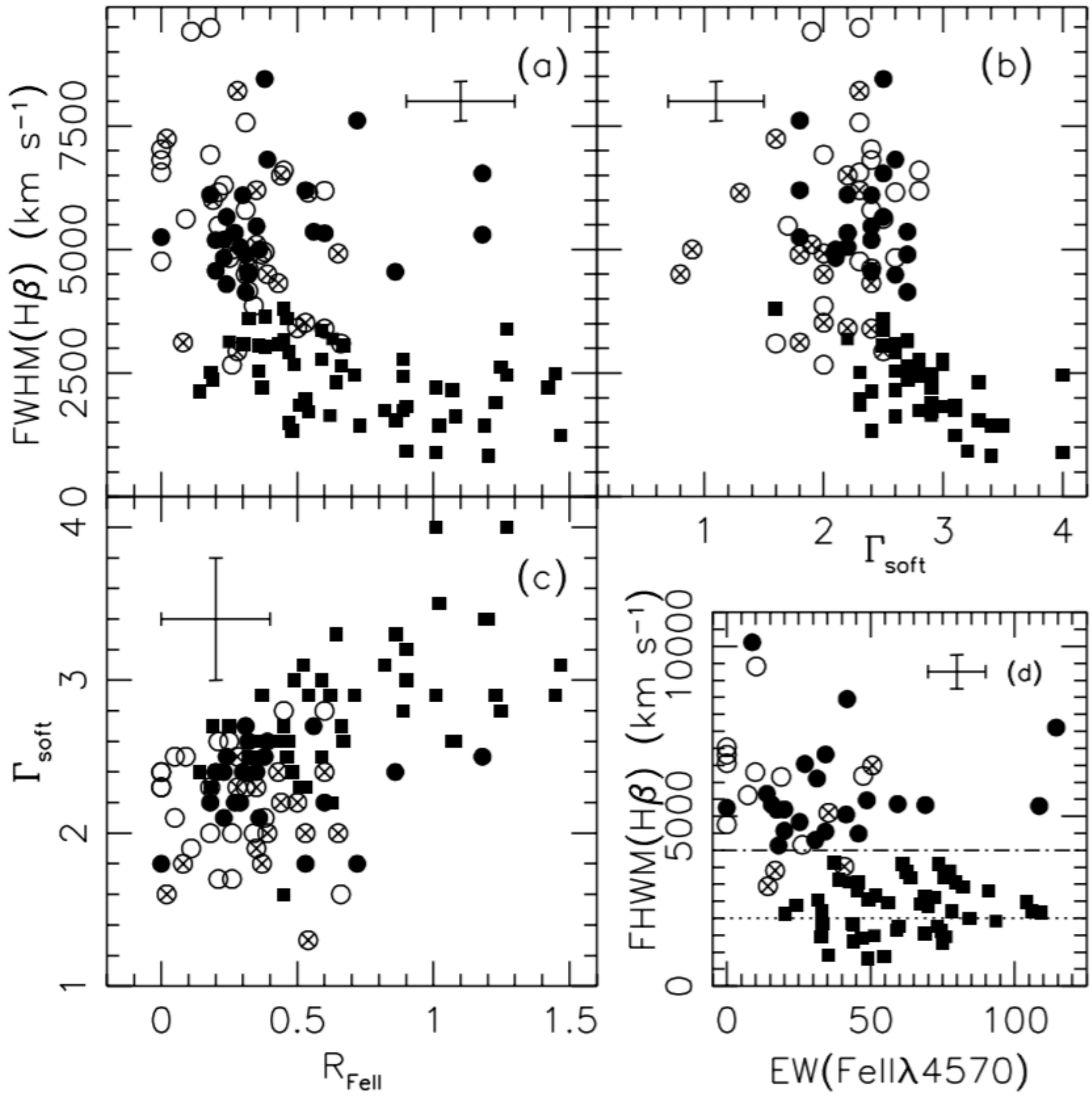

Figure 1.8: Two-dimensional projections of the Eigenvector 1 parameter space involving correlations between FWHM(H$\beta_{\rm BC}$), $\rm R_{Fe_{II}}$ and Γ_{soft}. Panels *a,b,c* show the three principal correlation planes of the E1. In all panels, solid symbols are radio-quiet sources (boxes: Pop. A, circles: Pop. B). Open symbols are radio-loud sources (open: core dominated, crossed: lobe dominated). Mean error bars are shown in a corner of each plot. Error bars (at a 2σ confidence level) are plotted for illustrative purposes only. Errors on FWHM(H$\beta_{\rm BC}$), on W(FeIIλ4570), and on $\rm R_{Fe_{II}}$ refer to an average point in the middle of the diagrams; the error bar on Γ_{soft} has been set as the median value of the errors reported for Γ_{soft} in the sample sources. *Panel d:* the Boroson & Green (1992b) sample plotted in the W(FeIIλ4570) vs. FWHM(H$\beta_{\rm BC}$) plane. The dotted line at 2000 km s^{-1} separates NLSy1 and the rest of the sample, while the dot-dashed line at 4000 km s^{-1} sets the limit between Pop. A and Pop. B. Figure and description from Sulentic et al. (2000c).

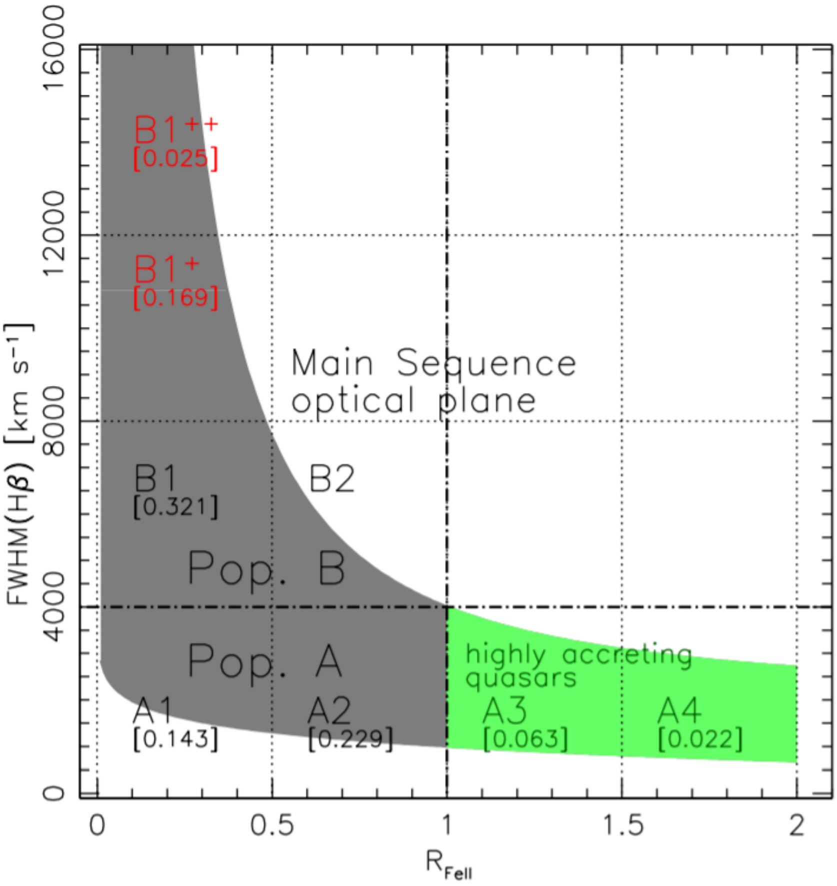

Figure 1.9: A sketch representing the occupation of Main Sequence quasars in the plane FWHM(H$\beta_{\rm BC}$) vs R$_{\rm Fe_{II}}$, the Main sequence "optical plane." Each bin in the plane corresponds to a spectral type. The ones associated with extreme Pop. B (red labels, top left) and the xA of highly-accreting quasars at the high end of the R$_{\rm Fe_{II}}$ distribution satisfying the condition R$_{\rm Fe_{II}} \geq 1$ (green area). The numbers in square brackets below each spectral type designation are the source fractional occupation in an optically-selected sample (Marziani et al., 2013). Figure and description taken from Marziani et al. (2021).

1.4.1 Population A and B

The optical plane of the 4DE1, FWHM(H$\beta_{\rm BC}$) vs. R$_{\rm Fe_{II}}$, shown in Figure 1.9, is a tool that provides us with an optimal discrimination between two categories of type 1 AGN by measuring the FWHM(H$\beta_{\rm BC}$): population A ≤ 4000 km s^{-1} and population B > 4000 km s^{-1}. Initially this distinction of populations was empirically defined by Sulentic et al. (2000b). However, Marziani et al. (2006) showed that this distinction is related to a difference in the structure of the broad line region in each population, these diferences were latter discussed in Marziani et al. (2018) were they described the BLR structure as following.

- Pop A. with a slim geometrically thick Advection-Dominated Accretion Disk;
- Pop. B. with a flat geometrically thin accretion disk.

The differences found in populations A and B are characterized for being contrasting populations. On one hand, we have population A with the majority of RQ sources, which show a strong/moderate emission of FeII and a blueshift/asymmetry present in lines with high ionization potential (e.g. CIVλ1549full profile). On the other

Table 1.2: Main trends along the 4DE1 sequence

Parameter	Population A	Population B	References
FWHM(H$\beta_{\rm BC}$)	800-4000 km s^{-1}	4000-10000 km s^{-1}	1, 2, 3, 4
R$_{\rm FeII}$	0.7	0.3	1,2
c($\frac{1}{2}$) C IV$_{\rm BC}$	-800 km s^{-1}	-250/+70 km s^{-1}	5, 6, 7, 8
Γ_{soft}	>2	≈2	2,9,4,10
EW(H$\beta_{\rm BC}$)	∼ 80 Å	∼ 100 Å	2
H$\beta_{\rm BC}$ line profile	Lorentzian	Double Gaussian	11, 12, 13
Si III]/ C III]	0.4	0.2	14, 15, 16
FWHM C IV$_{\rm BC}$	(2-6)10^3 km s^{-1}	(2-10)10^3 km s^{-1}	5, 17
EW(C IV$_{\rm BC}$)	≈ 60 Å	∼ 100 Å	4, 6, 7
AI(C IV$_{\rm BC}$)	-0.1	0.05	5
RL probability	≈ 3-4%	25%	4, 18
BAL	Extreme	Least extreme	23, 24
log n$_H^*$	$\gtrsim$ 11	$\gtrsim$ 9.5	14, 19
log U*	-2.0/-1.5	-1.0/-0.5	14, 19
log $\frac{M_{BH}}{M_\odot}$	6.5-8.5	8.0-9.5	7,8,20
L/L_{Edd}	≈ 0.2-1.0	∼ 0.01-≈ 0.2	1, 4, 7, 20, 21, 22

1: Boroson & Green 1992a; 2: Sulentic et al. (2000a); 3: Collin et al. (2006); 4: Shen & Ho (2014); 5: Sulentic et al. (2007a); 6: Baskin & Laor (2005); 7: Richards et al. (2011); 8: Sulentic et al. (2016); 9: Wang et al. (1996); 10: Bensch et al. (2015); 11: Véron-Cetty et al. (2001); 12: Sulentic et al. (2002); 13: Marziani et al. (2003); 14: Marziani et al. (2001); 15: Wills et al. (1999); 16: Bachev et al. (2004a); 17: Coatman et al. (2016); 18: Zamfir et al. (2008); 19: Negrete et al. (2012b); 20: Boroson (2002); 21: Peterson et al. (2004); 22: Kuraszkiewicz et al. (2000); 23; Reichard et al. (2003); 24: Sulentic et al. (2006a).
Extraccion de Tabla 1 de Fraix-Burnet et al. (2017).
* It refers to a dense region of low ionization that appears to vary throughout the 4DE1 sequence, and is associated with the reverberation response of H$\beta_{\rm BC}$(Negrete et al., 2013).

hand, population B presents a majority of RL sources, a low FeII emission and does not show strong asymmetries as population A in the emission lines (Sulentic et al., 2011). The characteristics of these populations are listed in Table 1.2.

In addition to providing us with the distinction of two populations of type 1 AGN, the 4DE1 optical plane is defined in intervals that help us distinguish the subpopulations derived from population A and B. For the ordinate axis, the interval is ΔFWHM(H$\beta_{\rm BC}$) = 4000 km s^{-1} within a range of 0 to 16000 km s^{-1}. The interval ΔFWHM(H$\beta_{\rm BC}$) mainly delimits population A from B in the first interval at 4000 kms. From this interval the subpopulations from B1 to B1$_{++}$ are defined in ascending order for the ordinate axis. For the abscissa axis, the interval is ΔR$_{\rm FeII}$= 0.5 which runs in a range from 0 to usually 2 where the accretion rate, defined in solar masses per year, increases from lower to higher values of R$_{\rm FeII}$. This interval defines subpopulations from 1 to 4 for both population A and B as observed in the optical plane of 4DE1 (Fig. 1.9).

1.4.2 Extreme accretors in the context of 4DE1

As mentioned in section 1.1, AGN generate their luminosity by accretion of material around the central supermassive black hole. There are cases in which the accretion rate reaches the maximum limit to generate luminosity through this process, that is, the source reaches its maximum luminosity. This is true when $L/L_{Edd} \approx 1$, where L is the bolometric luminosity which is the integrated luminosity at all wavelengths, L_{Edd} is the Eddington luminosity, the maximum luminosity generated by a mass source M fed by the spherical accretion of completely ionized gas. L/L_{Edd} is an indicator of the accretion rate of the black hole (this topic will be taken up in depth in the section 3.6).

Quasars with luminosities close to or greater than Eddington's have been called *Super-Eddington AGN* given the nature of their luminosity. This work aims to study these sources under the context of 4DE1, therefore, the name we will adopt for AGN with $L/L_{Edd} \approx 1$ is *extreme accretors* (xA).

The peculiar characteristics of extreme accretor objects have been useful to define criteria that help us to distinguish these types of sources in a concise way. The three most widely accepted criteria for classifying sources as extreme accretor under the context of 4DE1 are based primarily on emission line flux ratios:

1. $R_{\mathrm{FeII}} > 1$
2. Al IIIλ1860/ Si III] λ1892 ≥ 0.5
3. C III]λ1909/ Si III] λ1892 ≤ 1.0

Under these criteria the extreme accretor sources are delimited at 2 intervals within the 4DE1 optical plane that correspond to subpopulations A3 and A4 (Fig. 1.8).

The optical criteron ($R_{\mathrm{FeII}} > 1$) is commonly used in sources with low redshift ($z < 0.8$), while the UV criteria (AlIII/SiIII] ≥ 0.5 and CIII]/SiIII] ≤ 1.0) help to identify extreme accreting sources at high redshift due to the limit of the detectors to observe the optical region. Optical and UV counterparts have been examined in spectra with a wide redshift range, z = 0.4 - 3.0, and the criteria have been found to be satisfied at the same time (Martínez-Aldama et al., 2017).

In this type of quasars, it is possible to observe a strong wind effect associated with lines with high ionization potential, such as CIV. These outflows consist of partially ionized gas that moves out of the central region at slower speeds than jets, but can still reach up to a third of the speed of light. They are observed in spectra in form of absorptions (Arav, 2007) and asymmetric emissions. The latter are formed by material moving towards us according to our line of sight in which case the Doppler effect shifts the line towards the blue. It is believed that these winds may enrich of metals the host galaxy or the intergalactic environment (King & Pounds, 2015).

There have been previous claim of very high metallicity needed to account for the extreme FeII emission (Panda et al., 2018, 2019, 2020) as well as to account for the metallicity-sensitive UV emission line ratios (Baldwin et al., 2003; Warner et al., 2004; Shin et al., 2013; Sulentic et al., 2014). Some authors have established a typical metallicity of ~ 5 Z for gas in the broad line region. However, the case we are studying has indications of having greater metallicity than the proposed values, which may be related to the asymmetric profiles observed in the spectra

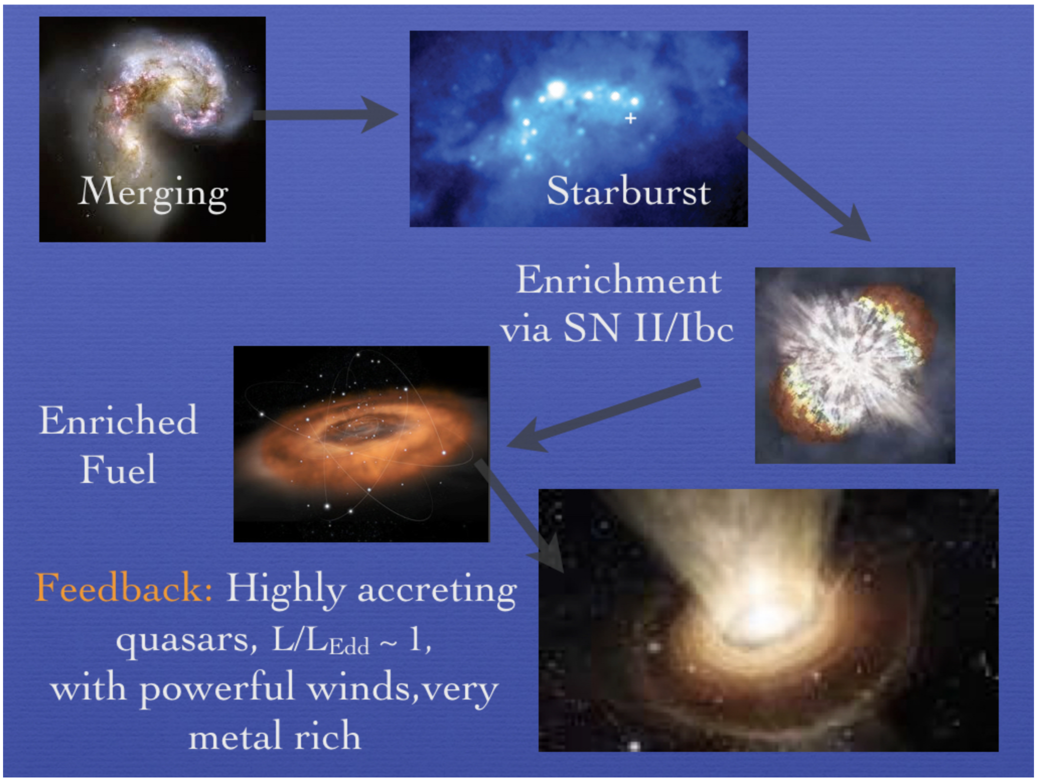

Figure 1.10: The early stages in the evolution of AGN and quasars: merging and strong interaction lead to accumulation of gas in the galaxy central regions, inducing a burst of star formation (top panels). Mass loss due to stellar winds and supernova explosions eventually provides accretion fuel for the massive black hole at the galaxy center. Radiation force and mechanical energy can then sweep the dust surrounding the black hole, at least within a cone coaxial with the accretion disk axis from where the radiative and mechanical output is free to escape into the host galaxy ISM (bottom panel) (Figure and description taken from D'Onofrio & Marziani, 2018).

1.5 Star formation in the circumnuclear region of AGN

According to D'Onofrio & Marziani (2018), the early stages in the evolution of AGN and quasars with low to high redshift ($0 \lesssim z \lesssim 6$) may follow the sequence:

1. merging and strong gravitational interaction;
2. a induced burst of star formation;
3. enriched material due to stellar winds and supernova explosions;
4. enriched fuel for the massive black hole at the galaxy center;

5. expected high accretion rate, yielding maximum radiative output per unit mass

resulting in an unboscured quasar, such as xA sources, this sequence is also shown in Fig. 1.10.

For quasars essentially unobscured, radiation and mechanical forces from their outflows must have already swept away the cocoon of gas and dust surrounding the accreting black hole in the early stages of the quasar evolution, at least within a cone coaxial within the accretion disk axis. The extreme accretors in our sample have emerged from the obscured phase, but are still affected by recent star formation in the chemical composition of the line emitting gas and by host galaxy star formation. The most luminous ones meet the definition of "cold quasars" (Kirkpatrick et al., 2020), with star formation rate (SFR) in excess of 200 $M_{\odot}yr^{-1}$.

Barthel et al. (2017) reported a SFR-absorption trend for the radio-loud QSRs, this suggests that starburst-driven superwinds on the 1-10 kpc scale are responsible for the associated metal absorption. More evidence of star formation in the circumnuclear region of AGN has been shown for Type-II AGN by Chen et al. (2009), these source generally show a young stellar population, and the higher the fraction of young stars, the higher the Eddington ratio. This intrinsic connection strengthens the evidence for the role of supernova (SN) in triggering BH activities, consistent with a scenario in which turbulence excited by SN is responsible for the transportation of gas to the central AGNs.

1.6 Outline of this thesis

In this thesis we analyze the relation of quasars with a high accretion rate with the evolution of galaxies in the Universe by studying its spectroscopic properties in the ultraviolet, to derive properties such as the luminosity and metallicity of the central region. The aim of this thesis is to investigate the metallicity-sensitive diagnostic ratios of the UV spectral range for a sample of extreme Population A quasars i.e., for highly accreting quasars, capitalizing on the recent developments by Śniegowska et al. (2021, hereafter S21). At variance with previous work, S21 relied on (1) the decomposition of the emission line profiles in a broad component, symmetric at rest frame, and a BLUE component associated with the prominent blue-shifted excess observed in high-ionization lines of these sources (e.g., Sulentic et al., 2017; Martinez-Aldama et al., 2018), and (2) the use of diagnostic intensity ratios involving metal lines and HeIIλ1640.

We use a sample of 42 quasars spectra from Sloan Digital Sky Survey Data Release 12, where we have the presence of 36 spectra with a type 1 spectral classification and the remaining 6 are classified as broad absorption line quasars (BALQ). The sample have a spectral coverage of 1000 to 3000 Å which places them in the UV range and their redshift is centered at z = 2.2. Under the context of 4DE1, our sample is classified as A3 and A4 according to criteria 2 and 3 mentioned in section 1.4.2, which by means of spectral flux ratios in the UV indicates that the sample presents a high accretion rate. The purpose of using observational data in this work is to compare flux ratios of spectral lines from the sample with synthetic flux ratios from models computed with the Cloudy photoionization code, following S21 approach. This comparison was only possible for the 36 type 1 spectra since for the 6 remaining BALQ some emissions were absorbed and therefore excluded from this analysis. In addition, physical parameters of these sources will be determined in order to find possible correlations that may be useful for subsequent studies.

This thesis is divided into 6 chapters. Chapter 1 shows the historical aspect of galaxies with an active nucleus as well as the context of the 4DE1 under which this work is approached. Chapter 2 is dedicated to explaining the sample selection and the observational data used in this study. Chapter 3 describes the analysis of the sample: the multi-component procedure, the determination of physical parameters, and the numerical simulations performed with the Cloudy photoionization code. The main results obtained in this study are presented in Chapter 4 and its respective discussion is in Chapter 5. The conclusions as well as the future work are described in Chapter 6. Finally, Appendix A show the Figures of the `specfit` results for the 42 sources of the sample. Appendix B lists the tables of flux ratios dependent on metallicity and its error.

The following work present the methods and results from Garnica et al. (2022, hereafter G22), submitted to Astronomy & Astrophysics. G22 is the second paper in a series, being S21 the first one, therefore we are following the same analysis guideline. As a thesis, it is important to us to specify the work done by the defender to the one done by the collaboration, therefore, we present a list of the sections were the defender did not contribute entirely.

- Section 3.7: The Cloudy Simulations were performed by P. Marziani and S. Panda, since they have a bast experience computing photoionization models and also they have access to the computational facilities required to performed them. However, these models were analysed and visualized by the defender and hence the results shown in Sec. 4.5.1 are her product.
- Section 4.5.2: The Z estimates for relaxing constraints (U, $n_{\rm H}$) were carried out by P. Marziani. We decided to include this result in the thesis to compare them with the Z estimates for fixed constrains and the results of S21.
- Chapter 5: The defender contribute actively among the sections of Chapter 5 but the work presented in this Chapter is a general product of the G22 collaboration.

Chapter 2

The Sample

2.1 Sloan Digital Sky Survey

The Sloan Digital Sky Survey (SDSS) is a comprehensive mapping project, aims to map the vast majority of the sky in detail, determining the positions, color indexes and brightness of almost 100 million objects (mainly galaxies and stars in our galaxy). To obtain data, the SDSS uses the telescope located at the Apache Point Observatory in New Mexico and, since the phase IV, also the Irénée du Pont Telescope at Las Campanas Observatory in Chile, both with a size of 2.5 m.

The mappings are composed of multi-color images for one third of the sky and spectra of millions of astronomical objects. This mapping project began operations in 2000, having already more than a decade of design and construction. The SDSS has gone through several phases:

- SDSS-I (2000-2005)
- SDSS-II (2005-2008)
- SDSS-III (2008-2014)
- SDSS-IV (2014-2020)
- SDSS-V (2020-2025)

The phase used to collect the data in this work was the data release 12 (DR12) of the SDSS-III phase, which includes observations up to July 2014. The DR12 also includes all spectra and derived stellar parameters measured by the Sloan Extension for Galactic Understanding and Exploration (SEGUE), as well as all spectra from the original Sloan Digital Sky Survey. Each Data Release can include four types of data:

- images
- optical spectra
- infrared spectra
- cataloged data

The DR12 consists of comprehensive data sets from BOSS, APOGEE, and MARVELS radial stellar velocity measurements. The DR12 includes the complete SDSS-III optical spectroscopy: over four million spectra. These spectra include all the spectra of galaxies, quasars and stars collected by the Baryon Oscillation Spectroscopic Study (BOSS), along with catalogs of galaxy parameters estimated in diverse ways.

2.1.1 Apache Point Observatory

The Apache Point Observatory located in southeastern New Mexico (latitude 32° 46'49.30 " N, longitude 105° 49'13.50 " E) at 2788 m a.s.l. has an altazimuth telescope 2.5 m f/5 Ritchey-Chrétien modified from the Sloan Foundation. This telescope has a 1.08 m secondary mirror and two correction lenses that provide a distortion-free field of view. One of these lenses is the Gascoigne Astigmatism Corrector, while the other is one of a pair of highly aspherical correctors. Among these two, one is for imaging and the other for spectroscopy. The telescope is powered by a wide area multiband CCD and two fiber-fed dual spectrographs. The first light of this telescope was in 1998 and began operations in 2000 (Gunn et al., 2006).

The great advances in detectors and computational processing, together with new capabilities for instrument control, gave the possibility to carry out a study of the sky over wide areas of the optical sky in this new observatory. In order to carry out this type of study, to create spectroscopic samples of galaxies and quasars that exceed the amount that already exist, it was necessary to carry out significant innovations:

1. A large, optically, mechanically and electronically complex camera for collecting image data and providing proper astrometric calibration. The SDSS camera consists of 30 CCDs with 2048x2048 resolution and 24 CCD with 2048x400 resolution.

2. A spectroscopic system that can simultaneously obtain 640 spectra with wide wavelength coverage (3800–9200 Å) and efficiently configured for each field in the sky. The SDSS uses two dual fiber optic powered spectrographs.

3. A data acquisition system that can reliably store incoming data and provide minimal real-time analysis for quality control, focus, etc.

4. A data processing system that can automatically and rapidly calibrate observations, identify objects, and measure their properties from the tens of gigabytes of data produced in a typical night of imagery observations, to select the spectroscopic targets within a short time of image data acquisition.

5. A telescope featuring an extremely low-distortion, wide-angle focal plane and extremely precise units, allowing rapid switching between imaging and spectroscopic modes to adapt to changing weather and viewing conditions.

2.2 Sample Definition

Our sample consists of quasars showing an Eddington ratio $L/L_{edd} \approx 1$, which characterizes them for having a high accretion rate and hence as xA sources (Marziani & Sulentic, 2014a). In optical images, they can be observed as point-like objects (e.g., Figures 2.1a and 2.1b) similar to stars but their spectra show a power law continuum, absorption and emission lines which provide us with diagnostics of the physical and dynamical conditions of these sources by means of the analysis of spectral lines flux ratios and the profile or emission shape.

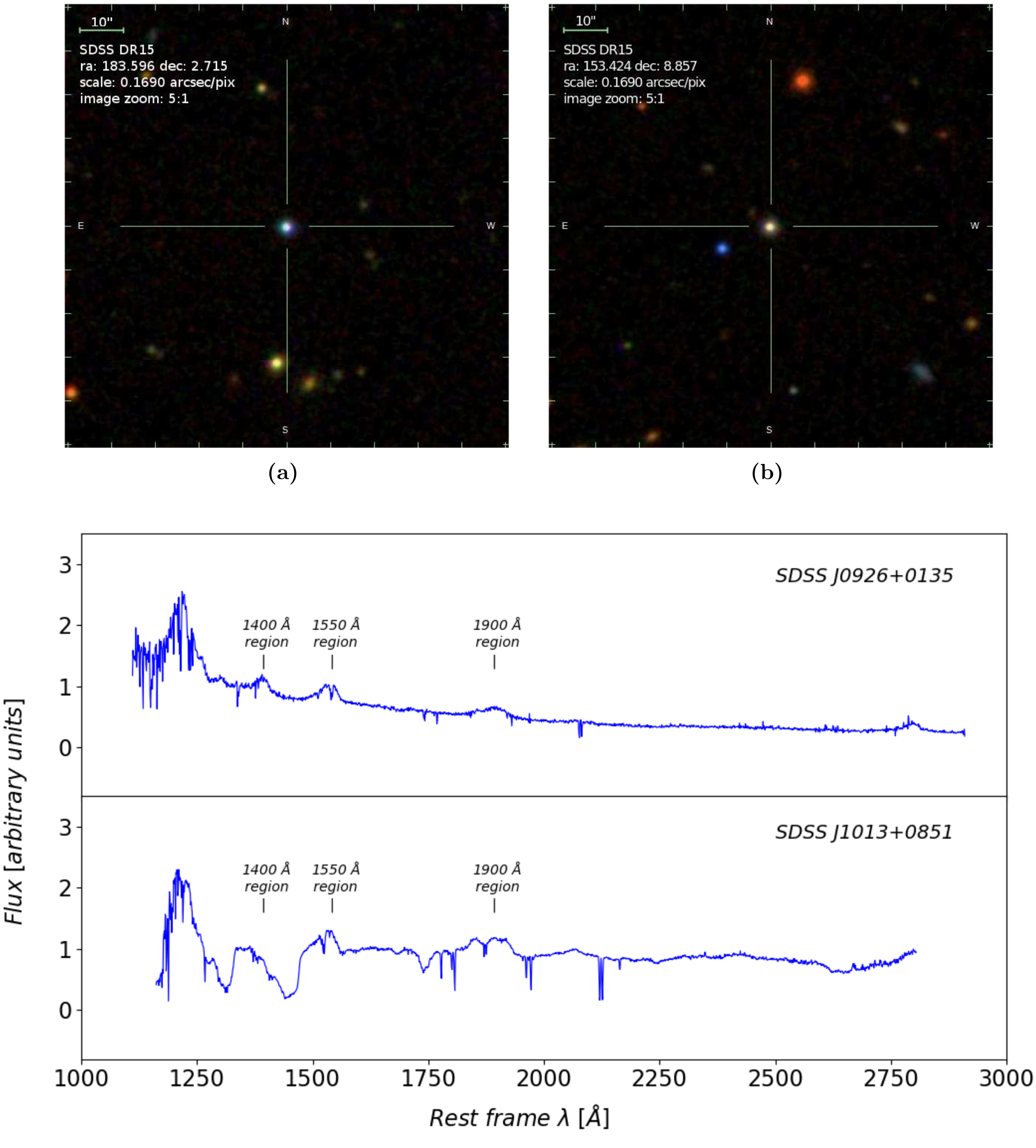

(a) **(b)**

(c)

Figure 2.1: UV spectra of a Type 1 and BALQ sources. (*a*, *b*) SDSS J0926+0135 and SDSS J1013+0851 optical images from the skyserver.sdss.org. (*c*) *Top.* SDSS J0926+0135 spectra as an example of a regular Type 1 source in our sample, the three regions of interest centered at 1400, 1550 and 1900 Å are clearly identified. *Bottom.* SDSS J1013+0851 spectra as an example of a BALQ source. The 1400 Å region is completely absorbed as well as the blue side of the region centered at 1550 Å.

The xA sources sources considered in this study have rest-frame UV spectra from SDSS DR12 with a coverage of 1000-3000 Å where we can find: (1) the strongest high ionization lines (HIL) associated with resonance transitions (i.e., SiIVλ1397, CIVλ1549), (2) usually weak low ionization lines (LIL; e.g., SiII, [OI]λ1304) and (3) several inter-mediate ionization lines (IIL) from transitions leading to the ground state (e.g., AlIIIλ1860, and the intercombination lines SiIII]λ1892, CIII]λ1909). Additionally, the flux ratios of spectral lines are sensitive to (1) density, if one of the lines involved in the ratio has a defined critical density, (2) ionization level, for line ratios that come from transitions that occur in different ionic species of the same element and (3) chemical composition if the line ratios involve a line of a heavy element and HeIIλ1640 or CIVλ1549 (Marziani et al., 2015). This spectroscopic information corresponds to the clouds surrounding the accretion disk at a distance believe to be $\lesssim$ 1000 gravitational radii (Kaspi et al., 2007), one of the regions closest to the central supermassive black hole that these sources contain in its nucleus and helps us to know the conditions of the emitting region.

Our DR12 initial sample consisted of 526 objects with a redshift range centered at z = 1.5-2.2 and a moderate-to-high S/N in the continua. The redshift was chosen in this range so the UV range could be observed by the spectrograph of the SDSS in the optical. Based on a semi-automatic selection using the AlIII/ CIII] flux ratio as a high accretion rate indicator according to (MS14), the original sample was reduced to 120 objects. Subsequently we restricted the redshift range centering it at $z \approx 2.2$ so it would be possible to observe these objects in the H band (between 1.5-1.8 μm) and to obtain observations of Hβ in the infrared. This will give us the possibility of an eventual comparison of high accretion rate indicators at different regions of the electromagnetic spectrum such as (Hβ/Fe) Finally, this restriction vets our sample to 42 objects that are used in this work, where they are all type-1 quasars, with 6 of them classified as Broad Absorption Line Quasars (BALQ).

In summary, the 42 SDSS sources in this study are bright quasars ($r < 19$) with S/N from 10 up to 50 around 1400 Å. They are located between $-11^\circ < \delta < 10^\circ$ under a redshift coverage of $2.13 < z < 2.42$. Each spectrum is similar to one another, except for a few outliers which will be analyzed in Chapter 4. The 6 sources identified as BALQ were discarded from the fitting procedure of the 1400 Å region, for the 1550 Å region we only discarded 4 sources this is due to the strong absorptions in these regions were the emission feature is almost completely blur out. We delimited the sample to our 36 type 1 spectra study sources for the analysis shown in Chapter 4.

2.2.1 Sample Processing

The SDSS is in charge of the data reduction they collect to optimize the observational information.

The Apache Point Observatory data from the camera, photometric telescope and spectrograph are transferred to Fermilab to be processed and calibrated using the *pipelines* originally described in Stoughton et al. (2002) and updated for each Data Release. Spectroscopic *pipelines* are used for the spectra, which consist of two important steps: `spectro2d` and `spectro1d`.

- `spectro2d`: it is responsible for reducing the raw data (two-dimensional spectrograms) produced by the spectrograph and calibrating them by flux units.

  First the subtraction of the *bias* is carried out, this is the intrinsic noise produced by the operation of the CCD, after this, each raw image is divided by a flat field image that was uniformly illuminated to obtain pixel by pixel variations.

  The resulting spectrum is calibrated by wavelength using a wavelength scale at rest, adjusting slightly to match the known positions of certain sky lines and correcting to the galaxy rest frame. The wavelength calibration has an accuracy of 10 km s^{-1} or better.

  Starting from 32 fibers per plate, a “ supersky ” is generated which is resampled at each pixel in the spectrum and then subtracted.

  Finally, a spectrophotometric flux calibration of the individual exposures is performed. The final result of `spectro2d` are calibrated spectra by wavelength [Å] and flux density [10^{-17} ergs cm^{-2} s^{-1} Å^{-1}].

- `spectro1d`: it analyzes the output spectra produced with `spectro2d` and determines the classification of the source whether it is galaxy, quasar, star or unknown and also determines the redshift of these objects.

  This routine is in charge of identifying the candidates for spectral lines using a wavelet transform to the continuum subtracted from the spectrum and compares the candidates with a list of spectral lines commonly found in galaxies and quasars to identify them. Once the spectral lines have been identified according to the level of confidence associated with the routine, it is possible to associate a redshift to the spectrum. If the lines with which the source's redshift was determined are found only in quasars then the source is provisionally classified as a quasar.

  Another routine looks for high redshift quasars ($z > 2.3$) by identifying spectra with the characteristics of the Ly_α forest: a broad emission feature with more fluctuations on its blue wing than on its red one.

  All objects get a classification using `specClass`. This classification can be quasar, high redshift quasar, galaxy, star, late-type star, or unknown. If the object has been identified as a quasar by the emission line routine, and if the redshift of the emission line is chosen as the final redshift, then the object retains its quasar classification.

2.2.2 Additional redshift correction

xA sources are characterized by a strong asymmetric blue-shifted component mainly in the regions centered at 1400 and 1550 Å (e.g., Sulentic et al., 2007b, 2017; Vietri et al., 2018), the most prominent emission features of our sample and the ones employed by the SDSS *pipeline*. Even if the AlIIIλ1860 line is in most cases unshifted (within ± 200 km s^{-1}) with respect to the rest frame (Buendia-Rios et al. 2022, in preparation), this blue component is occasionally present in the blue wing of the AlIIIλ1860 doublet causing a wrong measurement of the rest frame of this emission and therefore a misinterpretation of the source's redshift and the blend components in the region (Martínez-Aldama et al., 2017; Marinello et al., 2020).

We decide to verify our sample redshift alongside Mg IIλ2800 rest frame, which is a low-ionization potential emission line usually characterized by a symmetric line profile. For A3 and A4 bins, this emission may present a blue displacement but not up to 300 km s^{-1} (Marziani et al., 2013), which does not lead to any drastic misinterpretation of the line blends. We fitted a Gaussian for the Mg IIλ2800 using the IRAF `splot` task to measure its central wavelength and then add a redshift correction if necessary using the IRAF *dopcor* task. These z corrections were up to 0.012 (as shown in Column 4 of Table 2.1), which guarantee us a more precise analysis of the individual components specially for the strong blueshifted features at λ1400 and λ1550. For the few cases with a lower spectral coverage we cautiously use the rest frame of the Al III doublet as a guidance.

We decide to use the Mg IIλ2800 line because it is a very strong emission line that appears in almost all spectra. Other lines such as Si II or [O I]λ1304 are weaker lines affected in some cases by low S/N and in other cases contaminated by absorption lines. In the case of C III] and Si III], in xA objects both lines are heavily blended, also because they are expected to have similar fluxes, so is not possible to use them to set the restframe.

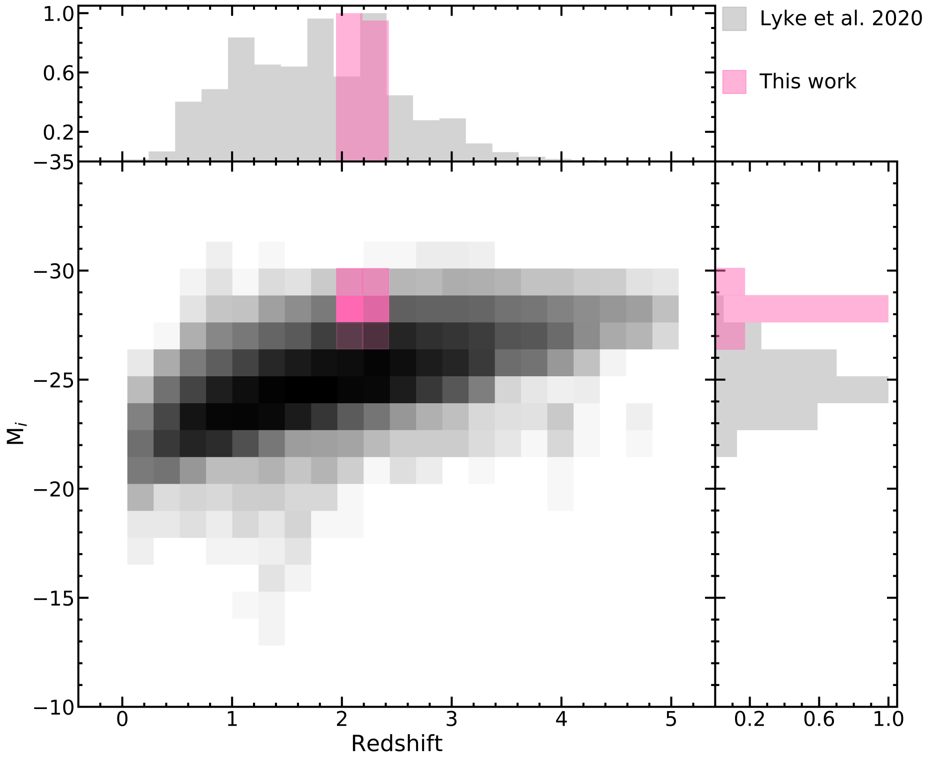

Figure 2.2: Redshift distribution of the sample as a function of the absolute $i-$band magnitude. The gray scale squares show the Lyke et al. (2020) data and the pink squares is the sample used in this work. *Upper panel* shows the normalized redshift distributions, the pink distribution shows our adittional corrected redshift. *Right panel* the normalized absolute $i-$band magnitude distributions for both Lyke et al. (2020) and our sample.

2.2.3 Sample properties

The basic properties of our sample are presented in Table 2.1: (1) SDSS name, (2) redshift from the SDSS, (3) the difference between our redshift estimation using MgIIλ2800 and the SDSS redshift $\delta z = z - z_{SDSS}$, (4) the g-band magnitude provided by SDSS Sky Server, (5) the $g - r$ color index, (6) and (7) are the rest-frame specific continuum flux at 1700 Å and 1350 Å respectively, (8) the S/N in the continuum around 1450 Å, and (9) indicates the BAL QSOs and the cross-match objects from the S21 sample.

We chose the Lyke et al. (2020) to compare our sample with a larger sample of quasars and also to cross-match a measure of the brightness of our sample. Lyke et al. (2020) provide a quasar catalog of over ∼750,000 sources that lists a "superset” of all SDSS-IV/eBOSS objects targeted as quasars. Fig.2.2 and Table 2.1 indicate that the sources of our sample are very luminous (at the high-end of the luminosity distribution of BOSS sources at redshift $z \approx 2$, and of rather homogeneous properties. As a consequence, we may not expect strong correlations with physical properties such as L, $M_{\rm BH}$, $L/L_{\rm Edd}$. The sample is best suited to confirm the main results seen by S21, and to improve their statistical significance.

In addition, the scatter in the color index SIQR (semi interquartile range) $g-r \approx 0.07$ with a median $g-r \approx 0.27$ suggests that the sample is not suffering strong extinction save J151636.79+002940.4 ($g-r \approx 1$) and other sources with $g-r \approx 0.4-0.5$ that are all BALQ and were not considered for the analysis.

Table 2.1: Source identification and basic properties

SDSS FULL JCODE (1)	z_{SDSS} (2)	δz (3)	g (4)	$g-r$ (5)	f_{1700} (6)	f_{1350} (7)	S/N (8)	Notes (9)
J002023.12+074041.1	2.4172	0.0047	19.01	0.19	293	424	21	
J003411.37−032618.2	2.1771	0.0049	19.01	0.19	206	412	25	
J003751.90−023845.2	2.2734	-	18.92	0.21	146	351	16	
J010328.71−110414.4	2.1912	-	18.31	0.31	689	1016	20	
J010657.94−085500.1	2.3550	0.0054	18.18	0.11	665	972	20	S21
J012303.46+032900.1	2.3328	0.0032	18.35	0.25	666	969	29	
J021039.51−082303.6	2.1898	0.0043	19.04	0.34	393	551	12	
J021606.40+011509.5	2.2294	-0.0019	18.82	0.52	369	516	28	BALQ
J025255.65−042022.8	2.1309	-0.0033	19.09	0.44	269	229	15	BALQ
J082714.60+030616.1	2.2106	-	19.10	0.32	296	526	14	
J082936.30+080140.6	2.1891	0.0070	18.37	0.31	687	957	36	S21
J083611.10+054806.1	2.2575	0.0035	18.87	0.22	357	549	22	
J084525.84+072222.3	2.2687	0.0196	18.20	0.33	647	975	26	S21
J084719.12+094323.4	2.2947	0.0043	18.87	0.15	388	504	21	S21
J085856.00+015219.4	2.1598	0.0044	17.92	0.26	701	1188	45	S21
J090312.22+070832.4	2.2225	0.0085	18.93	0.26	387	503	30	
J091500.43−020228.5	2.2806	-	18.95	0.13	96	230	15	
J092641.41+013506.6	2.1809	0.0059	18.59	0.34	385	625	28	S21
J092919.45+033303.4	2.2275	0.0048	18.90	0.20	266	395	19	
J093251.98+023727.0	2.1529	0.0049	18.32	0.29	537	684	36	BALQ
J094637.83−012411.5	2.2125	0.0017	18.56	0.18	400	612	40	S21
J101341.85+085126.1	2.2526	0.0100	17.95	0.63	1272	1330	40	BALQ
J102421.32+024520.2	2.3195	0.0081	18.49	0.18	460	695	34	S21
J102606.67+011459.0	2.2596	0.0071	18.98	0.20	440	543	24	S21
J114557.84+080029.0	2.3389	0.0092	18.55	0.37	250	357	13	S21
J120550.19+020131.5	2.1548	0.0022	17.46	0.41	1635	1840	45	BALQ
J121423.01+024252.8	2.1894	0.0129	17.64	0.23	1100	1450	35	
J121506.00+032642.6	2.2240	0.0029	18.49	0.24	683	993	31	
J121906.02+025433.5	2.2976	-0.0066	18.46	0.14	615	869	30	
J123120.55+072552.6	2.3872	-	18.01	-0.08	658	1039	45	
J124409.88+082155.2	2.3569	0.0065	18.58	0.18	614	877	34	
J125934.29+075200.7	2.4188	0.0017	17.92	0.16	862	1354	29	
J131452.64+092735.3	2.2367	0.0098	18.85	0.27	439	624	18	
J141925.48+074953.5	2.3837	0.0030	17.51	0.15	997	1495	50	
J150959.16+074450.1	2.2529	0.0099	18.94	0.28	253	342	17	S21
J151636.79+002940.4	2.2659	-0.0057	18.77	0.96	320	238	25	
J151929.45+072328.7	2.3942	0.0079	18.66	0.17	384	502	21	S21
J154503.23+015614.7	2.1607	0.0122	18.25	0.35	813	1107	24	
J160955.41+065401.9	2.1413	0.0074	18.44	0.33	697	925	28	
J161801.70+070450.3	2.2324	0.0032	18.48	0.26	490	674	26	
J211651.48+044123.7	2.3517	-	18.82	0.22	410	565	43	S21
J214502.56−075805.6	2.1455	0.0025	18.58	0.22	540	744	17	
μ	2.2552	0.0052	18.53	0.27	542	756	27	
σ	0.0623	0.0025	0.29	0.07	159	236	7	
SIQR	0.0817	0.0050	0.43	0.16	301	373	10	

Notes. Columns are as follows: (1) SDSS coordinate name; (2) SDSS redshift; (3) correction to redshift estimated in the present work ($\delta z = z - z_{\mathrm{SDSS}}$); (4) g-band magnitude from SDSS Sky Server; (5) color index $g - r$; (6) continuum flux measured at 1700 Å in units of 10^{-17} erg s $^{-1}$ cm $^{-2}$ Å^{-1}; (7) continuum flux measured at 1350 Å in the same units; (8) S/N measured at continuum level at 1450 Å; (9) additional notes per source. Last row shows the mean values as listed in the columns.

Chapter 3

Methods

This thesis is based on the paper G22, written the most part by the defender. G22 is the second paper in the series (the first being S21) with an extended sample, and therefore we followed the same basic methodology:

1) multi-component analysis of the emission blends in the UV spectra;

2) `CLOUDY` photoionization modelling;

3) metallicity estimates of the sample by comparing observed fluxes and `CLOUDY` synthetic fluxes at different U and n_{H} values.

The 13 sources from S21 are also presented in this work (as described in Chapter 2) but they were re-processed and re-fitted according the following sections.

Unlike S21, the defender created a routine using Python to estimate the errors of the fitting procedures (Sec. 3.4) and an alternative procedure to measure the intensity of the emissions in a much simpler way (Sec. 3.5). Also, we estimated physical parameters (Sec. 3.6) in order to seek for correlations among them and emission line fluxes.

3.1 Line interpretation and diagnostic ratios

As mentioned in Chapter 2, our spectral coverage is characterized by HIL, IIL and LIL. These emissions need a favorable environment for their associated transitions to occur, and in turn they provide insight on the gas surrounding the ionization source. Population A sources are characterized mainly by broad components described with symmetric profiles plus strong asymmetric blueshifted components associated with high-ionization emission (Leighly & Moore, 2004; Marziani et al., 2010). We are not considering the substraction of an inner part of the NLR in our models because as described in Sulentic & Marziani (1999) we believe we are observing only the BLR, especially in extreme Population A. Hence, we decomposed our regions of interest mainly using two emission profiles a central broad component and a blueshifhted component.

- The broad component (BC), a rest-frame emission modeled with a Lorentzian profile. This symmetric profile is believed to be associated with a virialized system.
- The blueshifted component (BLUE), a strong flux excess mainly in the blue wing of HILs (for our sample CIVλ1549 and SiIVλ1397) that are resonance transitions, ultimately ascribed to high velocity winds. We modeled this emission with a very broad skew Gaussian profile as an interpretation of the high velocity winds in which these emissions occur.

The profiles of both BC and BLUE are constrained by the reduction to minimum χ^2 on the full extent of the line.

3.1.1 Broad component

The analysis follow the same procedure of S21, and relies mainly on the ratios AlIII, CIV, SiIV +OIV] over HeII. These ratios give us more direct information about the metal content even if HeII is a weak emission mixed in the red wing of CIV. It might be underestimated and set an unrealistic upper limit for the metallicity. The issue will be discussed in Section 3.2.

In addition, we considered the line ratios (SiIV+OIV])/CIV, AlIII/CIV, and AlIII/SiIII]. The first ratio is frequently computed in metallicity studies of the BLR (Nagao et al., 2006b; Shin et al., 2013). The second one is more related to the possibility of AlIII overabundance,there could be two ways of increasing AlIII with respect to SiIII] (1) a selective enhancement of the Al abundance with respect to Si or (2) collisional ionization due to a heating mechanism different from photoionization (Negrete et al., 2012b). The third ratio is associated with the selection of xA sources and is strongly dependent, for a fixed SED, on both Z and n_{H} (Marziani et al., 2020). These topics will be resumed in Chapter 5.

3.1.2 BLUE component

We measured BLUE components for three blends: the one at λ1400, mostly due to SiIV and OIV] emission, and ones for the CIV and HeII at the 1550 Å region. So we will base our analysis on three ratios, with only two of them being independent: CIV/HeIIλ1640, (SiIV+OIV])/HeIIλ1640 and (SiIV+OIV])/CIV. We also sporadically measure a component on the blue side of AlIII (Columns 5-8 of Table 4.1), although we would not considered diagnostic ratios involving BLUE AlIII because this component shows a profile narrower than those of CIV, SiIV+OIV] and HeIIλ1640. Also, the measurement of AlIII BLUE intensity is uncertain, as it is affected by the SiII emission. Specific to the BLUE intensity ratios, we note that the (SiIV+OIV]) is often affected by heavy absorptions (even more than CIV) that may systematically lower the Z estimates from the ratio (SiIV+OIV])/HeIIλ1640.

Table 3.1: Internally defined functions in `specfit`

Function	Description
linear	linear continuum at F_λ
power law	power law continuum at F_λ
blackbody	blackbody continuum at F_λ
recomb	optically thin recombination continuum
gaussian	Gaussian line profile
lorentz	modified Lorentzian profile
labsorp	Gaussian absorption line profile
usercont	user-supplied continuum
userline	user-supplied emission line profile
userabs	user-supplied absorption line profile

Kriss (1994) table 1 extraction.

3.2 Multi-component fitting procedure

We analysed our sample using the `specfit` task (Kriss, 1994) to deblend our regions of interest centered at 1400, 1550 and 1900 Å in our spectra. This task runs in the Space Telescope Science Data Analysis System (`STSDAS`) contrib package, the software system for calibrating and analyzing data from the Hubble Space Telescope. `STSDAS` is part of the Image Reduction and Analysis Facility (`IRAF`) (Tody, 1993) software developed at the National Optical Astronomy Observatory (NOAO) in Tucson, Arizona (Baggett et al., 2002).

`Specfit` is an interactive task used for fitting a wide variety of emission-line, absorption-line, and continuum models to an input spectrum, which can be an unidimensional image or an ASCII file. This routine has a wide variety of internally defined functions such as those mentioned in Table 3.1. In addition, the *usercont*, *userline* and *userabs* functions allow the user to include complex models for the continuum, emission lines and absorption lines respectively. `Specfit` use these functions to create models based on an input file of parameters which describe the model by initial guesses, all components used to create a model are assumed as additive except for absorptions.

The input file is an ASCII document, its first line indicates the name of the model, proceed by `begin`, which must match the name of the file. Subsequently,

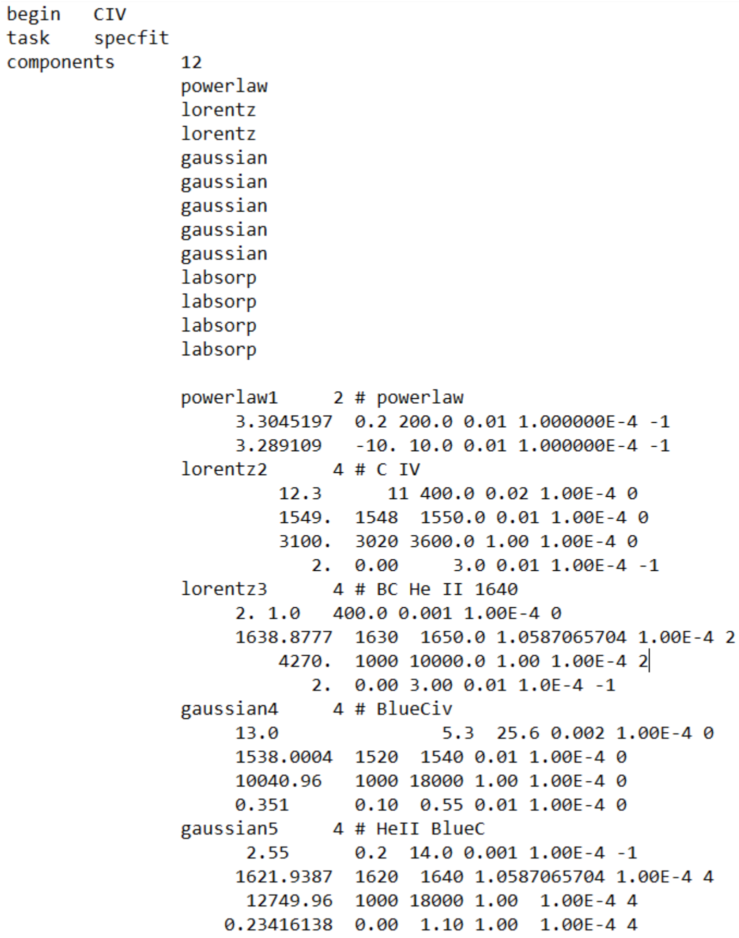

```
begin   CIV
task    specfit
components      12
                powerlaw
                lorentz
                lorentz
                gaussian
                gaussian
                gaussian
                gaussian
                gaussian
                labsorp
                labsorp
                labsorp
                labsorp

                powerlaw1     2 # powerlaw
                     3.3045197  0.2 200.0 0.01 1.000000E-4 -1
                     3.289109   -10. 10.0 0.01 1.000000E-4 -1
                lorentz2      4 # C IV
                         12.3      11 400.0 0.02 1.00E-4 0
                         1549.  1548  1550.0 0.01 1.00E-4 0
                         3100.  3020 3600.0 1.00 1.00E-4 0
                            2.  0.00     3.0 0.01 1.00E-4 -1
                lorentz3      4 # BC He II 1640
                     2. 1.0   400.0 0.001 1.00E-4 0
                     1638.8777  1630  1650.0 1.0587065704 1.00E-4 2
                         4270.  1000 10000.0 1.00 1.00E-4 2
                            2.  0.00 3.00 0.01 1.0E-4 -1
                gaussian4     4 # BlueCiv
                     13.0               5.3  25.6 0.002 1.00E-4 0
                     1538.0004  1520  1540 0.01 1.00E-4 0
                     10040.96   1000 18000 1.00 1.00E-4 0
                     0.351      0.10  0.55 0.01 1.00E-4 0
                gaussian5     4 # HeII BlueC
                      2.55      0.2  14.0 0.001 1.00E-4 -1
                     1621.9387  1620  1640 1.0587065704 1.00E-4 4
                      12749.96  1000 18000 1.00  1.00E-4 4
                    0.23416138  0.00  1.10 1.00  1.00E-4 4
```

Figure 3.1: 1550 Å region input file extraction. This input file is useful for the 1550 Å fitting procedure: CIVλ1549 and HeIIλ1640 broad and blueshifted components. The first line indicates the file name, follow by the total number of components and the list of functions. Subsequent, following the order given in the list of functions, each function is described according to the number of lines necessary per function.

the total number of components to be used to create the model and its functions are listed. To specify the function values of it is necessary to write the name of the function with the component number that corresponds to it followed by the number of lines of parameters necessary to describe it. For example, in the Figure 3.1 in the first component `powerlaw1` is followed by the number `2` which indicates that the power law continuum depends on two variables (parameter lines) which correspond to the flux at 1000 Å and the power law exponent. Another example for the case of an emission is `gaussian4` which is followed by the number `4` which corresponds to the four variables necessary to describe a Gaussian emission profile which are flux, $\lambda_{central}$, FWHM in km s^{-1} and the skewness index. Each parameter line provide in order 1) the value of the parameter, 2) the minimum allowed value, 3) the maximum allowed value, 4) the step size of for minimization search, 5) the tolerance for judging convergence of the fit and 6) a flag indicating wheter the parameter is free to vary (0), fixed at the given value (-1) or linked to another parameter (a positive integer according the number of the component linked).

The `specfit` multi-component fitting procedure is an interactive task, is based on the input file described in the paragraphs above. The parameters values of the input file are only initial guesses to model the components, each parameter can be improved by means of a minimization fit that the routine provides. This fitting is carried out by χ^2 minimization selecting one of five different algorithms, these algorithms are:

- Numrecipe, it is based on Numerical Recipes (Press et al., 2007) marquardt algorithm, usually is the most effective and fastest method. This method is used far from the minimum, continuously changing the preceding value as the minimum is approached.

- Simplex, it uses a mobile simplex in the design space to circle the sweet spot and then reduce the simplex until its dimensions meet a specified error tolerance.

- Marquardt, it is a combination of the gradient slope method and the Gauss-Newton method. The algorithm uses a parameter to decide the size of the step, which takes large values in the first iterations and small values in the later stages. This algorithm occasionally encounters floating point exceptions in complex nonlinear models.

- Gridfit, this algorithm take one or two parameters to then give these parameters a lower limit value specified by the user and increase this value in steps. The steps size are specified by the user until an upper limit is reached.

- Alternate, this method alternately calls the Numrecipe and Simplex methods.

Finally, as a result two files are obtained: (1) log file, which saves the parameters values of the best model and the errors associated with the software; (2) ASCII file suitable for graphing the input spectrum with the generated model and its respective components.

3.3 Regions of interest

We focus our analysis in three regions centered at 1400, 1550 and 1900 Å. These regions are a mix of emission lines (such as blueshifted and broad components) and narrow absorption lines, making it necessary to obtain the best fit according to the minimum χ^2 computed by a non-linear multicomponent program `specfit` within `IRAF`. Each source is fitted individually per region, imposing an overall consistency on the continuum shape. The Figures of the fitting procedure are shown in Appendix A, their upper panel show the continuum shape and its continuum placements while the bottom panels show a zoom to the fitting regions layering its final model and the fit of the blended lines with the appropriate components.

The sample fits were improved through the Simplex minimization method among the options that `specfit` provides, since this method was the most stable to use with the available computer equipment. Each region was analyzed according to Negrete et al. (2012a), and the components specific to the three spectral regions used are in the following sections.

3.3.1 1900 Å region

We start by fitting the continuum, modeled as a local power law, using line-free windows prior and posterior to the emission regions around 1680 Å and 2100 Å. Our continuum sets the range for the fitting procedure, which goes from ∼ 1740 to 2000Å.

We continue adding the broad components such as the AlIIIλ1860 doublet and SiIII]λ1892, modeled using symmetric Lorentzian profiles sharing the same FWHM, since both emissions have a ionization potential below 20 eV in most cases. We fit the CIII]λ1909 emission, using a symmetric Lorentzian profile with an independent FWHM. Surrounding the CIII] emission we can found the FeIII emission, we modeled using the Bruhweiler & Verner (2008) templates, with maximum in the red wing

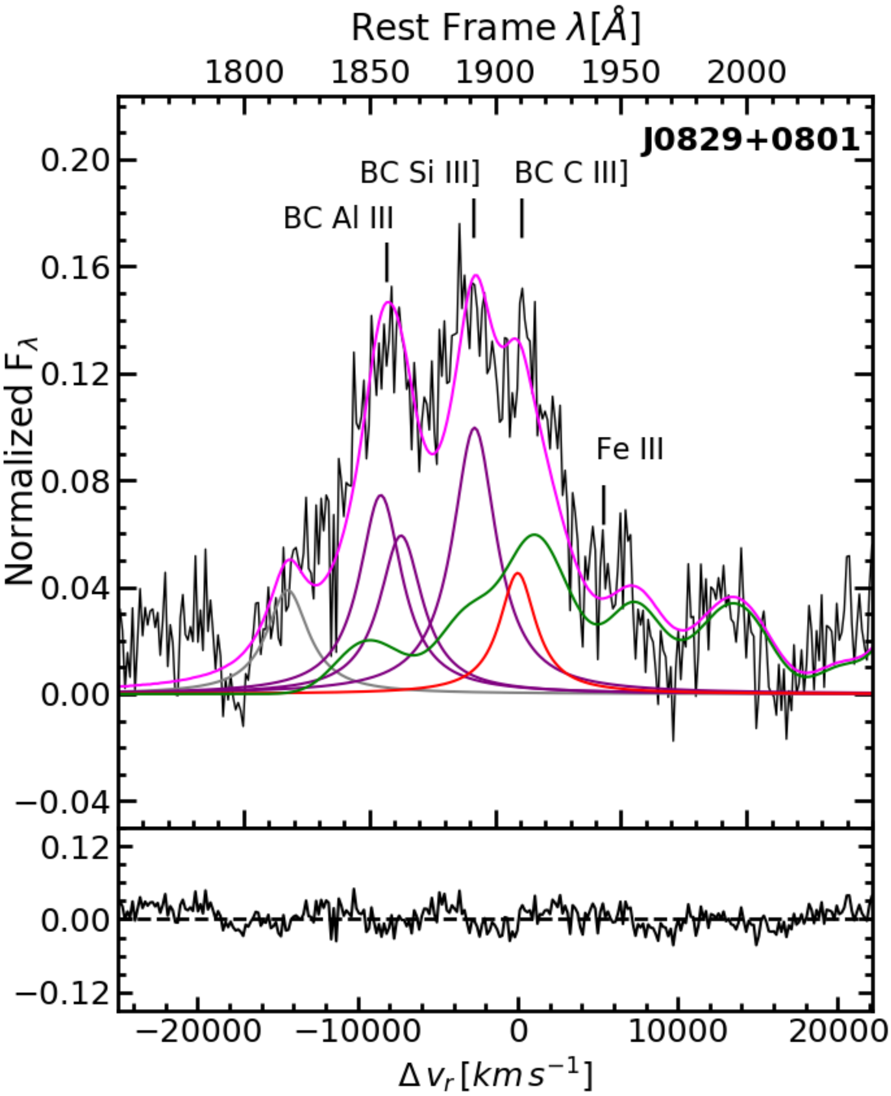

Figure 3.2: 1900 Å region fitting example of a regular type 1 spectra. The Figure shows in black the observed spectra minus the continuum, in pink the `specfit` fitting result, the BC emission of AlIII and SiIII] are shown in purple, CIII] emission is in red, in grey the SiII emission and in green the FeIII template. Upper abscissa is the rest frame wavelength in Å, lower abscissa is in velocity units, and ordinate is normalized flux at 1350Å and continuum subtracted, in arbitrary units. Top right corner indicates the source name.

of the 1900 Å region. It is been shown that these emission lines behave as low ionization lines such as $H\beta$ (Negrete et al., 2014), which supports our emission line profiles choices. Figure 3.2 shows a fitting example of a regular type 1 spectra, the components described above are identified.

Occasionally, we found FeIII emission (for a third of the sample), a FeIII template could not model our data so we individually fit the emission at $\sim$ 1915 Å with a Lorentzian profile and allowed it to vary from general input parameters, we

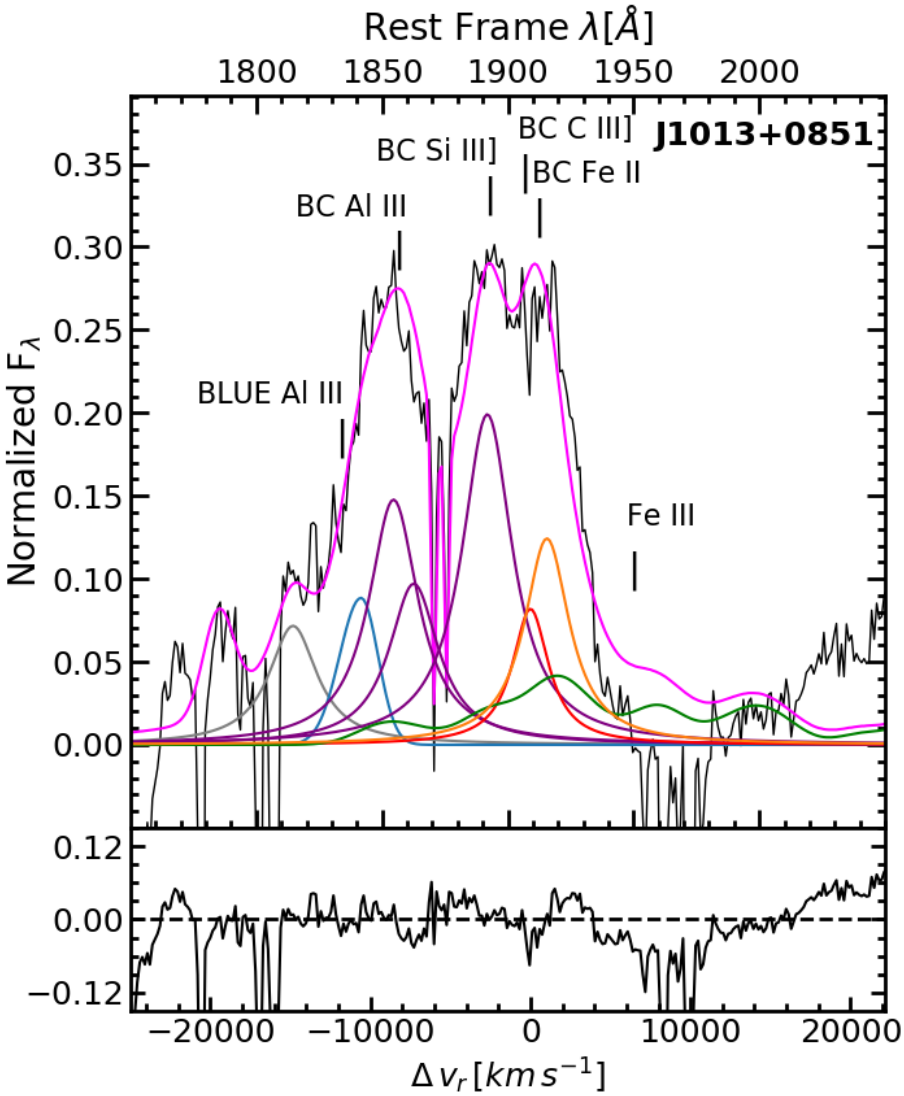

Figure 3.3: 1900 Å region fitting example. The Figure shows in black the observed spectra minus the continuum, in pink the `specfit` fitting result, the BC emission of AlIII and SiIII] are shown in purple, CIII] emission is in red, in grey the SiII emission and in green the FeIII template, the additional FeIII emission is shown in orange. The asymmetric blueshifted emission of AlIII is shown in blue. Upper abscissa is the rest frame wavelength in Å, lower abscissa is in velocity units, and ordinate is normalized flux at 1350Å and continuum subtracted, in arbitrary units. Top right corner indicates the source name.

considered its shift as a free parameter but restricted to vary ± 2Å.. Although this region is believed to be a virialized system, we found evidence of outflows in the blue wing of AlIII. This emission was modeled using a blueshifted asymmetric profile and is identified in this work as BLUE AlIII. Figure 3.3 shows a fitting example for a BALQ spectra with BLUE AlIII and FeII emissions, all components are identified. BLUE AlIII emissions are not exclusive for BALQ sources as shown in the appendix Figures A.5, A.16, A.24 and A.40.

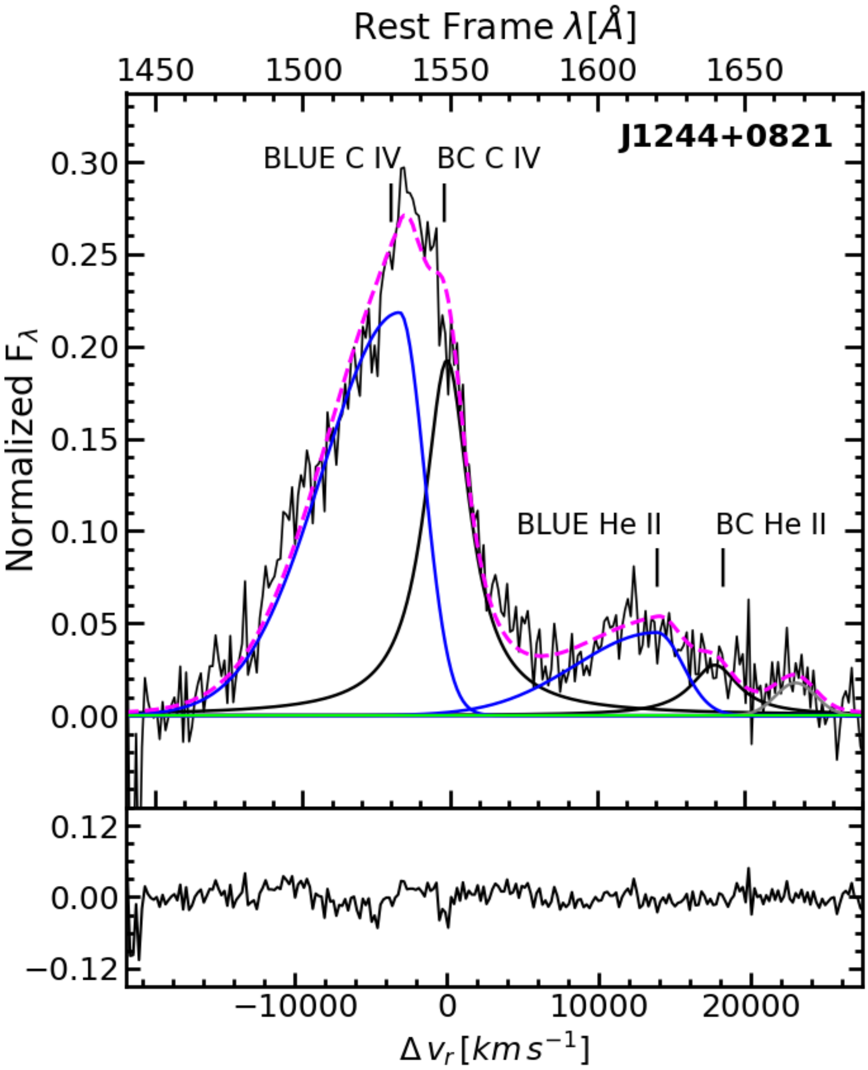

Figure 3.4: 1550 Å region fitting example. The Figure shows in black the observed spectra minus the continuum, in pink the `specfit` fitting result, the BC emission of CIV and HeIIλ1640 are shown in black and their BLUE emission are the blue Gaussians. Upper abscissa is the rest frame wavelength in Å, lower abscissa is in velocity units, and ordinate is normalized flux at 1350Å and continuum subtracted, in arbitrary units. Top right corner indicates the source name.

3.3.2 1550 Å region

We start fitting an continuum as a local power law using emission line free windows near 1450 and 1680 Å. Our continuum sets the base and range for the fitting procedure, which goes from $\sim$ 1450 to 1700 Å.

We continue adding the broad components: CIV and HeIIλ1640. These components where modeled with a Lorentzian profile sharing the same FWHM, black Lorentzians in Figure 3.4. CIV is a stronger emission than HeIIλ1640, which tends

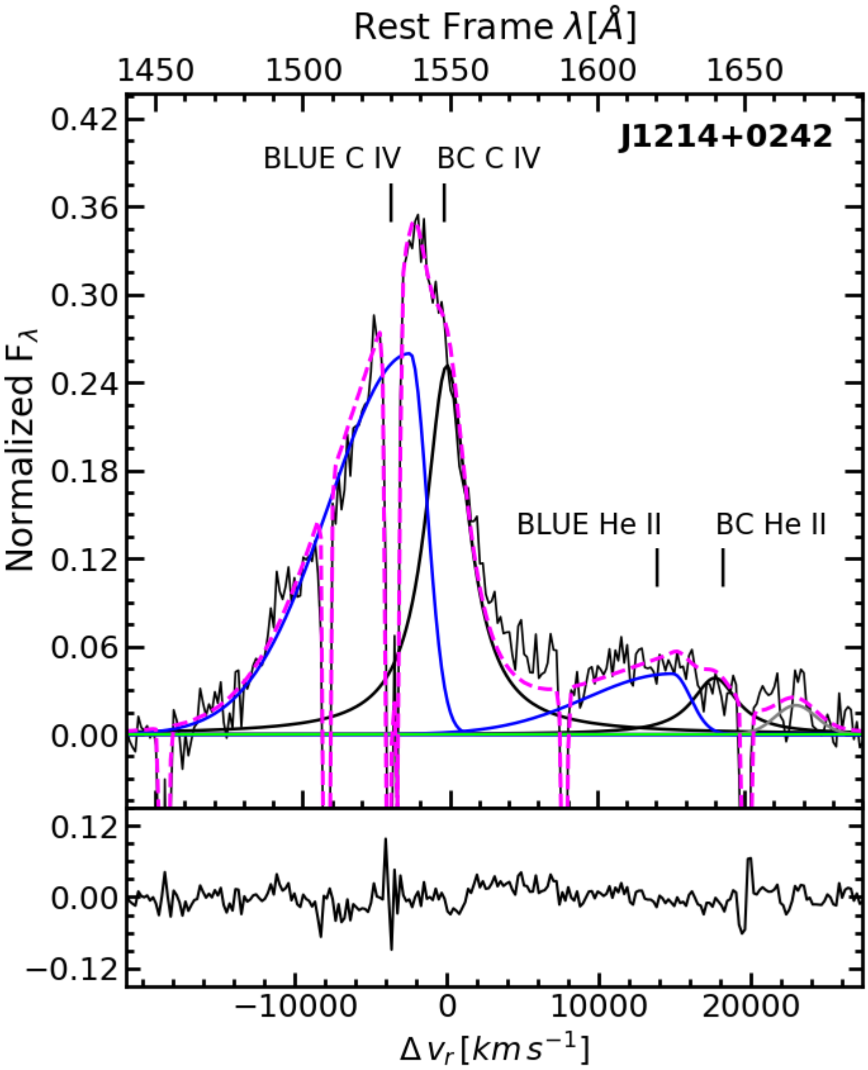

Figure 3.5: 1550 Å region fitting example. The Figure shows in black the observed spectra minus the continuum, in pink the `specfit` fitting result, the BC emission of CIV and HeIIλ1640 are shown in black and their BLUE emission are the blue Gaussians. The hollow sections of the region are absorptions. Upper abscissa is the rest frame wavelength in Å, lower abscissa is in velocity units, and ordinate is normalized flux at 1350Å and continuum subtracted, in arbitrary units. Top right corner indicates the source name.

to be underestimated for low S/N. We also fitted the AlII + OII (grey line in Figure 3.4) to minimize the `specfit` χ^2.

All the sample shows a strong excess in the blue wing of the broad components even after our redshift correction (see Sec. 2.2.2). We fitted this blue excess as BLUE components for CIV and HeIIλ1640 modeled with asymmetric Gaussian profiles (one Gaussian for each component) sharing the same FWHM and displacement from its restframe broad component (blue Gaussians in Figure 3.4). Both blue emissions tend

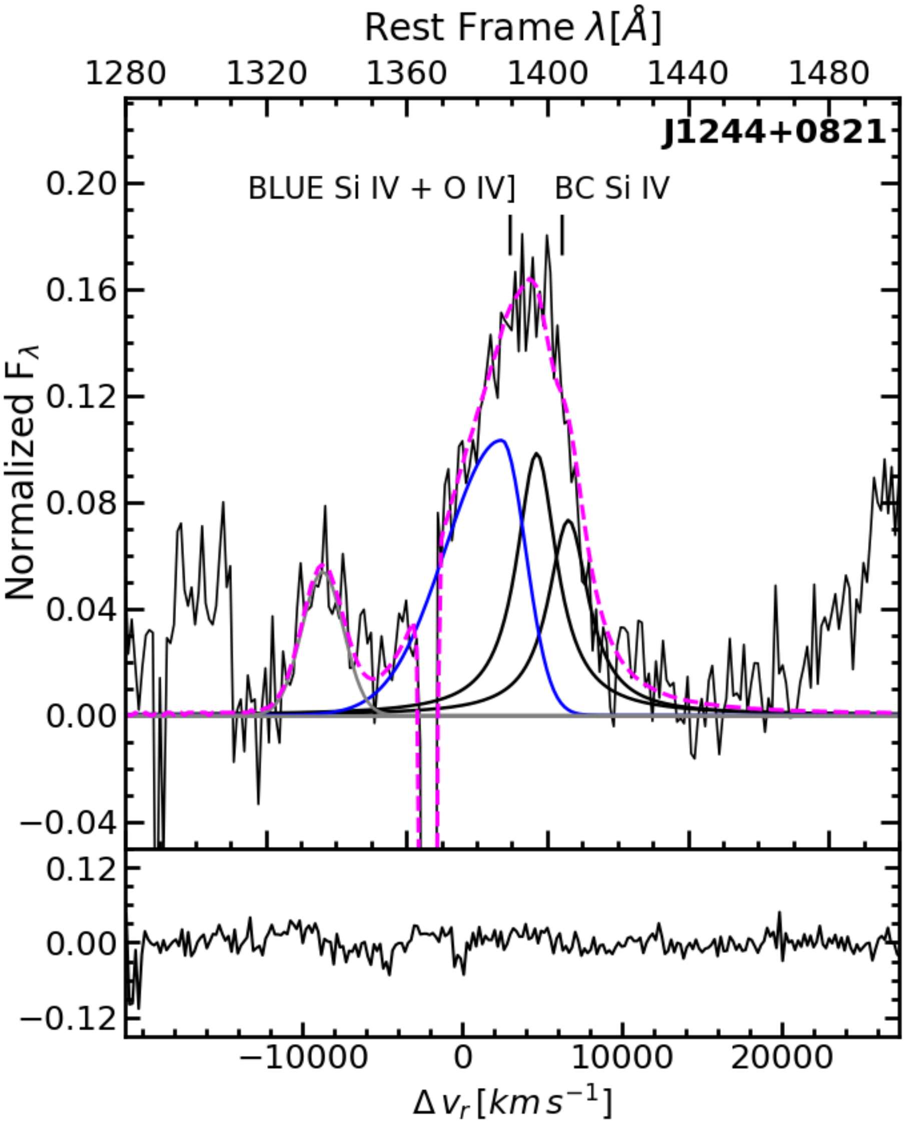

Figure 3.6: 1400 Å region fitting example. The Figure shows in black the observed spectra minus the continuum, in pink the `specfit` fitting result, the BC emission of SiIV is shown in black and the BLUE SiIV+ OIV] emission is the blue Gaussian. The hollow sections of the region are absorptions. Upper abscissa is the rest frame wavelength in Å, lower abscissa is in velocity units, and ordinate is normalized flux at 1350Å and continuum subtracted, in arbitrary units. Top right corner indicates the source name.

to dominate this region with FWHM up to ∼ 15,000 km s^{-1}. If needed, we also fitted absorption lines modeled as narrow Gaussians and included when necessary to improve the fit, especially in the blue wing of the profile as shown in Figure 3.5.

3.3.3 1400 Å region

We start fitting an continuum as a local power law using emission line free windows near 1280 and 1450 Å. Our continuum sets the base and range for the fitting procedure, which goes from $\sim$ 1320 to 1450 Å.

The modeling was done as for the 1550 Å region but skipping the BC emission of , since this emission is associated with a transition between levels with a well-defined and relatively low critical density (Marziani et al., 2020), so that its BC intensity is probably low. We fitted the broad components of the SiIV doublet ($\lambda\lambda$1394,1402) modeled with a Lorentzian profile sharing the same FWHM, black Lorentzians in Figure 3.6. If detected, we fitted the CIIλ1335 (grey line in Figure 3.6) with a symmetric profile to minimize the `specfit` χ^2.

We also found a strong excess in the blue wing of the region as in 1550 Å region. We fitted this component as a broad asymmetric Gaussian profile of the blend emission of SiIV+ OIV]. The absorptions lines (hollow sections in Figure 3.6) tend to be more stronger than in 1550 Å region and we modeled as well as narrow Gaussians and included when necessary to improve the fit, especially in the blue wing of the region.

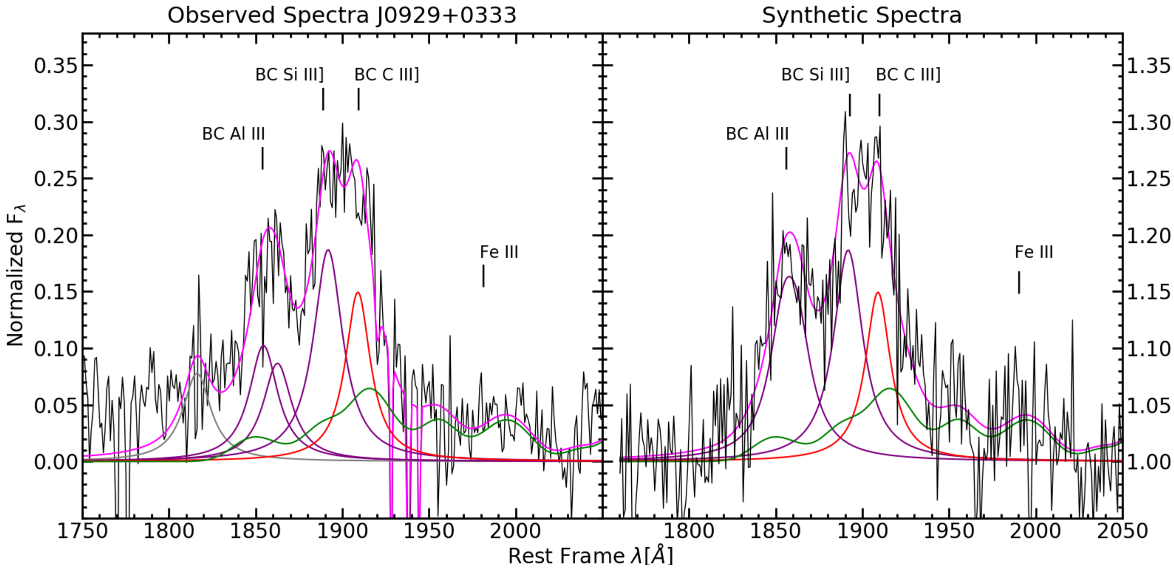

Figure 3.7: The panels show both the observed and synthetic spectra of J0929+0333. Abscissa correspond to the rest frame wavelength in Å and ordinate normalized flux. *Left:* In black is the observed spectra of minus the continuum, in pink the `specfit` fitting result, the BC emission of AlIII and SiIII] are shown in purple, CIII] emission is in red and in green the FeIII template. *Right:* In black is the synthetic signal, the sum of the components plus a noise, the BC emmision of AlIII (the sum of the doublet) and SiIII] are shown in purple, CIII] emission is in red and in green the FeIII template.

3.4 Error estimation on line fluxes

As described above, the regions of interest in our spectra are blended into a very broad spectral emission. Each final model is affected by the interpretation of the authors; however, the final parameters of each model component were determined by `specfit` via an objective determination of the minimum χ^2 i.e., of the lowest residuals. We believe the main source of uncertainty in our measurements are the noise and the continuum placement which affects the deblending interpretation, once the model components have been selected.

To estimate the flux, centroid and FWHM errors we created a Python routine that consist of five basic steps:

1) Create an array of possible values for each free parameter, these free parameters are:

    - Flux: we vary the amplitude of the emission line ± 50 % in steps of 1 % the original amplitude.

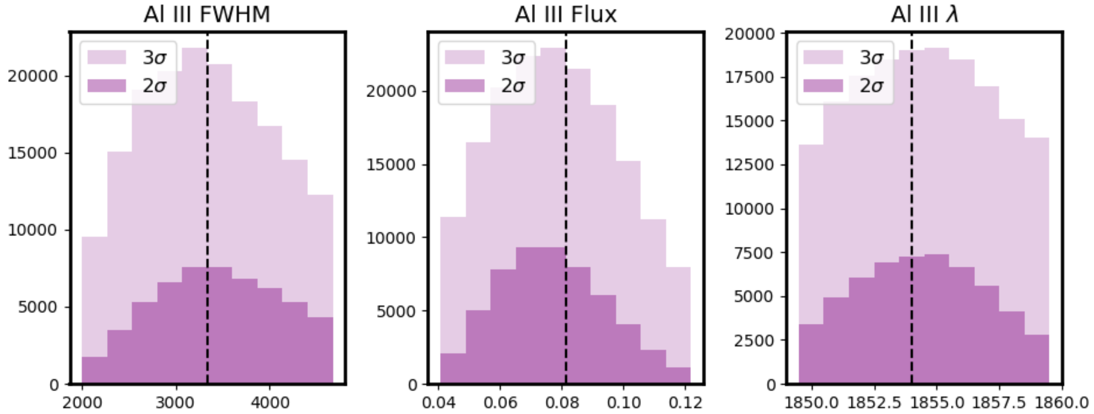

Figure 3.8: Distributions from our error routine for the FWHM , flux and wavelength of AlIII. The light and middle purple regions show the sort of the respective array at a confidence level of 3σ and 2σ as label in the figure.

- Centroid: we vary the centroid position ±5 Å for symmetric emissions and ±10 Å for asymmetric emissions in steps of 0.1 Å.
- FWHM: we vary the width of the emission ± 40 % in steps of 1 km s^{-1}.

2) Create a model, using our routine, with random parameters from our arrays;
3) Iterate the routine as want it, we decided to settled for 500,000 iterations which translates into 500,000 random models;
4) Sort the 500,000 arrays of iterations imposing a 3σ confidence level;
5) Measure the dispersion of the distribution for each array of free parameters.

The input of the routine to create the arrays is a synthetic spectrum created with the data from a `specfit` model plus noise to create a compatible spectrum with the characteristics of our sample, as shown in fig. 3.7. As mention above, we iterate this routine 500,000 times to get an array of models of the given input. For each iteration we also calculate the reduced χ^2_ν of the random model according to:

$$\chi^2_\nu = \frac{1}{n_\mathrm{d}} \sum_{\mathrm{i}=1}^{n} \frac{(f^\mathrm{o}_\mathrm{i} - f^\mathrm{e}_\mathrm{i})^2}{\sigma^2_\mathrm{i}}, \tag{3.1}$$

where f^o is an element of the random model array, f^e is an element of the given input, σ^2 is the quadratic spread of the random model with the original signal, and

Table 3.2: Error models for spectra with EW ∼23 and no additional components

(1)	Al III FLUX (2)	Si III] FLUX (3)	C III] FLUX (4)	Fe III FLUX (5)	Al III λ (6)	Si III] λ (7)	C III] λ (8)	1900 FWHM (9)	C III] FWHM (10)
BESTFIT	0.081	0.169	0.104	0.042	1854.5	1891.8	1909.0	3337	2924
					S/N=50				
$\mu_{1/2}$	0.077	0.169	0.093	0.044	1854.3	1892.3	1908.2	3492	3067
μ	0.078	0.168	0.094	0.043	1854.2	1892.3	1908.3	3505	3030
σ	0.013	0.025	0.025	0.011	1.9	1.8	2.5	535	652
					S/N=40				
$\mu_{1/2}$	0.073	0.162	0.097	0.041	1854.7	1890.7	1908.2	3540	2922
μ	0.074	0.162	0.098	0.042	1854.7	1890.8	1908.3	3536	2923
σ	0.016	0.029	0.027	0.012	2.5	2.1	2.5	612	664
					S/N=30				
$\mu_{1/2}$	0.077	0.170	0.107	0.044	1854.9	1891.9	1909.5	3434	3025
μ	0.078	0.170	0.106	0.044	1854.8	1891.8	1909.4	3433	2995
σ	0.019	0.037	0.028	0.012	2.7	2.5	2.7	671	661
					S/N=20				
$\mu_{1/2}$	0.078	0.167	0.101	0.041	1854.8	1891.9	1908.5	3241	2905
μ	0.079	0.168	0.102	0.041	1854.7	1891.9	1908.6	3275	2912
σ	0.021	0.043	0.029	0.012	2.8	2.7	2.8	706	669
					S/N=10				
$\mu_{1/2}$	0.081	0.169	0.104	0.042	1854.5	1891.8	1909.0	3338	2924
μ	0.081	0.168	0.104	0.042	1854.5	1891.8	1909.0	3338	2925
σ	0.023	0.049	0.030	0.012	2.9	2.9	2.9	770	676

Notes. These error models were built through J0020+0740 `specfit` best fit shown on Figure A.1 of the appendix. Columns 2, 3, 4 and 5 are label as flux but the data shown refers to the amplitude of the emission profile of single components.

$n_{\rm d}$ the number of degrees of freedom (283 for our simplest models). The summation runs up to n, the length of the arrays which match the length of the input spectra array (i.e., the analyzed spectral region resampled to 1 Å). To set the confidence level of our error estimation at 3σ we sort this 500,000 element χ^2 array, imposing a maximum χ^2 consistent with the χ^2 at a 3σ confidence level. Figure 3.8 shows an example of the sorts we implement in our routine, the light purple regions show the sort at a confidence level of 3σ and contains ∼30% values of a specific free parameter from the original 500,000 models while the medium purple regions show the sort at a confidence level of 2σ and contains ~10% or less data from the original 500,000. Therefore, we settle for the 3σ sort in order to get enough data points to measure its distribution. Finally, we measure the dispersion in the distribution for each array of free parameters. In this way we get an error for each free parameters of the model.

Even though our spectra are homogeneous, they mostly differ on S/N and components fitted (e.g Blue AlIII, FeIIIλ1914). We create models based on observed spectra from our sample. We choose examples meant to be representative of the S/N ratio, EW and FWHM. We used `specfit` fit as an input signal and run them different times using S/N = 10, 20, 30, 40, 50. We finally relate each error model with a `specfit` model according to its S/N and EW.

For the 1900 Å region we choose 7 characteristic spectra as models:

- Model 1: based on J1259+0752, used for spectra with EW < 11 and no additional components.
- Model 2: based on J0020+0740, used for spectra with EW ~ 23 and no additional components.
- Model 3: based on J1419+0749, used for spectra with EW ~ 15 and no additional components.
- Model 4: based on J2145−0758, used for spectra with EW ~ 20 and the presence of FeIIIλ1915 emission.
- Model 5: based on J1231+0726, used for spectra with EW ~ 19, a general FWHM of ~ 2000 and the presence of FeIIIλ1915 emission.
- Model 6: based on J1618+0705, used for spectra with EW < 11 and the presence of BLUE AlIII.
- Model 7: based on J0107−0855, used for spectra with EW ~ 17 and the presence of FeIIIλ1915 emission and BLUE AlIII.

All the basic emission lines and additional emission are allowed to vary, as described above, but for the FeIII template we only vary its amplitude (flux) and we fixed its position (centroid) and width.

For the 1500 Å region we choose 5 characteristic spectra as models:

- Model 1: based on J1259+0752, used for spectra with EW < 10.
- Model 2: based on J1214+0242, used for spectra with EW ~ 14.
- Model 3: based on J0929+0333, used for spectra with 17<EW <30 and FWHM(BLUE)<10,000 km s^{-1}.
- Model 4: based on J0847+0943, used for spectra with 17<EW <30 and FWHM(BLUE)>10,000 km s^{-1}.
- Model 5: based on J1231+0726, used for spectra with EW> 30.

Since the 1400 Å and 1500 Å region are similar in components and shape the same dispersion obtained with the 1550 Å region models will be used for the 1400 Å region error propagation.

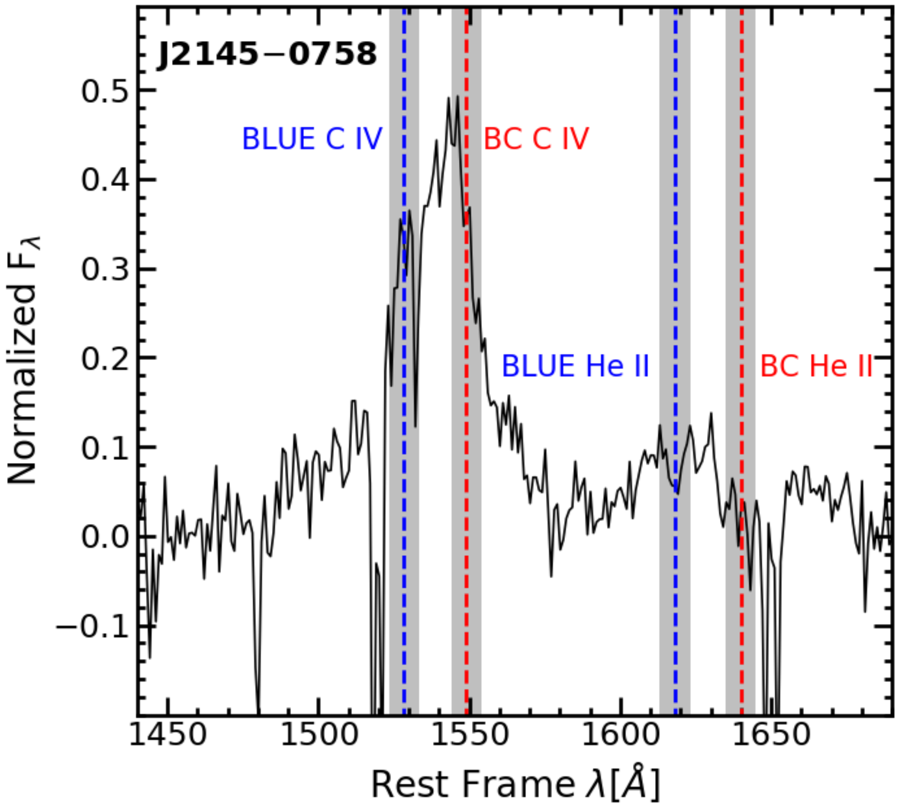

Figure 3.9: 1550 Å region of profile measurements ranges. The Figure shows in black the observed spectra minus the continuum. The red dashed lines indicate the rest frame wavelength of CIV and HeII, the gray area surrounding these lines show the ±1000 km s^{-1} range of measurement. The blue dashed lines indicate the BLUE emissions and are -4000 km s^{-1} from their broad component companion, the gray area surrounding these lines also show the ±1000 km s^{-1} range of measurement. Abscissa correspond to the rest frame wavelength in Å and ordinate normalized flux.

3.5 Measurements of profile normalized intensities

The `specfit` multi-components fits are time-consuming procedures. In order to compare `specfit` results with a simpler procedure we measure the intensity in specific radial velocity ranges of the emission lines to be used as metallicity indicators.

We create a routine using Python which yields the amplitude in the region given an input central wavelength and around it ±1000 km s^{-1}. The first range is centered at 0 km s^{-1} and corresponds to the wavelengths where the BC emission is dominating (red dashed lines in Figure 3.9). To represent the BLUE component with any actual profile decomposition, we measure the line intensity on the profile at -4000 km s^{-1} from the broad component (blue dashed lines in Figure 3.9) and ±1000 km s^{-1} around this wavelength (gray area in Figure 3.9). We chose the BLUE component position carefully with an offset with respect to the rest frame in order to avoid absorptions and to sample a spectral range where we expect emission from outflowing gas. In the case of an absorption line within the range of our measurement this results in negative values, which are not physical meaningful and therefore were ignored. To estimate errors we measured the distribution of the amplitudes within ±1000 km s^{-1} for each central wavelength component.

Even though the BC CIV is the main emission of the 1550 Å region, Figure 3.9 shows that the peak of maximum intensity is on the blue side of the region despite of the MgIIλ2800 redshift correction. This behavior is present in the majority of the sample which lead as to believe that the BLUE emissions are a constant in the process in xA sources instead of a occasionally emission.

3.6 Estimate of physical parameters

We determine some basic physical parameters using the continuum `splot` measurements, such as the bolometric luminosity (L_{bol}), the central supermassive black hole mass ($M_{\rm BH}$), and the Eddington ratio ($L/L_{\rm Edd}$); in addition, we computed the virial luminosity ($L_{\rm vir}$). The estimated parameters are reported in Table 3.3, and details of the computations are reported below.

3.6.1 Bolometric Luminosity

We used the conventional way to derive the luminosity, $L = 4F\pi r^2$. First, we estimate λf_λ at 1350 Å and the distance to the source r, we considered the co-moving distance (ec. 3.2) according to Sulentic et al. (2006b) which assumes $\Omega_M \neq 0$, $\Omega_\Lambda \neq 0$ and $\Omega_K = 0$

$$d_c = \frac{c}{H_0}\int_0^z \frac{dz'}{\sqrt{\Omega_M(1+z)^3+\Omega_\Lambda}}. \tag{3.2}$$

This integral can be approximate to the following expression:

$$d_{\mathrm{c}} \approx \frac{c}{H_0}\left[1.500(1-e^{-\frac{z}{6.309}})+0.996(1-e^{-\frac{z}{1.266}})\right], \tag{3.3}$$

where c is the speed of light, H_0 the Hubble constant assumed as 70 km s^{-1} and z the source final redshift. Finally estimate the luminosity and applied a value of bolometric correction factor of 5 according to Richards et al. (2006).

3.6.2 Black Hole Mass

One of the most powerful techniques for studying the physical properties of emission line regions in the vicinity of AGN is the *reverberation mapping* (Longair, 2011) technique. This observation technique involves long-term monitoring of the UV-optical spectra and intensities of the AGN continuum.

The key discovery was a time lag between variations in the ionizing ultraviolet continuum and corresponding variations in the broad line spectrum. This result conclusively demonstrated that the broad line regions are excited and photoionized by continuous UV radiation from the nucleus and also allowed a direct estimate of the distance between these clouds and the nucleus, since ultraviolet photons travel from the nucleus to the emitting region at the speed of light.

To estimate the mass of the central supermassive black hole (M_{BH}) we use a mass scale relation obtained from data based on reverberation mappings. According to Peterson & Horne (2004), there is strong evidence that gravitational acceleration from the central source is important. This leads directly to calculating the masses of black holes, based on reverb mappings, from the virial equation

$$M_{BH} = \frac{f_s r(\delta v)^2}{G}, \tag{3.4}$$

where G is the gravitational constant, f_s is a scaling factor of unit order that depends on the geometry and kinematics of the BLR, r for this case is considered the radius of the BLR and δv is an indicator of the dispersion of virial velocities.

The most common black hole mass scaling relations are based on CIV but these relations tend to over-estimated the mass because of the strong blue excess of this emission (Marziani et al., 2019). In an effort to obtain a more accurate estimation we used the AlIII-based mass scaling relation (eq. 3.5) proposed by Marziani et al. (2022, submitted). The AlIII profile shows the least displacement and asymmetry from its rest-frame and therefore is compatible with a virialized system (unlike CIV full profile). The scaling law can be written as:

$$\begin{aligned} \log M_{\rm BH}(\text{Al III}) &\approx (0.579^{+0.031}_{-0.029}) \log L_{1700,44} + \\ & 2\log[\text{FWHM}(\text{Al III})] + (0.490^{+0.110}_{-0.060}). \end{aligned} \tag{3.5}$$

This relation requires only two parameters $L_{1700,44}$ the continuum luminosity at 1700Å normalized by 10^{44} and the FWHM of the BC of AlIII in units of km s^{-1}. It also considers that AlIIIλ1860 is an emission with a low ionization potential and presents a symmetrical profile which indicates that it is emitted in a region governed by a virialized system.

3.6.3 Mass and Luminosity dependent parameters

3.6.3.1 Eddington Luminosity

There is a limit to the luminosity generated by a mass source M powered by the spherical accretion of fully ionized gas. This limiting luminosity, known as the Eddington luminosity, is found by balancing the inward force of gravity against the outward radiation pressure.

For matter to fall, the radiation force must be less than the force of gravity. For each electron there is a proton, and these two types of particles are electromagnetically coupled. The gravitational force per electron-proton pair is given by

$$F_{grav} = \frac{GM_{BH}}{r^2}(m_p + m_e) \approx \frac{GM_{BH}m_p}{r^2}. \tag{3.6}$$

The condition $F_{grav} < F_{rad}$ for the gravity domain can be written as

$$\frac{\sigma_T L}{4\pi r^2 c} < \frac{GM_{BH}m_p}{r^2}, \tag{3.7}$$

solving for L

$$L < L_{Edd} = \frac{4\pi G c m_p}{\sigma_T} M_{BH}. \tag{3.8}$$

This limiting luminosity is independent of the radius r and depends only on the mass M of the emitting region (eq. 3.5), the luminosity expression can be written as

$$L_{Edd} = 1.3\text{x}10^{38} \left(\frac{M}{M_\odot}\right) \mathrm{erg\,s^{-1}}. \tag{3.9}$$

Given this luminosity we also obtained the Eddington ratio ($\lambda_{Edd} = L_{bol}/L_{Edd}$), which is an indicator of the BH accretion rate.

3.6.3.2 Virial Luminosity

The ratio of the bolometric luminosity and the black hole mass from a radiating source to the Eddington ratio (λ_{Edd}) can be expressed as

$$\frac{L}{M} \approx 10^{4.53} \lambda_{Edd} \left(\frac{L}{M_{BH}}\right)_\odot \approx 10^{4.81} \lambda_{Edd}. \tag{3.10}$$

According to Marziani & Sulentic (2014b) if we assume virial movement and insert eq. 3.4 for M, the bolometric luminosity is

$$L \approx 10^{4.81} \lambda_{Edd} M \approx 10^{4.81} \lambda_{Edd} \frac{f_s r (\delta v)^2}{G}. \tag{3.11}$$

where f_s is the structure factor, δv a dispersion estimator of the virial velocity, G the gravitational constant and r the radius of the broad line region.

Returning to the ionization parameter (U), eq. 1.3, we can consider r as the distance between the central source of ionizing radiation and the part of the region of emission lines that responds to changes in the continuum. If the product $n_H \times U$ is known we can define r in an alternative way

$$r = \left[\frac{\int_{\nu_1}^{\infty} \frac{L_\nu}{h\nu} d\nu}{4\pi U c n_H}\right]^{1/2} = \left(\frac{\kappa L}{4\pi c U n_H h \bar{\nu}_i}\right)^{1/2}, \tag{3.12}$$

where c is the speed of light, n_H is the numerical density of hydrogen and h is Planck's constant. The ionizing luminosity is assumed to be $L_{ion} = \kappa L$, with $\kappa \approx 0.5$. The number of ionizing photons is given by $\kappa L/h\bar{\nu}_i$, where $\bar{\nu}_i$ is the average frequency of the ionizing photons. Inserting the equation 3.12 into the equation 3.11

$$L \approx \frac{10^{4.81}}{\sqrt{4\pi chG}} \frac{\lambda_{Edd} f_s \kappa^{1/2}}{\bar{\nu}_i^{1/2}} \frac{L^{1/2}}{(n_H U)^{1/2}} (\delta v)^2 \approx \frac{10^{9.62}}{4\pi chG^2} \frac{\lambda_{Edd}^2 f_s^2 \kappa}{\bar{\nu}_i} \frac{1}{n_H U} (\delta v)^4 \tag{3.13}$$

hence,

$$L \approx 7.8\text{x}10^{44} \frac{\lambda_{Edd,1}^2 \kappa_{0.5} f_{s,2}^2}{h\bar{\nu}_{i,100_{eV}}} \frac{1}{(n_H U)_{10^{9.6}}} (\delta v)_{1000}^4, \tag{3.14}$$

where the energy value has been normalized at 100 eV, the product $n_H U$ to the typical value $10^{9.6}$ cm $^{-3}$ and δv at 1000 km s^{-1}. The first quotient can be assumed constant and equal to 1 for the xA population (more details are provided by Negrete et al., 2018; Dultzin et al., 2020).

In practice, the virial luminosity has been computed by multiplying the numerical factor and the viral estimator δv (FWHM AlIII), raised to the fourth power (eq. 3.15).

$$L \approx 7.8\text{x}10^{44} \left(\frac{FWHM(Al\ III)}{1000\ km\ s^{-1}} \right)^4 \ erg\ s^{-1}. \tag{3.15}$$

The equation 3.14 and its equivalents (e.g. eq. 3.15) are called virial luminosity and are valid for any L/L_{Edd}. In this case we set the Eddington ratio equal to 1 because we are dealing with highly accreting sources. The provide us with a redshift independent luminosity since redshifth dependent luminosity estimations tend to be problematic in quasars with blended emission regions. The comparison of the two luminosity methods will be discussed in sec. 4.4.

Table 3.3: Physical Parameters

SDSS JCODE (1)	$\log M_{\rm BH}$ $[M_\odot]$ (2)	$\log L_{\rm bol}$ [erg s^{-1}] (3)	$\log L_{\rm vir}$ [erg s^{-1}] (4)	$\lambda_{\rm Edd}$ (5)
J0020+0740	9.26	46.98	46.99	0.78
J0034−0326	9.04	46.78	46.76	0.81
J0037−0238	9.00	46.65	46.83	0.65
J0103−1104	9.24	47.31	46.55	1.82
J0106−0855	9.43	47.33	46.92	1.22
J0123+0329	9.40	47.32	46.87	1.29
J0210−0823	9.24	47.07	46.85	1.00
J0216+0115*	9.21	47.05	46.81	1.02
J0252−0420*	9.16	46.89	46.89	0.78
J0827+0306	9.07	46.95	46.63	1.12
J0829+0801	9.45	47.31	46.99	1.10
J0836+0548	9.43	47.04	47.26	0.60
J0845+0722	9.45	47.30	46.99	1.09
J0847+0943	9.35	47.08	47.04	0.81
J0858+0152	9.36	47.31	46.80	1.37
J0903+0708	9.40	47.07	47.17	0.69
J0915−0202	8.60	46.47	46.25	1.04
J0926+0135	9.41	47.06	47.20	0.66
J0929+0333	9.19	46.91	46.93	0.76
J0932+0237*	9.52	47.19	47.26	0.71
J0946−0124	8.86	47.08	46.07	2.46
J1013+0851*	9.74	47.59	47.24	1.12
J1024+0245	9.32	47.16	46.89	1.06
J1026+0114	9.26	47.13	46.80	1.13
J1145+0800	9.12	46.90	46.79	0.89
J1205+0201*	9.88	47.68	47.41	1.00
J1214+0242	9.71	47.52	47.26	1.01
J1215+0326	9.34	47.31	46.75	1.46
J1219+0254	9.57	47.28	47.25	0.79
J1231+0725	9.02	47.33	46.10	3.14
J1244+0821	9.49	47.29	47.08	0.97
J1259+0752	9.50	47.45	46.91	1.41
J1314+0927	9.26	47.13	46.81	1.11
J1419+0749	9.57	47.51	46.99	1.37
J1509+0744	9.20	46.89	46.97	0.72
J1516+0029*	9.11	46.99	46.67	1.12
J1519+0723	9.30	47.10	46.93	0.94
J1545+0156	9.53	47.38	47.07	1.08
J1609+0654	9.55	47.31	47.19	0.87
J1618+0704	9.39	47.17	47.02	0.92
J2116+0441	9.29	47.12	46.89	1.00
J2145−0758	9.27	47.20	46.75	1.29
μ	9.33 ± 0.13	47.15 ± 0.14	46.91 ± 0.13	1.01 ± 0.16
σ	0.24	0.24	0.29	0.47

Notes. Columns are as follows: (1) SDSS short name, (2) log of black hole mass in solar masses, (3) log of bolometric luminosity in units of erg s^{-1}, (4) log of viral luminosity in units of erg s^{-1} and (5) the Eddington ratio. Last row shows the mean values as listed in the columns. (*) BALQ.

3.7 Metal content estimates

In order to interpret the multi-component procedure results, we computed photoionization models of the broad line region with the Cloudy photoinization code Ferland et al. (2017). This software simulates conditions in astrophysical environments within a non-equilibrium gas possibly exposed to an external radiation source, and predicts the resulting spectrum. This allows many observational quantities to be predicted by specifying only the properties of the cloud and the incident radiation field (Ferland et al., 2013).

We chose six synthetic flux ratios predicted by the Cloudy photoinization models, according to their characteristics as metallicity indicators. These ratios will be compared with the observational flux ratios obtained with the multi-component procedure performed with $specfit$. The following section explains the operation of the Cloudy photoinization code and shows the parameters used to simulate the conditions of the broad line region of the sample.

3.7.1 BLR photoionization models

Cloudy is a photoionization code that simulates astrophysical scenarios under physical input conditions. In this work, we used version 17.0 to simulate the AGN broad line region as reference for comparison with the observed line intensity ratios. These simulations were computed by P. Marziani and S. Panda, co-authors of G22, under the assumption that

- the column density is $N_{\mathrm{c}} = 10^{23}$ cm^{-2};
- the continuum is represented by the model continuum of Mathews & Ferland (1987) which is believed to be appropriate for Population A quasars;
- microturbulence is negligible.

Our modeling cover a broad range of parameter for a better description of the BC (low ionization potential) and BLUE (high ionization potential) emission regions. In the observational sample, both lines with high ionization potential and low ionization potential were found. Our simulation arrays cover:

- hydrogen density range of $7.00 \leq \log(n_{\mathrm{H}}) \leq 14.00$, in intervals of 0.25 dex;
- ionization parameter of $-4.5 \leq \log(U) \leq 1.00$, in intervals of 0.25 dex.

They are repeated for values of metallicities in a range encompassing five orders of magnitude: 0.01, 0.1, 1, 2, 5, 10, 20, 50, 100, 200, 500 and 1000 $Z_{\odot}$. Scaled values of Cloudy's default solar composition were used for all models. In this composition the abundance of He is a typical value for nebulae with almost solar compositions (Ferland et al., 2017). The abundances of C and O come from the photospheric study of Allende Prieto et al. (2001, 2002). The abundances of N, Ne, Mg, Si and Fe come from the study of Holweger (2001) and the rest of the first thirty elements of the periodic table come from the study of Grevesse & Sauval (1998).

Extremely high metallicity $Z \gtrsim 100Z_{\odot}$ is considered physically unrealistic ($Z \approx 100Z_{\odot}$ implies that more than half of the gas mass is made up by metals!), unless the enrichment is provided *in situ* within the disk, a possibility briefly discussed in Section 5.3.3. In several cases, simulations suffered convergence problems if $Z \gtrsim 500Z_{\odot}$.

Since we used different metallicities, we were able to describe the metallicity trend with the intesity flux ratios. We defined two sets, one for the BC and one for the BLUE emissions, with three metallicity indicators each. These indicators were later used to determine a relationship of flux ratio vs metallicity , under fixed U and n_{H}, and estimate the metal content in our sample (Sec. 4.5.1).

Chapter 4

Results

We aim to estimate the metallicity of the xA sources, as well as the correlations between Z and physical parameters. The Chapter is divided as follows:

- Sec. 4.1 reports the *immediate results*: the measurements of the emission line components. All tables report the mean values (μ), dispersion (σ), and semi interquartile ranges (SIQR) of the values listed.
- Sec. 4.2 shows the figures displaying BC and BLUE *intensity ratios.* Each figure shows the distribution of the sample ratios and the individual ratios with error bars.
- Sec. 4.3 confirms the xA nature for most sources of our sample.
- Sec. 4.4 reports the correlation between diagnostic ratios and physical parameters with two correlation matrix.
- Sec. 4.5 reports the *metallicity inferences* for the sample, first (Sec. 4.5.1) assuming fixed physical conditions (i.e., for a given n_{H} and U, different for the regions associated with BLUE and BC), and then considering n_{H} and U free to vary (Sect. 4.5.2).

4.1 Immediate Results

The analysis of the spectra involve the deblend of broad and BLUE components. The rest-frame spectra with the continuum placements, and the fits to the blends of the spectra are shown in Appendix A. We deblend the components in two ways:

1) using the IRAF `specfit` task;

2) measuring the amplitude of the emission ± 1000 km s^{-1} around a central wavelength.

4.1.1 `Specfit` measurements.

Tables 4.1 and 4.2 list the results for the fitting procedure on the 1900 Å region. The BALQ sources are identified with an asterisk (*). Table 4.1 lists the results for the AlIII emissions, columns are as follow 1) SDSS identification short code, 2) equivalent width, 3) broad component FWHM in km s^{-1}, 4) broad component total flux normalized at 1350 Å, 5) blueshifted component FWHM in km s^{-1}, 6) blueshifthed component flux normalized at 1350 Å, 7) separation from the BC AlIII rest frame in Å and 8) `specfit` asymmetry (the skew parameter). Table 4.2 list the results for the rest of the main components of the region, columns are as follow 1) SDSS identification short code, (2,3) FWHM and flux of SiIII] emission, (4,5) FWHM and flux of CIII] emission and (6,7) FWHM and flux of the itinerant emission of FeIII. We do not include the W of each emission line because it can be computed taking the W(AlIII) and the flux ratio of the emission line in consideration and the AlIII line.

Tables 4.3 and 4.4 report the measurements of the 1500 Å region. The BALQ sources are identified with an asterisk (*). Table 4.3 list the results for the broad components, columns are as follow 1) SDSS identification short code, 2) equivalent width, 3) FWHM in km s^{-1}and (4,5) CIV and HeII fluxes. Table 4.4 list the results for the BLUE emissions, columns are as follow 1) SDSS identification short code, 2) FWHM in km s^{-1}, (3,4) BLUE CIV and BLUE HeII fluxes, 5) the separation (or shift) in Å from the BLUE component to the broad component and 6) `specfit`

Table 4.1: Measurements in the 1900Å blend region: AlIII broad and blueshifted components.

SDSS JCODE	AlIII	BC AlIII		BLUE AlIII			
	W	FWHM	Flux	FWHM	Flux	$\Delta\lambda$	skew
(1)	(2)	(3)	(4)	(5)	(6)	(7)	(8)
J0020+0740	6	3337 ± 719	4.7 ± 1.3				
J0034−0326	4	2930 ± 573	3.0 ± 0.7				
J0037−0238	6	3057 ± 659	2.7 ± 0.7				
J0103−1104	7	2600 ± 517	2.2 ± 0.6				
J0106−0855	7	3212 ± 696	3.3 ± 0.9	2641 ± 491	0.6 ± 0.2	14.8 ± 5.7	0.80
J0123+0329	7	3119 ± 579	3.1 ± 0.7				
J0210−0823	10	3079 ± 707	3.6 ± 1.1				
J0216+0115	8	3016 ± 514	5.2 ± 1.3				
J0252−0420	5	3161 ± 675	6.5 ± 1.8				
J0827+0306	6	2723 ± 625	2.2 ± 0.6				
J0829+0801	8	3341 ± 578	4.3 ± 0.9				
J0836+0548	12	3900 ± 841	7.2 ± 2.0				
J0845+0722	5	3340 ± 653	3.9 ± 1.0				
J0847+0943	9	3439 ± 741	5.5 ± 1.5				
J0858+0152	6	3003 ± 380	2.9 ± 0.5				
J0903+0708	11	3708 ± 847	3.0 ± 0.8	2676 ± 511	0.8 ± 0.2	11.1 ± 2.9	0.71
J0915−0202	8	2186 ± 488	1.9 ± 0.6				
J0926+0135	9	3770 ± 737	3.1 ± 0.8				
J0929+0333	7	3241 ± 698	6.0 ± 1.6				
J0932+0237	7	3900 ± 675	7.3 ± 1.6				
J0946−0124	11	1973 ± 366	2.7 ± 0.6				
J1013+0851	10	3856 ± 626	9.2 ± 2.3	3279 ± 604	1.7 ± 0.5	12.9 ± 5.3	0.79
J1024+0245	6	3151 ± 616	3.9 ± 1.0				
J1026+0114	6	2997 ± 649	5.2 ± 1.5	3043 ± 566	0.8 ± 0.2	8.9 ± 5.7	0.30
J1145+0800	9	2989 ± 686	5.2 ± 1.5				
J1205+0201	8	4272 ± 902	5.3 ± 1.2	4290 ± 814	1.02 ± 0.3	11.8 ± 2.8	0.36
J1214+0242	6	3900 ± 675	4.5 ± 1.0				
J1215+0326	5	2910 ± 496	3.3 ± 0.8				
J1219+0254	8	3881 ± 662	4.9 ± 1.3				
J1231+0725	5	2000 ± 303	2.3 ± 0.4				
J1244+0821	8	3529 ± 690	4.0 ± 1.0				
J1259+0752	6	3187 ± 736	1.7 ± 0.5				
J1314+0927	5	3019 ± 697	2.4 ± 0.7				
J1419+0749	6	3337 ± 486	2.7 ± 0.5				
J1509+0744	9	3299 ± 704	3.8 ± 1.1				
J1516+0029	8	2788 ± 475	12.9 ± 3.3				
J1519+0723	5	3229 ± 696	5.2 ± 1.4				
J1545+0156	7	3500 ± 748	4.5 ± 1.3				
J1609+0654	3	3753 ± 866	4.1 ± 1.2				
J1618+0704	6	3395 ± 776	3.0 ± 0.9	2876 ± 549	0.5 ± 0.1	9.2 ± 2.9	0.21
J2116+0441	6	3156 ± 510	3.0 ± 0.6				
J2145−0758	6	2907 ± 579	3.8 ± 1.0				
μ	7	3216 ± 639	4.3 ± 1.1	3134 ± 589	0.9 ± 0.3	11.4 ± 4	0.53
σ	2	494 ± 132	2.1 ± 0.6	614 ± 117	0.4 ± 0.1	2.2 ± 1	0.27
SIQR	1	243 ± 66	1.1 ± 0.3	247 ± 37	0.2 ± 0.0	1.5 ± 1	0.23

Notes. Columns are as follows: (1) SDSS short name; (2) Equivalent width of the AlIII emission in Å, its errors are similar to the AlII flux errors; (3) FWHM of AlIII in km s^{-1}; (4) AlIII flux normaliazed at 1350 Å; (5)FWHM of the blue components of AlIII in km s^{-1}; (6) normalized flux of the AlIII BLUE component; (7) separation of the peak of the BLUE from the rest-frame AlIII emission in Å; (8) asymmetry reported by `specfit`.

Table 4.2: Measurements in the 1900Å blend region: Si III], C III] and Fe III broad components.

SDSS JCODE	BC Si III]		BC C III]		BC Fe III	
	FWHM	Flux	FWHM	Flux	FWHM	Flux
(1)	(2)	(3)	(4)	(5)	(6)	(7)
J0020+0740	3337 ± 719	5.6 ± 1.4	2924 ± 672	3.0 ± 0.9		
J0034−0326	2930 ± 573	2.6 ± 0.6	2066 ± 456	1.0 ± 0.3		
J0037−0238	3057 ± 659	2.3 ± 0.6	3207 ± 737	2.1 ± 0.6		
J0103−1104	2600 ± 517	2.5 ± 0.6	2923 ± 663	4.2 ± 1.2	2947 ± 673	2.1 ± 0.4
J0106−0855*	3212 ± 696	4.8 ± 1.3	2272 ± 522	1.1 ± 0.3	2662 ± 612	1.3 ± 0.3
J0123+0329	3620 ± 672	4.0 ± 0.9	2833 ± 641	2.0 ± 0.6		
J0210−0823	3079 ± 707	2.4 ± 0.7	2980 ± 688	2.0 ± 0.6		
J0216+0115	3016 ± 514	3.3 ± 0.6	2816 ± 596	1.3 ± 0.3	2562 ± 562	2.4 ± 0.4
J0252−0420	3161 ± 675	6.5 ± 1.8	2270 ± 522	5.3 ± 1.5		
J0827+0306	2723 ± 625	2.0 ± 0.6	2219 ± 512	0.9 ± 0.3		
J0829+0801	3341 ± 578	3.3 ± 0.6	2755 ± 626	1.2 ± 0.3		
J0836+0548	3900 ± 841	5.2 ± 1.3	3154 ± 725	2.7 ± 0.8		
J0845+0722	3340 ± 653	3.3 ± 0.7	2430 ± 536	1.3 ± 0.3		
J0847+0943	3439 ± 741	4.6 ± 1.2	2333 ± 536	1.9 ± 0.5		
J0858+0152	3003 ± 380	3.5 ± 0.4	2326 ± 494	1.5 ± 0.3	2694 ± 608	0.9 ± 0.2
J0903+0708*	3708 ± 847	2.2 ± 0.6	2312 ± 532	0.7 ± 0.2		
J0915−0202	2186 ± 488	1.6 ± 0.4	2200 ± 476	1.0 ± 0.2	2125 ± 476	0.9 ± 0.2
J0926+0135	3770 ± 737	4.9 ± 1.1	3061 ± 676	1.9 ± 0.5		
J0929+0333	3241 ± 698	6.0 ± 1.6	2759 ± 634	4.1 ± 1.2		
J0932+0237	3900 ± 675	7.4 ± 1.3	3702 ± 841	5.5 ± 1.5		
J0946−0124	1973 ± 366	2.9 ± 0.6	2213 ± 416	3.2 ± 0.6	2468 ± 548	4.2 ± 0.8
J1013+0851*	3856 ± 626	7.6 ± 1.4	2748 ± 614	2.3 ± 0.6	3400 ± 767	4.2 ± 0.8
J1024+0245	3151 ± 616	4.0 ± 0.9	2819 ± 622	2.2 ± 0.6		
J1026+0114*	2997 ± 649	3.9 ± 1.1	2287 ± 525	1.6 ± 0.5		
J1145+0800	2989 ± 686	4.5 ± 1.3	2479 ± 573	1.8 ± 0.5		
J1205+0201*	4272 ± 902	4.4 ± 1.1	3686 ± 842	2.4 ± 0.7		
J1214+0242	3900 ± 675	4.7 ± 0.8	3672 ± 834	2.9 ± 0.8		
J1215+0326	2910 ± 496	4.4 ± 0.9	2933 ± 621	2.2 ± 0.5	2560 ± 561	2.5 ± 0.5
J1219+0254	3881 ± 662	7.0 ± 1.3	3225 ± 683	2.7 ± 0.7	2783 ± 610	2.6 ± 0.5
J1231+0725	2000 ± 303	2.7 ± 0.4	2107 ± 388	3.9 ± 0.6	2145 ± 389	3.2 ± 0.6
J1244+0821	3529 ± 690	4.3 ± 0.9	2591 ± 572	2.0 ± 0.5		
J1259+0752	3187 ± 736	1.3 ± 0.4	2547 ± 589	0.4 ± 0.1		
J1314+0927	3019 ± 697	2.7 ± 0.8	2934 ± 678	1.7 ± 0.5		
J1419+0749	3337 ± 486	3.8 ± 0.8	2977 ± 674	2.3 ± 0.7		
J1509+0744	3299 ± 704	5.0 ± 1.4	2214 ± 506	1.3 ± 0.4		
J1516+0029	2788 ± 475	6.4 ± 1.2	2729 ± 578	3.5 ± 0.8	3097 ± 679	4.5 ± 0.8
J1519+0723	3229 ± 696	6.2 ± 1.6	2126 ± 489	3.0 ± 0.8		
J1545+0156	3500 ± 748	3.7 ± 1.0	3093 ± 706	1.6 ± 0.5		
J1609+0654	3753 ± 866	3.3 ± 1.0	2468 ± 570	0.9 ± 0.3		
J1618+0704*	3395 ± 776	1.6 ± 0.5	2328 ± 536	1.0 ± 0.3		
J2116+0441	3156 ± 510	3.6 ± 0.7	2424 ± 526	2.5 ± 0.6		
J2145−0758	2907 ± 579	6.2 ± 1.5	2299 ± 522	2.5 ± 0.7	2658 ± 607	2.5 ± 0.5
μ	3228 ± 579	4.1 ± 1.0	2677 ± 599	2.2 ± 0.6	2675 ± 591	2.6 ± 0.5
σ	497 ± 132	1.6 ± 0.4	440 ± 107	1.2 ± 0.3	362 ± 97	1.2 ± 0.2
SIQR	262 ± 66	1.1 ± 0.3	315 ± 75	0.7 ± 0.2	143 ± 34	0.8 ± 0.1

Notes. Columns are as follows: (1) SDSS short name; (2,3) FWHM in km s^{-1} and normalized flux at 1350 Å of Si III]; (4,5) FWHM in km s^{-1} and normalized flux at 1350 Å of C III]; (6,7) FWHM in km s^{-1} and normalized flux at 1350 Å of Fe III. . BALQ are identified with an asterisk (*), their spectra can be seen in appendix A.

Table 4.3: Measurements in the λ1550 region: CIV and HeII broad components.

SDSS JCODE (1)	1550 W (2)	BC FWHM (3)	CIV Flux (4)	HeII Flux (5)
J0020+0740	12	3528 ± 742	9.7 ± 1.8	1.5 ± 0.4
J0034−0326	7	2842 ± 650	3.0 ± 0.8	1.4 ± 0.4
J0037−0238	18	3800 ± 800	12.8 ± 2.4	2.1 ± 0.6
J0103−1104	7	3800 ± 848	6.6 ± 1.3	1.2 ± 0.4
J0106−0855	7	3021 ± 674	3.3 ± 0.7	1.1 ± 0.3
J0123+0329	4	3254 ± 670	2.5 ± 0.4	0.8 ± 0.2
J0210−0823	3	3388 ± 760	2.7 ± 0.7	0.8 ± 0.2
J0216+0115*	9	3260 ± 746	7.2 ± 2.0	1.1 ± 0.3
J0827+0306	6	3282 ± 736	3.7 ± 1.0	1.1 ± 0.3
J0829+0801	6	3191 ± 578	4.2 ± 0.5	0.9 ± 0.2
J0836+0548	8	3401 ± 759	7.1 ± 1.4	1.0 ± 0.3
J0845+0722	5	3388 ± 697	4.9 ± 0.8	1.1 ± 0.3
J0847+0943	9	3399 ± 715	7.6 ± 1.4	1.3 ± 0.4
J0858+0152	8	3089 ± 524	4.6 ± 0.5	1.2 ± 0.3
J0903+0708	2	3266 ± 748	2.3 ± 0.6	1.1 ± 0.3
J0915−0202	10	3093 ± 690	4.9 ± 1.0	1.4 ± 0.4
J0926+0135	8	3400 ± 602	7.7 ± 1.1	1.4 ± 0.4
J0929+0333	14	3395 ± 714	9.2 ± 2.0	0.9 ± 0.3
J0932+0237*	17	3356 ± 266	11.8 ± 0.7	1.9 ± 0.5
J0946−0124	14	3400 ± 686	11.7 ± 1.2	1.8 ± 0.5
J1013+0851*	6	3399 ± 576	6.3 ± 0.7	2.4 ± 0.7
J1024+0245	6	3331 ± 686	5.2 ± 0.8	0.8 ± 0.2
J1026+0114	6	3113 ± 655	4.0 ± 0.7	1.0 ± 0.3
J1145+0800	4	3011 ± 675	4.4 ± 1.2	0.9 ± 0.3
J1205+0201*	5	3155 ± 589	3.6 ± 0.4	0.9 ± 0.3
J1214+0242	9	3400 ± 616	6.9 ± 0.9	1.1 ± 0.3
J1215+0326	12	3414 ± 604	10.1 ± 1.4	1.3 ± 0.4
J1219+0254	9	3500 ± 672	15.7 ± 2.1	2.1 ± 0.6
J1231+0725	21	3496 ± 277	18.2 ± 1.1	2.6 ± 0.8
J1244+0821	8	3600 ± 637	5.6 ± 0.8	0.8 ± 0.2
J1259+0752	3	3128 ± 716	2.2 ± 0.6	0.8 ± 0.2
J1314+0927	2	2925 ± 675	2.0 ± 0.6	0.8 ± 0.2
J1419+0749	7	3439 ± 642	5.2 ± 0.5	0.9 ± 0.3
J1509+0744	6	3264 ± 729	4.6 ± 0.9	1.2 ± 0.3
J1519+0723	7	3122 ± 657	5.8 ± 1.1	1.2 ± 0.3
J1545+0156	5	3117 ± 696	3.4 ± 0.7	1.2 ± 0.3
J1609+0654	5	3098 ± 638	3.7 ± 0.6	0.3 ± 0.1
J1618+0704	3	3352 ± 767	3.0 ± 0.8	0.8 ± 0.2
J2116+0441	9	3601 ± 653	8.8 ± 1.1	0.8 ± 0.2
J2145−0758	11	3297 ± 694	9.1 ± 2.0	1.2 ± 0.4
μ	8	3308 ± 662	6.4 ± 1.0	1.2 ± 0.3
σ	4	3314 ± 111	3.8 ± 0.5	0.5 ± 0.1
SIQR	2	3302 ± 41	2.2 ± 0.3	0.2 ± 0.1

Notes.(1) SDSS short name; (2) Equivalent width of the CIV BC emission in Å; (3) FWHM of the CIV and HeII broad components; (4,5) normalized flux of CIV and HeII broad components. (*) BALQ. The measurements of J0252−0420 and J1516+0029 BALQ are excluded from this Table because CIV(BC) is severely affected by the absorption.

Table 4.4: Measurements in the $\lambda1550$ region: C IV and He II asymmetric components.

SDSS JCODE (1)	BLUE FWHM (2)	C IV Flux (3)	He II Flux (4)	$\Delta\lambda$ (5)	skew (6)
J0020+0740	13117 ± 1514	12.4 ± 1.5	2.9 ± 0.8	13.6 ± 1.8	0.28
J0034−0326	8091 ± 1510	8.2 ± 1.6	1.7 ± 0.5	14.9 ± 4.6	0.56
J0037−0238	10207 ± 1178	6.9 ± 0.8	1.8 ± 0.5	14.5 ± 1.8	0.28
J0103−1104	10841 ± 1470	5.3 ± 0.7	1.0 ± 0.3	13.8 ± 3	0.25
J0106−0855	10505 ± 1425	10.9 ± 1.5	1.9 ± 0.5	17.3 ± 3	0.45
J0123+0329	11305 ± 1294	8.1 ± 0.9	1.1 ± 0.3	20.4 ± 3	0.43
J0210−0823	12133 ± 2168	6.4 ± 1.7	1.6 ± 0.5	26.5 ± 5.1	0.48
J0216+0115*	6303 ± 1176	5.3 ± 1.0	0.9 ± 0.3	9.0 ± 4.6	0.45
J0827+0306	13751 ± 2457	7.3 ± 1.9	1.3 ± 0.4	13.2 ± 5.1	0.22
J0829+0801	11802 ± 860	10.4 ± 0.8	1.7 ± 0.5	20.2 ± 1.8	0.39
J0836+0548	11974 ± 1624	6.6 ± 0.9	1.6 ± 0.5	12.2 ± 3	0.15
J0845+0722	13961 ± 1598	9.9 ± 1.1	1.7 ± 0.5	16.3 ± 3	0.26
J0847+0943	12944 ± 1494	12.6 ± 1.5	2.7 ± 0.7	10.9 ± 1.8	0.17
J0858+0152	15923 ± 1084	15 ± 1.1	2.7 ± 0.7	15.2 ± 1.1	0.25
J0903+0708	14584 ± 2721	5.7 ± 1.1	1.1 ± 0.3	19.2 ± 4.6	0.37
J0915−0202	11479 ± 1557	9.3 ± 1.3	2.2 ± 0.6	12.9 ± 3.0	0.32
J0926+0135	11100 ± 910	8.6 ± 0.7	1.6 ± 0.4	16.6 ± 1.4	0.26
J0929+0333	9984 ± 1374	12.2 ± 1.8	1.8 ± 0.5	9 ± 2.8	0.26
J0932+0237*	8979 ± 1246	18.1 ± 2.4	3.0 ± 0.8	10.3 ± 5.1	0.35
J0946−0124	8928 ± 607	5.6 ± 0.5	1.7 ± 0.5	12.4 ± 1.6	0.4
J1013+0851*	10824 ± 737	10.3 ± 0.7	2.3 ± 0.6	13.1 ± 1.1	0.24
J1024+0245	11969 ± 1370	10.6 ± 1.2	2.2 ± 0.6	17.5 ± 3	0.38
J1026+0114	15812 ± 1825	12.6 ± 1.5	1.9 ± 0.5	13.6 ± 1.8	0.19
J1145+0800	11432 ± 2043	11.2 ± 2.9	1.9 ± 0.5	15.9 ± 5.1	0.36
J1205+0201*	13004 ± 921	8.1 ± 0.6	0.8 ± 0.2	17 ± 1.5	0.31
J1214+0242	12643 ± 921	10.8 ± 0.9	1.8 ± 0.5	12.5 ± 1.8	0.21
J1215+0326	10520 ± 863	11.2 ± 0.9	2.7 ± 0.7	11.4 ± 1.4	0.28
J1219+0254	9008 ± 863	9.1 ± 1.0	2.9 ± 0.8	13 ± 2.1	0.34
J1231+0725	12467 ± 1730	8.0 ± 1.0	2.6 ± 0.7	12.0 ± 5.1	0.66
J1244+0821	12083 ± 991	9.5 ± 0.8	2.1 ± 0.6	16.1 ± 1.4	0.32
J1259+0752	12427 ± 2319	6.8 ± 1.3	1.4 ± 0.4	20.1 ± 4.6	0.46
J1314+0927	13244 ± 2806	5.3 ± 1.5	0.8 ± 0.2	20.8 ± 5.2	0.32
J1419+0749	11735 ± 831	7.2 ± 0.6	1.7 ± 0.5	16.0 ± 1.5	0.34
J1509+0744	13001 ± 1763	9.9 ± 1.4	1.6 ± 0.4	17.1 ± 3.0	0.28
J1519+0723	12118 ± 1399	12.9 ± 1.6	2.4 ± 0.6	15.1 ± 1.8	0.27
J1545+0156	13128 ± 1780	7.9 ± 1.1	1.2 ± 0.3	18.3 ± 3.0	0.35
J1609+0654	12761 ± 1460	10.6 ± 1.2	1.6 ± 0.5	18.0 ± 3.0	0.32
J1618+0704	13050 ± 2435	4.7 ± 0.9	0.5 ± 0.1	16.4 ± 4.6	0.25
J2116+0441	12940 ± 943	5.0 ± 0.4	2.5 ± 0.7	13.6 ± 1.8	0.63
J2145−0758	9937 ± 1368	8.5 ± 1.3	3.0 ± 0.9	9.0 ± 2.8	0.20
μ	11800 ± 1466	9.1 ± 1.2	1.8 ± 0.5	15.1 ± 2.9	0.33
σ	1950 ± 552	2.9 ± 0.5	0.6 ± 0.2	3.7 ± 1.4	0.12
SIQR	1127 ± 380	2 ± 0.3	0.4 ± 0.1	2.1 ± 1.4	0.06

Notes.(1) SDSS short name; (2) FWHM of the C IV and He II BLUE components; (3,4) normalized flux of the C IV and He II BLUE components; (5) separation from the rest-frame C IV emission in Å; (6) SPECFIT asymmetry. (*) BALQ. The measurements of J0252−0420 and J1516+0029 BALQ are excluded from this Table.

Table 4.5: Measurements in the λ1400 region: SiIV broad component and SiIV + OIV] asymmetric component.

SDSS JCODE (1)	1400 W (2)	BC FWHM (3)	SiIV Flux (4)	BLUE FWHM (5)	SiIV+OIV] Flux (6)	$\Delta\lambda$ (7)	skew (8)
J0020+0740	10	3275 ± 689	10.1 ± 1.8	9204 ± 1062	4.2 ± 0.5	10.4 ± 1.6	0.31
J0034−0326	4	3236 ± 741	4.1 ± 1.2	8891 ± 1659	2.1 ± 0.4	8.8 ± 4.2	0.35
J0037−0238	10	3184 ± 670	10.3 ± 1.9	9099 ± 1050	3.0 ± 0.4	8.0 ± 1.6	0.22
J0103−1104	4	2844 ± 635	5.2 ± 1.0	8014 ± 1087	1.4 ± 0.2	6.8 ± 2.7	0.19
J0106−0855	6	3298 ± 736	6.4 ± 1.3	9908 ± 1344	5.3 ± 0.7	10.4 ± 2.7	0.35
J0123+0329	6	2791 ± 575	5.1 ± 0.8	9047 ± 1035	4.2 ± 0.5	10.9 ± 2.8	0.25
J0210−0823	1	2302 ± 516	2.4 ± 0.7	9203 ± 1645	2.5 ± 0.7	11.7 ± 4.6	0.21
J0827+0306	5	3014 ± 676	4.3 ± 1.2	7999 ± 1429	1.8 ± 0.5	7.6 ± 4.7	0.29
J0829+0801	5	2614 ± 474	4.5 ± 0.6	7971 ± 581	4.1 ± 0.3	12.1 ± 1.6	0.35
J0836+0548	6	2904 ± 648	7.5 ± 1.5	8010 ± 1086	3.4 ± 0.5	7.7 ± 2.7	0.23
J0845+0722	6	3307 ± 681	6.3 ± 1.0	10612 ± 1214	4.3 ± 0.5	14.0 ± 2.7	0.33
J0847+0943	9	3006 ± 633	6.1 ± 1.1	7914 ± 913	6.5 ± 0.8	8.5 ± 1.6	0.45
J0858+0152	5	2999 ± 508	5.4 ± 0.6	12065 ± 821	6.8 ± 0.5	13.6 ± 1.0	0.35
J0903+0708	2	2601 ± 595	2.0 ± 0.6	7500 ± 1399	2.0 ± 0.4	9.7 ± 4.2	0.31
J0915−0202	9	3038 ± 678	7.4 ± 1.5	8016 ± 1087	3.2 ± 0.5	8.5 ± 2.7	0.28
J0926+0135	7	2876 ± 509	6.6 ± 0.9	9357 ± 767	4.4 ± 0.4	8.4 ± 1.3	0.20
J0929+0333	11	3016 ± 635	9.2 ± 2.0	9007 ± 1240	6.5 ± 1.0	8.7 ± 2.5	0.36
J0946−0124	10	2762 ± 558	10.3 ± 1.1	9111 ± 620	3.2 ± 0.3	8.6 ± 1.5	0.19
J1024+0245	6	3014 ± 620	4.8 ± 0.8	9004 ± 1030	4.5 ± 0.5	9.7 ± 2.8	0.42
J1026+0114	6	3160 ± 665	6.3 ± 1.2	9041 ± 1044	4.4 ± 0.5	9.6 ± 1.6	0.24
J1145+0800	7	3264 ± 732	7.8 ± 2.1	9085 ± 1623	4.8 ± 1.3	12.0 ± 4.6	0.30
J1214+0242	6	3122 ± 566	5.8 ± 0.7	8021 ± 584	3.4 ± 0.3	9.4 ± 1.6	0.34
J1215+0326	7	2405 ± 426	8.8 ± 1.2	7993 ± 655	2.6 ± 0.2	10.1 ± 1.3	0.34
J1219+0254	11	3236 ± 622	11.2 ± 1.5	7012 ± 672	2.8 ± 0.3	10.2 ± 1.9	0.35
J1231+0725	8	2421 ± 192	7.4 ± 0.4	9046 ± 1255	3.2 ± 0.4	11.1 ± 4.6	0.50
J1244+0821	6	3157 ± 559	5.6 ± 0.8	8999 ± 738	3.7 ± 0.3	8.6 ± 1.3	0.28
J1259+0752	4	3421 ± 783	4.7 ± 1.3	8034 ± 1499	2.0 ± 0.4	10.0 ± 4.2	0.19
J1314+0927	3	3628 ± 837	2.6 ± 0.8	8573 ± 1816	2.2 ± 0.6	12.3 ± 4.7	0.28
J1419+0749	5	2977 ± 556	3.7 ± 0.4	8143 ± 577	2.9 ± 0.2	9.9 ± 1.4	0.42
J1509+0744	6	3129 ± 699	4.2 ± 0.8	8245 ± 1118	4.2 ± 0.6	8.3 ± 2.7	0.30
J1519+0723	8	3124 ± 657	6.5 ± 1.2	8305 ± 959	6.3 ± 0.8	10.3 ± 1.6	0.42
J1545+0156	5	3004 ± 671	3.7 ± 0.7	8290 ± 1124	4.3 ± 0.6	11.0 ± 2.7	0.38
J1609+0654	4	3037 ± 625	4.4 ± 0.7	9305 ± 1065	3.8 ± 0.4	11.8 ± 2.7	0.30
J1618+0704	3	3048 ± 698	3.6 ± 1.0	8264 ± 1542	2.2 ± 0.4	11.4 ± 4.1	0.35
J2116+0441	4	3112 ± 564	6.6 ± 0.8	8699 ± 634	1.5 ± 0.1	8.6 ± 1.6	0.17
J2145−0758	6	3000 ± 631	6.8 ± 1.5	8921 ± 1228	2.8 ± 0.4	10.7 ± 2.5	0.27
μ	6	3009 ± 618	6.0 ± 1.1	8720 ± 1089	3.6 ± 0.5	10.0 ± 2.6	0.31
σ	2	282 ± 113	2.3 ± 0.4	906 ± 343	1.4 ± 0.2	1.7 ± 1.2	0.08
SIQR	1	134 ± 58	1.5 ± 0.3	534 ± 235	0.9 ± 0.1	1.2 ± 0.7	0.05

Notes. Columns are as follows: (1) SDSS short name; (2) Equivalent width between 1340-1450 Å; (3,4) FWHM and flux of the SiIV broad component respectively; (5,6) FWHM and flux of the SiIV + OIV] asymmetric emission respectively; (7) separation from de BC SiIV in units of Å; (8) SPECFIT asymmetry. The measurements of the six BALQ were excluded from this Table.

asymmetry (skewness of the gaussian).

Last, Table 4.5 lists the results for the 1400 Å region in the following order: (1) SDSS identification short code, (2) equivalent width, (3) broad component FWHM, (4) flux of SiIVBC, (5) BLUE component FWHM, (6) flux of SiIV+OIV] BLUE, (7) the separation from the rest-frame wavelength of SiIV BC in units of angstroms, and (8) the asymmetry of the emission line.

The tables reporting the flux ratios and its propagated error for the metallicity indicators that will be used to estimate the metal content alongside CLOUDY simulations (Table B.1 and B.2) are found at the end of the document in Appendix B.

4.1.2 Normalized intensities measurements

Tables 4.6 and 4.7 report the measurements of the three regions according to the procedure described in Sec. 3.5, an asterisk (*) identified the BALQ sources and the ellipsis (...) inconsistent measurements. Table 4.6 reports the broad component measurements (the center of the range of measurement is the rest frame wavelent of the emission line) for AlIII, SiIII], CIV, HeII and SiIV emissions. The columns list in order: (1) SDSS identification short code, (2, 3, 4, 5, 6) the normalized intensity measure with its error.

For the CIV and SiIV regions, we also measure a second range center at -4000 km s^{-1} from the rest frame wavelength to represent the BLUE emission of these regions. Table 4.7 reports these BLUE measurements for BLUE CIV, BLUE HeII and SiIV+ OIV]. The columns list in order: (1) SDSS identification short code, (2, 3, 4) the normalized intensity measure with its error.

The tables reporting the flux ratios and its propagated error for the metallicity indicators that will be used to estimate the metal content alongside CLOUDY simulations (Table B.3 and B.4) are found at the end of the document in Appendix B.

Table 4.6: Normalized intensities of Al III, Si III], C IV, He II and Si IV broad components.

SDSS JCODE (1)	Al III λ1860 (2)	Si III] λ1891 (3)	C IV λ1549 (4)	He II λ1640 (5)	Si IV λ1400 (6)
J0020+0740	0.141 ± 0.024	0.201 ± 0.021	0.34 ± 0.09	0.054 ± 0.018	0.31 ± 0.03
J0034−0326	0.089 ± 0.027	0.116 ± 0.021	0.15 ± 0.11	0.04 ± 0.016	0.13 ± 0.03
J0037−0238	0.099 ± 0.017	0.111 ± 0.015	0.38 ± 0.04	0.05 ± 0.016	0.32 ± 0.03
J0103−1104	0.081 ± 0.015	0.132 ± 0.03	0.2 ± 0.03	0.046 ± 0.024	0.18 ± 0.03
J0106−0855	0.102 ± 0.018	0.164 ± 0.018	0.18 ± 0.05	0.028 ± 0.012	0.23 ± 0.04
J0123+0329	0.086 ± 0.015	0.111 ± 0.023	0.1 ± 0.03	0.005 ± 0.023	0.15 ± 0.03
J0210−0823	0.11 ± 0.027	0.147 ± 0.041	0.1 ± 0.06	0.039 ± 0.031	0.03 ± 0.03
J0216+0115*	0.157 ± 0.015	0.153 ± 0.018	0.34 ± 0.04	0.03 ± 0.012	...
J0252−0420*	0.198 ± 0.035	0.226 ± 0.098	...	...	...
J0827+0306	0.082 ± 0.027	0.083 ± 0.02	0.16 ± 0.04	0.016 ± 0.028	0.15 ± 0.04
J0829+0801	0.129 ± 0.012	0.144 ± 0.014	0.16 ± 0.05	0.027 ± 0.014	0.17 ± 0.02
J0836+0548	0.118 ± 0.016	0.189 ± 0.022	0.22 ± 0.04	0.025 ± 0.012	0.26 ± 0.03
J0845+0722	0.104 ± 0.023	0.126 ± 0.016	0.2 ± 0.04	0.027 ± 0.019	0.2 ± 0.05
J0847+0943	0.158 ± 0.034	0.137 ± 0.082	0.3 ± 0.08	0.044 ± 0.02	0.3 ± 0.05
J0858+0152	0.086 ± 0.013	0.13 ± 0.007	0.18 ± 0.09	0.023 ± 0.009	0.17 ± 0.03
J0903+0708	0.084 ± 0.015	0.084 ± 0.016	0.04 ± 0.09	0.022 ± 0.019	0.08 ± 0.02
J0915−0202	0.067 ± 0.024	0.094 ± 0.043	0.21 ± 0.11	0.047 ± 0.02	0.25 ± 0.04
J0926+0135	0.1 ± 0.01	0.156 ± 0.022	0.26 ± 0.04	0.051 ± 0.015	0.23 ± 0.02
J0929+0333	0.179 ± 0.037	0.249 ± 0.022	0.41 ± 0.12	0.044 ± 0.028	0.38 ± 0.05
J0932+0237*	0.177 ± 0.063	0.217 ± 0.095	0.59 ± 0.15	0.069 ± 0.023	...
J0946−0124	0.114 ± 0.016	0.161 ± 0.053	0.42 ± 0.05	0.065 ± 0.01	0.34 ± 0.05
J1013+0851*	0.239 ± 0.029	0.286 ± 0.01	0.21 ± 0.05	0.08 ± 0.019	...
J1024+0245	0.117 ± 0.019	0.151 ± 0.016	0.16 ± 0.07	0.023 ± 0.019	0.2 ± 0.02
J1026+0114	0.164 ± 0.024	0.172 ± 0.028	0.18 ± 0.04	0.034 ± 0.013	0.21 ± 0.02
J1145+0800	0.146 ± 0.03	0.188 ± 0.046	0.07 ± 0.25	0.028 ± 0.019	0.23 ± 0.03
J1205+0201*	0.104 ± 0.026	0.14 ± 0.011	0.15 ± 0.03	0.018 ± 0.01	...
J1214+0242	0.12 ± 0.011	0.162 ± 0.007	0.25 ± 0.05	0.028 ± 0.008	0.21 ± 0.02
J1215+0326	0.098 ± 0.013	0.168 ± 0.029	0.3 ± 0.15	0.047 ± 0.01	0.31 ± 0.02
J1219+0254	0.131 ± 0.018	0.226 ± 0.016	0.52 ± 0.04	0.084 ± 0.017	0.33 ± 0.02
J1231+0725	0.096 ± 0.022	0.161 ± 0.04	0.67 ± 0.07	0.11 ± 0.009	0.3 ± 0.04
J1244+0821	0.098 ± 0.024	0.142 ± 0.011	0.21 ± 0.03	0.027 ± 0.01	0.19 ± 0.06
J1259+0752	0.05 ± 0.011	0.052 ± 0.013	0.05 ± 0.07	0.019 ± 0.013	0.11 ± 0.06
J1314+0927	0.092 ± 0.02	0.098 ± 0.027	0.03 ± 0.05	0.026 ± 0.026	0.05 ± 0.05
J1419+0749	0.089 ± 0.016	0.137 ± 0.011	0.2 ± 0.03	0.029 ± 0.03	0.16 ± 0.02
J1509+0744	0.109 ± 0.017	0.169 ± 0.028	0.16 ± 0.05	0.032 ± 0.015	0.18 ± 0.02
J1516+0029*	0.487 ± 0.053	0.389 ± 0.085	...	...	...
J1519+0723	0.153 ± 0.026	0.238 ± 0.022	0.22 ± 0.06	0.033 ± 0.019	0.2 ± 0.15
J1545+0156	0.143 ± 0.017	0.158 ± 0.014	0.15 ± 0.03	0.025 ± 0.033	0.14 ± 0.02
J1609+0654	0.101 ± 0.028	0.12 ± 0.011	0.13 ± 0.07	0.014 ± 0.013	0.15 ± 0.03
J1618+0704	0.088 ± 0.018	0.092 ± 0.017	0.09 ± 0.03	0.012 ± 0.017	0.12 ± 0.02
J2116+0441	0.092 ± 0.016	0.135 ± 0.02	0.34 ± 0.03	0.031 ± 0.011	0.19 ± 0.03
J2145−0758	0.124 ± 0.035	0.237 ± 0.028	0.35 ± 0.09	0.021 ± 0.033	0.23 ± 0.05
μ	0.126 ± 0.023	0.161 ± 0.028	0.23 ± 0.07	0.037 ± 0.018	0.2 ± 0.04
σ	0.068 ± 0.011	0.061 ± 0.023	0.14 ± 0.04	0.021 ± 0.007	0.08 ± 0.02
SIQR	0.025 ± 0.006	0.028 ± 0.007	0.08 ± 0.02	0.011 ± 0.005	0.05 ± 0.01

Notes. All intensities are normalized to the continuum flux at 1350 Å (Col.7 of Table 2.1). BALQ are marked with an asterisk(*) .

Table 4.7: Normalized intensities of BLUE C IV, BLUE He II and BLUE Si IV+ O IV].

SDSS JCODE (1)	BLUE C IV λ1536 (2)	BLUE He II λ1626 (3)	BLUE Si IV+ O IV] λ1385 (4)
J0020+0740	0.33 ± 0.03	0.064 ± 0.024	0.175 ± 0.04
J0034−0326	0.17 ± 0.11	0.012 ± 0.08	0.055 ± 0.044
J0037−0238	0.26 ± 0.04	0.06 ± 0.012	0.153 ± 0.046
J0103−1104	0.17 ± 0.04	0.031 ± 0.021	0.064 ± 0.036
J0106−0855	0.26 ± 0.02	0.039 ± 0.026	0.14 ± 0.066
J0123+0329	0.19 ± 0.02	0.03 ± 0.016	0.089 ± 0.151
J0210−0823	0.11 ± 0.05	0.042 ± 0.02	0.088 ± 0.045
J0216+0115*	...	0.039 ± 0.02	...
J0252−0420*	...	...	...
J0827+0306	0.13 ± 0.049	0.043 ± 0.026	0.078 ± 0.042
J0829+0801	0.255 ± 0.021	0.048 ± 0.014	0.115 ± 0.067
J0836+0548	0.201 ± 0.094	0.05 ± 0.022	0.146 ± 0.041
J0845+0722	0.241 ± 0.024	0.051 ± 0.018	0.16 ± 0.023
J0847+0943	0.351 ± 0.027	0.066 ± 0.02	0.206 ± 0.036
J0858+0152	0.205 ± 0.137	0.043 ± 0.009	0.069 ± 0.141
J0903+0708	0.13 ± 0.014	0.02 ± 0.015	0.085 ± 0.028
J0915−0202	0.228 ± 0.025	0.053 ± 0.017	0.137 ± 0.038
J0926+0135	0.273 ± 0.021	0.047 ± 0.008	0.119 ± 0.089
J0929+0333	0.354 ± 0.056	0.058 ± 0.024	0.196 ± 0.071
J0932+0237*	0.52 ± 0.071	0.102 ± 0.024	...
J0946−0124	0.22 ± 0.047	0.054 ± 0.011	0.086 ± 0.03
J1013+0851*	0.188 ± 0.146	0.073 ± 0.011	...
J1024+0245	0.257 ± 0.025	0.04 ± 0.014	0.145 ± 0.027
J1026+0114	0.286 ± 0.027	0.042 ± 0.02	0.18 ± 0.021
J1145+0800	0.238 ± 0.052	0.032 ± 0.044	0.152 ± 0.037
J1205+0201*	0.188 ± 0.012	0.014 ± 0.011	...
J1214+0242	0.118 ± 0.177	0.049 ± 0.007	0.089 ± 0.135
J1215+0326	0.312 ± 0.089	0.062 ± 0.012	0.107 ± 0.054
J1219+0254	0.293 ± 0.037	0.087 ± 0.015	0.106 ± 0.055
J1231+0725	0.282 ± 0.057	0.067 ± 0.02	0.003 ± 0.08
J1244+0821	0.237 ± 0.033	0.046 ± 0.01	0.133 ± 0.019
J1259+0752	0.139 ± 0.025	0.027 ± 0.008	0.109 ± 0.015
J1314+0927	0.095 ± 0.024	0.021 ± 0.016	0.066 ± 0.038
J1419+0749	0.195 ± 0.02	0.037 ± 0.008	0.106 ± 0.019
J1509+0744	0.237 ± 0.029	0.05 ± 0.024	0.164 ± 0.054
J1516+0029*	...	...	...
J1519+0723	0.345 ± 0.038	0.072 ± 0.029	0.225 ± 0.041
J1545+0156	0.001 ± 0.163	0.03 ± 0.014	0.077 ± 0.093
J1609+0654	0.228 ± 0.016	0.001 ± 0.051	0.139 ± 0.016
J1618+0704	0.131 ± 0.021	0.022 ± 0.022	0.083 ± 0.04
J2116+0441	0.112 ± 0.046	0.045 ± 0.012	0.041 ± 0.067
J2145−0758	0.276 ± 0.073	0.086 ± 0.025	0.026 ± 0.111
μ	0.21 ± 0.06	0.046 ± 0.035	0.114 ± 0.054
σ	0.12 ± 0.06	0.021 ± 0.013	0.051 ± 0.035
SIQR	0.06 ± 0.02	0.013 ± 0.006	0.033 ± 0.016

Notes. All intensities are normalized to the continuum flux at 1350 Å (Col.7 of Table 2.1). BALQ are marked with an asterisk(*).

4.2 Intensity ratios

Our analysis depends on emission line flux ratios, hence in this section we show the flux ratios from our *specfit* measurements along side its propagated error. This section is divided into two sub-sections:

- BC intensity ratios
- BLUE intensity ratios

4.2.1 BC intensity ratios

Fig. 4.1 show ratios that we consider particular because includes the distributions of the individual ratios AlIII/SiIII] and CIII]/SiIII] help us to discriminate xA sources (see Fig. 4.5 in Sec. 4.3 for further explanation) as well as the SiIII]/HeII and CIII]/HeII distributions. The lower panels shows the results for individual non-BALQ sources and its errors, the vertical continuous lines show the mean values of the distributions and the dashed vertical lines are set to 1 for the SiIII]/HeII and CIII]/HeII distributions and for the AlIII/SiIII] and CIII]/SiIII] distributions the dashed vertical lines are set to 0.5. The outlying sources, whose values and error bars lie outside the AlIII/SiIII] and CIII]/SiIII] limits, are J0103−1104 (Fig. A.4), a low W source with a strong CIII] emission, and J1231+0725 (Fig. A.30), a BC-dominated spectrum with faint BLUE.

Fig. 4.2 shows the normalized distributions of the diagnostic intensity ratios AlIII/HeII, CIV/HeII and SiIV/HeII for the BC, and Fig. 4.3 shows the diagnostic intensity ratios of CIV/AlIII, SiIV/CIV and SiIV/AlIII also for the BC. The vertical lines identify the mean values of the distributions: μ(AlIII/HeII)=3.70, μ(CIV/HeII)=5.42, μ(SiIV/HeII)=5.55, μ(CIV/AlIII)=1.86, μ(SiIV/CIV)=1.01 and μ(SiIV/AlIII)=1.78. The dispersion for each ratio are: σ(AlIII/HeII)=2.3, σ(CIV/HeII)=2.5, σ(SiIV/HeII)=2.4, σ(CIV/AlIII)=1.4, σ(SiIV/CIV)=0.4 and σ(SiIV/AlIII)=0.9 (See. Table B.1).

The distribution of the data points involving HeII shows a small dispersion from the general mean with the exception of J1609+0654 (Fig. A.39), a type 1 QSO

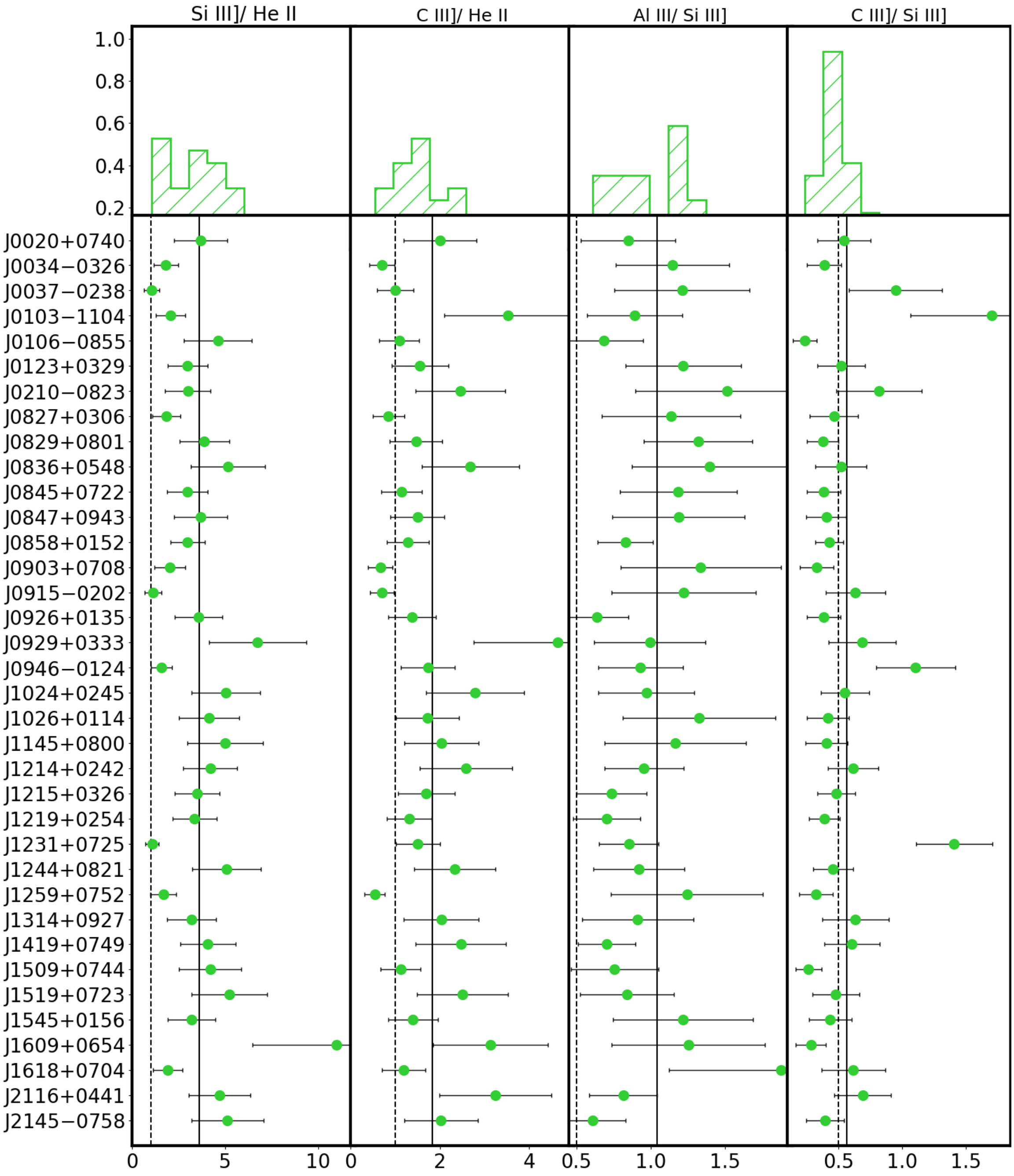

Figure 4.1: Distribution (top) and individual (bottom) intensity ratios between prominent lines not used for metallicity estimates. The two panels on the rights show the ratios involved in the identification of xA sources. The vertical solid lines identify the mean value of the distribution while the dashed lines are set to 1 for the SiIII]/HeII and CIII]/HeII distributions. For the AlIII/SiIII] and CIII]/SiIII] distributions the dashed vertical lines are set to 0.5. Left labels identified the sources.

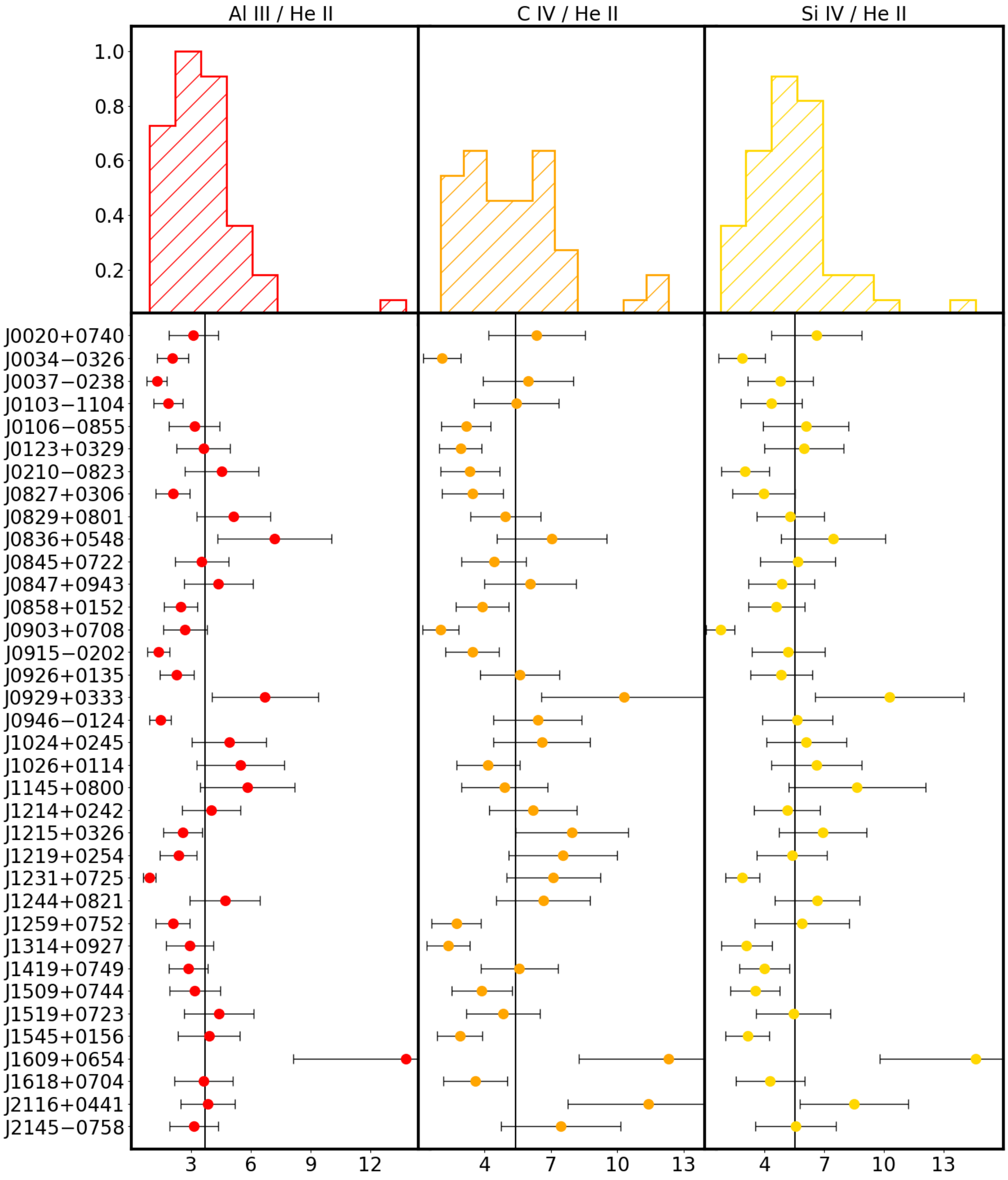

Figure 4.2: Distribution and individual BC intensity ratios used as metallicity diagnostic involving HeIIλ1640. Upper panels show the distributions for AlIII/HeII, CIV/HeII and SiIV/HeII ratios respectively. Lower panels show the individual ratios and their errors, the vertical lines identify the mean values of the distribution. Left labels identified the sources.

with weak broad components especially for HeII which for this case was more likely underestimated due to absorptions and low S/N near the area. Fig. 4.2 distributions show more sources outside the trend. An example is J1231+0725, a clear non-xA source. Higher values of the CIV/HeII and SiIV/HeII ratios are associated with

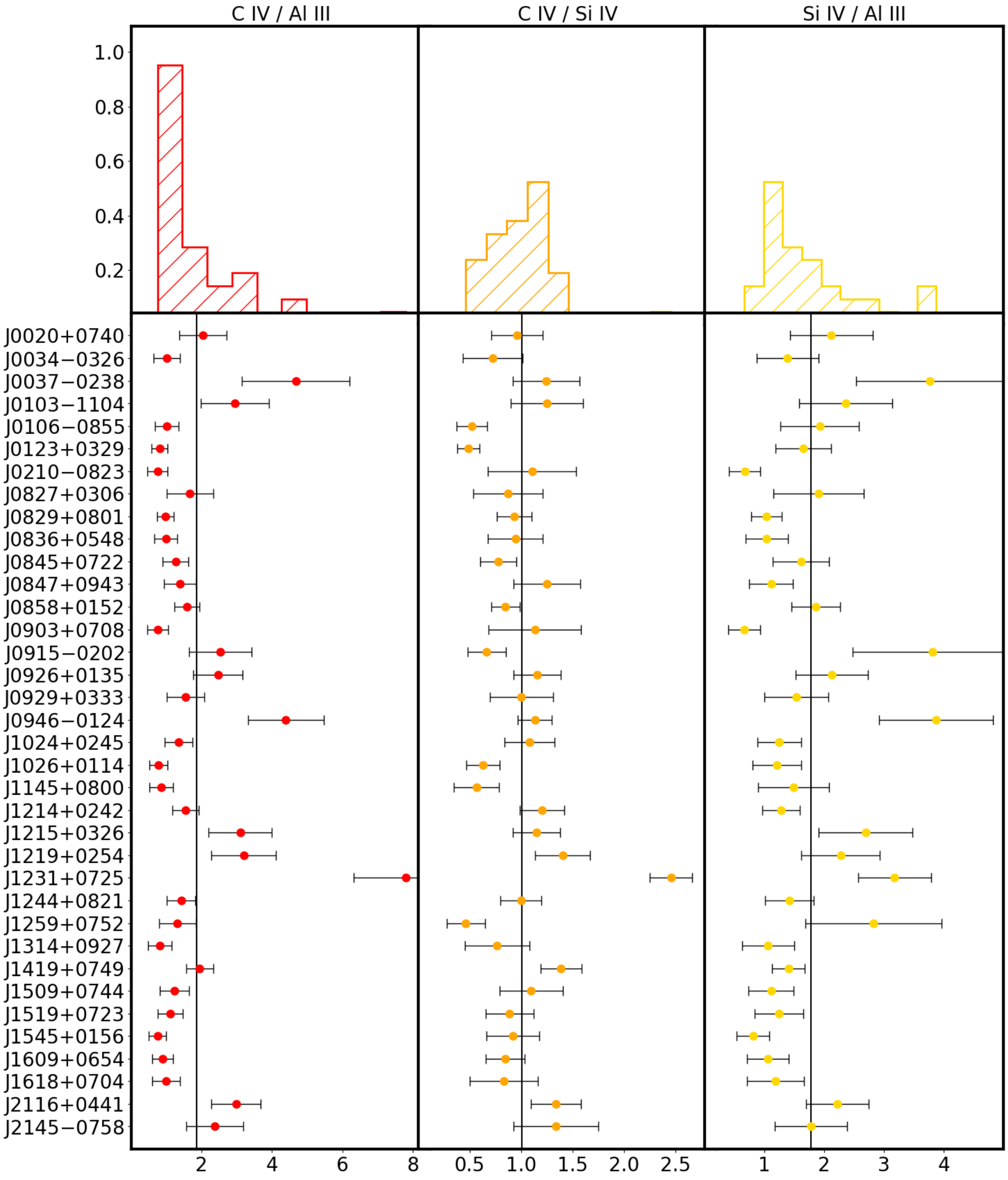

Figure 4.3: Distribution and individual BC intensity ratios used as metallicity diagnostic for non involving HeIIλ1640 ratios. Upper panels show the distributions for CIV/AlIII, SiIV/CIV and SiIV/AlIII ratios respectively. Lower panels show the individual ratios and their errors, the vertical lines identify the mean values of the distribution. Left labels identified the sources.

higher ionization parameter and with the 3 cases of non-xA and borderline sources (J0103-1104, J1231+0726, and J0946-0124) identified in Sec. 4.3

Since the three HeII ratios are, for fixed physical conditions, proportional to metallicity (see Sect. 4.5.1), we expect an overall consistency in their behavior i.e., if one object ratio is higher than the sample mean, the other intensity ratios of the same object should be also higher. The lower panels are helpful to identify sources for which only one intensity ratio deviates significantly from the rest of the sample. The lack of consistency shown in Fig. 4.3 distributions was also found for its `CLOUDY` metallicity relations for fixed physical conditions (see Sect. 4.5.1) so these relations won't be considered for further analysis.

4.2.2 BLUE intensity ratios

Fig. 4.4 shows the distributions of the diagnostic intensity ratios between the BLUE components of CIV/HeII, (SiIV+ OIV])/HeII and CIV/(SiIV+ OIV]). The vertical lines identify the mean values of the distributions, μ(CIV/HeII)= 5.17, μ((SiIV+ OIV])/HeII)=2.11, μ(CIV/(SiIV+ OIV]))=2.64.

The distributions show wide error bars as well as large dispersion: σ(CIV/HeII)= 1.5, σ((SiIV+ OIV])/HeII)=0.9, σ(CIV/(SiIV+ OIV]))=0.7 (See Table B.2). For most of the sources the SiIV+ OIV] BLUE component emission is slightly weaker than CIV BLUE component, resulting in well behaved distributions with the exception of J2116+0441 and J2145−0758 that show weak SiIV+ OIV] BLUE emission surrounded by absorptions and affected by poor S/N. BLUE CIV/(SiIV+ OIV]) ratios show an apparently more confused distribution. However, two groups can be identified: a majority one with median BLUE CIV/(SiIV+ OIV]$\approx$ 2.5, and a minority one (four sources) with larger BLUE CIV/(SiIV+ OIV]) $\approx$ 4. The higher ratios that can be reconduced to heavy absorptions affection the SiIV+ OIV] profile. The source J1215+0326 shows the highest ratio due to the strong absorption in both wings of the 1400 Å region. Indeed the BLUE ratios for J1215+0326 appear not to be fully consistent due to the absorption that affects also the red side of the SiIV profile and introduces a large source of uncertainty. In the case of these two sources the ratio CIV/(SiIV + OIV]) should not be considered reliable.

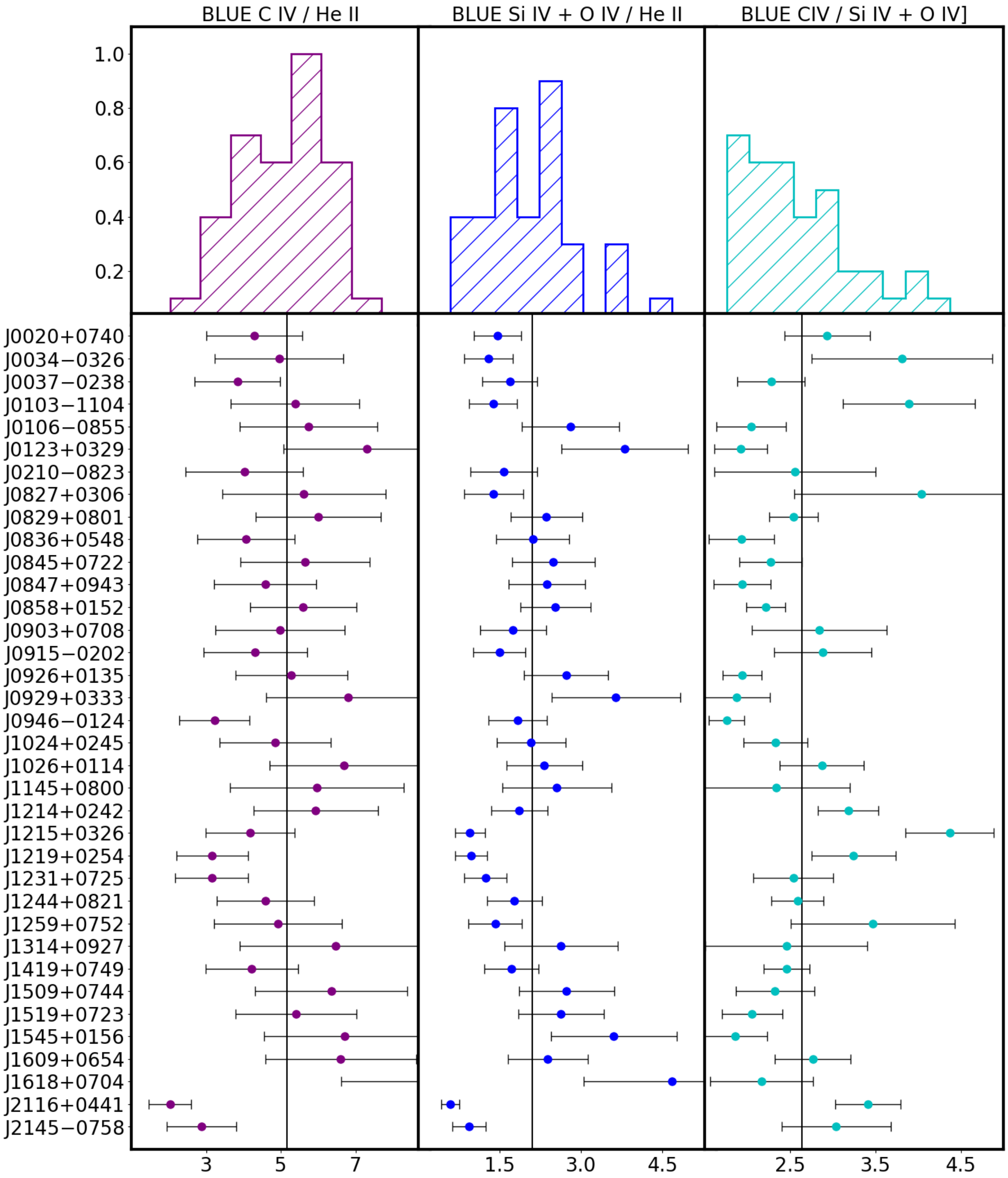

Figure 4.4: Distribution and individual BLUE intensity ratios used as metallicity diagnostic. Upper panels show the distributions for CIV/HeII, (SiIV+ OIV])/HeII and CIV/(SiIV+ OIV]) BLUE ratios respectively. Lower panels show the individual ratios and their errors, the vertical lines identify the mean values of the distribution. Left labels identified the sources.

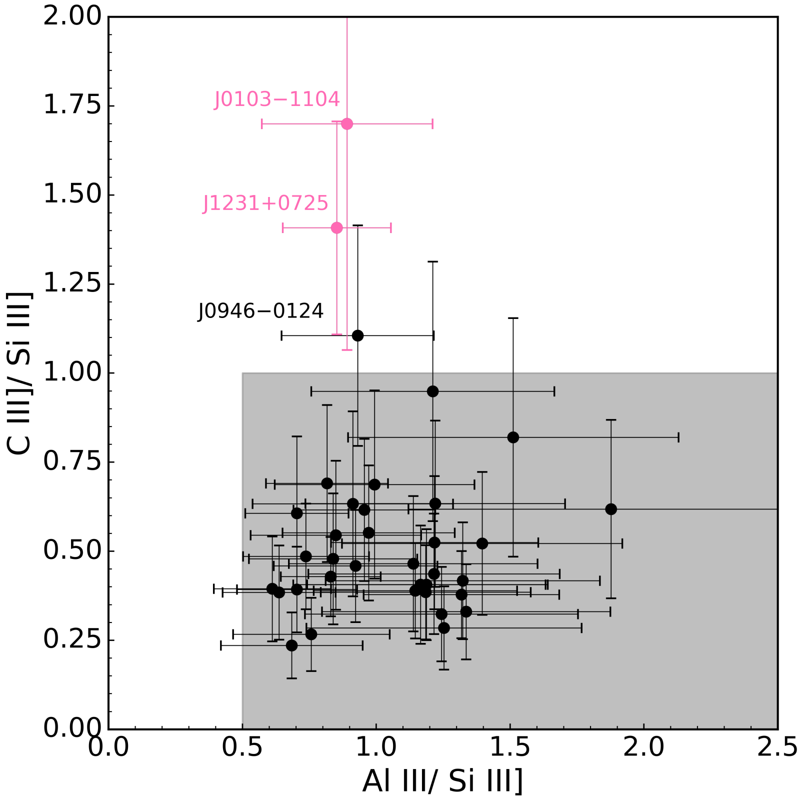

Figure 4.5: Relation between intensity ratios AlIIIλ1860/SiIII]λ1892 and CIII]λ1909/SiIII]λ1892. The gray area corresponds to the parameter space occupied by the xA sources. Outliers sources are in pink color.

4.3 Identification of xA sources and "intruders"

Figure 4.5 shows the UV-plane selection criteria. The vast majority of our sample are xA quasars except for the two sources, J0103−1104 and J1231+0726 that were previously identified as outlying sources. They show a spectra not consistent with the xA spectral type and will not be considered for further statistic analysis. On the converse, the borderline object J0946−0124 is outside the xA part of the parameter plane. However, its error bars indicate that the criteria are still satisfied within 1 σ confidence level. The overall appearance of the spectrum (Fig. A.11) supports the classification of J0946−0124 as an xA source.

The lack of a clear trend shown in Figure 4.5 may be due to the prior selection criteria for the xA bin in the 4DE1 parameter, because we are zooming into one bin of the 4DE1 that shows a small dispersion around well-defined parameter values.

4.4 Correlation between diagnostic ratios and physical parameters

Figure 4.6 shows the correlations between all diagnostic ratios employed in this work. Blue plots (left lower matrix) show the correlations between the diagnostic ratios from Tables B.1 and B.2, for both broad and blue components. Green plots (upper right matrix) represent the correlations between the physical parameters derived for each object. The pink dots correspond to the intruders described in sec. 4.3 and are not considered for the statistic analysis. In order to get a better correlation we also excluded from the analysis, if needed, sources laying away from the main relation. These sources are shown as black dots and its subtraction create four sub-samples. The solid line shows the linear relation between the remaining sub-sample per panel, the shadow represents the confidence interval of the linear regression at 1σ, and top right corner of each panel shows the Spearman correlation coefficient.

Most of the relations in Figure 4.6 shows a weak trend, in spite of the elimination of outlying sources. This may be due, as mentioned, to the trend-less behavior of the spectral parameters in the xA bin of the 4DE1 and also to the single epoch criteria, i.e. that have a single observation.

The panels involving BLUE CIV/(SiIV+ OIV]) (second row from bottom) show no significant correlation as the flux ratio remains approximately constant. This constant value may imply that the wind emission in the HILs is active throughout the sample, and that the emitting gas might be in similar physical conditions.

The relations that show the highest correlation coefficient ($r > 0.77$, last two panels of the last row) are between the BLUE components. However, these ratios are not statistically independent since they involve the same lines in abscissa and ordinate, and all of them are HILs and need similar conditions to occur.

Among all the ratios in our correlation matrix our most significant result is the relation between BLUE CIV/HeII and BC CIV/AlIII with a correlation coefficient of $r = 0.626$. showing a connection between the metallicity indicators for the BC and the BLUE which is consistent with the overall high-Z scenario emerging from the present work: BLUE CIV/HeII decreases with increasing CIV/AlIII, and both

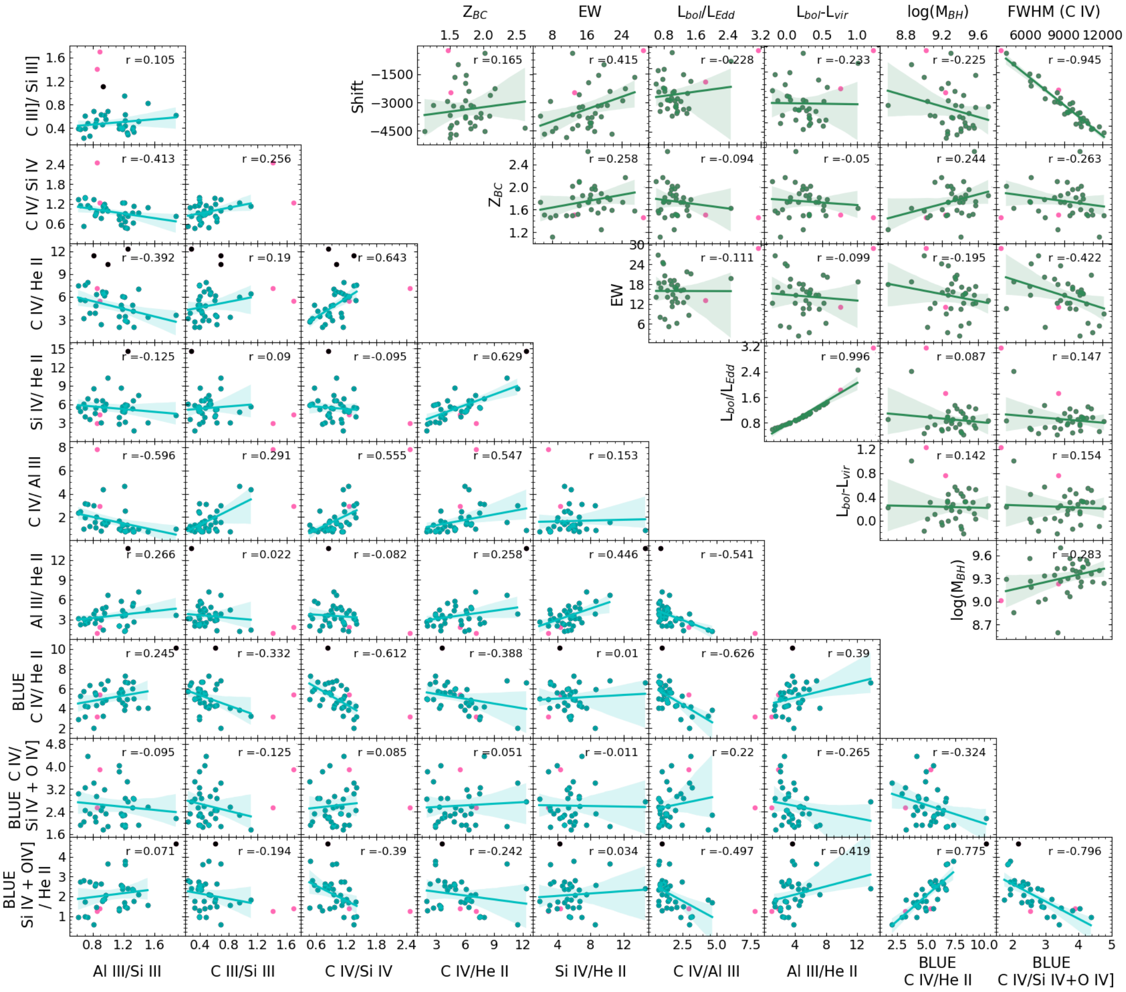

Figure 4.6: Correlation matrix between diagnostic ratios for BC and BLUE and physical parameters. The pink dots are the outliers sources described in sec. 4.3 and are not considered in the statistic analysis. For each panel we excluded, if necessary, the sources with the highest dispersion from the main relation (black dots). For both matrix, the solid lines show the linear fit for each subsample, the shadow represent the confidence interval of the lineal regression at 1σ, the color dots are to the remain sources and show the behavior of the ratios involved. For each panel, right top corner shows the Spearman correlation coefficient (r) of the remain sources.

ratios increase with decreasing metallicity (Section 4.5.1 and following). However, also this anti-correlation should be viewed with care: most of the data points cluster around a typical value.

4.5 Metallicity inferences

As mentioned in section 3.7, we use flux ratios as metallicy indicators of the broad line region. Among all the indicators proposed by different authors (e.g. Nagao et al., 2006b; Shin et al., 2013; Marziani & Sulentic, 2014a) we selected the six that show the greatest consistency for CLOUDY relations. We also considered the fitting complex for regions with $\lambda < 1300$ Å. However, even though N IV]λ1486 is present for most of our sample, we decided to avoid its fitting procedure because it appears to be weak, and in some cases it is severely affected by absorptions.

Since our metallicity indicators involve LIL, IIL and HIL, we decided to model the BLR using two types of clouds following S21

- virialized clouds, for LIL and IIL described with $\log(n_{\mathrm{H}})$ = 12-13 and $\log(U)$ = -2.5
- wind clouds, for HIL described with $\log(n_{\mathrm{H}}) = 9$ and $\log(U) = 0$.

We also inferred the metallicity in two ways, which structure this section:

Sec. 4.5.1: For fixed constraints on U and n_{H}

Sec. 4.5.2: For relaxing constraints on U and n_{H}.

4.5.1 Estimates of Z distributions at fixed (U, n_{H})

Our six metallicity indicators are shown in Figure 4.7. Left panel shows the low ionization zone metallicity indicators, and right panel shows the high ionization potential metallicity indicators or BLUE component indicators. For both panels the stars represent the flux ratios predicted by CLOUDY according to the specified physical conditions, we fitted each CLOUDY trend with a cubic spline (dashed lines) and derive the metallicity of our sample according to it. The thicker solid lines show the ranges of metallicity derived from our sample.

In order to seek for a better description of the BLR, we decided to use two cases of density $\log(n_{\mathrm{H}}) = 12$ and $\log(n_{\mathrm{H}}) = 13$ for the BC ratios but keeping the ionization parameter fixed at $\log(U)$= -2.5. Table 4.8 lists the derived metallicities

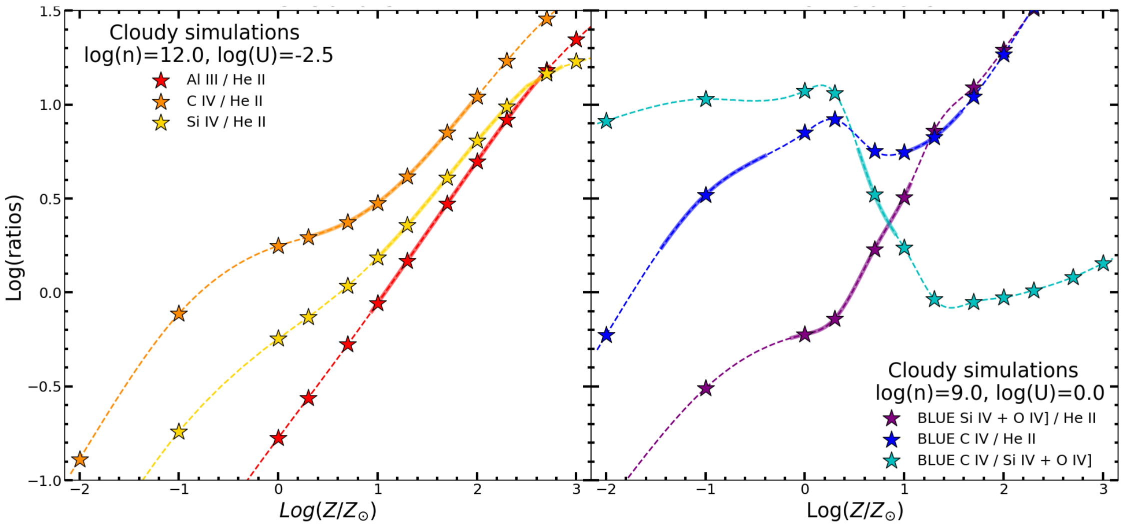

Figure 4.7: Intensity ratios trend predicted by CLOUDY as a function of metallicity, for physical parameters U and $n_{\rm H}$ fixed. The *left* panel show the relations for the low ionization zone metallicity indicatorsand the *right* panel the relations for the high ionization potential emissions (BLUE components). For both panels, the stars represent the ratios predicted by CLOUDY, the dashed lines show the continuous relations between the ratios and Z obtained by a cubic spline, the solid thick line in each relation shows the range covered by our sample.

for the three broad component metallicity indicators and their median value (Z$_{\mu_{1/2}}$) for the log($n_{\rm H}$) = 12 and Table 4.9 lists the values for the log($n_{\rm H}$) = 13 case. Left panel of Figure 4.7 shows only the case for log($n_{\rm H}$) = 12, it can be seen that our three BC indicators show a consistent trend. The derived median value is Z = 1.73 ± 0.15Z$_\odot$ for the virialized clouds as reported in table 4.8. The errors for the metallicity estimates, both BC and BLUE relations, were estimated following the flux ratio error propagation but considering them as relative errors for their logarithmic display.

The wind clouds were described with a density of log($n_{\rm H}$) = 9 and a ionization parameter of log(U) = 0, as shown in the right panel of Fig 4.7. These ratios do not show consistent relations, especially for the BLUE CIV/HeII ratio with a no-monotonic trend (also shown in Fig. 17 of S21). The non-monotonic behavior occur in the interval from sub-solar to super solar metallicity, which means that one value of the BLUE CIV/HeII ratio may correspond to three values of the metallicity. Thus, for the sources that cross the trend (blue dashed line in Fig. 4.7) in three points we decided to take the average value. Table 4.10 lists the derived metallicities for our

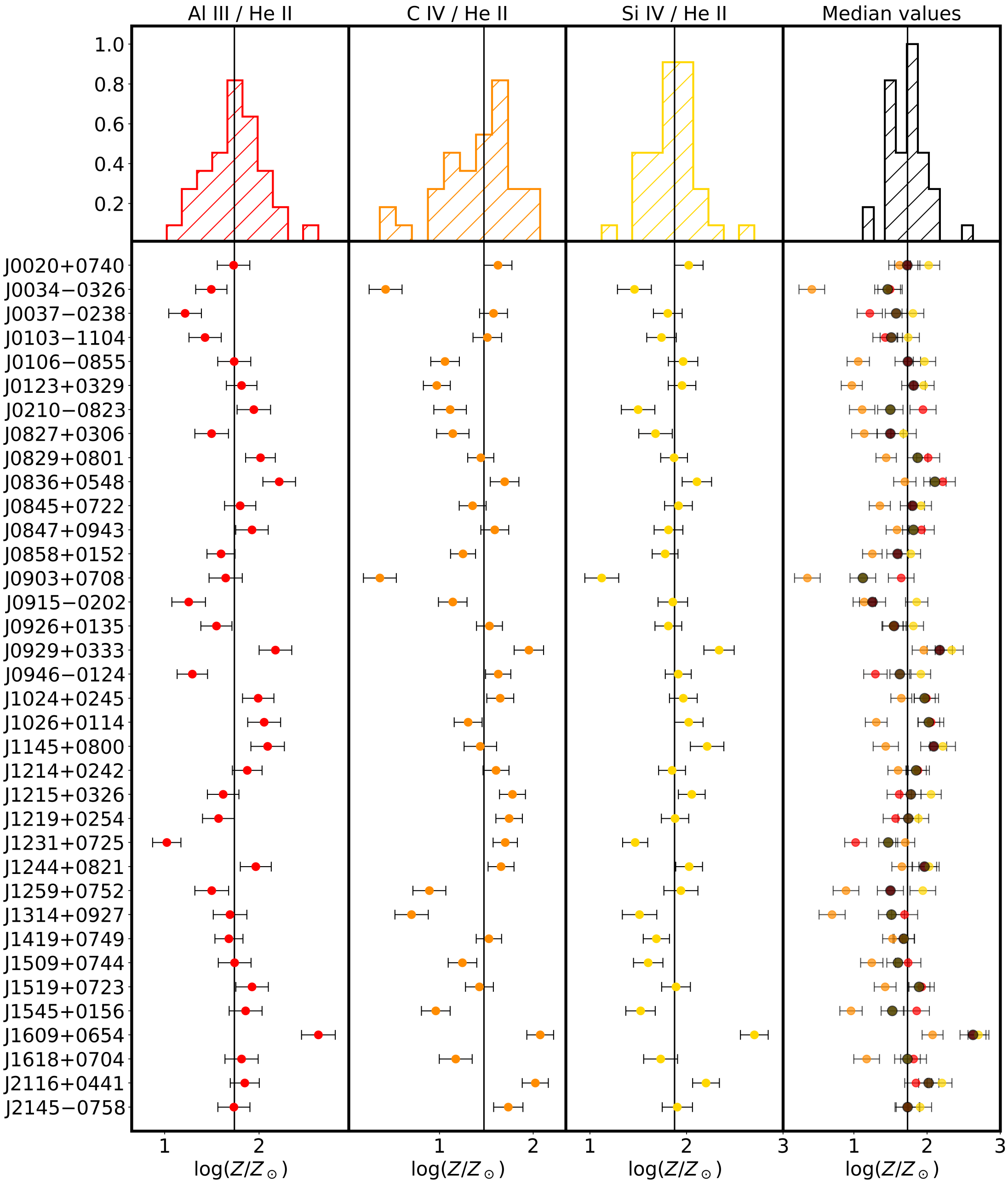

Figure 4.8: Distribution and individual BC metallicity estimates involving HeIIλ1640. Upper panels show the distributions of the metallicity estimated from AlIII/HeII, CIV/HeII and SiIV/HeII `CLOUDY` relations respectively and in black the median values of the derivev metallicity. Lower panels show the individual metallicity estimates and their errors, the vertical lines identify the median values of the distribution. Left labels identified the sources.

three BLUE metallicity indicators and their median value, with a general median value of Z = 0.77 ± 0.13 $Z_\odot$ (as reported in table 4.10), setting a lower metallicity limit for our sample.

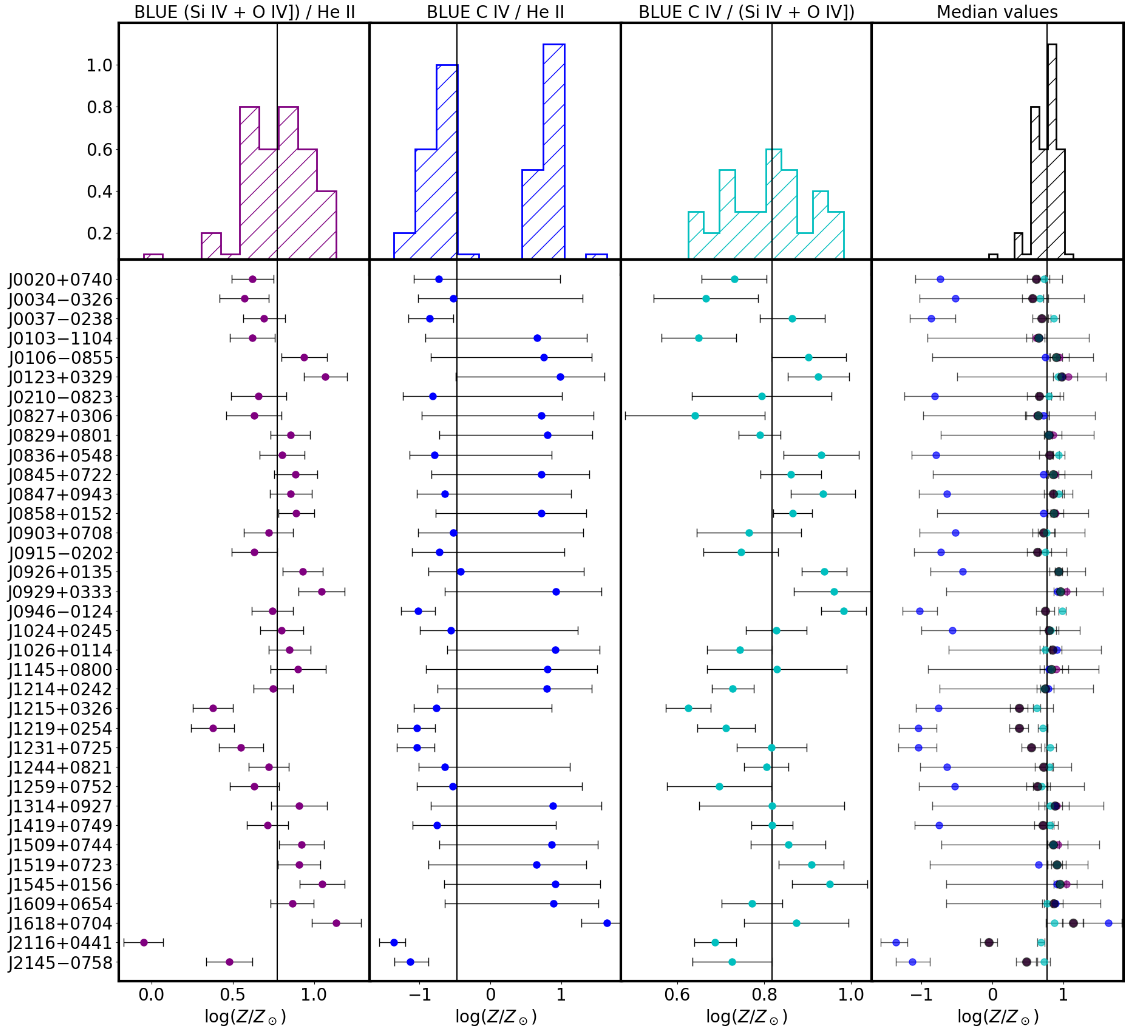

Figure 4.9: Distribution and individual BC metallicity estimates involving HeIIλ1640. Upper panels show the distributions of the metallicity estimated from AlIII/HeII, CIV/HeII and SiIV/HeII `CLOUDY` relations respectively and in black the median values of the derivev metallicity. Lower panels show the individual metallicity estimates and their errors, the vertical lines identify the median values of the distribution. Left labels identified the sources.

Figure 4.8 shows the metallicity estimates distributions in log(Z/Z$_\odot$) for the BC intensity ratios shown in Fig. 4.2. The right top and bottom panels show the superimposed estimates from the three ratios and their median values in black. The values derived from the BC CIV/HeII relation are the ones with higher dispersion from the general median especially those with a strong HeII feature such as J0034−0326 (Fig. A.2) and J0903+0708 (Fig. A.16).

Figure 4.9 show the metallicity estimates distributions in log(Z/Z$_\odot$) for the BLUE intensity ratios shown in Fig. 4.4. The right top and bottom panels show the superimposed estimates from the three ratios and their median values in black. What stands out the most is the bi-valuated behavior of the BLUE CIV/HeII estimates, this is caused by the non-monotonic behavior of the respective CLOUDY relation shown in Fig. 4.7. For the sources crossing the trend in three points, the dots are the mean of the three possible values and the error bars are extended to lowest point where the source cross the trend (negative error bar) and the highest point where the source cross the trend (positive error bar).

Table 4.8: Metallicity (log Z) of the BC assuming fixed log(U)=-2.5 and log(n_{H})=12

SDSS JCODE (1)	Al III/He II (2)	C IV/He II (3)	Si IV/He II (4)	$Z_{\mu_{1/2}}$ (5)
J0020+0740	1.73 ± 0.17	1.62 ± 0.15	2.02 ± 0.15	1.73 ± 0.15
J0034−0326	1.49 ± 0.17	0.42 ± 0.18	1.46 ± 0.18	1.46 ± 0.18
J0037−0238	1.22 ± 0.17	1.58 ± 0.15	1.8 ± 0.15	1.58 ± 0.15
J0103−1104	1.43 ± 0.17	1.51 ± 0.15	1.74 ± 0.15	1.51 ± 0.15
J0106−0855	1.74 ± 0.17	1.06 ± 0.15	1.96 ± 0.15	1.74 ± 0.15
J0123+0329	1.81 ± 0.16	0.97 ± 0.14	1.95 ± 0.14	1.81 ± 0.14
J0210−0823	1.94 ± 0.18	1.11 ± 0.17	1.5 ± 0.17	1.5 ± 0.17
J0827+0306	1.5 ± 0.18	1.14 ± 0.17	1.68 ± 0.17	1.5 ± 0.17
J0829+0801	2.01 ± 0.16	1.44 ± 0.14	1.87 ± 0.14	1.87 ± 0.14
J0836+0548	2.21 ± 0.17	1.69 ± 0.15	2.11 ± 0.15	2.11 ± 0.15
J0845+0722	1.8 ± 0.17	1.35 ± 0.14	1.92 ± 0.14	1.8 ± 0.14
J0847+0943	1.92 ± 0.17	1.59 ± 0.15	1.81 ± 0.15	1.81 ± 0.15
J0858+0152	1.6 ± 0.15	1.25 ± 0.13	1.78 ± 0.13	1.6 ± 0.13
J0903+0708	1.65 ± 0.18	0.36 ± 0.18	1.12 ± 0.18	1.12 ± 0.18
J0915−0202	1.25 ± 0.18	1.14 ± 0.15	1.86 ± 0.15	1.25 ± 0.15
J0926+0135	1.55 ± 0.16	1.53 ± 0.14	1.81 ± 0.14	1.55 ± 0.14
J0929+0333	2.17 ± 0.17	1.95 ± 0.16	2.34 ± 0.16	2.17 ± 0.16
J0946−0124	1.29 ± 0.16	1.63 ± 0.13	1.91 ± 0.13	1.63 ± 0.13
J1024+0245	1.99 ± 0.17	1.65 ± 0.14	1.97 ± 0.14	1.97 ± 0.14
J1026+0114	2.05 ± 0.17	1.3 ± 0.15	2.02 ± 0.15	2.02 ± 0.15
J1145+0800	2.09 ± 0.18	1.43 ± 0.17	2.21 ± 0.17	2.09 ± 0.17
J1214+0242	1.87 ± 0.16	1.6 ± 0.14	1.85 ± 0.14	1.85 ± 0.14
J1215+0326	1.62 ± 0.17	1.78 ± 0.14	2.05 ± 0.14	1.78 ± 0.14
J1219+0254	1.57 ± 0.17	1.74 ± 0.14	1.88 ± 0.14	1.74 ± 0.14
J1231+0725	1.02 ± 0.15	1.7 ± 0.13	1.47 ± 0.13	1.47 ± 0.13
J1244+0821	1.96 ± 0.16	1.66 ± 0.14	2.03 ± 0.14	1.96 ± 0.14
J1259+0752	1.5 ± 0.18	0.89 ± 0.18	1.94 ± 0.18	1.5 ± 0.18
J1314+0927	1.69 ± 0.18	0.7 ± 0.18	1.51 ± 0.18	1.51 ± 0.18
J1419+0749	1.68 ± 0.15	1.53 ± 0.14	1.69 ± 0.14	1.68 ± 0.14
J1509+0744	1.74 ± 0.17	1.24 ± 0.15	1.6 ± 0.15	1.6 ± 0.15
J1519+0723	1.92 ± 0.17	1.43 ± 0.15	1.89 ± 0.15	1.89 ± 0.15
J1545+0156	1.86 ± 0.17	0.96 ± 0.15	1.52 ± 0.15	1.52 ± 0.15
J1609+0654	2.63 ± 0.18	2.07 ± 0.14	2.7 ± 0.14	2.63 ± 0.14
J1618+0704	1.81 ± 0.18	1.17 ± 0.18	1.73 ± 0.18	1.73 ± 0.18
J2116+0441	1.85 ± 0.15	2.02 ± 0.14	2.2 ± 0.14	2.02 ± 0.14
J2145−0758	1.73 ± 0.17	1.73 ± 0.16	1.9 ± 0.16	1.73 ± 0.16
μ	1.74 ± 0.17	1.47 ± 0.15	1.88 ± 0.15	1.73 ± 0.15
σ	0.31 ± 0.01	0.4 ± 0.01	0.28 ± 0.01	0.28 ± 0.01
SIQR	0.18 ± 0.01	0.25 ± 0.01	0.13 ± 0.01	0.18 ± 0.01

Notes. Columns: (1) SDSS identification, (2), (3) and (4) metallicity values for C IV/He IIλ1640 Si IV+O IV]/He IIλ1640 and Al III/He IIλ1640 with uncertainties. The measurements of the six BALQ were excluded from this table.

Table 4.9: Metallicity ($\log Z$) of the BC assuming fixed $\log(U)$=-2.5 and $\log(n_{\mathrm{H}})$=13

SDSS JCODE (1)	Al III/He II (2)	C IV/He II (3)	Si IV/He II (4)	$Z_{\mu_{1/2}}$ (5)
J0020+0740	2.00 ± 0.17	2.02 ± 0.15	2.26 ± 0.15	2.02 ± 0.15
J0034−0326	1.76 ± 0.17	1.30 ± 0.18	1.79 ± 0.18	1.76 ± 0.18
J0037−0238	1.46 ± 0.17	1.99 ± 0.15	2.09 ± 0.15	1.99 ± 0.15
J0103−1104	1.69 ± 0.17	1.94 ± 0.15	2.04 ± 0.15	1.94 ± 0.15
J0106−0855	2.00 ± 0.17	1.57 ± 0.15	2.22 ± 0.15	2.00 ± 0.15
J0123+0329	2.07 ± 0.16	1.51 ± 0.14	2.21 ± 0.14	2.07 ± 0.14
J0210−0823	2.19 ± 0.18	1.62 ± 0.17	1.82 ± 0.17	1.82 ± 0.17
J0827+0306	1.77 ± 0.18	1.65 ± 0.17	1.98 ± 0.17	1.77 ± 0.17
J0829+0801	2.25 ± 0.16	1.89 ± 0.14	2.14 ± 0.14	2.14 ± 0.14
J0836+0548	2.41 ± 0.17	2.07 ± 0.15	2.33 ± 0.15	2.33 ± 0.15
J0845+0722	2.06 ± 0.17	1.82 ± 0.14	2.18 ± 0.14	2.06 ± 0.14
J0847+0943	2.17 ± 0.17	2.00 ± 0.15	2.10 ± 0.15	2.10 ± 0.15
J0858+0152	1.87 ± 0.15	1.74 ± 0.13	2.07 ± 0.13	1.87 ± 0.13
J0903+0708	1.92 ± 0.18	1.29 ± 0.18	1.49 ± 0.18	1.49 ± 0.18
J0915−0202	1.50 ± 0.18	1.64 ± 0.15	2.13 ± 0.15	1.64 ± 0.15
J0926+0135	1.82 ± 0.16	1.96 ± 0.14	2.09 ± 0.14	1.96 ± 0.14
J0929+0333	2.38 ± 0.17	2.27 ± 0.16	2.53 ± 0.16	2.38 ± 0.16
J0946−0124	1.55 ± 0.16	2.03 ± 0.13	2.18 ± 0.13	2.03 ± 0.13
J1024+0245	2.23 ± 0.17	2.04 ± 0.14	2.22 ± 0.14	2.22 ± 0.14
J1026+0114	2.28 ± 0.17	1.78 ± 0.15	2.26 ± 0.15	2.26 ± 0.15
J1145+0800	2.31 ± 0.18	1.88 ± 0.17	2.42 ± 0.17	2.31 ± 0.17
J1214+0242	2.13 ± 0.16	2.01 ± 0.14	2.13 ± 0.14	2.13 ± 0.14
J1215+0326	1.89 ± 0.17	2.14 ± 0.14	2.29 ± 0.14	2.14 ± 0.14
J1219+0254	1.84 ± 0.17	2.11 ± 0.14	2.15 ± 0.14	2.11 ± 0.14
J1231+0725	1.23 ± 0.15	2.08 ± 0.13	1.80 ± 0.13	1.80 ± 0.13
J1244+0821	2.20 ± 0.16	2.05 ± 0.14	2.27 ± 0.14	2.20 ± 0.14
J1259+0752	1.77 ± 0.18	1.45 ± 0.18	2.20 ± 0.18	1.77 ± 0.18
J1314+0927	1.96 ± 0.18	1.36 ± 0.18	1.84 ± 0.18	1.84 ± 0.18
J1419+0749	1.95 ± 0.15	1.95 ± 0.14	1.99 ± 0.14	1.95 ± 0.14
J1509+0744	2.01 ± 0.17	1.73 ± 0.15	1.92 ± 0.15	1.92 ± 0.15
J1519+0723	2.17 ± 0.17	1.88 ± 0.15	2.16 ± 0.15	2.16 ± 0.15
J1545+0156	2.11 ± 0.17	1.50 ± 0.15	1.85 ± 0.15	1.85 ± 0.15
J1609+0654	2.72 ± 0.18	2.36 ± 0.14	2.75 ± 0.14	2.72 ± 0.14
J1618+0704	2.07 ± 0.18	1.67 ± 0.18	2.03 ± 0.18	2.03 ± 0.18
J2116+0441	2.10 ± 0.15	2.32 ± 0.14	2.41 ± 0.14	2.32 ± 0.14
J2145−0758	2.00 ± 0.17	2.10 ± 0.16	2.17 ± 0.16	2.10 ± 0.16
μ	2.00 ± 0.17	1.91 ± 0.15	2.15 ± 0.15	2.03 ± 0.15
σ	0.29 ± 0.01	0.28 ± 0.01	0.23 ± 0.01	0.23 ± 0.01
SIQR	0.17 ± 0.01	0.20 ± 0.01	0.11 ± 0.01	0.14 ± 0.01

Notes. Columns: (1) SDSS identification, (2), (3) and (4) metallicity values for C IV/He IIλ1640 Si IV+O IV]/He IIλ1640 and Al III/He IIλ1640 with uncertainties. The measurements of the six BALQ were excluded from this table.

Table 4.10: Metallicity ($\log Z$) of BLUE assuming fixed U, $n_{\rm H}$

		$\log(n_{\rm H}) = 9$		
SDSS JCODE (1)	SiIV+OIV]/HeII (2)	CIV/HeII (3)	CIV/SiIV+OIV] (4)	$Z_{\mu_{1/2}}$ (5)
J0020+0740	0.62 ± 0.13	$-0.73\pm^{1.72}_{0.35}$	0.73 ± 0.07	$0.62\pm^{0.13}_{0.13}$
J0034−0326	0.57 ± 0.15	$-0.52\pm^{1.81}_{0.50}$	0.67 ± 0.12	$0.57\pm^{0.15}_{0.15}$
J0037−0238	0.69 ± 0.13	$-0.86\pm^{0.34}_{0.30}$	0.86 ± 0.07	$0.69\pm^{0.13}_{0.13}$
J0103−1104	0.62 ± 0.14	$0.66\pm^{0.70}_{1.58}$	0.65 ± 0.09	$0.65\pm^{0.14}_{0.14}$
J0106−0855	0.94 ± 0.14	$0.75\pm^{0.67}_{1.59}$	0.90 ± 0.09	$0.90\pm^{0.14}_{0.14}$
J0123+0329	1.07 ± 0.13	$0.98\pm^{0.62}_{1.47}$	0.93 ± 0.07	$0.98\pm^{0.13}_{0.13}$
J0210−0823	0.66 ± 0.17	$-0.81\pm^{1.82}_{0.42}$	0.79 ± 0.16	$0.66\pm^{0.17}_{0.17}$
J0827+0306	0.63 ± 0.17	$0.72\pm^{0.73}_{1.69}$	0.64 ± 0.16	$0.64\pm^{0.17}_{0.17}$
J0829+0801	0.85 ± 0.12	$0.80\pm^{0.63}_{1.52}$	0.79 ± 0.05	$0.80\pm^{0.12}_{0.12}$
J0836+0548	0.80 ± 0.14	$-0.79\pm^{1.65}_{0.35}$	0.93 ± 0.09	$0.80\pm^{0.14}_{0.14}$
J0845+0722	0.89 ± 0.13	$0.72\pm^{0.68}_{1.55}$	0.86 ± 0.07	$0.86\pm^{0.13}_{0.13}$
J0847+0943	0.86 ± 0.13	$-0.64\pm^{1.78}_{0.40}$	0.94 ± 0.07	$0.86\pm^{0.13}_{0.13}$
J0858+0152	0.89 ± 0.11	$0.72\pm^{0.63}_{1.49}$	0.87 ± 0.04	$0.87\pm^{0.11}_{0.11}$
J0903+0708	0.72 ± 0.15	$-0.52\pm^{1.82}_{0.50}$	0.77 ± 0.12	$0.72\pm^{0.15}_{0.15}$
J0915−0202	0.63 ± 0.14	$-0.72\pm^{1.76}_{0.38}$	0.75 ± 0.09	$0.63\pm^{0.14}_{0.14}$
J0926+0135	0.93 ± 0.12	$-0.42\pm^{1.73}_{0.45}$	0.94 ± 0.05	$0.93\pm^{0.12}_{0.12}$
J0929+0333	1.05 ± 0.14	$0.92\pm^{0.64}_{1.57}$	0.96 ± 0.09	$0.96\pm^{0.14}_{0.14}$
J0946−0124	0.74 ± 0.13	$-1.02\pm^{0.24}_{0.24}$	0.98 ± 0.05	$0.74\pm^{0.13}_{0.13}$
J1024+0245	0.80 ± 0.13	$-0.56\pm^{1.79}_{0.43}$	0.83 ± 0.07	$0.80\pm^{0.13}_{0.13}$
J1026+0114	0.85 ± 0.13	$0.91\pm^{0.63}_{1.52}$	0.74 ± 0.07	$0.85\pm^{0.13}_{0.13}$
J1145+0800	0.90 ± 0.17	$0.80\pm^{0.70}_{1.71}$	0.83 ± 0.16	$0.83\pm^{0.17}_{0.17}$
J1214+0242	0.75 ± 0.12	$0.79\pm^{0.64}_{1.53}$	0.73 ± 0.05	$0.75\pm^{0.12}_{0.12}$
J1215+0326	0.38 ± 0.12	$-0.76\pm^{1.62}_{0.32}$	0.63 ± 0.05	$0.38\pm^{0.12}_{0.12}$
J1219+0254	0.38 ± 0.13	$-1.04\pm^{0.26}_{0.27}$	0.71 ± 0.07	$0.38\pm^{0.13}_{0.13}$
J1231+0725	0.55 ± 0.14	$-1.04\pm^{0.25}_{0.28}$	0.82 ± 0.08	$0.55\pm^{0.14}_{0.14}$
J1244+0821	0.72 ± 0.12	$-0.64\pm^{1.76}_{0.37}$	0.81 ± 0.05	$0.72\pm^{0.12}_{0.12}$
J1259+0752	0.63 ± 0.15	$-0.53\pm^{1.82}_{0.51}$	0.70 ± 0.12	$0.63\pm^{0.15}_{0.15}$
J1314+0927	0.91 ± 0.17	$0.88\pm^{0.69}_{1.72}$	0.82 ± 0.17	$0.88\pm^{0.17}_{0.17}$
J1419+0749	0.72 ± 0.13	$-0.75\pm^{1.67}_{0.34}$	0.82 ± 0.05	$0.72\pm^{0.13}_{0.13}$
J1509+0744	0.92 ± 0.14	$0.86\pm^{0.65}_{1.58}$	0.86 ± 0.09	$0.86\pm^{0.14}_{0.14}$
J1519+0723	0.91 ± 0.13	$0.65\pm^{0.70}_{1.53}$	0.91 ± 0.07	$0.91\pm^{0.13}_{0.13}$
J1545+0156	1.05 ± 0.14	$0.91\pm^{0.64}_{1.56}$	0.95 ± 0.09	$0.95\pm^{0.14}_{0.14}$
J1609+0654	0.87 ± 0.13	$0.89\pm^{0.63}_{1.54}$	0.77 ± 0.07	$0.87\pm^{0.13}_{0.13}$
J1618+0704	1.14 ± 0.15	$1.64\pm^{0.19}_{0.36}$	0.87 ± 0.12	$1.14\pm^{0.15}_{0.15}$
J2116+0441	-0.05 ± 0.12	$-1.36\pm^{0.16}_{0.21}$	0.69 ± 0.05	$-0.05\pm^{0.12}_{0.12}$
J2145−0758	0.48 ± 0.14	$-1.13\pm^{0.25}_{0.23}$	0.73 ± 0.09	$0.48\pm^{0.14}_{0.14}$
μ	0.77 ± 0.13	$-0.47\pm^{0.68}_{0.50}$	0.82 ± 0.07	0.77 ± 0.13
σ	0.23 ± 0.01	$0.86\pm^{0.61}_{0.62}$	0.10 ± 0.03	0.21 ± 0.01
SIQR	0.14 ± 0.01	$0.78\pm^{0.54}_{0.60}$	0.08 ± 0.01	0.11 ± 0.01

Notes. Columns: (1) SDSS identification, (2), (3) and (4) metallicity values for SiIV+OIV]/HeIIλ1640 CIV/SiIV+OIV] and CIV/HeIIλ1640 with uncertainties. The measurements of the six BALQ were excluded from this table.

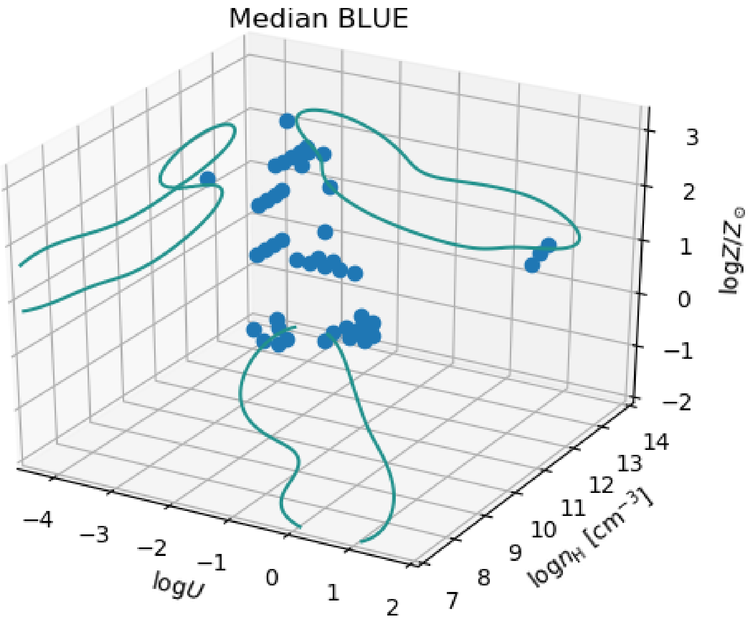

Figure 4.10: The parameter space $n_{\rm H}$, U, Z for BLUE component. Data points were computed from the emission line ratios referring to the median values in Table 4.12. The individual contour line was smoothed with a Gaussian kernel.

4.5.2 Estimates of Z relaxing the constraints on U and $n_{\rm H}$

Following the S21, we computed the χ^2 in the following form

$$\chi^2_{kc}(n_H, U, Z) = \sum_i w_{ci} \left(\frac{R_{kci} - R_{kci,mod}(n_H, U, Z)}{\delta R_{kci}} \right)^2 \tag{4.1}$$

to identify the value of the metallicity for median values of the diagnostic ratios and for the diagnostic ratios of individual objects relaxing the assumption of fixed density and ionization parameters. The summation is done over the available diagnostic ratios, and the χ^2 is computed with respect to the results of the CLOUDY simulations as a function of U, $n_{\rm H}$, and Z (subscript 'mod'). Weights $w_{ci} = 1$ were assigned to Civ/Heiiλ1640, Siiv/Heiiλ1640, and Aliii/Heiiλ1640; $w_{ci} = 0$ or 0.5 were assigned to Civ/Aliiiand and Civ/Siiv. For BLUE, the three diagnostic ratios were all assigned $w_{ci} = 1$. The Z estimates for the BC are based on the three ratios involving Heiiλ1640normalization.

Table 4.11 reports the results of the analysis relaxing the assumptions of fixed

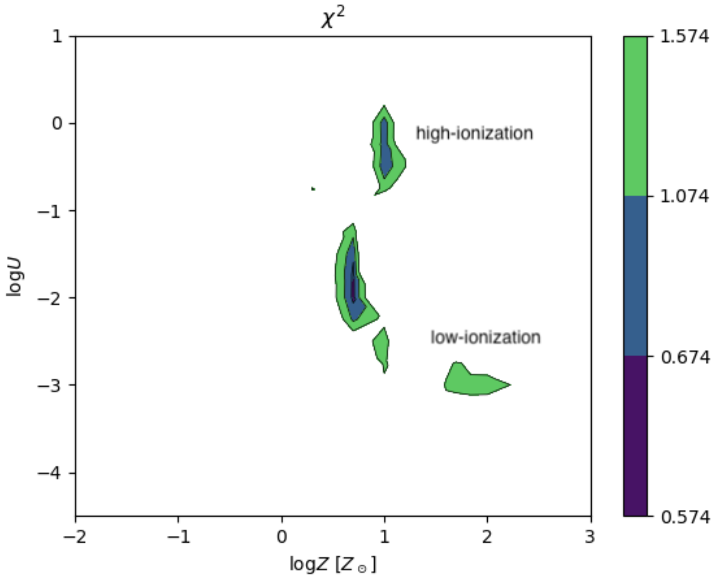

Figure 4.11: The plane $\log U$ vs $\log Z$. The outer isophotal contours delimit the region $\chi_{\rm min}+1$, where the $\chi_{\rm min}$ is the value after smoothing with a Gaussian filter. The low- and high-ionization solutions are marked.

values of $n_{\rm H}$, U. The $\log Z$, $\log U$, $\log n_{\rm H}$ and their associated uncertainties are reported for 33 sources of the sample (excluding BAL QSOs, and sources that are not xA). The exclusion of sources that are not xA is due to the fact that their SED may not be consistent with the ones of the Population A sources: even if the intensity ratio can be measured with good precision, the present set of `CLOUDY` simulation cannot be used to predict the metallicity of these sources, since the simulations were optimized for xA objects, using a spectral energy distribution that is appropriate for them. The simulation arrays should be repeated if sources have very different SED.. The last two rows list the results for the median computed from the median of the ratios of the individual sources , $\mu_{\frac{1}{2}}$(Ratios), i.e., for an additional virtual source with median ratios, and the one computed from the medians of the individual object parameter values, $\mu_{\frac{1}{2}}$ (Objects). The parameters reported in Table 4.11 cluster around well-defined values, with medians $\approx 50\ Z_{\odot}$, ionization parameter $\log U \approx -2$, and very high density log $n_{\rm H} \approx 13.75$. These values are in good agreement with S21, implying that the additional sources that are now the majority of the sample and meet the selection criteria for being xA, also show ionization degrees and metallicity values in the same range. The result is largely a consequence of the inclusion of

AlIII in the diagnostics. This line, involved also in the selection criteria, is very strong in xA with respect to quasars belonging to other spectral types along the main sequence (Aoki & Yoshida, 1999; Bachev et al., 2004b), and AlIII strength is favored at high Z, high n_{H}.

Two groups of sources stand out. The first one shows: (1) sources that are extreme with $Z \sim 100Z_{\odot}$. These sources have a large fraction of their gas mass made of metals (S21); (2) sources with relatively high $U \sim -1.5$. Five out of seven sources from the 1st group show the highest SiIV compared to CIV and are at the low end of the distribution in CIV and AlIII equivalent widths. However, J2116+0441 and J2145-0758 show relatively prominent CIV and lower SiIV, probably as an effected of a higher ionization parameter. The second group has higher CIV/AlIII than average, although this has no strong implication for Z: if $\log U \sim -1.75$, the median $\log Z \sim 1.7$ $[Z_{\odot}]$; only in two cases with $\log U \sim -1.5$, the median $\log Z \sim 1.3$ $[Z_{\odot}]$, lower than the median.

Table 4.12 provides the information on metallicity that is possible to extract from the BLUE intensity ratio. No n_{H} and U values are reported, as they are very poorly constrained (Fig. 4.10). The right panel shows the existence of two main emitting regions in the parameter plane U vs Z in the median case, and the range reported in Table 4.12 is the Z range possible for the high-ionization and the intermediate ionization range ($U \sim -2$).

Table 4.11: Z, U, $n_{\rm H}$ of individual sources and median derived from the BC

SDSS JCODE (1)	$\chi^2_{\rm min}$ (2)	$\log Z$ [$Z_\odot$] (3)	$\delta \log Z$ [$Z_\odot$] (4)	$\log U$ (5)	$\delta \log U$ (6)	log $n_{\rm H}$ (7)	δ log $n_{\rm H}$
J0020+0740	0.094	2.00	2.00 – 2.00	-2.00	-2.00 – -1.75	13.25	13.00 – 13.50
J0034−0326	2.128	1.30	0.00 – 3.00	-2.25	-3.75 – -1.50	13.50	7.25 – 14.00
J0037−0238	0.192	1.30	1.30 – 1.30	-1.50	-1.75 – -1.00	11.75	11.50 – 12.00
J0103−1104	0.046	1.70	1.70 – 1.70	-2.00	-2.00 – -2.00	12.75	12.75 – 12.75
J0106−0855	2.725	1.30	1.70 – 1.70	-1.75	-3.50 – 0.00	14.00	11.25 – 14.00
J0123+0329	4.549	0.70	0.00 – 3.00	-3.75	-3.75 – 1.00	14.00	7.00 – 14.00
J0210−0823	0.837	0.70	0.70 – 1.70	-3.75	-3.75 – -3.75	14.00	13.75 – 14.00
J0827+0306	0.346	1.30	1.30 – 1.70	-2.00	-2.25 – -1.75	13.75	13.00 – 13.75
J0829+0801	1.881	1.70	0.70 – 2.00	-2.00	-3.75 – -1.50	13.75	12.00 – 14.00
J0836+0548	1.610	1.70	1.00 – 2.30	-2.00	-3.75 – -1.50	14.00	12.00 – 14.00
J0845+0722	1.156	1.70	1.00 – 2.00	-1.75	-2.50 – -1.50	13.75	12.75 – 14.00
J0847+0943	0.494	2.00	1.00 – 2.00	-2.50	-2.75 – -2.25	12.75	12.25 – 14.00
J0858+0152	0.645	1.30	1.30 – 1.70	-2.25	-2.50 – -2.00	13.75	12.75 – 13.75
J0903+0708	0.979	0.30	0.00 – 1.30	-3.75	-3.75 – -3.50	14.00	13.75 – 14.00
J0915−0202	0.249	1.30	1.30 – 1.30	-1.50	-1.75 – -1.25	13.50	13.50 – 14.00
J0926+0135	0.146	1.70	1.70 – 1.70	-2.25	-2.25 – -2.00	12.50	12.50 – 12.75
J0929+0333	0.334	1.70	1.70 – 2.30	-2.25	-2.25 – -1.75	14.00	12.75 – 14.00
J0946−0124	0.109	1.30	1.30 – 1.30	-0.75	-1.00 – -0.75	11.00	11.00 – 11.25
J1024+0245	0.578	2.00	1.00 – 2.00	-2.25	-2.50 – -2.00	13.50	12.50 – 14.00
J1026+0114	2.638	1.70	0.30 – 3.00	-1.75	-3.75 – -0.25	13.75	10.25 – 14.00
J1145+0800	1.997	1.70	0.70 – 2.70	-1.75	-3.75 – -0.50	14.00	12.50 – 14.00
J1214+0242	0.271	1.70	1.70 – 2.00	-2.25	-2.50 – -2.25	13.75	12.75 – 13.75
J1215+0326	0.116	1.70	1.70 – 1.70	-1.75	-2.00 – -1.75	12.25	12.25 – 12.25
J1219+0254	0.139	1.70	1.70 – 1.70	-2.25	-2.25 – -2.00	12.25	12.25 – 12.50
J1231+0725	0.037	1.00	1.00 – 1.00	-2.00	-2.00 – -2.00	11.25	11.25 – 11.25
J1244+0821	0.596	2.00	1.30 – 2.00	-2.25	-2.50 – -1.75	13.50	12.50 – 14.00
J1259+0752	1.952	1.30	0.00 – 1.70	-1.75	-3.50 – -0.50	13.75	12.00 – 14.00
J1314+0927	2.378	0.00	0.00 – 3.00	-3.50	-3.75 – -0.50	14.00	7.25 – 14.00
J1419+0749	0.146	2.00	1.00 – 2.00	-2.50	-2.50 – -2.25	13.00	12.25 – 14.00
J1509+0744	0.733	1.70	1.30 – 1.70	-2.50	-2.75 – -2.00	13.50	12.50 – 13.75
J1519+0723	1.309	1.70	0.70 – 2.00	-2.00	-2.75 – -1.50	13.75	12.25 – 14.00
J1545+0156	1.648	0.70	0.30 – 1.70	-3.75	-3.75 – -1.75	14.00	12.75 – 14.00
J1609+0654	1.673	2.00	1.70 – 3.00	-2.00	-3.75 – -0.50	14.00	10.00 – 14.00
J1618+0704	1.472	1.70	0.30 – 2.00	-2.25	-3.75 – -1.25	13.50	12.00 – 14.00
J2116+0441	0.063	2.00	2.00 – 2.00	-2.00	-2.00 – -2.00	12.50	12.50 – 12.50
J2145−0758	0.127	2.00	1.30 – 2.00	-2.25	-2.25 – -2.00	13.00	12.00 – 14.00
$\mu_{\frac{1}{2}}$(Ratios)	0.277	1.70	1.30 – 2.00	-2.00	-2.25 – -2.00	13.75	13.25 – 14.00
$\mu_{\frac{1}{2}}$(Objects)	…	1.70	1.50 – 1.90	-2.00	-2.25 – -1.75	13.75	13.25 – 14.00

Notes. The measurements of the six BALQ were excluded from this table.

Table 4.12: Z, U, $n_{\rm H}$ of individual sources and median derived from BLUE

SDSS JCODE (1)	χ^2 (2)	$\log Z$ $[Z_\odot]$ (3)	$\delta \log Z$ $[Z_\odot]$ (4)	Notes (5)
J0020+0740	0.001845	0.3 – 1.0	0.2 – 1.1	
J0034−0326	0.00657	0.7	0.0 – 1.3	1400 blend absorbed
J0037−0238	0.02968	0.7 – 1.0	0.3 – 1.3	
J0106−0855	0.00667	1.0	0.7 – 1.7	
J0123+0329	0.04137	1.0	0.7 – 1.7	
J0210−0823	0.00469	1.0	0.3 – 1.7	low EW low S/N
J0216+0115*	...	...	...	no 1400 blend
J0252−0420*	...	...	...	only 1900 blend available
J0827+0306	0.00756	0.7 – 1.0	0.0 – 1.3	low S/N
J0829+0801	0.02020	0.7	0.6 – 1.1	
J0836+0548	0.00302	0.7	0.5 – 1.7	
J0845+0722	0.00926	1.0	0.7 – 1.7	
J0847+0943	0.0173	1.3	0.65 – 1.75	
J0858+0152	0.0206	0.7	0.0 – 1.5	1400 blend problematic
J0903+0708	0.0027	1.0	0.3 – 1.7	
J0915−0202	0.00128	1.0	0.1 – 1.3	
J0926+0135	0.03320	1.3	0.6 – 1.7	
J0929+0333	0.01158	1.0	0.7 – 2.0	
J0932+0237*	...	...	...	no 1400 blend
J0946−0124	0.0235	0.7	0.5 – 1	borderline
J1013+0851*	...	...	...	no 1400 blend
J1024+0245	0.0055	0.7 – 1.0	0.6 – 1.5	
J1026+0114	0.0036	0.7	0.6 – 1.3	
J1145+0800	0.0109	1.0	0.3 – 1.7	
J1205+0201*	...	...	...	no 1400 blend
J1214+0242	0.0154	0.7	0.2 – 0.8	
J1215+0326	0.0509	1.0	0 – 1.3	
J1219+0254	0.0136	0.0	-0.7 – 1.0	
J1244+0821	0.0246	1.0	0.5 – 1.2	
J1259+0752	0.0228	0.7	0.0 – 1.3	
J1314+0927	0.0078	0.7	0.4 – 1.7	low S/N
J1419+0749	0.0171	1.0	0.5 – 1.3	
J1509+0744	0.0175	1.0	0.7 – 1.7	
J1516+0029*	...	...	...	only 1900 blend available
J1519+0723	0.0043	1.0	0.6 – 1.7	
J1545+0156	0.0082	1.0	0.7 – 1.7	Abs.
J1609+0654	0.0163	0.7	0.6 – 1.0	
J1618+0704	0.0123	1.0	0.7 – 2	
J2116+0441	0.0356	...	...	Abs. at 1400 no high ion. solution
J2145−0758	0.0214	...	...	Abs. at 1400 no high ion. solution
$\mu_{\frac{1}{2}}$(Ratios)	0.7 – 1.0	0.6 – 1.2		
$\mu_{\frac{1}{2}}$(Objects)	1.0	0.85 – 1.15		

Notes.BALQ are marked with an asterisk(*).

Chapter 5

Discussion

We focus the discussion on three main topics: (1) the adequacy of the fitting methods, comparing the results on diagnostic ratios for `specfit` and the normalized intensity measurements as well as the the Z estimates obtained in this thesis for both fitting methods and the ones in common with S21; (2) the correlation between Z and relevant physical and observational parameters. Of them, the C IV integrated properties appear to be especially relevant; (3) the possibility of elemental pollution i.e., that the relative abundances of the elements deviate from the ones of solar chemical composition.

5.1 Fitting methods

5.1.1 `specfit` vs profile ratios

Fig. 5.1 compares the measurements of our six metallicity indicators for the two methods employee in this work, the `specfit` analysis (Sec. 3.2) and the ratios of profile normalized intensities (Sec. 3.5). Each panel shows the equality line (black solid line) and the errors bars according to the fitting method. Top panels correspond to the BC ratios and bottom panels to the BLUE ratios. The identified black dots are sources that stray out from the rest of the sample, the cause of this behavior is different for BC and BLUE ratios:

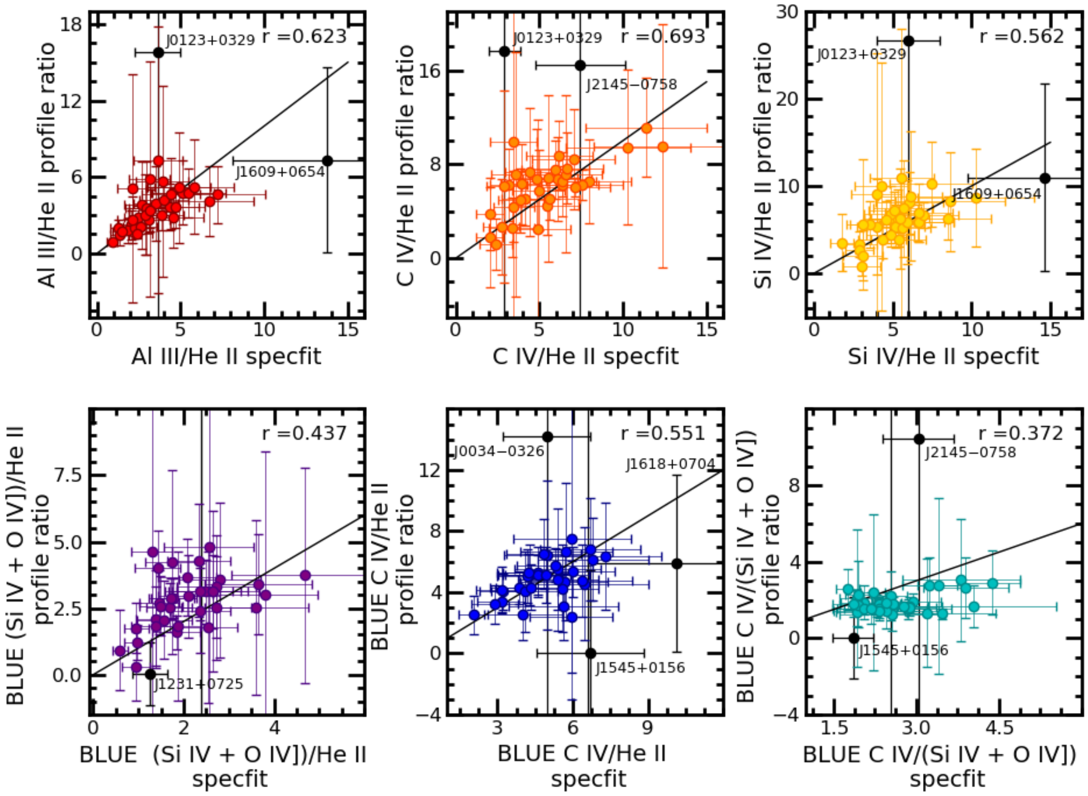

Figure 5.1: Top, from left to right: Relation between intensity ratios Civ/Heiiλ1640, Aliii/Heiiλ1640 and Civ/Heiiλ1640 BLUE computed with `specfit` and with profile ratio technique described in Section 5.1.1. Bottom: comparison of intensity ratios for (Siiv+Oiv]])/Heiiλ1640, in correspondence of BC (left) and BLUE (right). Sources with the largest discrepancy from equality line are identified in black.

- BC ratios black dots (e.g. J0123+0329, J1545+0156, J1609+0654): this is due to deficient measurements of the Heii emission which tend to be underestimated beside the Civ feature. The `specfit` modeling can compensate the surrounding narrow or broad absorptions while the profile measurements take the median intensity over a selected range directly from the spectra and can return close to zero or negative results for low S/N spectra.

- BLUE ratios black dots (e.g J1231+0725, J0034−0326, J2145−0758): what causes the discrepancies for the BLUE ratios is the strong absorptions in these three features. Similar to the discussed for BC ratios, the `specfit` modeling can compensates the missing information from the original signal while the profile measurements only takes the median of the existence intensity within a given range and for the case of absorptions the resulting median intensity is

> diminished, as briefly explained in Sec. 3.5, compare to the `specfit` measurements. We could modify the routine to skip the negative intensities (for the case of strong absorptions) but for profiles with less intense absorptions the result will still be the same.

The two measurements agree within the uncertainties in the wide majority of cases, being the BLUE CIV/(SiIV+OIV]) ratio the one showing the lower degree of correlation with a trend mainly constant. As reference we consider r$\gtrsim$0.4 as a lower limit for statistical significant correlation (with $\lesssim$ 1% of probability of not being correlated) for our ∼36 sources data set. If the BC CIV/HeII ratios are compared, disagreements occur in the sense that the CIV/HeII ratio measured with `specfit` is much lower than the one from the profile ratio. This is due to the fact that the `specfit` modeling compensates for narrow or broad absoprtion and is probably less affected by low S/N. The reverse case J1609+0654 is associated with absorption and low S/N at the HeII rest frame that effects both the `specfit` results and the profile ratios. Similar considerations apply to the BLUE radial velocity domain: the outlier J1026+0114 is affected by an absorption that is interpolated across in the `specfit` model.

The comparison between the two methods of measurements show that, even in the fairly homogeneous sample of the present work, there is a range of values in the Z-sensitive diagnostic ratios: 2 $\lesssim$ CIV/HeIIλ1640 $\lesssim$ 10, 1 $\lesssim$ AlIII/HeIIλ1640$\lesssim$ 6, 3 $\lesssim$ CIV/HeIIλ1640 BLUE $\lesssim$ 10. Outside of these range, extraordinarily large or small values are more likely due to measurement issues than to physical differences.

5.1.2 Comparison with the results of S21

The agreement between the measurements in the present thesis and the ones in common with S21 is fair for a 13 sources data set, as shown in Fig. 5.2. For this subsample we are considering r$\gtrsim$0.7 as a lower limit for statistical significant correlation (with $\lesssim$ 1% of probability of not being correlated). The main reason for this difference is most likely to a subestimation of the HeII intensity in S21, yielding unrealistic values for the ratios involving HeII. The difference between the medians

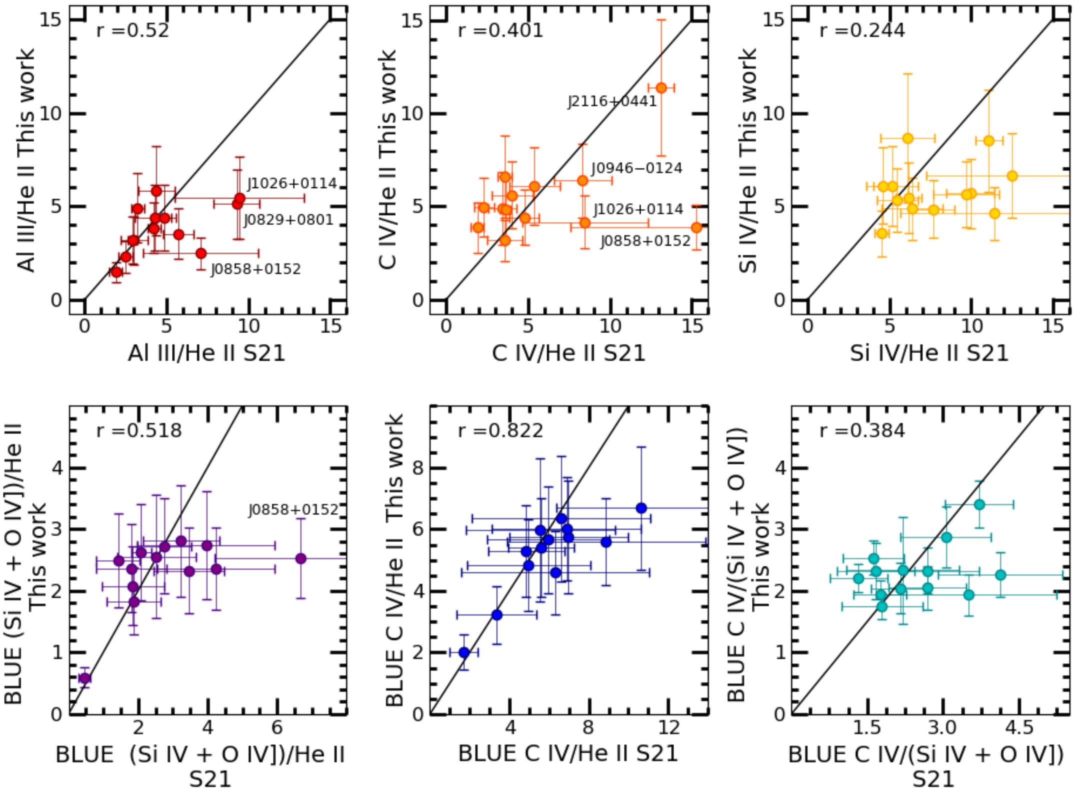

Figure 5.2: From left to right: Relation between intensity ratios C IV/He IIλ1640, Al III/He IIλ1640, C IV/He IIλ1640 BLUE, (Si IV+O IV]/)He IIλ1640, and (Si IV+O IV]/)He IIλ1640 BLUE for the 13 objects in common with S21. The labels identify sources with largest deviation from the 1:1 lines are identified.

for the two sets of measurements for the ratio C IV/He IIλ1640 BC is $\approx 0.05 \pm 0.11$ dex, i.e., within the observational uncertainty. The source that is deviating most in Fig. 5.2, J0858+0152 is associated with the difficult continuum placement around 1640 Å: the value of He IIλ1640 intensity reported by S21 is most likely an underestimate. The discrepancy brings attention to the need to consider high S/N for the measurement of the He IIλ1640 line. However, the measurements remain statistically consistent with a median deviation of $\approx -0.04 \pm 0.12$ for Al III/He IIλ1640. The BLUE C IV/He IIλ1640 ratio measurements appear to be fully consistent ($\mu \approx -0.02 \pm 0.04$ dex).

The derived Z values from the BC C IV/He IIλ1640 for fixed physical conditions are also in fair agreement. The median difference for the 13 objects in common is $\approx 0.11 \pm 0.22$, with the SIQR scatter less than a factor ≈ 2, correspondent to the uncertainties associated with the method.

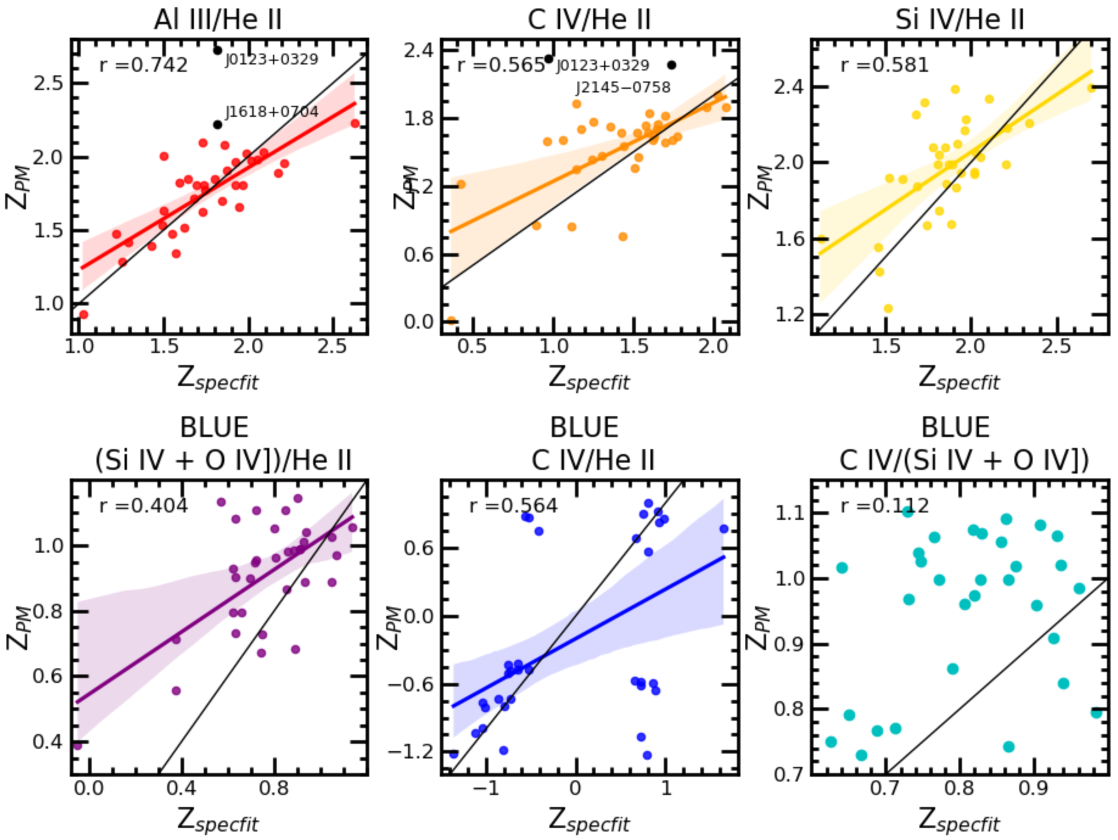

Figure 5.3: Metallicity comparison of our two fitting methods. Abscissas corresponds to `specfit` results and the ordinates to profile ratio measurements results . Each panel shows the values per metallicity relation, top left corner indicates the Spearman correlation coefficient, the black solid line shows the equality line. Sources with the largest discrepancy from equality line are discarded and identified as black dots. Colored bands show the range of uncertainty associated with the fit parameters.

Regarding the BLUE component, a comparison is possible only for 8 objects not strongly affected by absorptions. The free $\log Z$ estimates are ≈ 1.3 and 1.0 for S21 and the present work, suggesting metallicities typically in between 10 and 20 time the solar value.

5.1.3 Analysis of Z distributions at fixed $(U,\, n_{\mathrm{H}})$ for specfit and profile ratio measurements

We compare the metallicity results obtained with our two fitting methods, table 5.1 list the results for the profile normalized measurements. Some of our sources show a low S/N mainly around the 1400 Å and 1550 Å regions, this affects our measurements and metallicity estimates giving a ratio that can not find a solution with the `CLOUDY` metallicity relations, as list the blank spaces in the table.

Figure 5.3 shows metallicity comparison for our two fitting methods. The three upper panels show the comparison for AlIII/HeII, CIV/HeII, SiIV/HeIIλ1640 and demonstrate a high degree of correlation (considering r$\gtrsim$0.4 as a lower limit for a statistically significant correlation, in the case of $\sim$36 objects) between the two methods, with the slope of the best fitting line close to the 1:1 relation. For the BLUE component, the situation is less clear. The CIV/(SiIV+OIV]) ratio is basically a scatter-plot: all sources are apparently with typical metallicities in the range $\log Z/Z_{\odot} \sim 0.6-1.1$. Some of our sources show a low S/N mainly around the 1400 Å and 1550 Å regions. This affects our measurements and metallicity estimates giving a ratio that can not find a solution with the `CLOUDY` metallicity relations. The case of CIV/HeIIλ1640 is especially cumbersome: due to the non-linear relation between ratio and Z, for some of the sources the two methods produce highly discordant values.

Table 5.1: Metallicity of normalized intensities measurements

SDSS JCODE (1)	BC AlIII/HeII (2)	BC CIV/HeII (3)	BC SiIV/HeII (4)	BLUE (SiIV+OIV])/HeII (5)	BLUE CIV/HeII (6)	BLUE CIV/(SiIV+OIV]) (7)
J0020+0740	1.63 ± 0.17	1.61 ± 0.19	1.94 ± 0.15	0.93 ± 0.19	$-0.48\pm^{1.36}_{-1.05}$	0.97 ± 0.11
J0034−0326	1.53 ± 0.22	1.22 ± 0.35	1.55 ± 0.20	1.13 ± 2.98	$1.85\pm^{2.84}_{0.92}$	0.73 ± 0.46
J0037−0238	1.48 ± 0.16	1.74 ± 0.14	1.99 ± 0.14	0.90 ± 0.16	$-0.73\pm^{0.86}_{-1.03}$	1.00 ± 0.15
J0103−1104	1.39 ± 0.24	1.35 ± 0.24	1.67 ± 0.24	0.80 ± 0.39	$0.69\pm^{1.60}_{-1.51}$	0.79 ± 0.26
J0106−0855	1.81 ± 0.19	1.61 ± 0.21	2.17 ± 0.19	1.04 ± 0.35	$0.90\pm^{1.71}_{-1.32}$	0.96 ± 0.21
J0123+0329	2.73 ± 1.81	2.32 ± 1.81	*NaN* ± 1.81	0.97 ± 0.77	$0.86\pm^{1.63}_{-1.13}$	0.91 ± 0.74
J0210−0823	1.66 ± 0.36	0.85 ± 0.42	0.33 ± 0.59	0.80 ± 0.31	$-1.19\pm^{-0.72}_{-1.86}$	1.19 ± 0.30
J0827+0306	2.01 ± 0.77	1.92 ± 0.76	2.25 ± 0.76	0.73 ± 0.35	$-1.07\pm^{-0.45}_{-1.88}$	1.02 ± 0.28
J0829+0801	1.97 ± 0.22	1.56 ± 0.26	1.99 ± 0.23	0.87 ± 0.28	$0.57\pm^{1.34}_{-0.92}$	0.86 ± 0.26
J0836+0548	1.96 ± 0.21	1.82 ± 0.22	2.34 ± 0.21	0.96 ± 0.23	$-0.80\pm^{1.30}_{-1.53}$	1.06 ± 0.24
J0845+0722	1.85 ± 0.32	1.73 ± 0.32	2.10 ± 0.33	0.99 ± 0.17	$-0.61\pm^{1.25}_{-1.11}$	1.09 ± 0.08
J0847+0943	1.81 ± 0.22	1.67 ± 0.23	2.04 ± 0.21	0.98 ± 0.15	$-0.42\pm^{1.34}_{-0.90}$	1.02 ± 0.08
J0858+0152	1.82 ± 0.19	1.77 ± 0.27	2.08 ± 0.20	0.68 ± 0.90	$-0.58\pm^{1.48}_{-1.54}$	0.74 ± 0.94
J0903+0708	1.85 ± 0.39	0.01 ± 1.04	1.60 ± 0.40	1.11 ± 0.35	$0.87\pm^{1.72}_{-1.50}$	1.06 ± 0.15
J0915−0202	1.29 ± 0.24	1.35 ± 0.30	1.89 ± 0.20	0.90 ± 0.19	$-0.73\pm^{1.08}_{-1.13}$	1.03 ± 0.13
J0926+0135	1.47 ± 0.14	1.45 ± 0.15	1.75 ± 0.14	0.89 ± 0.33	$0.75\pm^{1.33}_{-0.63}$	0.84 ± 0.33
J0929+0333	1.89 ± 0.29	1.90 ± 0.30	2.21 ± 0.28	1.03 ± 0.24	$0.82\pm^{1.55}_{-0.97}$	0.99 ± 0.17
J0946−0124	1.42 ± 0.09	1.64 ± 0.08	1.86 ± 0.09	0.67 ± 0.17	$-0.80\pm^{-0.44}_{-1.13}$	0.80 ± 0.18
J1024+0245	2.02 ± 0.36	1.70 ± 0.40	2.23 ± 0.36	1.05 ± 0.17	$0.88\pm^{1.55}_{-0.76}$	1.00 ± 0.09
J1026+0114	1.98 ± 0.17	1.46 ± 0.20	1.95 ± 0.17	1.11 ± 0.21	$0.92\pm^{1.64}_{-0.97}$	1.04 ± 0.07
J1145+0800	2.03 ± 0.30	0.76 ± 1.64	2.18 ± 0.30	1.14 ± 0.61	$1.00\pm^{1.99}_{-2.00}$	1.07 ± 0.14
J1214+0242	1.90 ± 0.13	1.84 ± 0.14	2.08 ± 0.13	0.73 ± 0.66	$-1.23\pm^{1.17}_{-2.00}$	1.10 ± 0.92
J1215+0326	1.52 ± 0.11	1.64 ± 0.24	2.03 ± 0.10	0.71 ± 0.23	$-0.50\pm^{1.31}_{-1.00}$	0.75 ± 0.25
J1219+0254	1.34 ± 0.10	1.61 ± 0.09	1.67 ± 0.09	0.56 ± 0.24	$-0.99\pm^{-0.79}_{-1.19}$	0.77 ± 0.23
J1231+0725	0.93 ± 0.11	1.59 ± 0.06	1.42 ± 0.06	...	$-0.76\pm^{1.03}_{-1.16}$	...
J1244+0821	1.81 ± 0.19	1.75 ± 0.17	2.05 ± 0.21	0.96 ± 0.11	$-0.47\pm^{1.25}_{-0.88}$	0.96 ± 0.09
J1259+0752	1.63 ± 0.30	0.85 ± 0.66	1.94 ± 0.36	1.08 ± 0.15	$-0.47\pm^{1.34}_{-1.02}$	1.16 ± 0.10
J1314+0927	1.81 ± 0.44	−0.64 ± 0.80	1.23 ± 0.59	0.99 ± 0.42	$-0.65\pm^{1.50}_{-1.76}$	1.07 ± 0.27
J1419+0749	1.71 ± 0.45	1.67 ± 0.45	1.88 ± 0.45	0.95 ± 0.12	$-0.43\pm^{1.26}_{-0.80}$	0.97 ± 0.09
J1509+0744	1.77 ± 0.21	1.44 ± 0.24	1.91 ± 0.21	1.01 ± 0.25	$-0.59\pm^{1.36}_{-1.24}$	1.06 ± 0.15
J1519+0723	1.97 ± 0.26	1.67 ± 0.27	1.99 ± 0.40	0.99 ± 0.19	$-0.57\pm^{1.32}_{-1.13}$	1.08 ± 0.09
J1545+0156	2.08 ± 0.57	1.59 ± 0.58	1.92 ± 0.57	0.89 ± 0.57	...	...
J1609+0654	2.23 ± 0.43	1.90 ± 0.47	2.39 ± 0.42	2.92 ± 15.93	...	1.00 ± 0.06
J1618+0704	2.22 ± 0.62	1.70 ± 0.63	2.32 ± 0.62	1.06 ± 0.47	$0.78\pm^{1.74}_{-2.00}$	1.02 ± 0.22
J2116+0441	1.70 ± 0.18	2.01 ± 0.16	1.99 ± 0.17	0.39 ± 0.71	$-1.21\pm^{-0.88}_{-1.63}$	0.77 ± 0.73
J2145−0758	2.10 ± 0.69	2.27 ± 0.68	2.39 ± 0.68	−1.01 ± 1.83	$-1.03\pm^{-0.68}_{-1.40}$	−1.30 ± 1.83
$\mu_{1/2}$	1.81 ± 0.23	1.64 ± 0.27	1.99 ± 0.22	0.96 ± 0.28	$-0.49\pm^{1.33}_{-1.13}$	1.00 ± 0.19
σ	0.32 ± 0.30	0.56 ± 0.39	0.38 ± 0.31	0.51 ± 2.67	$0.85\pm^{0.89}_{0.54}$	0.41 ± 0.36
SIQR	0.18 ± 0.10	0.15 ± 0.15	0.13 ± 0.12	0.12 ± 0.16	$0.76\pm^{0.22}_{0.27}$	0.11 ± 0.09

Notes. Columns are as follows: (1) SDSS short name, (2-7) . The measurements of the six BALQ were excluded from this table.

** The ellipsis correspond to missing measurements.

5.2 Correlation between diagnostic ratios and AGN physical properties: CIV full profile measurements

We measure the full profile of the CIV emission (BC + BLUE components) in order obtain a measurement independent from the deblending process. The results are shown in Table 5.2 as follows: Column 2 reports the equivalent width of the CIV emission, the centroids at quarter and half intensity are listed in Columns 3 and 4 respectively. The most negative values indicate higher blueshifts suggesting stronger outflows. Column 5 reports the FWHM of the whole CIV feature.

The CIV full profile parameters are not correlated with the accretion parameters. However, they are correlated among themselves. Especially striking is the correlation between CIV FWHM and centroid at $\frac{1}{4}$ maximum intensity (Fig. 4.6): the Pearson correlation coefficient is $r \approx -0.97$, and Spearman's is $r \approx -0.95$ which for a sample size of 36 objects, have extremely high significance. The inclusion of outliers and borderline sources is not affecting the FWHM – shift correlation.

A panel in the upper right of Fig. 4.6 shows the plot of the shift vs. difference between the luminosity computed with concordance cosmology and the virial luminosity (in log) computed from Eq. 3.11. The $\delta \log L = L - \log L_{\rm vir}$ vs shift correlation is much more affected than the FWHM – shift correlation by the inclusion of sources that are not xA or that suffer absorptions. In the first case the Eq. 3.11 is not applicable; in the second case, the absorptions reduce the CIV shifts. If these sources are not considered, the correlation coefficient is $r \approx -0.44$, implying that the shift amplitudes grow with $\delta \log L$. We suggest that this effect is mostly related to orientation, as the viewing angle is known to have a very strong effect on virial luminosity estimates (Negrete et al., 2018; Dultzin et al., 2020), and will be investigated elsewhere.

Table 5.2: Measurements of the CIV full profile.

SDSS JCODE (1)	EW [Å] (2)	c(1/4) [km s^{-1}] (3)	c(1/2) [km s^{-1}] (4)	FWHM [km s^{-1}] (5)
J0020+0740	24	-3974	-2899	8710
J0034−0326	8	-3372	-2938	7531
J0037−0238	27	-2516	-1673	7015
J0103−1104	13	-3140	-2481	8564
J0106−0855	16	-4449	-3810	9041
J0123+0329	13	-5028	-4386	9905
J0210−0823	11	-5576	-4869	12103
J0827+0306	13	-4675	-3654	9420
J0829+0801	17	-4975	-4243	10431
J0836+0548	14	-3464	-2596	8440
J0845+0722	17	-5048	-4063	10484
J0847+0943	21	-4082	-3138	8233
J0858+0152	22	-5948	-4688	11100
J0903+0708	8	-5584	-4527	11736
J0915−0202	19	-3964	-3137	8505
J0926+0135	18	-3840	-3185	9653
J0929+0333	25	-2935	-2251	6447
J0946−0124	20	-1870	-988	5071
J1024+0245	17	-4573	-3797	10042
J1026+0114	18	-5735	-4522	10320
J1145+0800	14	-4475	-3711	9257
J1214+0242	15	-4111	-3218	8730
J1215+0326	21	-3118	-2393	7458
J1219+0254	19	-2259	-1542	6315
J1231+0725	29	-989	-239	4119
J1244+0821	18	-4333	-3574	9657
J1259+0752	9	-5170	-4351	10833
J1314+0927	6	-5571	-4665	11220
J1419+0749	14	-4031	-3244	9433
J1509+0744	17	-4941	-4075	10254
J1519+0723	19	-4565	-3763	9279
J1545+0156	14	-5124	-4207	10751
J1609+0654	16	-5194	-4345	10235
J1618+0704	5	-4617	-3735	10241
J2116+0441	13	-1578	-397	4494
J2145−0758	16	-2658	-1958	6382
μ	16	−4097	−3257	8928
σ	5	1241	1206	1976
SIQR	3	860	825	1107

Notes. Columns are as follows: (1) SDSS short name; (2) Equivalent width of the sum of BC and BLUE components of CIV, (3) Centroid at quarter intensity; (3) Centroid at half intensity; (4) FWHM of the BC + BLUE components of CIV.

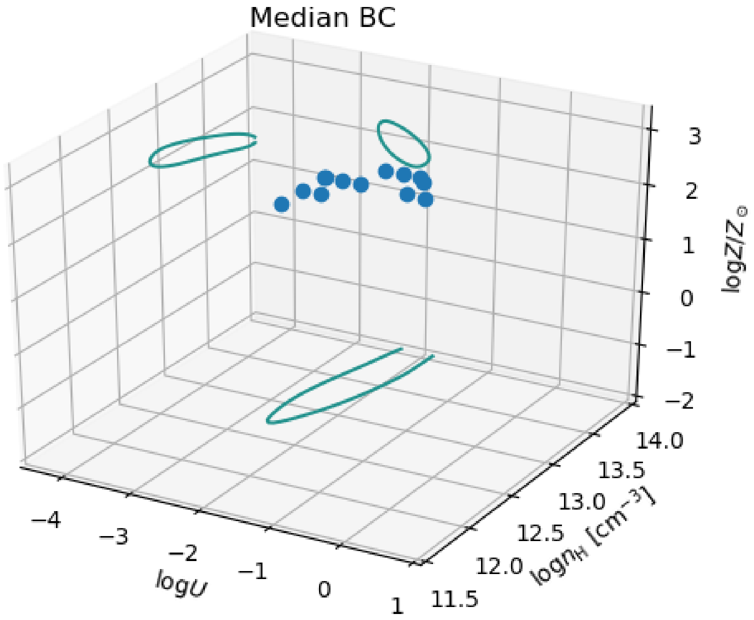

Figure 5.4: The parameter space n_{H}, U, Z. Data points in 3D space are elements in the grid of the parameter space selected for not being different from χ^2_{min} by more than $\delta\chi^2 \approx 1$, also satisfying the condition that the three intensity ratios used for the computation of the χ^2 individually agree with the ratios predicted within the errors 1σ confidence level. Data points were computed from the emission line ratios measured for the BC and referring to the median values in Table 4.11. The individual contour line was smoothed with a Gaussian kernel.

5.3 Elemental pollution

5.3.1 Highly-supersolar abundances

Accepted at face value, the Z derived for the virialized component of the BC implies metallicities 20 – 50 times the solar values. These determinations are consistent with the results of S21 who also found median values of 50, 20, 80 for the Z estimated from the AlIII/HeII, CIV/HeII, SiIV/HeII ratios, respectively. Similarly in both studies a median $Z \approx 50 Z_{\odot}$ is found if the condition of fixed n_{H} and U is relaxed. The consistency with S21 is in a way hardly surprising, since the method of measurement and analysis is the same, and the quasars belong to the same spectral class.

Changes in metallicity that are associated to changes in the physical conditions

(U, n_{H}) for the BC are modest. A small change in the Z estimates are possible if the U is increased by ~ 0.5 to 1 dex, up to $\log U \sim -1.5$. In this case, the median Z derived for our sample would decrease to $\log Z \approx 1.2 Z_{\odot}$. Increase of n_{H} or decrease in U would increase the Z estimates. The last 3 columns of Table **??** report the values if the density is increased to n_{H}= 10^{13} cm^{-3}: in this case the values remain very high $\sim 100 Z_{\odot}$, and the difference between the estimation from CIV and AlIII is reduced. The parameter space (n_{H}, U, Z) shown in Fig. 5.4 indicates that the Z is well-constrained, and that a change in physical conditions still satisfying the observed ratios would imply a change in Z $\delta \log Z \lesssim 0.5$.

The values we obtain for the BC are therefore consistent with $Z \gtrsim 20 Z_{\odot}$. This value should be taken as a reference for further discussion and are apparently very high: the highest Z value measured in molecular cloud is around $5 Z_{\odot}$ (Maiolino & Mannucci, 2019). It is however not much higher from the estimate obtained for high-z quasars in several previous studies (Baldwin et al., 2003; Warner et al., 2004; Nagao et al., 2006a; Shin et al., 2013; Sulentic et al., 2014) that indicate $Z \sim 10 Z_{\odot}$ in sources that are not as extreme as the one considered here, with lower AlIII and SiIV with respect to CIV. These conditions can be interpreted as associated to lower Z.

However, the nuclear and circumnuclear regions of quasars differ markedly from a normal interstellar environment. The passage of stars through the disk involves the formation of accretion modified objects – stars and compact objects accreting the disk material at high rate – that eventually reach high mass and explode, after a short evolution, as core collapse supernovae (Collin & Zahn, 1999; Cheng & Wang, 1999). Stars in the nuclear region can rapidly become very massive ($M \gtrsim 100 M_{\odot}$). These stars undergo core collapse, and contribute to polluting the disk with heavy elements through the high metal yields of supernova ejects (Cantiello et al., 2021). The compact remnants may continue accretion sweeping the accretion disk and giving rise to repeated supernova events (Lin, 1997). The metallicity enhancement is predicted to be $\sim 10-20 Z_{\odot}$ (Wang et al., 2011), consistent with the value obtained for the xA sources.

5.3.2 Metal segregation

The comparison between the Z derived from CIV BC fixed, and the Z for BLUE free can be carried out for both S21 and the present paper. The BC fixed medians are 1.7 (S21) and 1.3 (present paper), vs. 1.3 and 1.0 for the respective blue components. Considering that the uncertainty is $\delta \log Z \approx 0.3$ dex, the comparison suggests an overall consistency in the Z determinations. However, in both works there is a small discrepancy between the Z estimates for the BC and BLUE. Selective enrichment of BLUE and BC is in principle possible. Radiation driven winds are primarily accelerated via resonant scattering of metal lines (e.g., Proga et al. 2000; Proga & Kallman 2004, Giustini & Proga, 2019, and references therein). However, the metal ions are coupled to hydrogen and helium through Coulomb collisions, and physical conditions needed to lead a decoupling are extreme and outside the range considered for the BLR (Baskin & Laor, 2012). A second mechanism is associated with the interaction of compact objects crossing the disk and the disk itself (Wang et al., 2011): star formation in self-gravitating disks can give rise to metallicity gradients in broad-line regions, with the higher Z in the innermost regions where a radiation driven wind is expected to develop. Also in this case, the wind component should be the more metal rich. The expected condition is that BLUE might be more affected by metal segregation (if at all), so that $Z_{\rm BLUE} \gtrsim Z_{\rm BC}$) and not the converse and not $Z_{\rm BLUE} \sim Z_{\rm BC}$.

The very high Z estimates, reaching $Z \sim 100 Z_{\odot}$, are associated with the inclusion of the AlIII and SiIV lines. Z estimates from CIV/HeIIλ1640 may be consistent for BLUE and BC within the uncertainties, and suggest $Z \sim 10 Z_{\odot}$. Therefore, confirmatory data are needed for any discrepancy between BLUE and BC Z estimates, also considering that the diagnostics of the BLUE is poor (in addition to the difficulties in the measurement of the blue wings, the CIV/HeIIλ1640 has a non-monotonic behaviour with Z at high U as shown in the Appendix of S21). Our preliminary conclusion is that BLUE- and BC-derived Z values are consistent, if we exclude estimators that could be affected by elemental overabundance, as briefly discussed below.

5.3.3 Abundance pollution

xA sources were selected to have strong AlIII by definition, and the line is strongly sensitive to Z, for fixed physical condition. High n_{H} and moderate or relatively high U contribute to make the line stronger (Marziani et al., 2020). Figure 5.5 shows the distribution of the metallicity differences $\delta \log Z = \log Z(\mathrm{AlIII}) - \log Z(\mathrm{CIV})$ and $\log Z(\mathrm{SiIV}) - \log Z(\mathrm{CIV})$. For the most likely values of the ionization parameter $\log U \sim -2 - -2.5$, the value of Z is consistently higher if derived from the AlIII/HeIIλ1640 ratio or SiIV/HeIIλ1640 ratio than from the one derived from CIV/HeIIλ1640, by a factor of $\approx 1.5 - 2$. The very high Z values derived for the BC are due to the inclusion of the AlIII lines. While values $\approx 10 - 20$ seems to be possible for the xA sources, higher values $\sim 50 - 100 Z_{\odot}$, might be more associated with deviation from the relative solar elemental abundances. The CIV abundance might be less affected by pollution, and hence be more representative of the gas total metal content, under the assumption that the relative abundances of metal elements (excluding Al and Si) scale as solar.

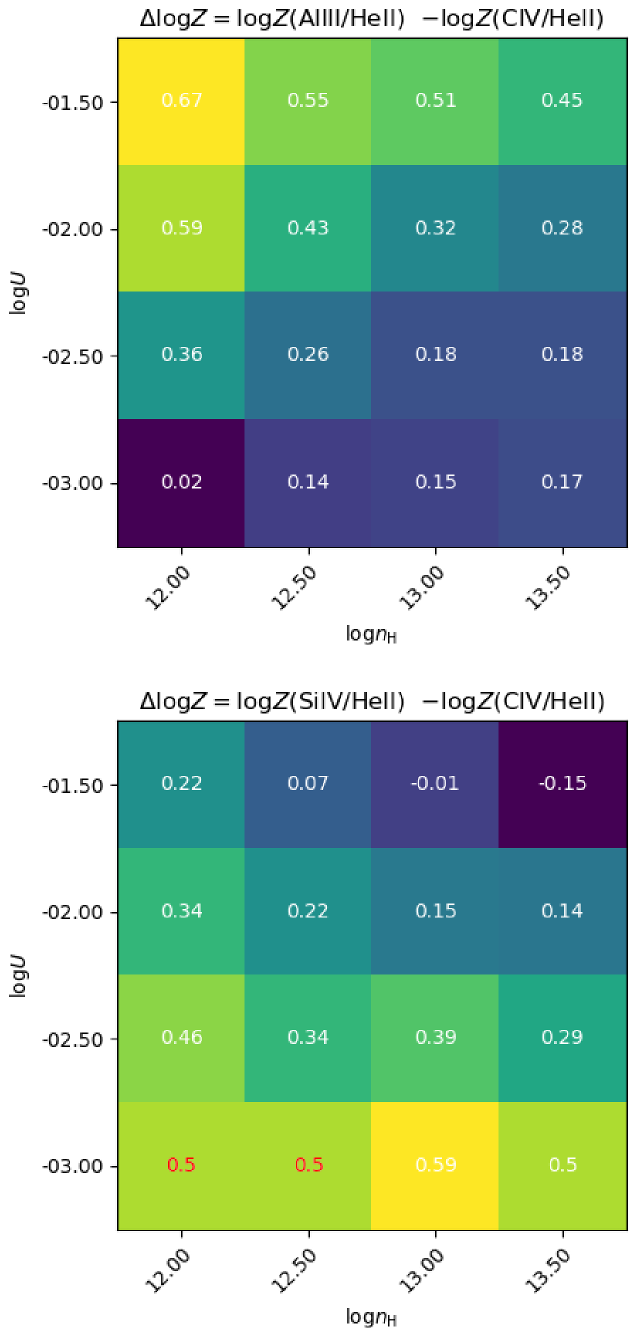

Figure 5.5: Top panel: Difference in the metallicity estimates from the AlIII/HeIIλ1640 intensity ratio and from the CIV/HeIIλ1640 ratio, as a function of ionization parameter and density. The difference remain significant at a 2σ confidence level down to $\Delta \log Z = \log Z$(AlIII/HeIIλ1640) - $\log Z$(CIV/HeIIλ1640) ≈ 0.3. Bottom: same, for difference in the metallicity estimates from the (SiIV+OIV])/HeIIλ1640 ratio ($\approx$ SiIV/HeIIλ1640) and from the CIV/HeIIλ1640 ratio. The two cases with red values are lower limits.

Chapter 6

Conclusions and Future Work

In this thesis we explored the UV spectroscopic properties and metal content of highly accreting quasars using a sample of xA quasars focusing on the metal content. The sample sources are an extension of the sample of S21 which included only 13 objects, and was mainly aimed to assess the applicability of a method based on the intensity of the strong emission lines CIV, AlIII, SiIV+OIV] relative to HeIIλ1640, with the heuristic separation between a virialized (symmetric and unshifted, BC), and a blueshifted component (BLUE). S21 included objects that were devoid of significant absorptions in the CIV and SiIVprofile, while the sample presented in this thesis might be more representative of a large sample of intermediate redshift quasars.

This chapter list the conclusions of Chapter 4 results, the main topics we explored are (1) metal content, comparing observed and synthetic flux ratios and (2) sample correlations, using physical parameters and flux ratios.

6.1 Metal content

The main result of the present investigation is the confirmation of very high metallicity values, in excess of 5 times solar, and more likely in the range 10 - 50 $Z_\odot$, as found by S21. We estimate metallicities for both BLUE and BC, for both components we conclude:

- For the BC, and the most likely fixed physical condition ($n_\mathrm{H}\sim 10^{12}$ cm^{-3}; $U \sim 10^{-2.5}$) suggests $Z \approx 50$, with a 40% scatter. We remark that this high value is a a consequence of the inclusion in the Z estimate of the AlIII/HeIIλ1640 and SiIV+OIV]/HeIIλ1640 ratios. If they are excluded, the CIV/HeIIλ1640 is the only remaining ratio and $Z \approx 30Z_\odot$.
- For the BLUE, again at fixed physical conditions, the most likely value is $Z \approx 6Z_\odot$. The discrepancy with the BC needs to be accounted for.
- Relaxing the assumption of fixed physical conditions, the three independent ratios allow for an independent estimate of n_H, U, Z. The results on Z are consistent with the case for fixed physical conditions ($Z \approx 50Z_\odot$), the ionization parameter is $\log U \sim -2$, and the derived n_H however significantly larger.
- Without fixed physical conditions, $Z \sim 10Z_\odot$ is found for BLUE, with U and n_H largely unconstrained.
- We noted that the Z derived from CIV/HeIIλ1640 ($Z \approx 30Z_\odot$) is lower than the ones from AlIII and SiIV+OIV]/HeIIλ1640. We explored the ratios between AlIII/HeIIλ1640 and CIV/HeIIλ1640 derived Z as a function of n_H and U, and found that the difference is preserved within factors 1.5 – 5 in the range $-2.5 \log U < -1.5$, and $12 \lesssim \log n_\mathrm{H} \lesssim 13$ cm^{-3}.
- We tentatively explained this result by abundance pollution, and suggest that the elemental abundances of the BLR gas might be significantly different from solar, especially for elements like Silicon and Aluminium. Our suggestion is supported by the models that attempts to account for the complexity of

the active nucleus, that encompasses star forming regions and even accretion-modified stars. The conditions of the xA sample are most likely very different from the ones expected in a passively evolving, elliptical host.

- Considering only the CIV/HeIIλ1640 as a Z, estimator, we are left in the uncomfortable situation that the relation between this ratio and Z is not monotonic at high U. This effect involves the highest U down to $\log U \sim -1$. Therefore we consider that the best estimator for solar-metallicity estimates is the BC CIV/HeIIλ1640 ratio, that yields values around $Z \approx 30$ with a sample standard deviation of 0.15 dex, implying $20 \lesssim Z \lesssim 40 Z_{\odot}$.

6.2 Sample correlations

- The main accretion parameters ($M_{\rm BH}$, L, $L/L_{\rm Edd}$) of the present sample cluster around a well defined value, with modest scatter comparable to the individual error of measurements. The spectral similarity also suggest that we are observing almost "clones" of the same AGN. The $L/L_{\rm Edd}$ value ~ 1 confirms that these sources are high radiators.

- The present sample shows that the CIV full profile parameters are highly correlated among themselves, as seen in previous studies (Coatman et al., 2016; Sulentic et al., 2017). Especially striking is the correlation between FWHM and centroid at half maximum. Since all relevant parameters are constrained in a small range, we suggest that the correlation is mainly due to orientation effects.

- The `specfit` analysis requires a multicomponent decomposition that may not be strictly unique. It is actually a model imposed to the data on the basis of trends observed along the quasar main sequence. To test the validity of this model, we also considered a model independent measure, based on the profile ratios in fixed wavelength range, where BC and BLUE give the maximum emission, but otherwise without profile decomposition.

The line profile method is in principle applicable to large samples of quasars that are highly accreting. However, it relies heavily on the HeIIλ1640 emission line which is weak and with a very broad profile (as true also for the optical HeIIλ1640 emission, Marziani & Sulentic 1993). Dedicated observations yielding high-S/N are needed to improve the precision of the Z estimates. This is not a standard refrain: the potential of the method exploiting the HeIIλ1640 profile measurements can be unleashed only with precise HeIIλ1640 measurements.

6.3 Future Work

We have estimated the metallicity mainly under a set of simplifying assumptions and physical parameters. This work can be further developed along the following lines.

- We may seek to characterize this high metallicity by studying the composition of the gas returned to the interstellar medium because of the evolution of a star forming region in proximity of the nucleus using , for example, `Starburst99`. To this aim, we may start from a systematic effect of pollution by supernovæ, and progress to develop models of the nuclear star cluster that might account for the observed abundances.
- The correlation between FWHM and shift of CIV and the correlation between shift and amd difference between virial and redshift based luminosity suggests an effect that should be further investigated. While Z estimates are mostlikely independent from the viewing angle, the correlation between CIV profile parameters suggest that there might be an effect mostly related to orientation.
- We can also study the optical counterpart of the spectrum through IR observations, in order to verify the 4DE1 optical criteria.

Bibliography

Allende Prieto, C., Lambert, D. L., & Asplund, M. 2001, ApJ, 556, L63

—. 2002, ApJ, 573, L137

Andernach, H., Jiménez-Andrade, E. F., & Willis, A. G. 2021, Galaxies, 9, 99

Antonucci, R. 1993, ARA&A, 31, 473

Aoki, K., & Yoshida, M. 1999, in Astronomical Society of the Pacific Conference Series, Vol. 162, Quasars and Cosmology, ed. G. Ferland & J. Baldwin, 385

Arav, N. 2007, Outflows from Active Galactic Nuclei, ed. R. Brown (STScI for NASA Goddard Space Flight Center), 101

Bañados, E., Novak, M., Neeleman, M., et al. 2019, ApJ, 881, L23

Bachev, R., Marziani, P., Sulentic, J. W., et al. 2004a, ApJ, 617, 171

—. 2004b, ApJ, 617, 171

Baggett, S., McMaster, M., Biretta, J., et al. 2002, HST Data Handbook for WFPC2, v. 4.0, ed. B. Mobasher (Baltimore: STScI)

Baldwin, J. A., Hamann, F., Korista, K. T., et al. 2003, ApJ, 583, 649

Barthel, P., Podigachoski, P., Wilkes, B., & Haas, M. 2017, ApJ, 843, L16

Baskin, A., & Laor, A. 2005, MNRAS, 356, 1029

—. 2012, MNRAS, 426, 1144

Beckmann, V., & Shrader, C. R. 2012, Active Galactic Nuclei

Bensch, K., del Olmo, A., Sulentic, J., Perea, J., & Marziani, P. 2015, Journal of Astrophysics and Astronomy, 36, 467

Boroson, T. A. 2002, ApJ, 565, 78

Boroson, T. A., & Green, R. F. 1992a, ApJS, 80, 109

—. 1992b, ApJS, 80, 109

Bruhweiler, F., & Verner, E. 2008, ApJ, 675, 83

Cantiello, M., Jermyn, A. S., & Lin, D. N. C. 2021, ApJ, 910, 94

Carroll, B. W., & Ostlie, D. A. 2007, An introduction to modern galactic astrophysics and cosmology (Addison-Wesley)

Chen, Y.-M., Wang, J.-M., Yan, C.-S., Hu, C., & Zhang, S. 2009, ApJ, 695, L130

Cheng, K. S., & Wang, J.-M. 1999, ApJ, 521, 502

Coatman, L., Hewett, P. C., Banerji, M., & Richards, G. T. 2016, MNRAS, 461, 647

Collin, S., Kawaguchi, T., Peterson, B. M., & Vestergaard, M. 2006, A&A, 456, 75

Collin, S., & Zahn, J.-P. 1999, Ap&SS, 265, 501

D'Onofrio, M., & Marziani, P. 2018, Frontiers in Astronomy and Space Sciences, 5, 31

Dultzin, D., Marziani, P., de Diego, J. A., et al. 2020, Frontiers in Astronomy and Space Sciences, 6, 80

Event Horizon Telescope Collaboration, Akiyama, K., Alberdi, A., et al. 2019a, ApJ, 875, L1

—. 2019b, ApJ, 875, L2

Ferland, G., Chatzikos, M., Guzmán, F., et al. 2017, Rev. Mexicana Astron. Astrofis., 53, 385

Ferland, G. J., Porter, R. L., van Hoof, P. A. M., et al. 2013, Rev. Mexicana Astron. Astrofis., 49, 137

Fraix-Burnet, D., Marziani, P., D'Onofrio, M., & Dultzin, D. 2017, Frontiers in Astronomy and Space Sciences, 4, 1

Giustini, M., & Proga, D. 2019, A&A, 630, A94

Grevesse, N., & Sauval, A. J. 1998, Space Sci. Rev., 85, 161

Gunn, J. E., Siegmund, W. A., Mannery, E. J., et al. 2006, The Astronomical Journal, 131, 2332

Harrison, C. 2014, PhD thesis, Durham University

Hickox, R. C., & Alexander, D. M. 2018, ARA&A, 56, 625

Holweger, H. 2001, in American Institute of Physics Conference Series, Vol. 598, Joint SOHO/ACE workshop "Solar and Galactic Composition", ed. R. F. Wimmer-Schweingruber, 23–30

Kaspi, S., Brandt, W. N., Maoz, D., et al. 2007, ApJ, 659, 997

Kellermann, K. I., Sramek, R., Schmidt, M., Shaffer, D. B., & Green, R. 1989, AJ, 98, 1195

King, A., & Pounds, K. 2015, ARA&A, 53, 115

Kirkpatrick, A., Urry, C. M., Brewster, J., et al. 2020, ApJ, 900, 5

Kormendy, J., & Richstone, D. 1995, ARA&A, 33, 581

Kriss, G. 1994, Astronomical Data Analysis Software and Systems III, A.S.P. Conference Series, 61, 437

Kuraszkiewicz, J., Wilkes, B. J., Czerny, B., & Mathur, S. 2000, ApJ, 542, 692

Leighly, K. M., & Moore, J. R. 2004, ApJ, 611, 107

Lin, D. N. C. 1997, in Astronomical Society of the Pacific Conference Series, Vol. 113, IAU Colloq. 159: Emission Lines in Active Galaxies: New Methods and Techniques, ed. B. M. Peterson, F.-Z. Cheng, & A. S. Wilson, 64

Longair, M. S. 2011, High energy astrophysics (Cambridge university press)

Lyke, B. W., Higley, A. N., McLane, J. N., et al. 2020, ApJS, 250, 8

Maiolino, R., & Mannucci, F. 2019, A&A Rev., 27, 3

Marinello, M., Rodríguez-Ardila, A., Marziani, P., Sigut, A., & Pradhan, A. 2020, MNRAS, 494, 4187

Martínez-Aldama, M. L., Del Olmo, A., Marziani, P., et al. 2017, Frontiers in Astronomy and Space Sciences, 4, 29

Martinez-Aldama, M. L., Del Olmo, A., Marziani, P., et al. 2018, Frontiers in Astronomy and Space Sciences, 4, 65

Martínez-Aldama, M. L., Del Olmo, A., Marziani, P., et al. 2017, Frontiers in Astronomy and Space Sciences, 4, 65

Marziani, P., del Olmo, A., Perea, J., D'Onofrio, M., & Panda, S. 2020, Atoms, 8, 94

Marziani, P., Dultzin-Hacyan, D., & Sulentic, J. W. 2006, Accretion onto Supermassive Black Holes in Quasars: Learning from Optical/UV Observations, ed. P. V. Kreitler (Nova Science Publishers), 123

Marziani, P., & Sulentic, J. W. 1993, ApJ, 409, 612

—. 2014a, MNRAS, 442, 1211

—. 2014b, MNRAS, 442, 1211

Marziani, P., Sulentic, J. W., Negrete, C. A., et al. 2015, Ap&SS, 356, 339

—. 2010, MNRAS, 409, 1033

Marziani, P., Sulentic, J. W., Plauchu-Frayn, I., & del Olmo, A. 2013, ApJ, 764, arXiv:1301.0520

Marziani, P., Sulentic, J. W., Zwitter, T., Dultzin-Hacyan, D., & Calvani, M. 2001, ApJ, 558, 553

Marziani, P., Zamanov, R. K., Sulentic, J. W., & Calvani, M. 2003, MNRAS, 345, 1133

Marziani, P., Dultzin, D., Sulentic, J. W., et al. 2018, Frontiers in Astronomy and Space Sciences, 5, 6

Marziani, P., del Olmo, A., Martínez-Carballo, M. A., et al. 2019, A&A, 627, A88

Marziani, P., Sniegowska, M., Panda, S., et al. 2021, Research Notes of the American Astronomical Society, 5, 25

Mathews, W. G., & Ferland, G. J. 1987, ApJ, 323, 456

Melia, F., & Falcke, H. 2001, ARA&A, 39, 309

Mickaelian, A. M. 2015, Iranian Journal of Astronomy and Astrophysics, Vol. 2, No. 1, p. 1-38, 2, 1

Nagao, T., Maiolino, R., & Marconi, A. 2006a, A&A, 447, 863

Nagao, T., Marconi, A., & Maiolino, R. 2006b, A&Ap, 447, 157

Negrete, A., Dultzin, D., Marziani, P., & Sulentic, J. 2012a, ApJ, 757, 62

Negrete, C. A., Dultzin, D., Marziani, P., & Sulentic, J. W. 2012b, ApJ, 757, 62

—. 2013, ApJ, 771, 31

—. 2014, ApJ, 794, 95

Negrete, C. A., Dultzin, D., Marziani, P., et al. 2018, A&A, 620, A118

Netzer, H. 2013, The Physics and Evolution of Active Galactic Nuclei

Osterbrock, D. E., & Ferland, G. J. 2006, Astrophysics of gaseous nebulae and active galactic nuclei

Padovani, P., Alexander, D., Assef, R., et al. 2017, The Astronomy and Astrophysics Review, 25, 2

Panda, S., Czerny, B., Adhikari, T. P., et al. 2018, ApJ, 866, 115

Panda, S., Martínez-Aldama, M. L., Marinello, M., et al. 2020, arXiv e-prints, arXiv:2004.05201

Panda, S., Marziani, P., & Czerny, B. 2019, ApJ, 882, 79

Peterson, B. M. 1997, An introduction to active galactic nuclei (Cambridge University Press)

Peterson, B. M., Ferrarese, L., Gilbert, K. M., et al. 2004, ApJ, 613, 682

Peterson, B. M., & Horne, K. 2004, Astronomische Nachrichten, 325, 248

Press, W. H., Teukolsky, S. A., Vetterling, W. T., & Flannery, B. P. 2007, Numerical recipes 3rd edition: The art of scientific computing (Cambridge university press)

Proga, D., & Kallman, T. R. 2004, ApJ, 616, 688

Proga, D., Stone, J. M., & Kallman, T. R. 2000, ApJ, 543, 686

Reichard, T. A., Richards, G. T., Schneider, D. P., et al. 2003, AJ, 125, 1711

Richards, G. T., Kruczek, N. E., Gallagher, S. C., et al. 2011, AJ, 141, 167

Richards, G. T., Lacy, M., Storrie-Lombardi, L. J., et al. 2006, ApJS, 166, 470

Richstone, D., Ajhar, E. A., Bender, R., et al. 1998, Nature, 395, A14

Schmidt, M. 1969, in Quasars and high-energy astronomy, Proceedings of the 2nd Texas Symposium on Relativistic Astrophysics, held in Austin, December 15-19, 1964 Edited by KN Douglas, I. Robinson, A. Schild, EL Schucking, JA Wheeler, and NJ Woolf. New York: Gordon &Breach, 1969, p. 55, 55

Schneider, P. 2006, Extragalactic Astronomy and Cosmology, by Peter Schneider

Schödel, R., Ott, T., Genzel, R., et al. 2002, Nature, 419, 694

Shen, Y., & Ho, L. C. 2014, Nature, 513, 210

Shin, J., Woo, J.-H., Nagao, T., & Kim, S. C. 2013, ApJ, 763, 58

Śniegowska, M., Marziani, P., Czerny, B., et al. 2021, ApJ, 910, 115

Stoughton, C., Lupton, R. H., Bernardi, M., et al. 2002, The Astronomical Journal, 123, 485

Sulentic, J., Marziani, P., & Zamfir, S. 2011, Baltic Astronomy, 20, 427

Sulentic, J. W., Bachev, R., Marziani, P., Negrete, C. A., & Dultzin, D. 2007a, ApJ, 666, 757

—. 2007b, ApJ, 666, 757

Sulentic, J. W., & Marziani, P. 1999, ApJ, 518, L9

Sulentic, J. W., Marziani, P., del Olmo, A., et al. 2014, A&A, 570, A96

Sulentic, J. W., Marziani, P., Del Olmo, A., & Zamfir, S. 2016, Ap&SS, 361, 55

Sulentic, J. W., Marziani, P., & Dultzin-Hacyan, D. 2000a, ARA&A, 38, 521

Sulentic, J. W., Marziani, P., Zamanov, R., et al. 2002, ApJ, 566, L71

Sulentic, J. W., Repetto, P., Stirpe, G. M., et al. 2006a, A&A, 456, 929

—. 2006b, A&Ap, 456, 929

Sulentic, J. W., Zwitter, T., Marziani, P., & Dultzin-Hacyan, D. 2000b, ApJ, 536, L5

—. 2000c, ApJL, 536, L5

Sulentic, J. W., del Olmo, A., Marziani, P., et al. 2017, A&A, 608, A122

Tadhunter, C. 2008, New A Rev., 52, 227

Tody, D. 1993, in Astronomical Society of the Pacific Conference Series, Vol. 52, Astronomical Data Analysis Software and Systems II, ed. R. J. Hanisch, R. J. V. Brissenden, & J. Barnes, 173

Urry, C. M., & Padovani, P. 1996, in Extragalactic Radio Sources, ed. R. D. Ekers, C. Fanti, & L. Padrielli, Vol. 175, 379

Véron-Cetty, M.-P., Véron, P., & Gonçalves, A. C. 2001, A&A, 372, 730

Vietri, G., Piconcelli, E., Bischetti, M., et al. 2018, A&A, 617, A81

Wang, J.-M., Ge, J.-Q., Hu, C., et al. 2011, ApJ, 739, 3

Wang, T., Brinkmann, W., & Bergeron, J. 1996, A&A, 309, 81

Warner, C., Hamann, F., & Dietrich, M. 2004, ApJ, 608, 136

Wills, B. J., Laor, A., Brotherton, M. S., et al. 1999, ApJ, 515, L53

Yang, J., Wang, F., Fan, X., et al. 2021, ApJ, 923, 262

Zamfir, S., Sulentic, J. W., & Marziani, P. 2008, MNRAS, 387, 856

Appendix A

Rest-frame spectra and fits

The following Figures show the results of the `specfit` analysis described in sec. 3.2.

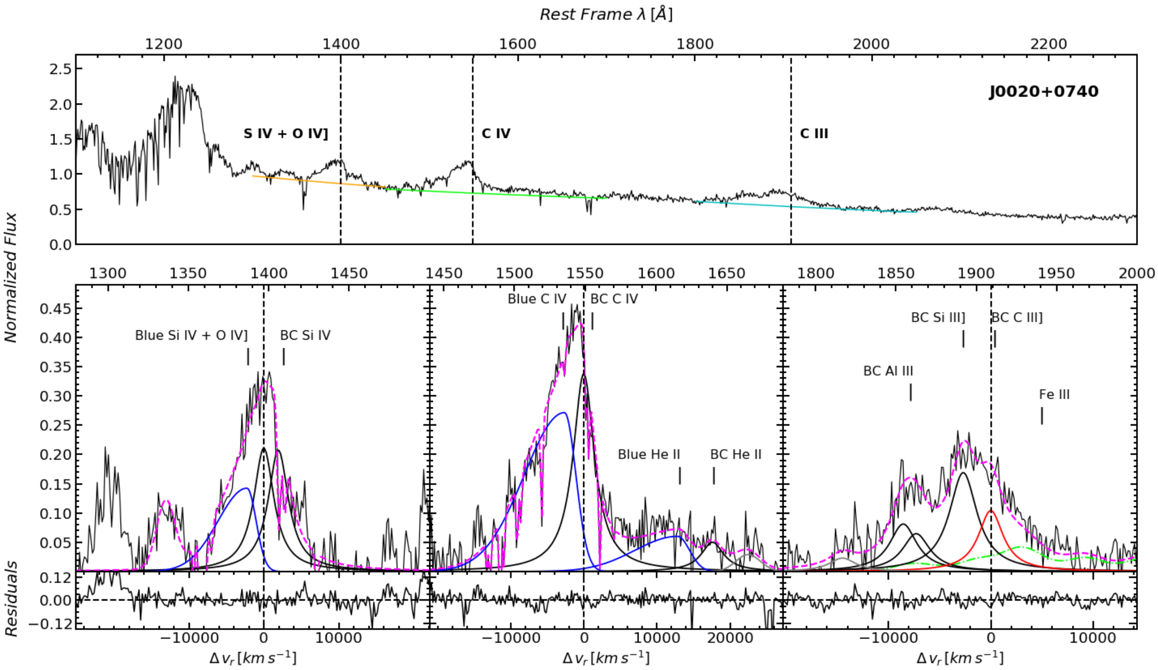

Figure A.1: *Top.* Spectrum of J0020+0740. In orange, lime and cyan we can find the local continuum used to fit the blends where we can find the main emissions of Si IV + O IV]λ1400, CIVλ1549 and CIII]λ1909 respectively. *Bottom.* The panels show a zoom of the spectrum fitting regions, the lower panels under the fits show the residuals. Upper abscissa is the rest frame wavelength in Å, lower abscissa is in velocity units, and ordinate is specific flux. Vertical dashed lines show the rest frame of the main emission of the region. In black is the spectrum of the source minus the continuum, in pink the fitting model and in purple the broad components. In the regions at 1400Å (left) and 1550Å (medium) in blue is the asymmetric blueshifted components. In the region at 1900Å (right), in red is the emission of C III] and the green dashed line represents the Fe III template.

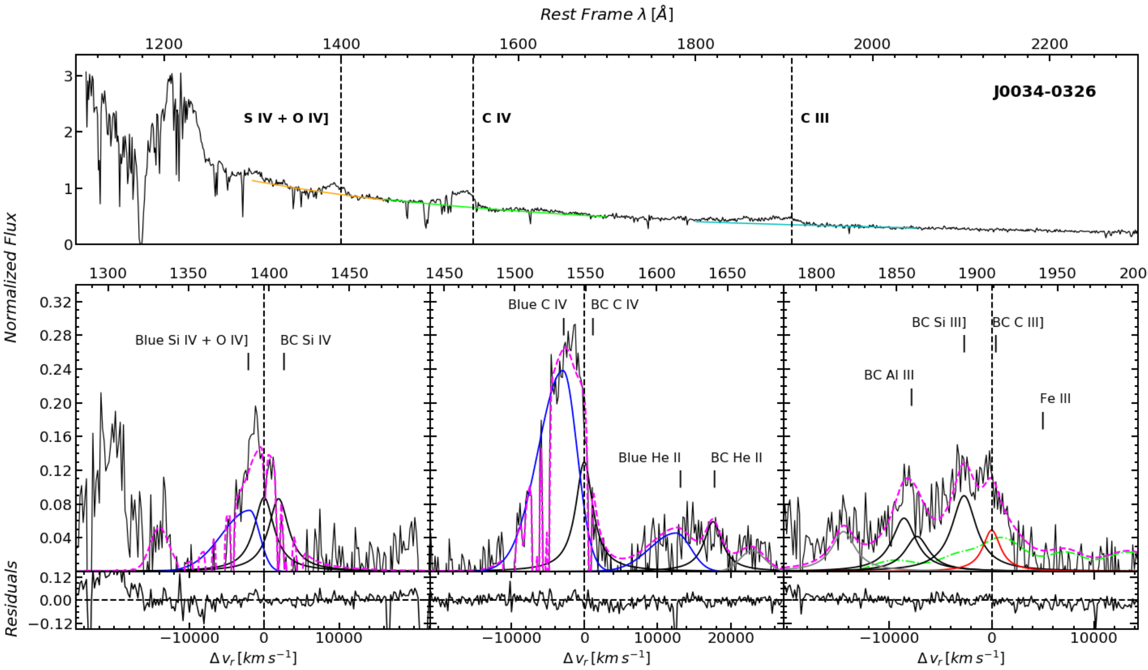

Figure A.2

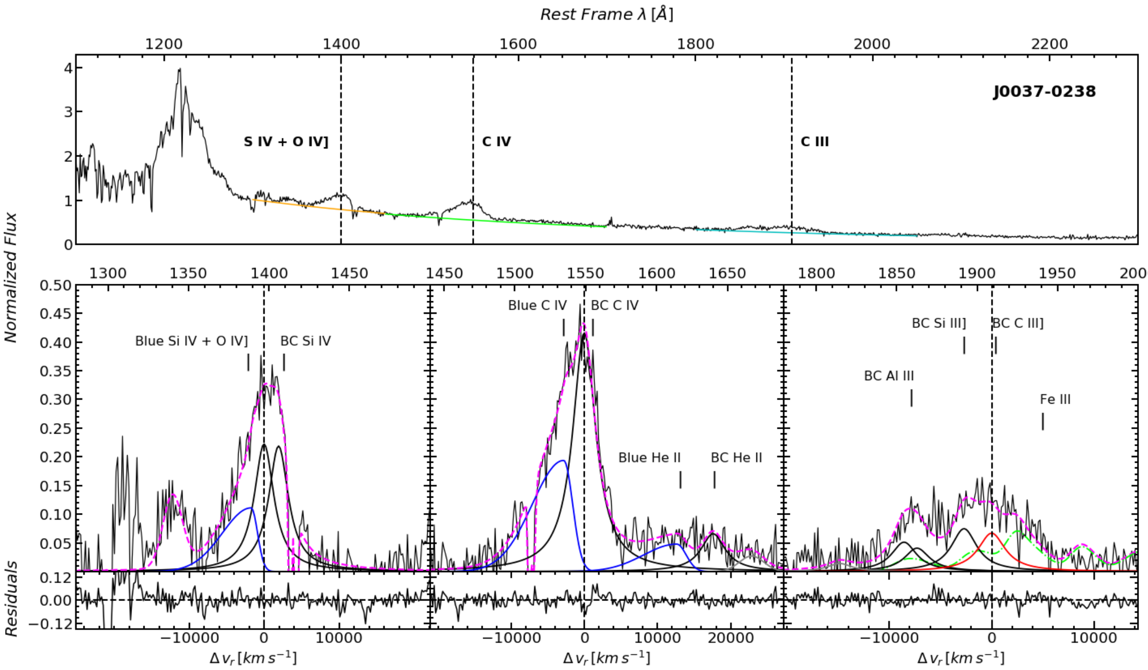

Figure A.3

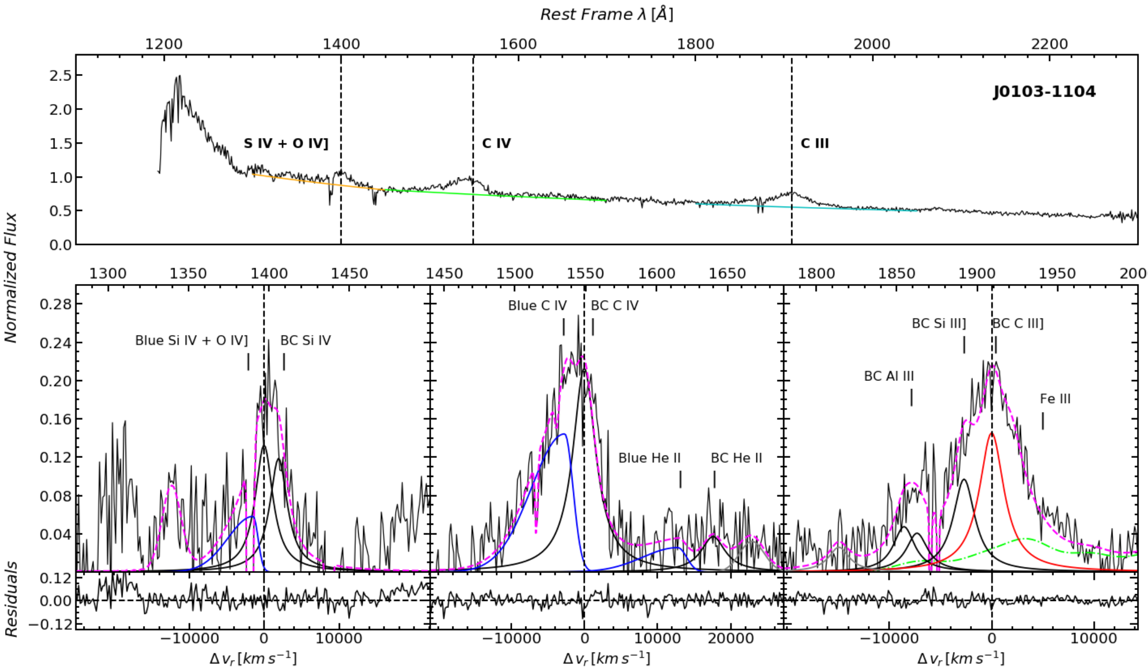

Figure A.4

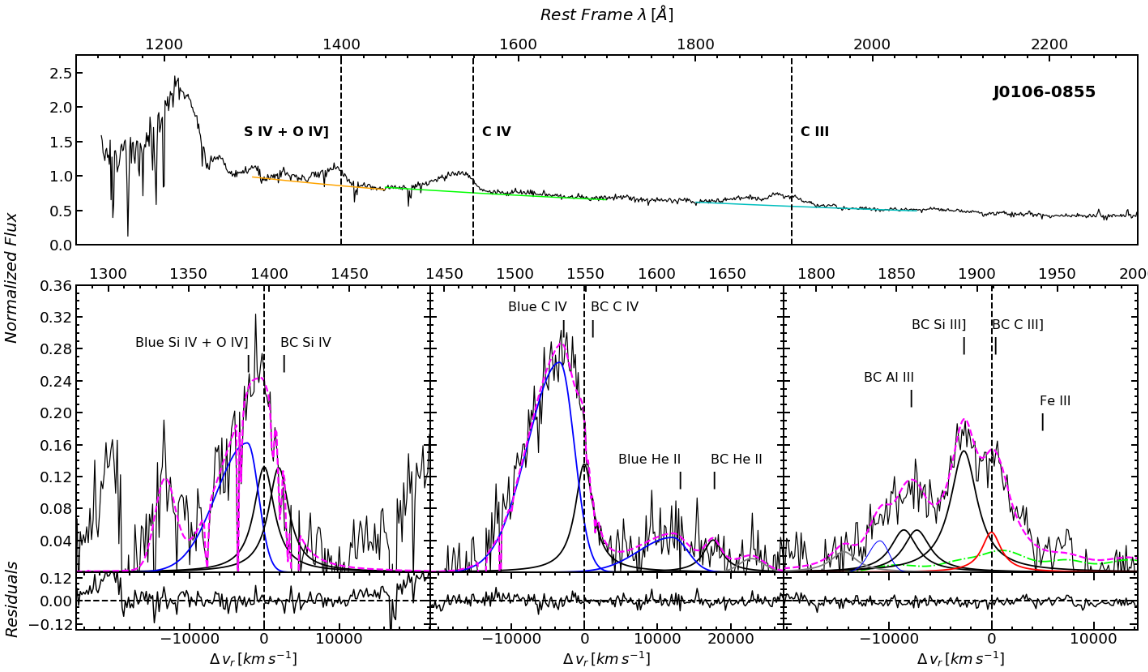

Figure A.5

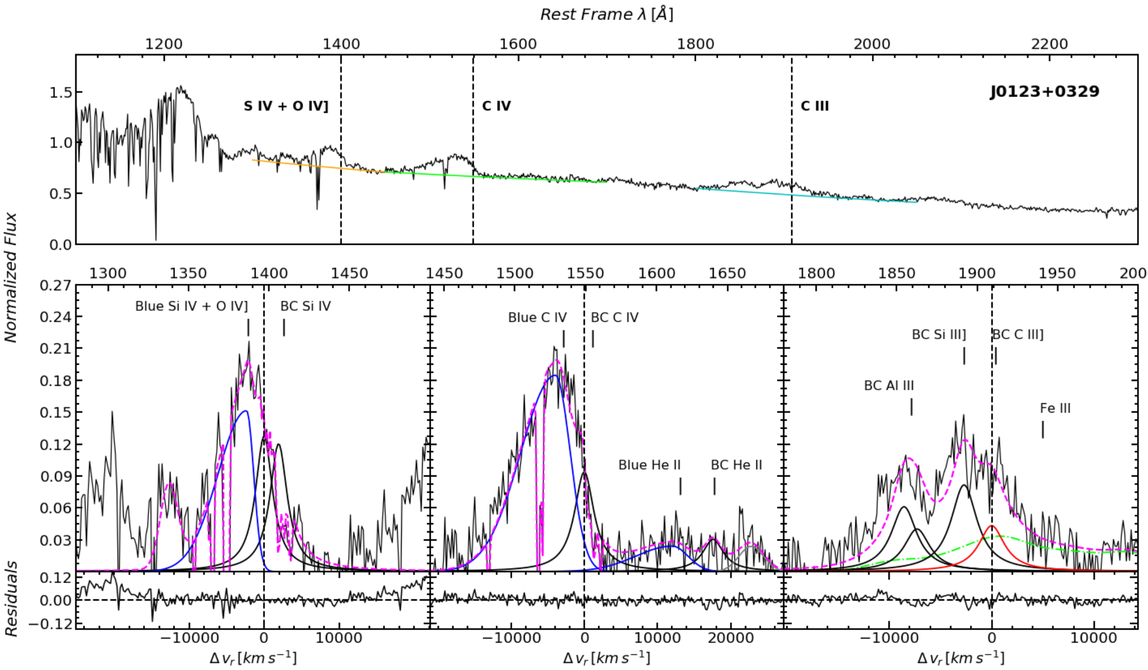

Figure A.6

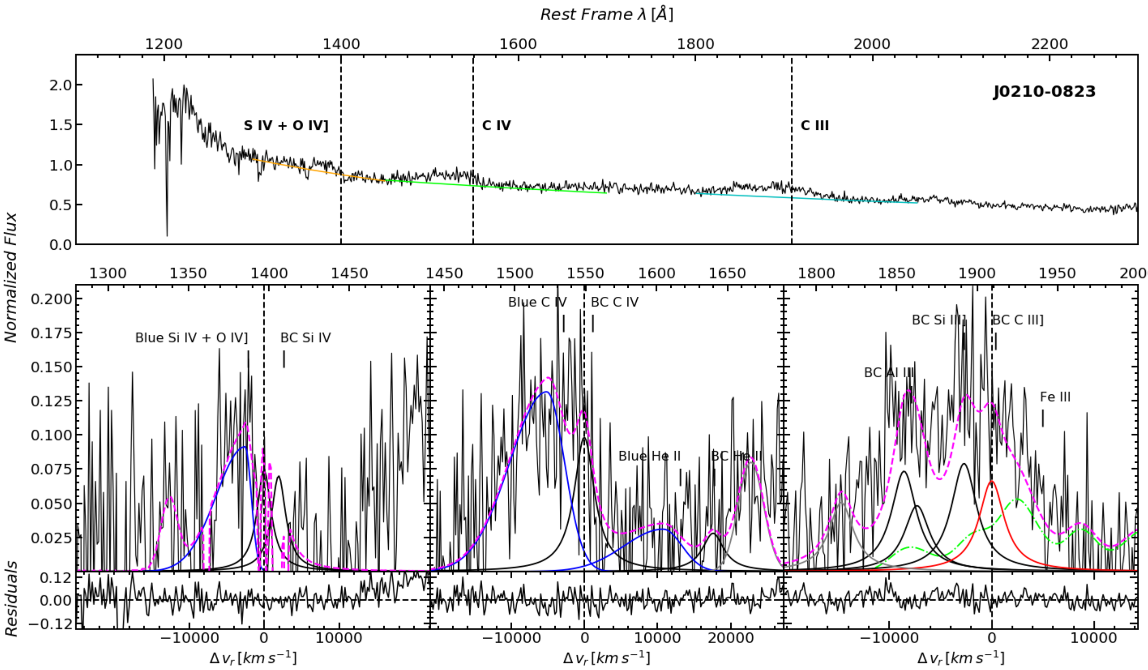

Figure A.7

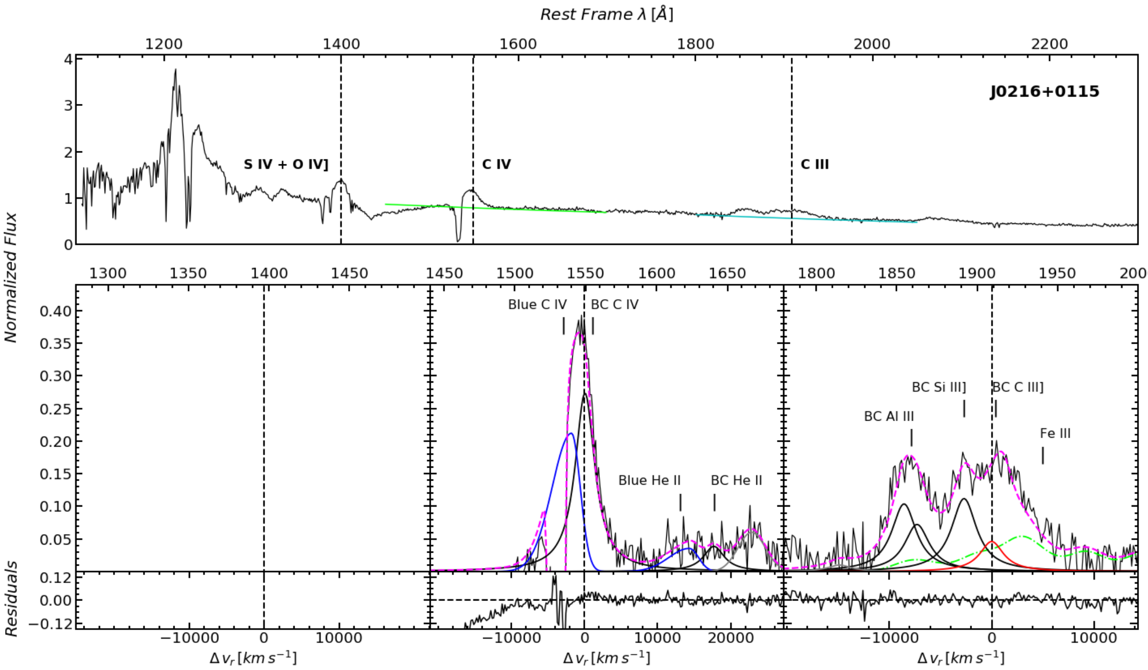

Figure A.8

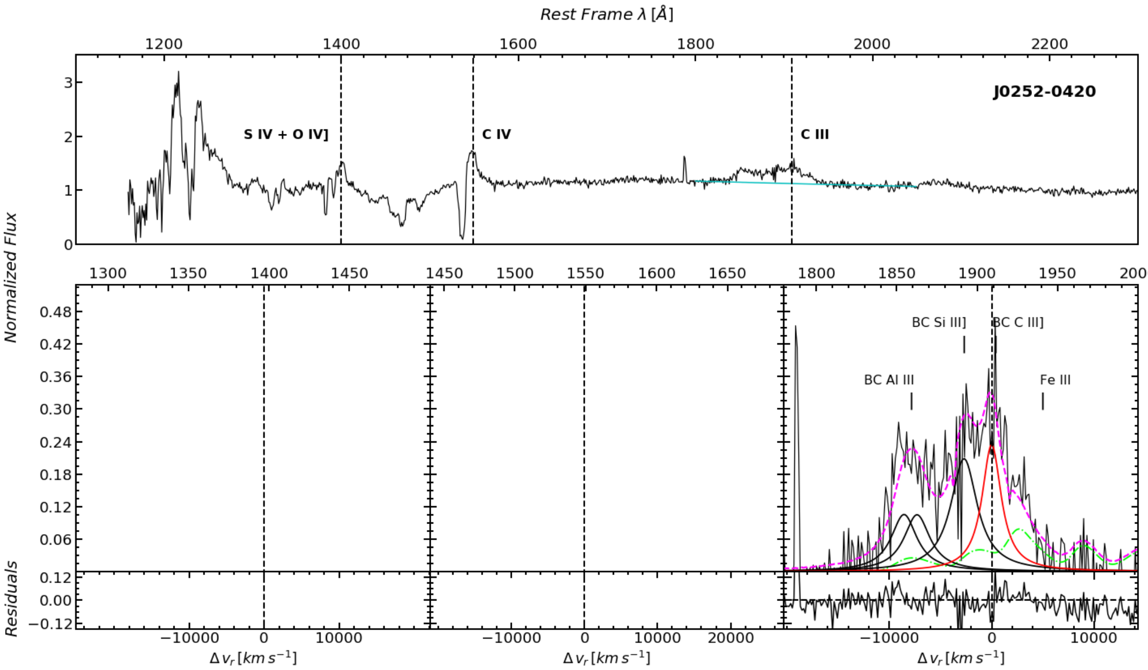

Figure A.9

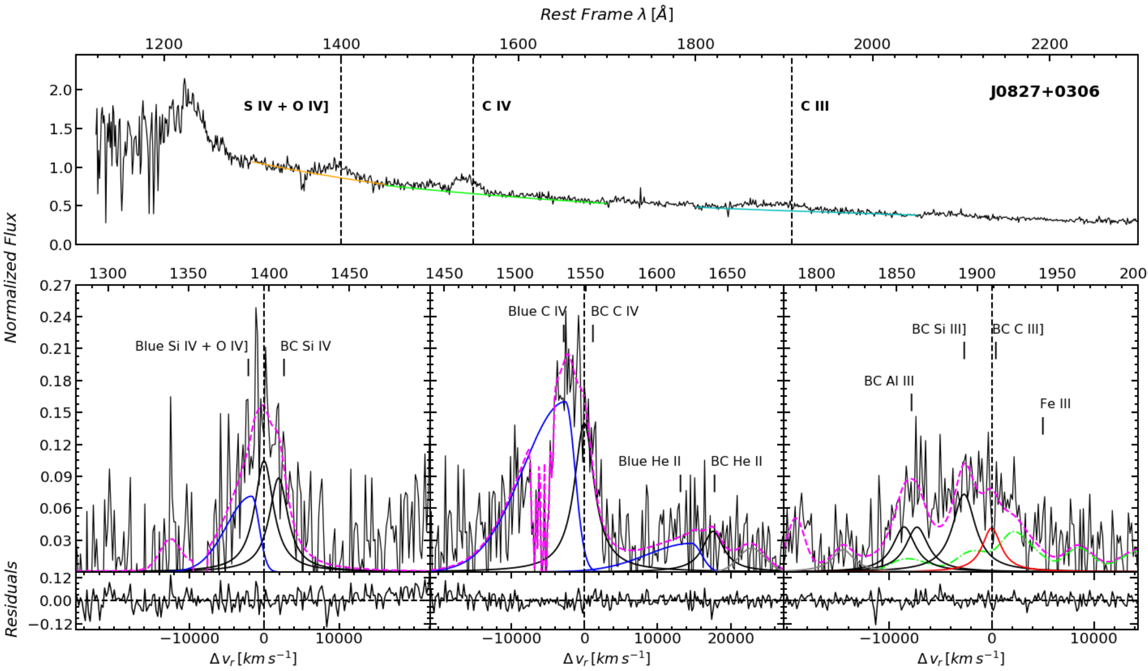

Figure A.10

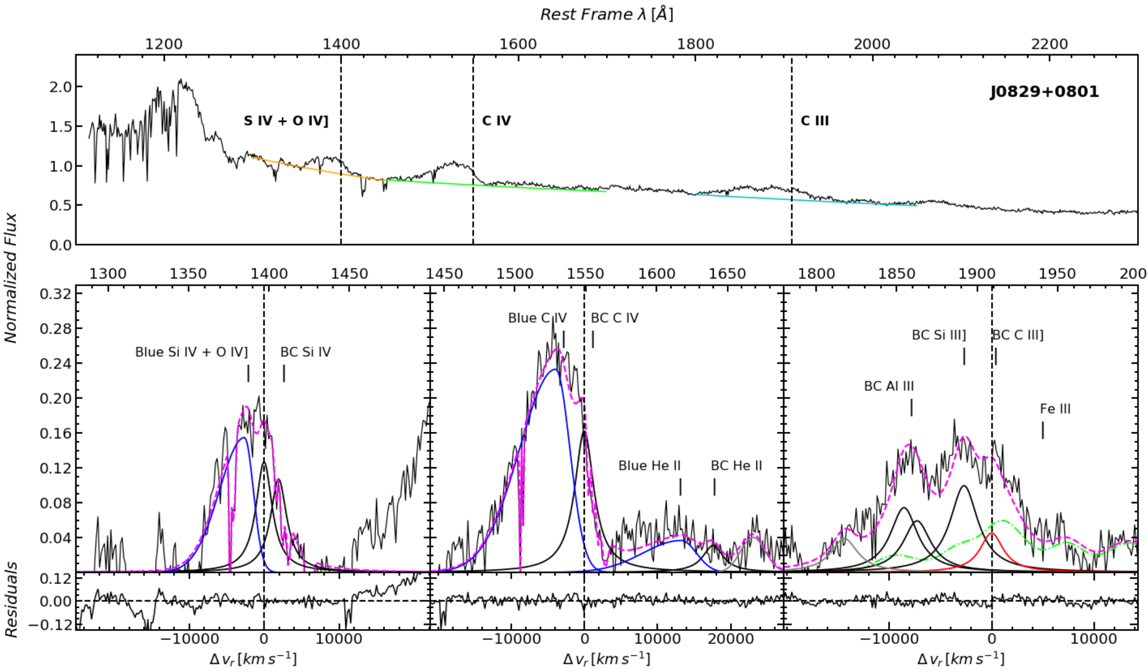

Figure A.11

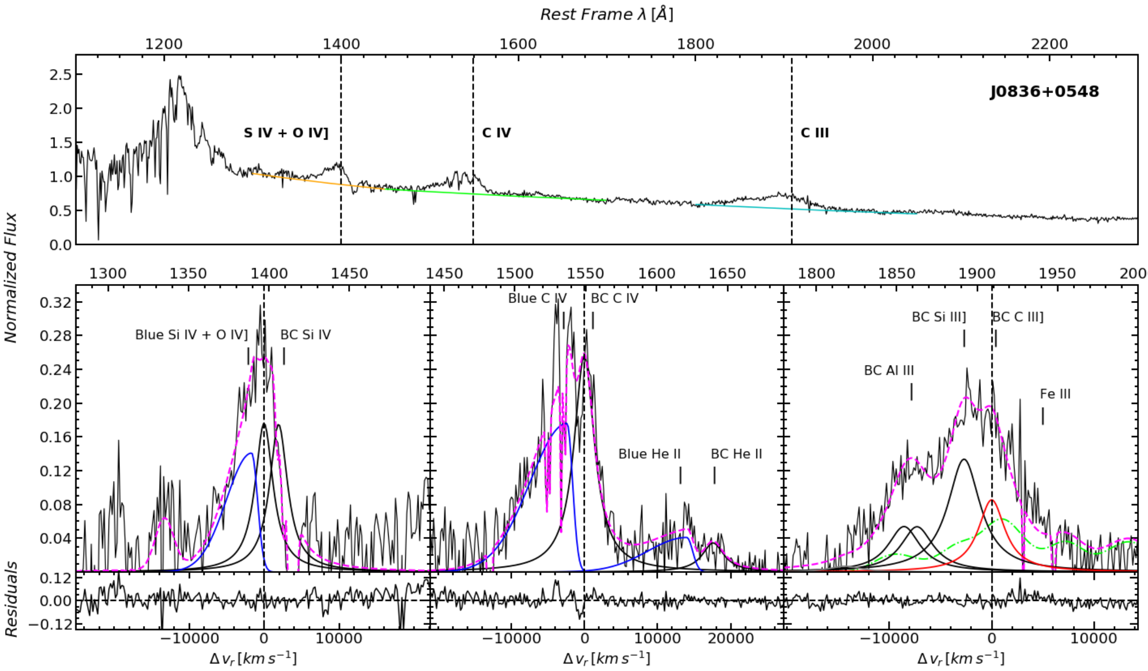

Figure A.12

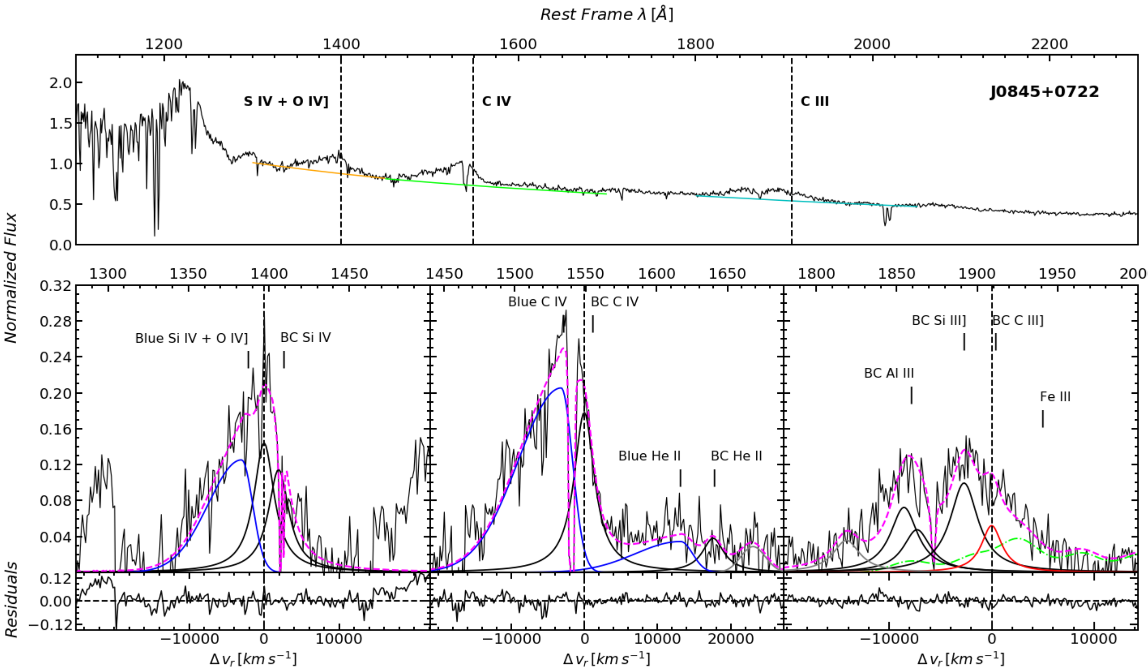

Figure A.13

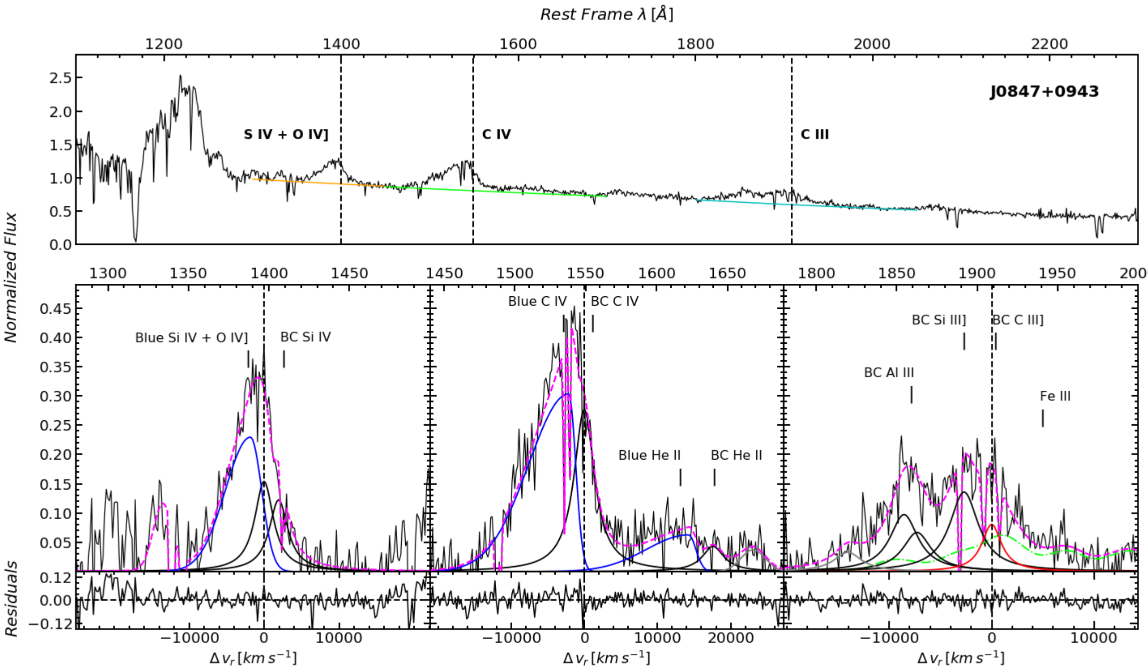

Figure A.14

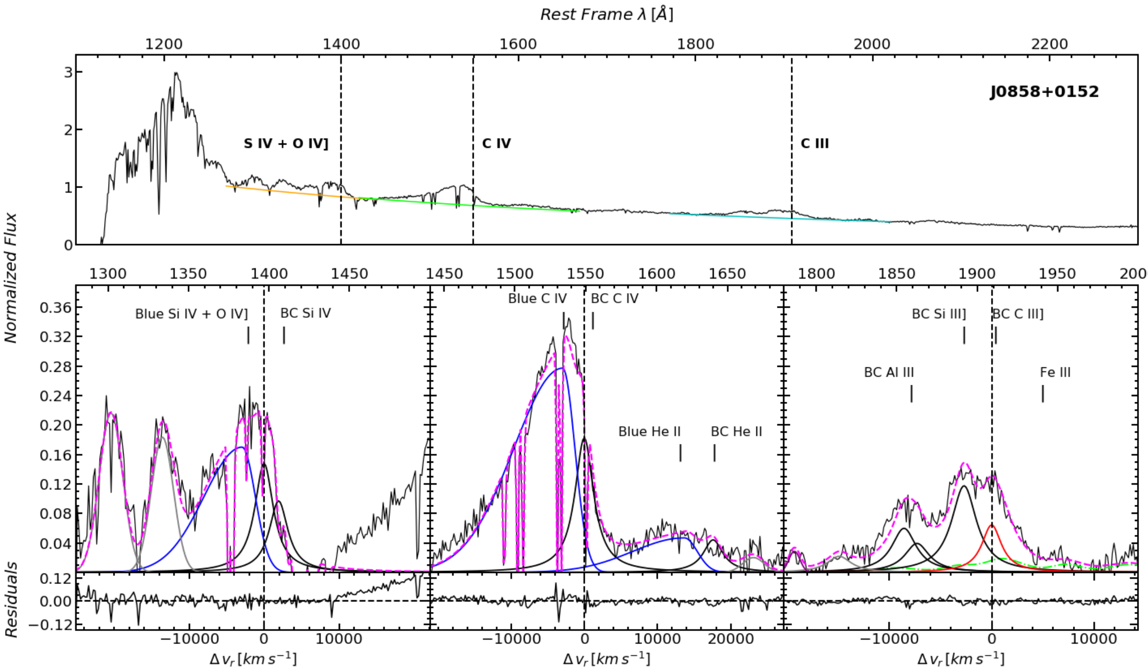

Figure A.15

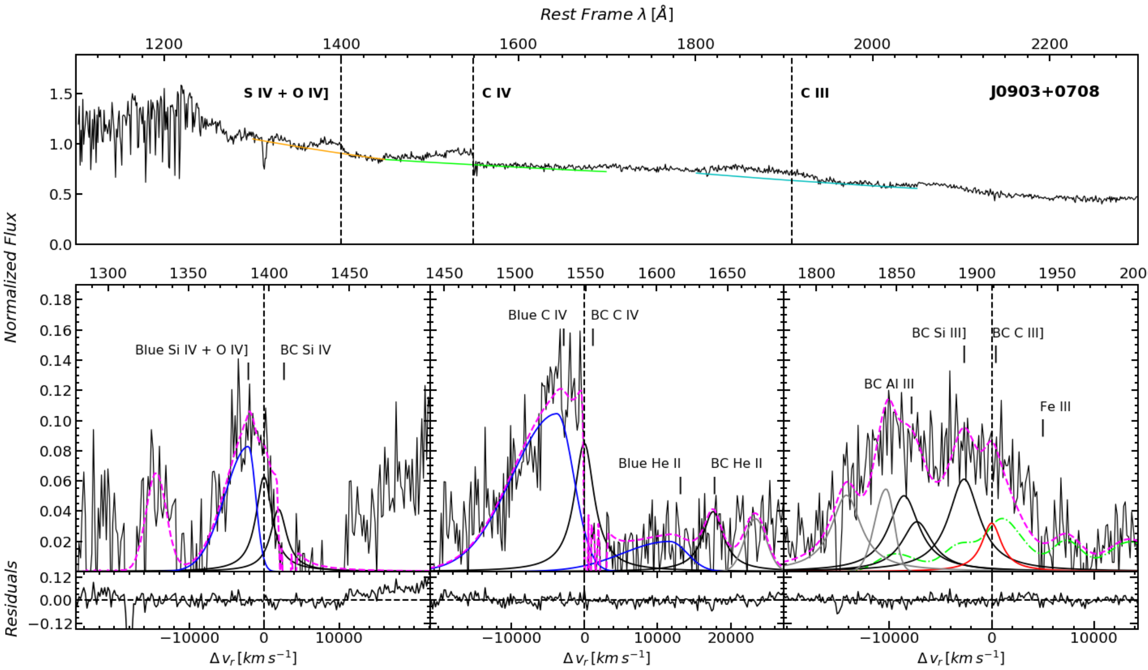

Figure A.16

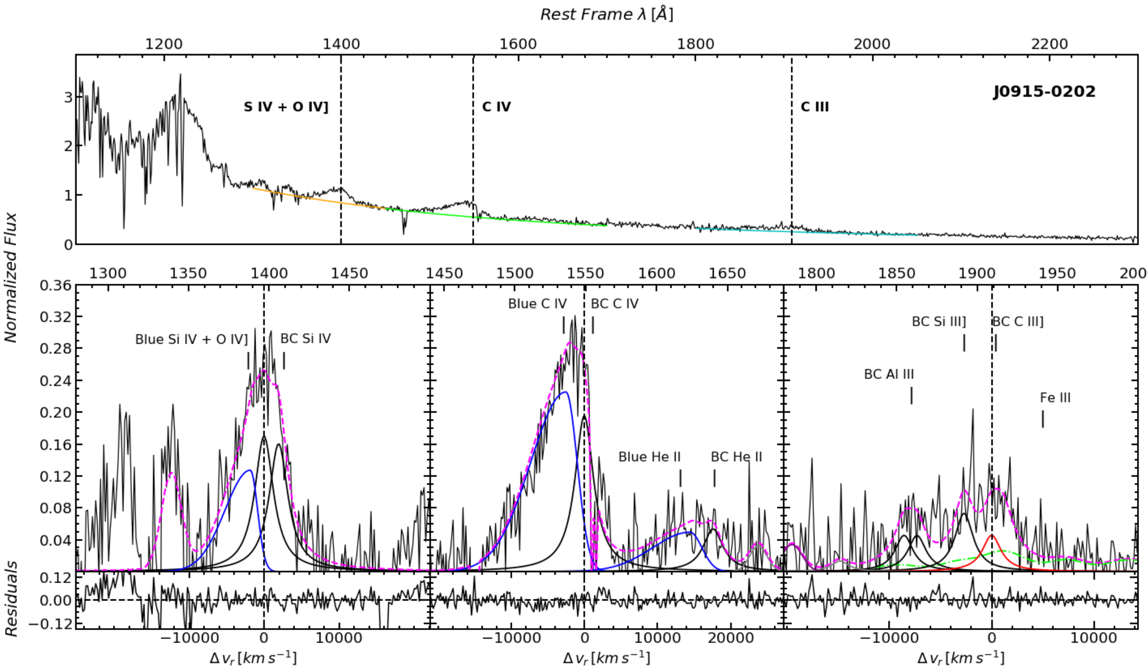

Figure A.17

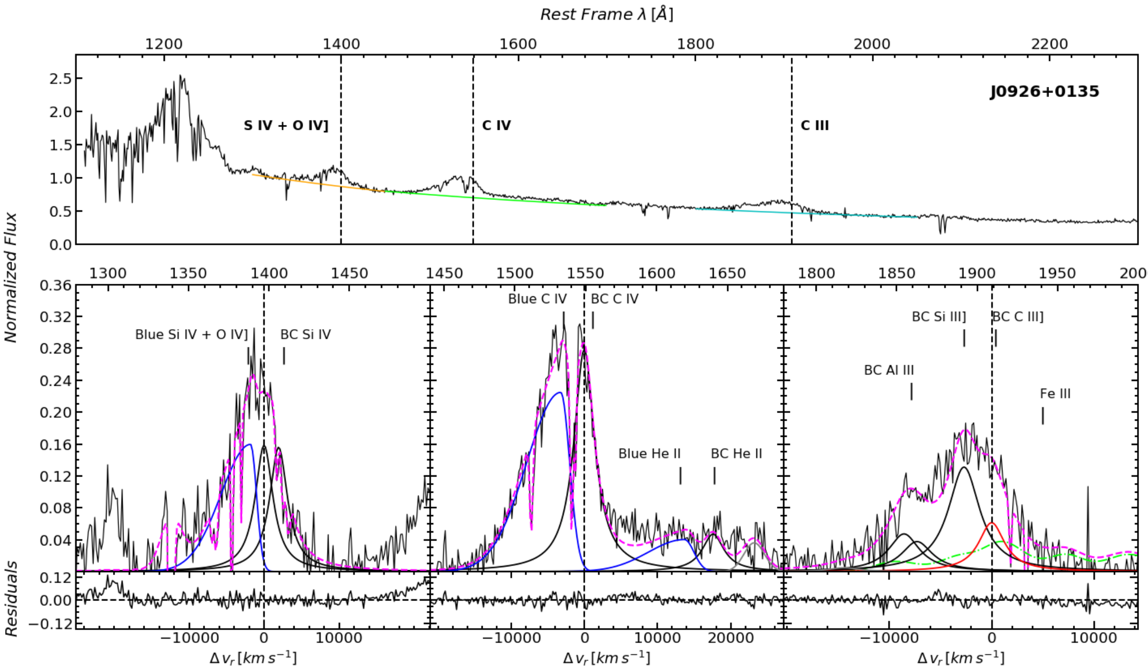

Figure A.18

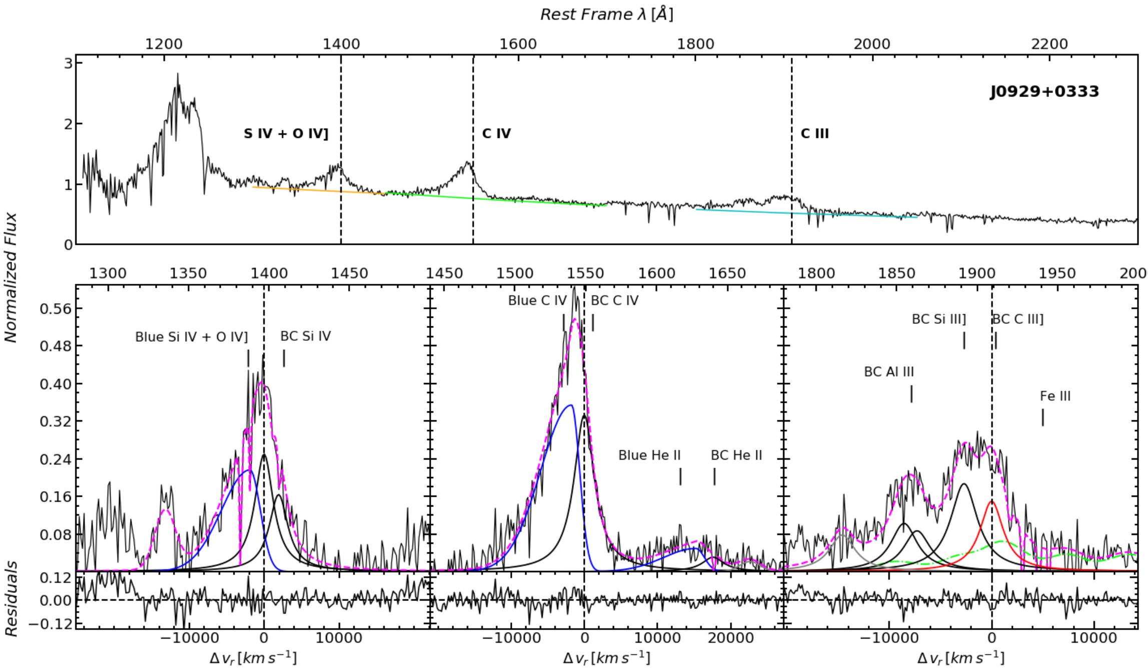

Figure A.19

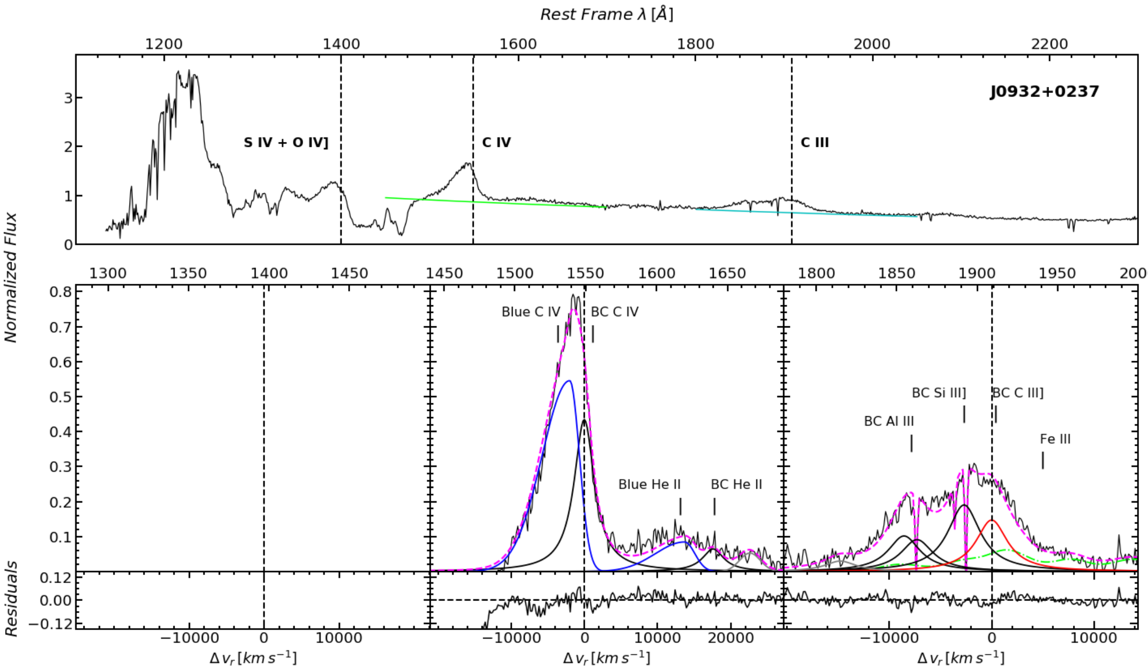

Figure A.20

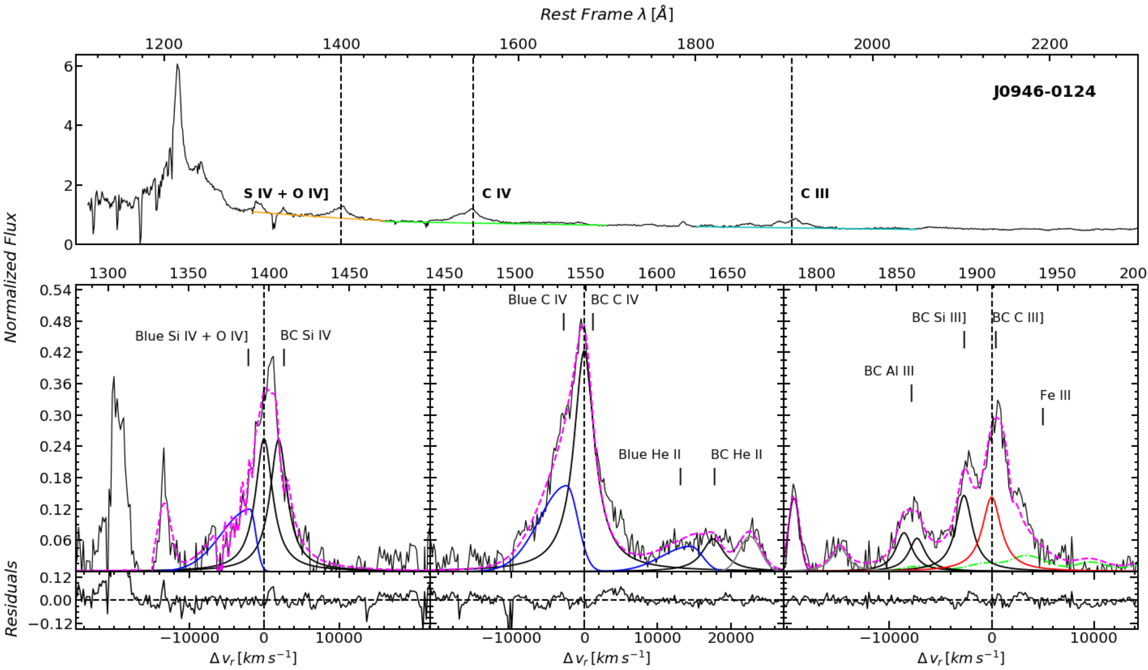

Figure A.21

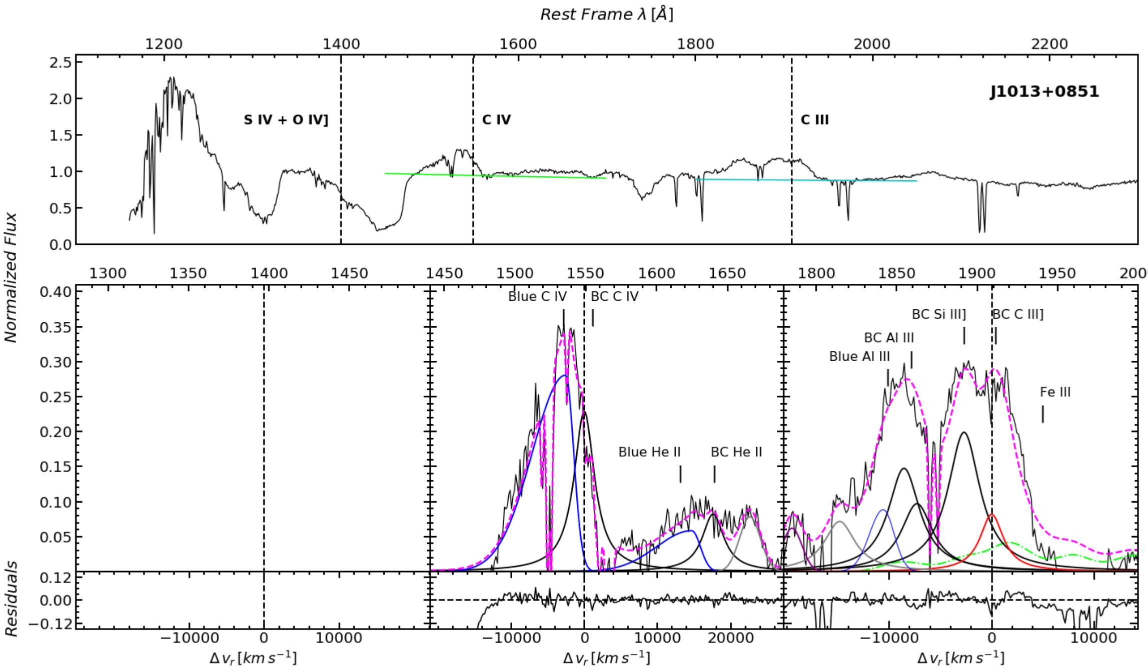

Figure A.22

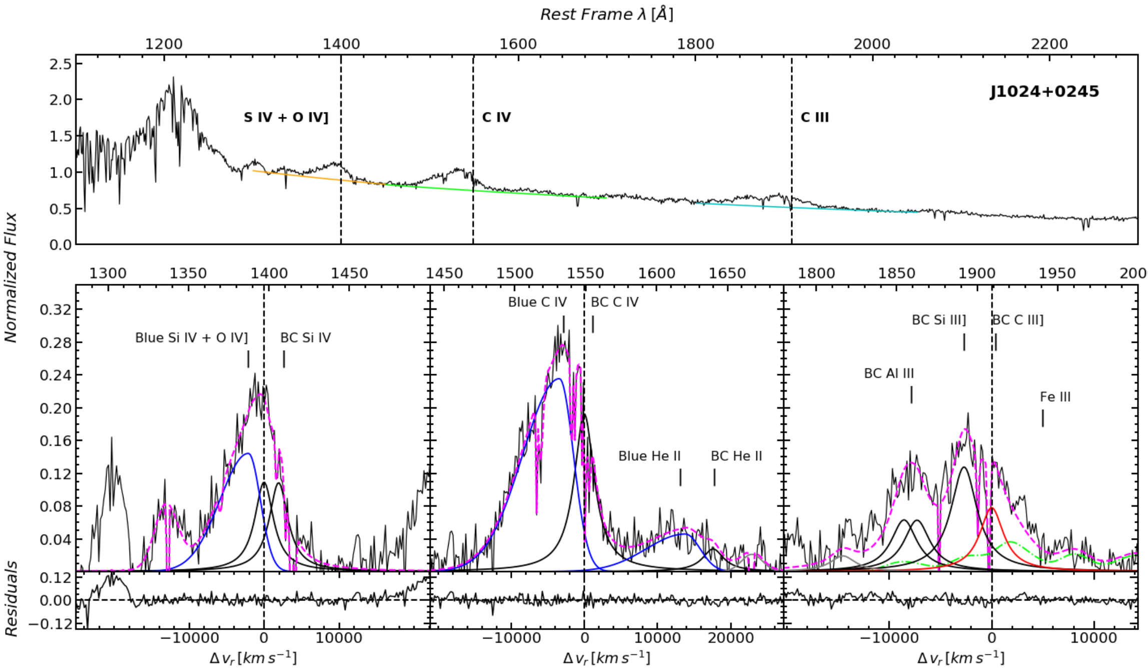

Figure A.23

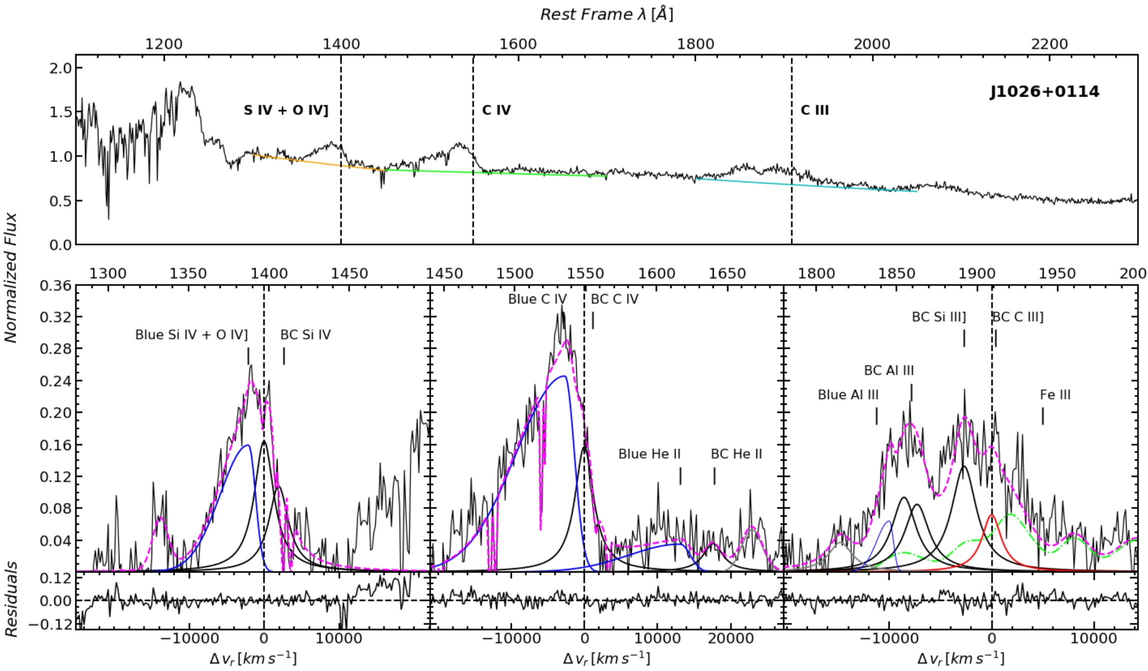

Figure A.24

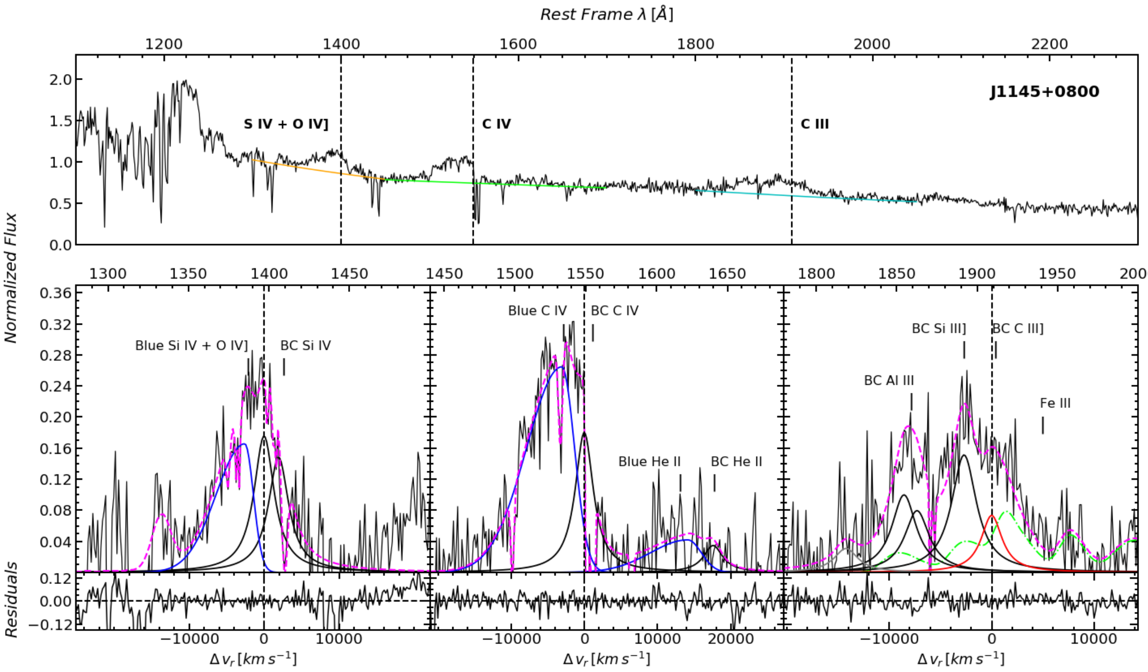

Figure A.25

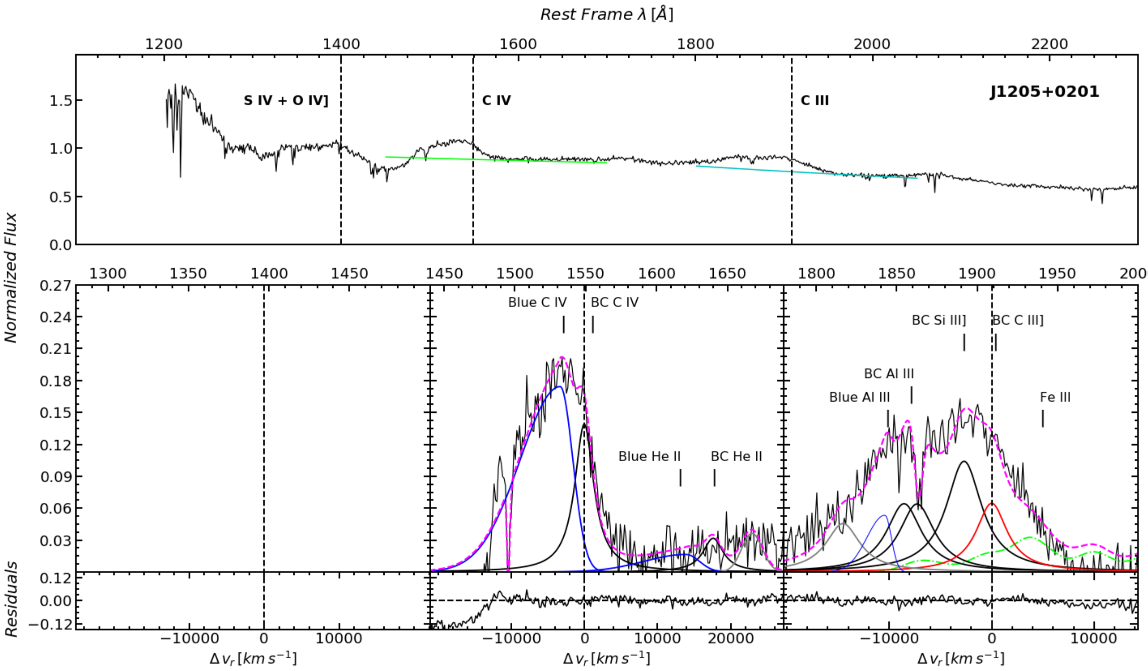

Figure A.26

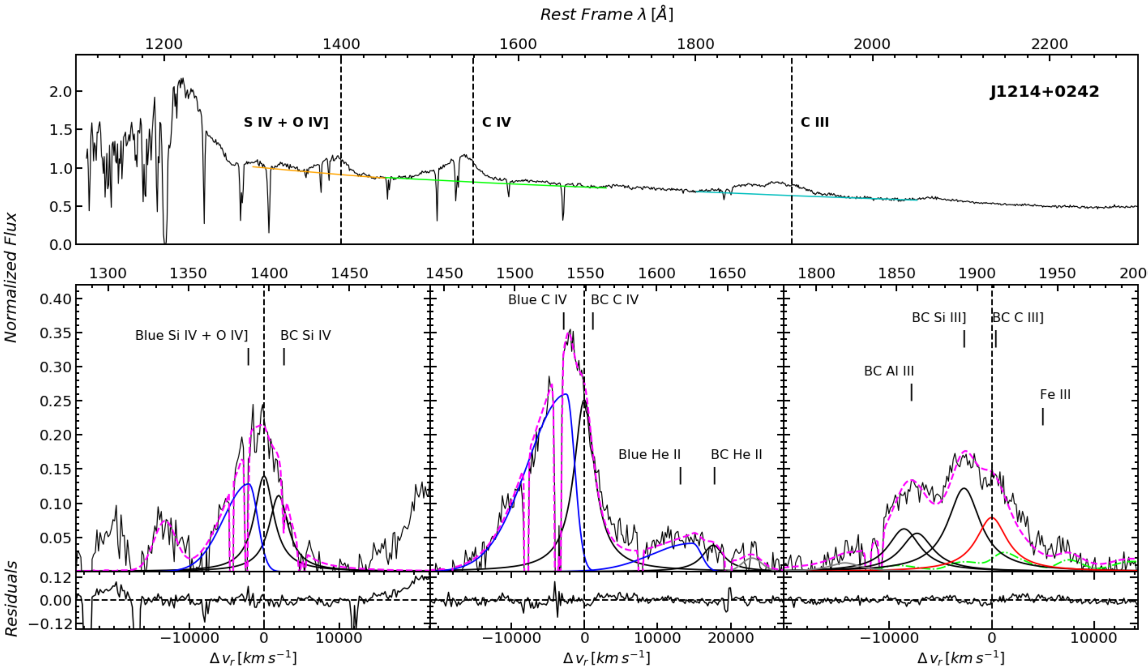

Figure A.27

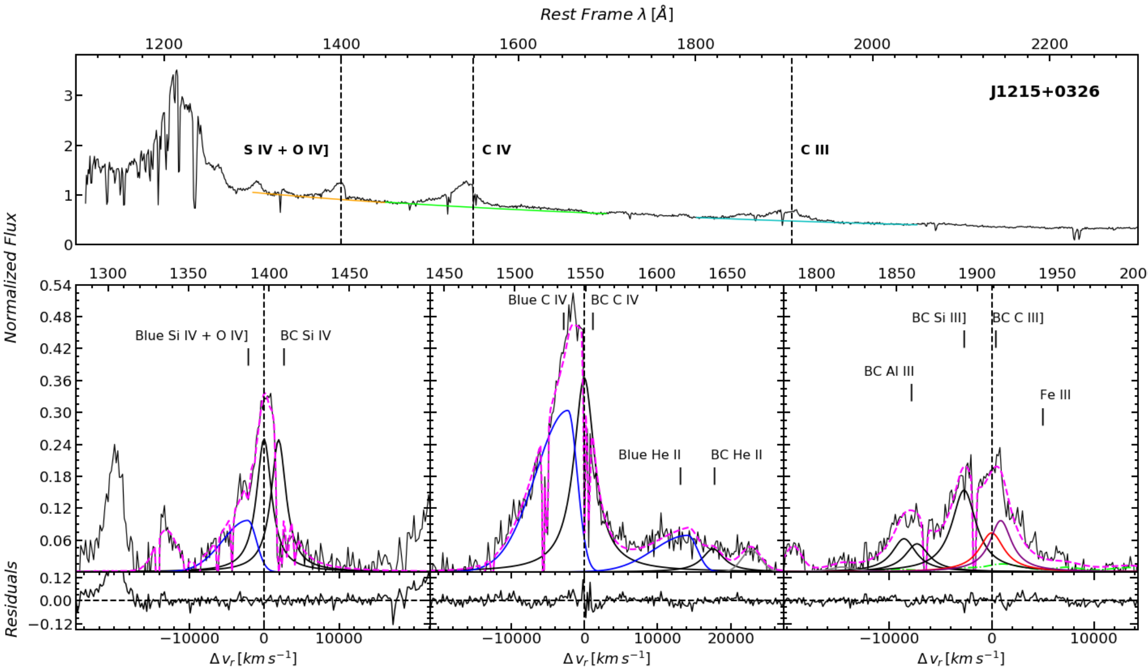

Figure A.28

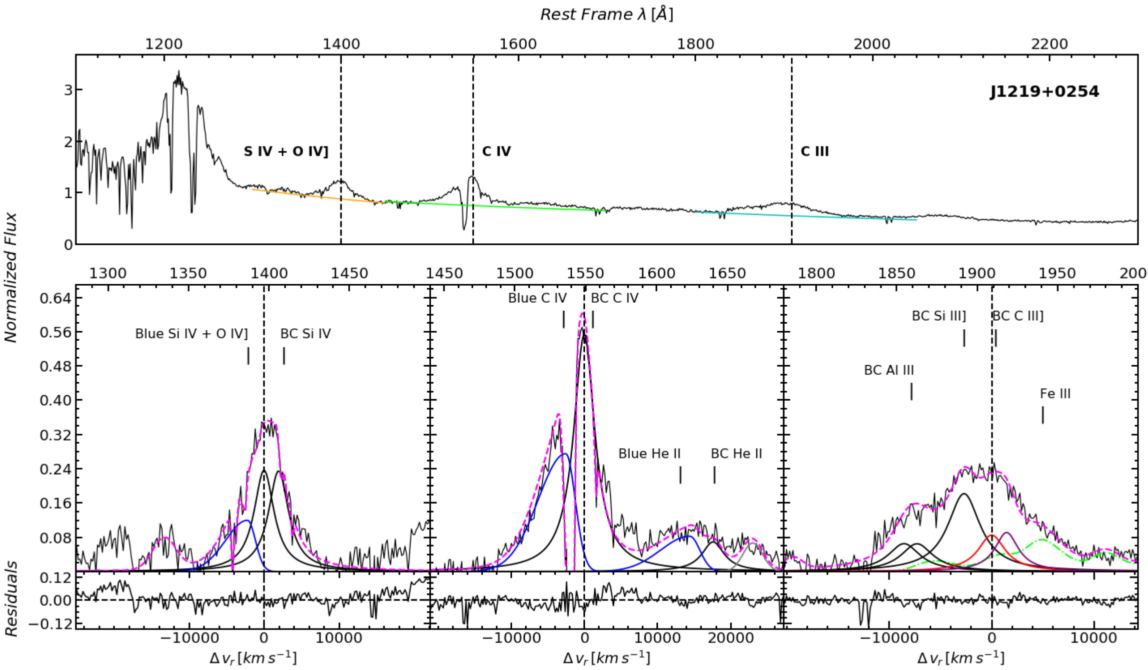

Figure A.29

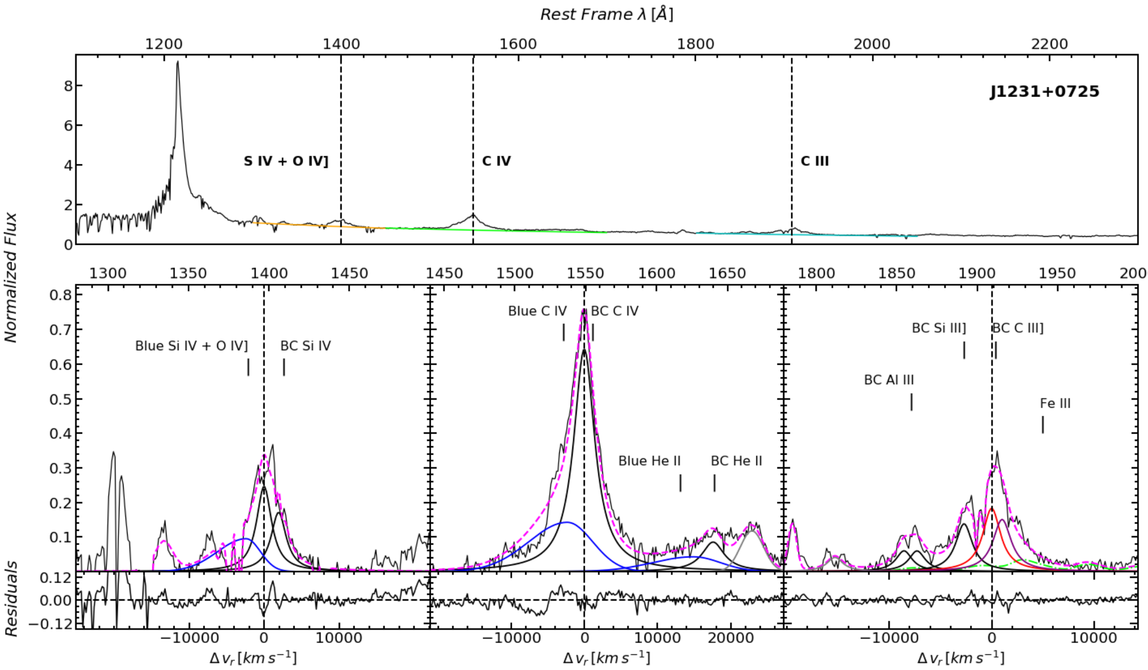

Figure A.30

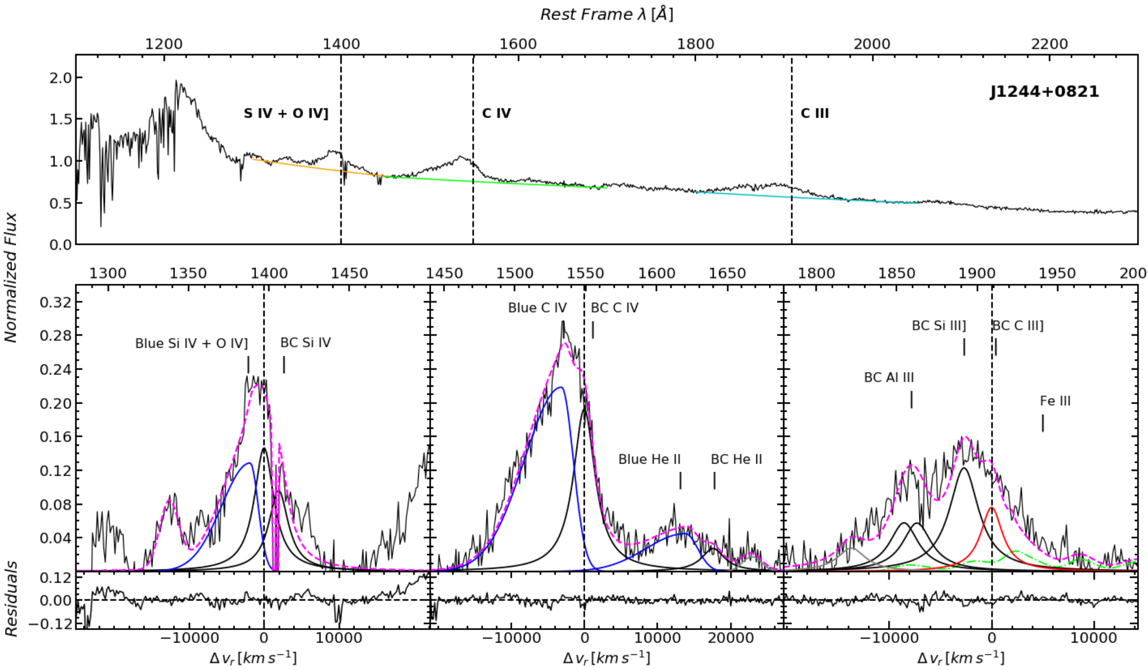

Figure A.31

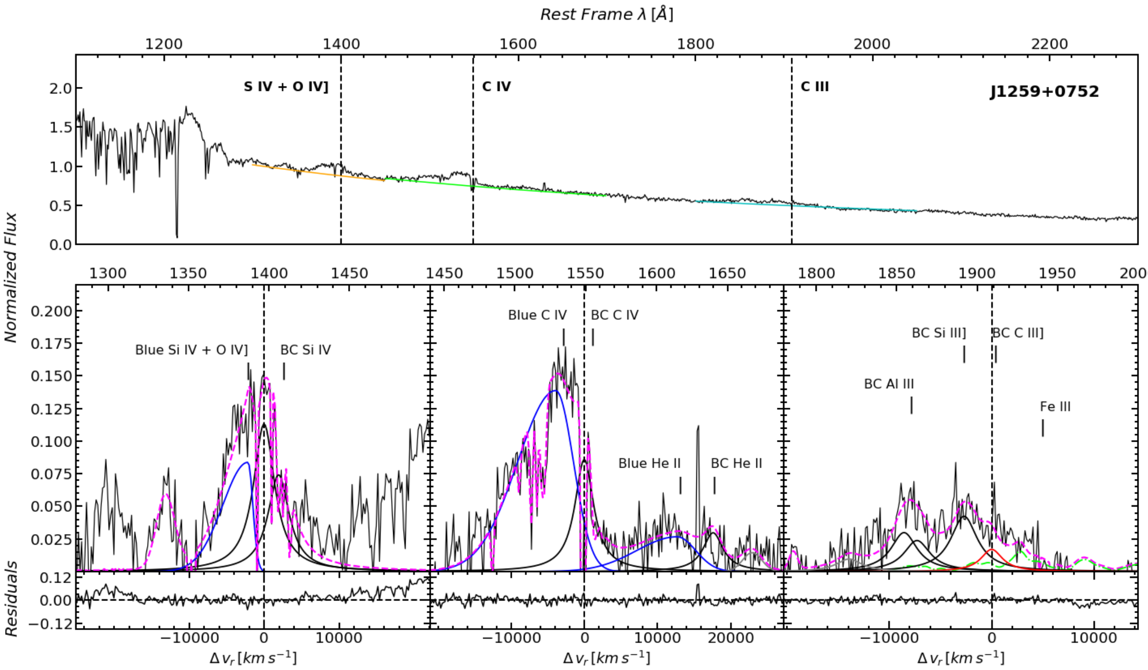

Figure A.32

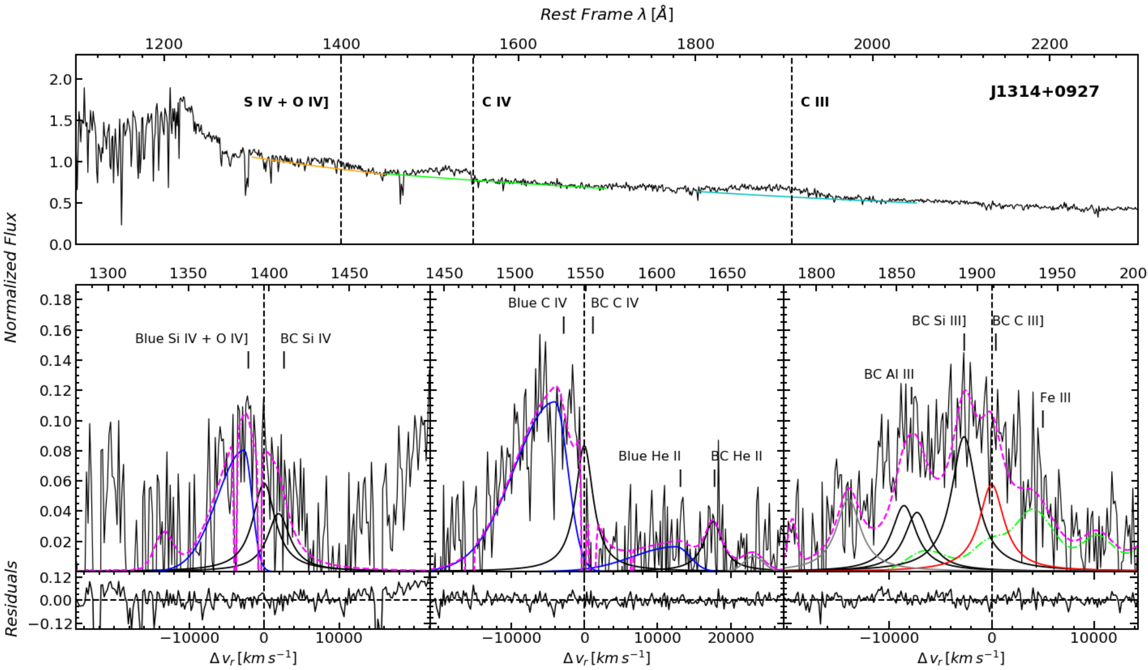

Figure A.33

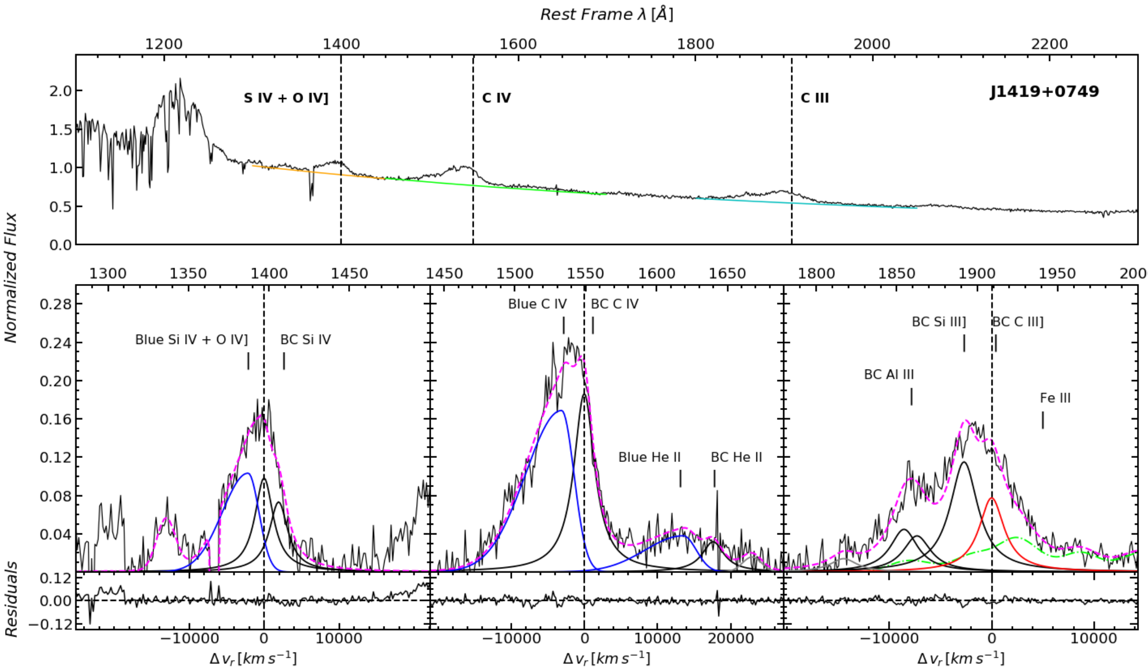

Figure A.34

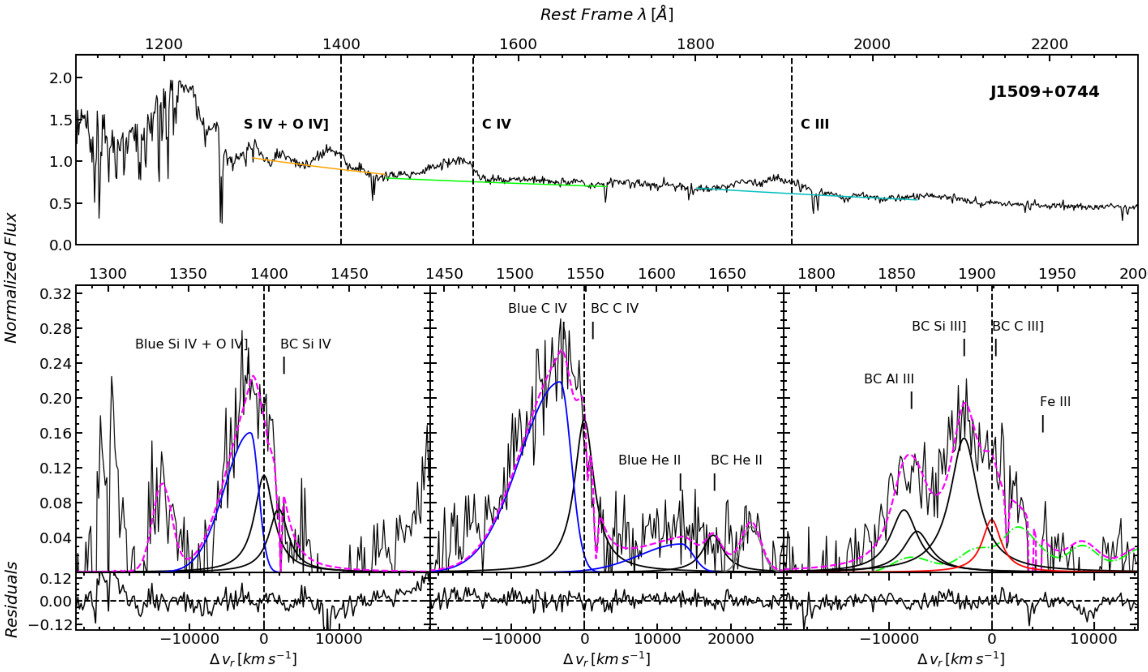

Figure A.35

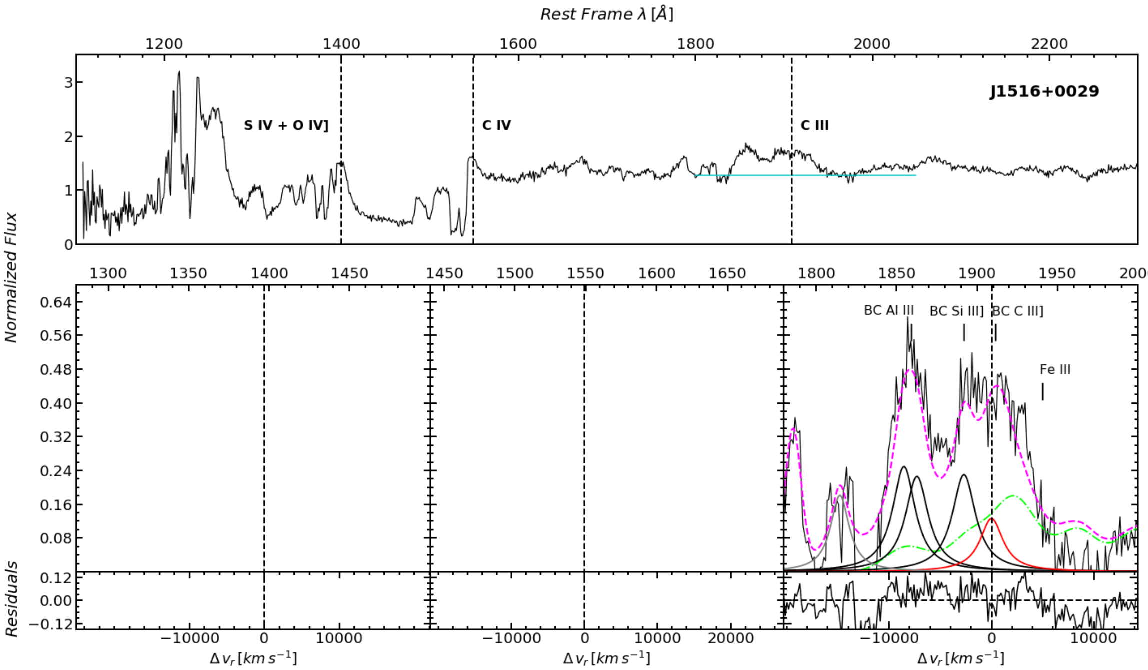

Figure A.36

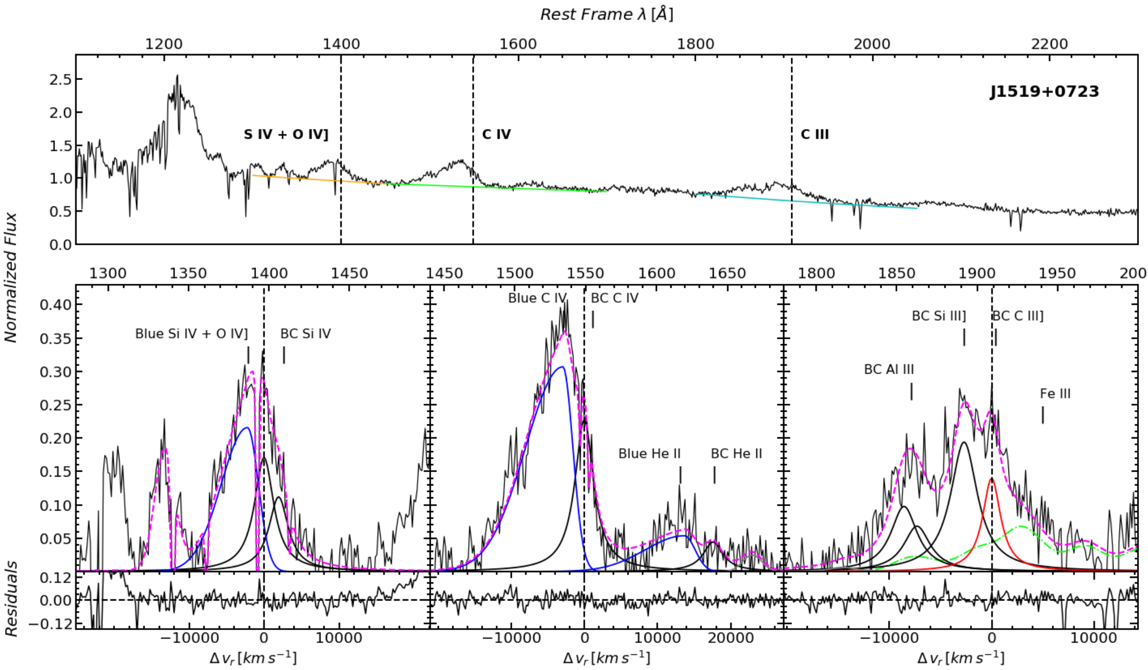

Figure A.37

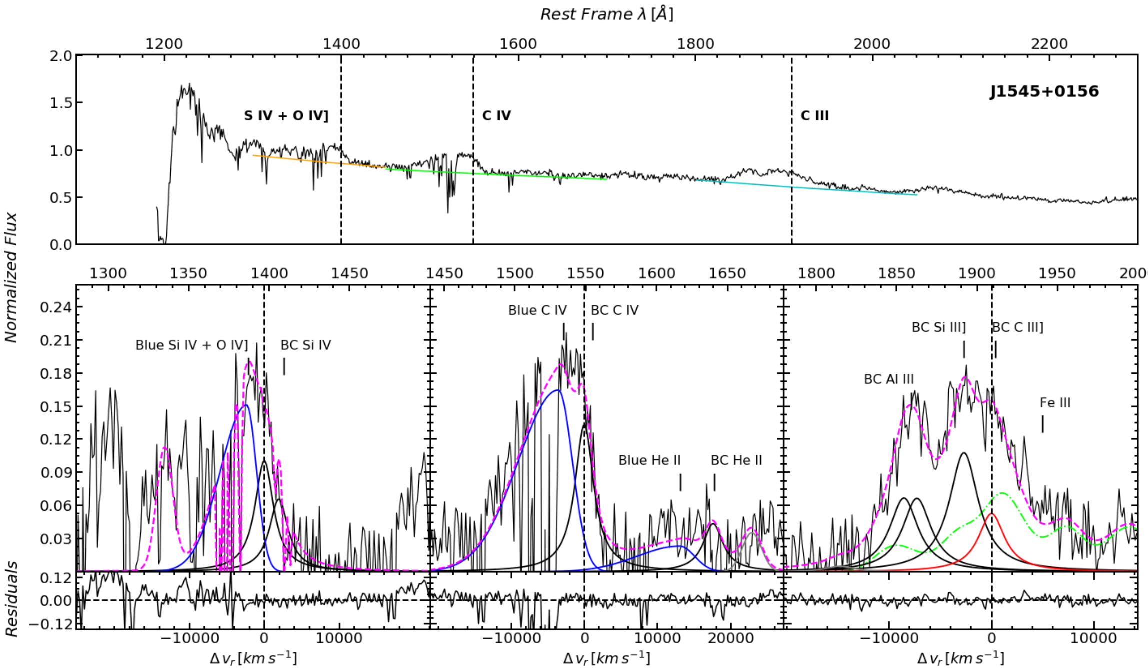

Figure A.38

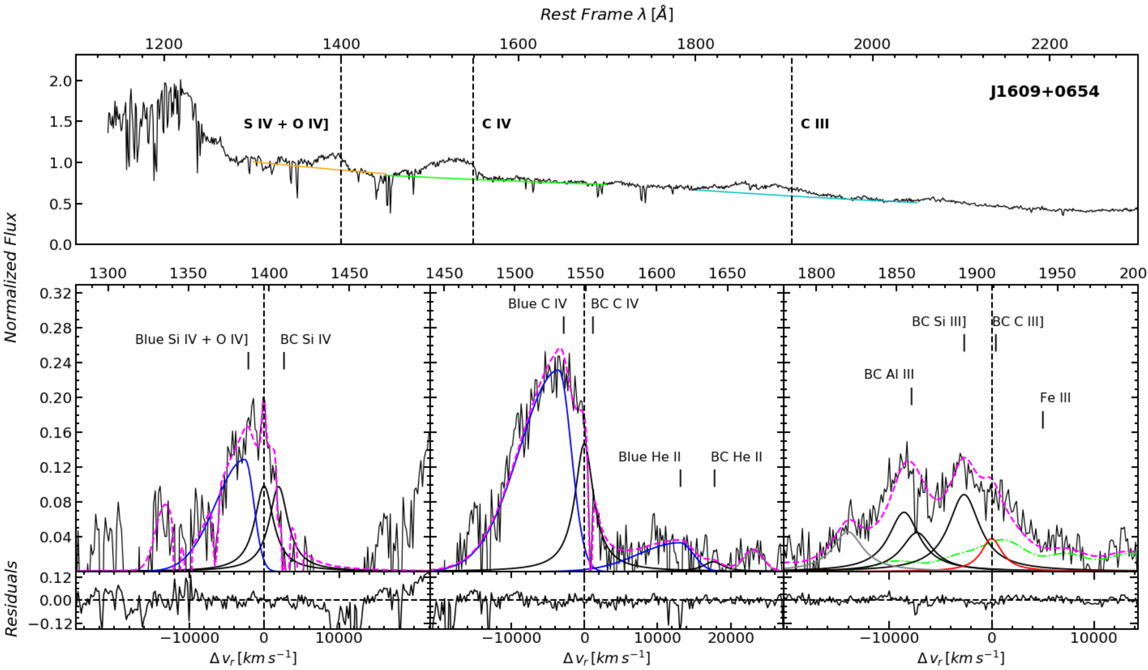

Figure A.39

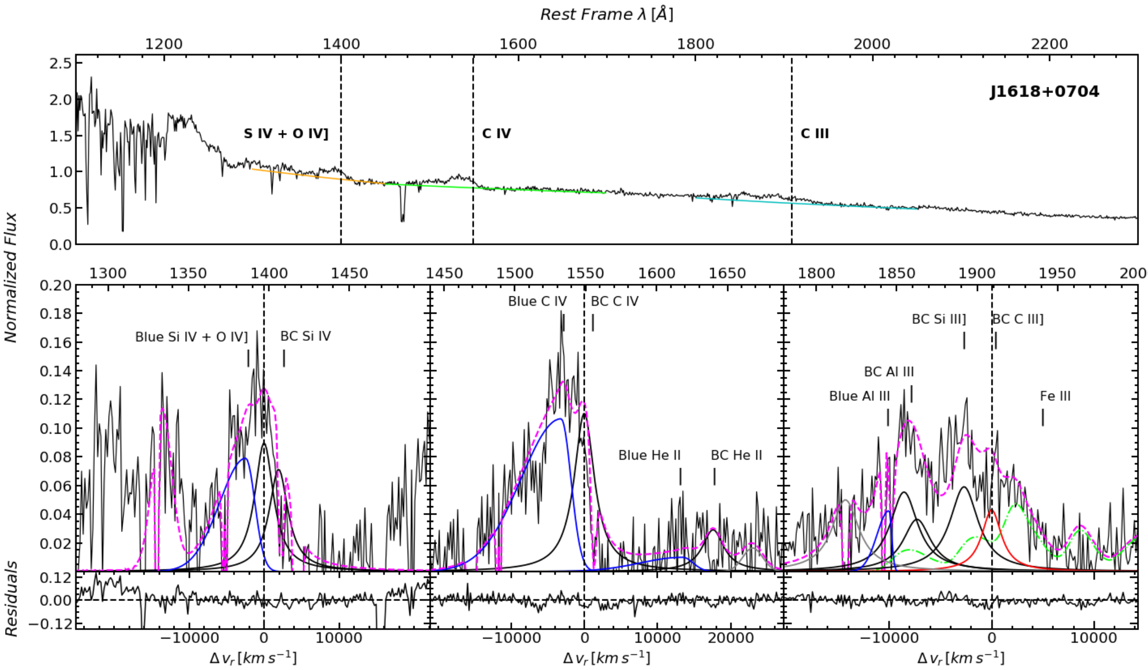

Figure A.40

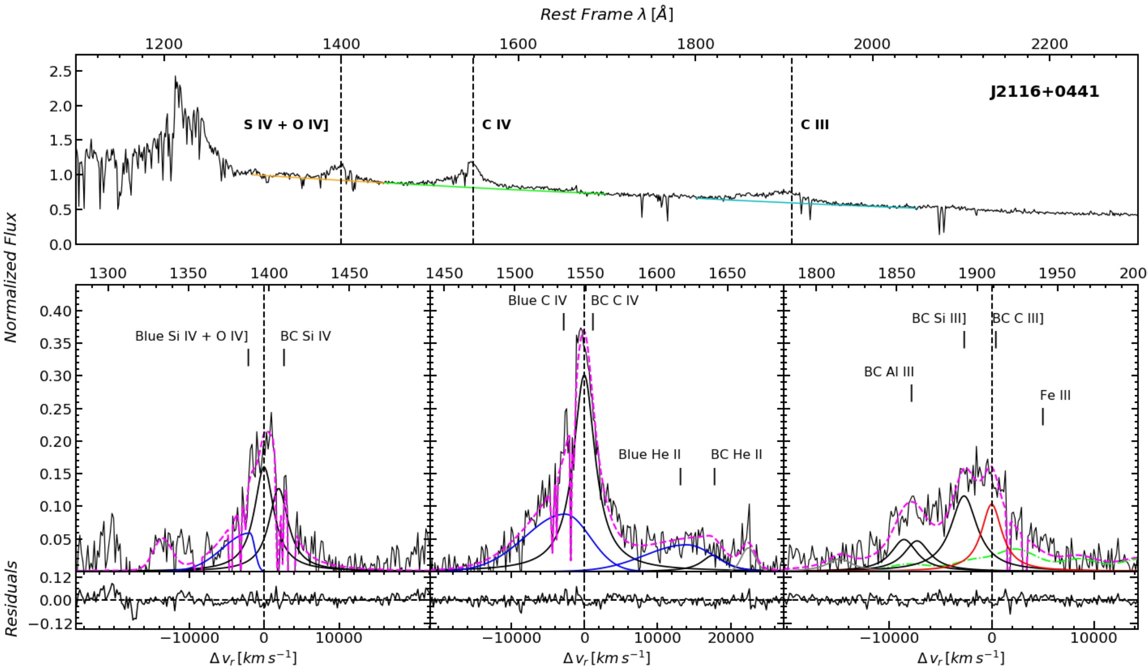

Figure A.41

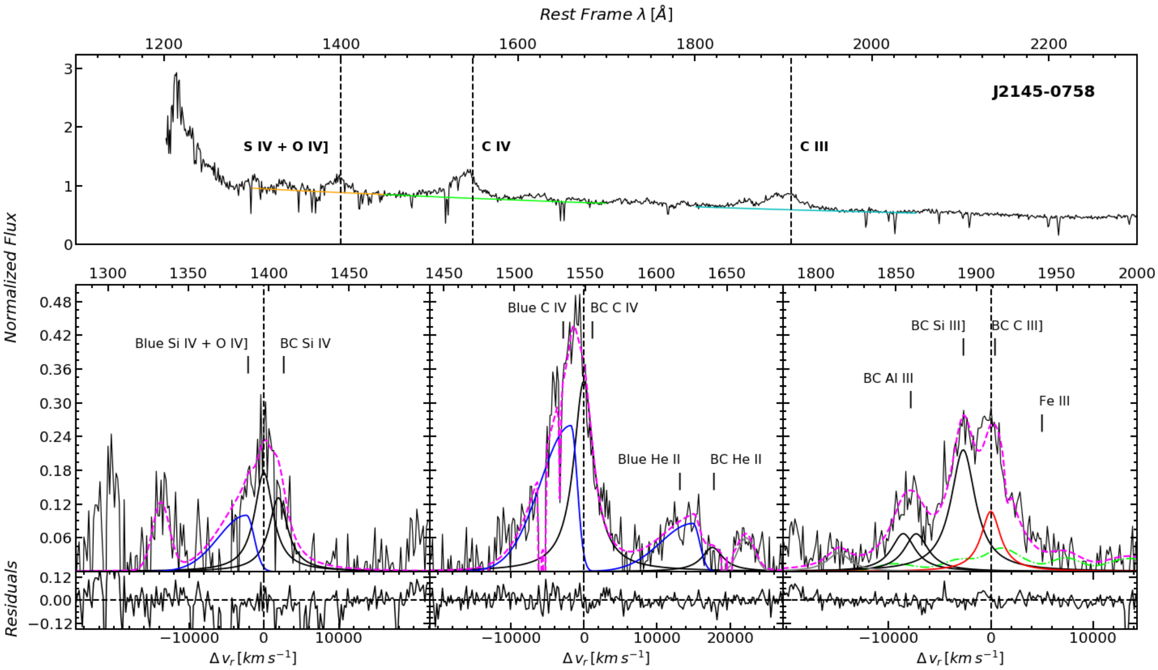
Rest Frame λ [Å]
1200
1400
1600
1800
2000
2200
J2145-0758
S IV + O IV]
C IV
C III
0
1
2
3
Normalized Flux
1300
1350
1400
1450
1450
1500
1550
1600
1650
1800
1850
1900
1950
2000
0.48
0.42
0.36
0.30
0.24
0.18
0.12
0.06
Blue Si IV + O IV]
BC Si IV
Blue C IV
BC C IV
Blue He II
BC He II
BC Al III
BC Si III]
BC C III]
Fe III
Residuals
0.12
0.00
−0.12
−10000
0
10000
20000
Δ v_r [km s^−1]

Figure A.42

Appendix B

Tables

The following section list the flux ratios tables for `specfit` and the profile measurement methods. These tables are located in this Appendix because the ratio values can be easily computed from the flux and normalized intensity values reported in Chapter 4.

Table B.1: `specfit` Flux ratios dependent on metallicity for BC emissions

SDSS JCODE (1)	BC Al III/He II (2)	BC C IV/He II (3)	BC Si IV/He II (4)	BC C IV/Al III (5)	BC Si IV/C IV (6)	BC Si IV/Al III (7)
J0020+0740	3.1 ± 1.2	6.4 ± 2.2	6.6 ± 2.3	2 ± 0.7	1 ± 0.2	2.1 ± 0.7
J0034−0326	2.1 ± 0.8	2.1 ± 0.8	2.9 ± 1.2	1 ± 0.4	0.7 ± 0.3	1.4 ± 0.5
J0037−0238	1.3 ± 0.5	6 ± 2	4.8 ± 1.6	4.7 ± 1.5	1.2 ± 0.3	3.8 ± 1.2
J0103−1104	1.8 ± 0.7	5.4 ± 1.9	4.3 ± 1.5	2.9 ± 1	1.2 ± 0.4	2.4 ± 0.8
J0106−0855	3.2 ± 1.3	3.2 ± 1.1	6.1 ± 2.1	1 ± 0.3	0.5 ± 0.1	1.9 ± 0.7
J0123+0329	3.6 ± 1.3	2.9 ± 1	6 ± 2	0.8 ± 0.2	0.5 ± 0.1	1.7 ± 0.5
J0210−0823	4.5 ± 1.9	3.4 ± 1.3	3 ± 1.2	0.7 ± 0.3	1.1 ± 0.4	0.7 ± 0.3
J0827+0306	2.1 ± 0.9	3.5 ± 1.4	4 ± 1.6	1.7 ± 0.7	0.9 ± 0.3	1.9 ± 0.8
J0829+0801	5.1 ± 1.9	4.9 ± 1.6	5.3 ± 1.7	1 ± 0.2	0.9 ± 0.2	1 ± 0.3
J0836+0548	7.2 ± 2.9	7 ± 2.5	7.5 ± 2.6	1 ± 0.3	0.9 ± 0.3	1 ± 0.3
J0845+0722	3.5 ± 1.3	4.4 ± 1.5	5.7 ± 1.9	1.3 ± 0.4	0.8 ± 0.2	1.6 ± 0.5
J0847+0943	4.4 ± 1.7	6.1 ± 2.1	4.9 ± 1.7	1.4 ± 0.5	1.2 ± 0.3	1.1 ± 0.4
J0858+0152	2.5 ± 0.8	3.9 ± 1.2	4.6 ± 1.4	1.6 ± 0.3	0.8 ± 0.1	1.9 ± 0.4
J0903+0708	2.7 ± 1.1	2 ± 0.8	1.8 ± 0.7	0.8 ± 0.3	1.1 ± 0.5	0.7 ± 0.3
J0915−0202	1.4 ± 0.6	3.5 ± 1.2	5.2 ± 1.8	2.5 ± 0.9	0.7 ± 0.2	3.8 ± 1.3
J0926+0135	2.3 ± 0.9	5.6 ± 1.8	4.8 ± 1.5	2.5 ± 0.7	1.2 ± 0.2	2.1 ± 0.6
J0929+0333	6.7 ± 2.7	10.3 ± 3.7	10.3 ± 3.7	1.5 ± 0.5	1 ± 0.3	1.5 ± 0.5
J0946−0124	1.5 ± 0.5	6.4 ± 2	5.6 ± 1.8	4.4 ± 1.1	1.1 ± 0.2	3.9 ± 1
J1024+0245	4.9 ± 1.9	6.6 ± 2.2	6.1 ± 2	1.3 ± 0.4	1.1 ± 0.2	1.2 ± 0.4
J1026+0114	5.5 ± 2.2	4.2 ± 1.4	6.6 ± 2.3	0.8 ± 0.3	0.6 ± 0.2	1.2 ± 0.4
J1145+0800	5.8 ± 2.4	4.9 ± 2	8.7 ± 3.5	0.8 ± 0.3	0.6 ± 0.2	1.5 ± 0.6
J1214+0242	4 ± 1.5	6.2 ± 2	5.1 ± 1.6	1.5 ± 0.4	1.2 ± 0.2	1.3 ± 0.3
J1215+0326	2.6 ± 1	8 ± 2.5	6.9 ± 2.2	3.1 ± 0.9	1.1 ± 0.2	2.7 ± 0.8
J1219+0254	2.4 ± 0.9	7.5 ± 2.5	5.4 ± 1.7	3.2 ± 0.9	1.4 ± 0.3	2.3 ± 0.7
J1231+0725	0.9 ± 0.3	7.1 ± 2.1	2.9 ± 0.9	7.8 ± 1.5	2.5 ± 0.2	3.2 ± 0.6
J1244+0821	4.7 ± 1.8	6.7 ± 2.1	6.7 ± 2.1	1.4 ± 0.4	1 ± 0.2	1.4 ± 0.4
J1259+0752	2.1 ± 0.9	2.7 ± 1.1	5.9 ± 2.4	1.3 ± 0.5	0.5 ± 0.2	2.8 ± 1.1
J1314+0927	2.9 ± 1.2	2.4 ± 1	3.1 ± 1.3	0.8 ± 0.3	0.8 ± 0.3	1.1 ± 0.4
J1419+0749	2.9 ± 1	5.6 ± 1.7	4 ± 1.3	1.9 ± 0.4	1.4 ± 0.2	1.4 ± 0.3
J1509+0744	3.2 ± 1.3	3.9 ± 1.4	3.5 ± 1.2	1.2 ± 0.4	1.1 ± 0.3	1.1 ± 0.4
J1519+0723	4.4 ± 1.7	4.8 ± 1.7	5.5 ± 1.9	1.1 ± 0.4	0.9 ± 0.2	1.2 ± 0.4
J1545+0156	3.9 ± 1.6	2.9 ± 1	3.1 ± 1.1	0.7 ± 0.3	0.9 ± 0.3	0.8 ± 0.3
J1609+0654	13.8 ± 5.6	12.3 ± 4.1	14.6 ± 4.8	0.9 ± 0.3	0.8 ± 0.2	1.1 ± 0.4
J1618+0704	3.6 ± 1.5	3.6 ± 1.4	4.3 ± 1.7	1 ± 0.4	0.8 ± 0.3	1.2 ± 0.5
J2116+0441	3.8 ± 1.4	11.4 ± 3.6	8.5 ± 2.7	3 ± 0.7	1.3 ± 0.2	2.2 ± 0.5
J2145−0758	3.1 ± 1.2	7.5 ± 2.7	5.6 ± 2	2.4 ± 0.8	1.3 ± 0.4	1.8 ± 0.6
μ	3.7 ± 1.4	5.4 ± 1.9	5.5 ± 1.9	1.9 ± 0.6	1 ± 0.3	1.8 ± 0.6
σ	2.3 ± 0.9	2.5 ± 0.8	2.4 ± 0.8	1.4 ± 0.3	0.4 ± 0.1	0.9 ± 0.3
SIQR	1 ± 0.4	1.6 ± 0.4	1 ± 0.3	0.7 ± 0.2	0.2 ± 0.1	0.5 ± 0.1

Notes.(1) SDSS name, (2-7) line ratios of the broad components, (8-10) line ratios of the BLUE components. The measurements of the six BALQ were excluded from this table.

Table B.2: `specfit` Flux ratios dependent on metallicity for BLUE emissions

SDSS JCODE (1)	BLUE CIV/HeII (2)	BLUE (SiIV+OIV])/ HeII (3)	BLUE CIV/ (SiIV+OIV]) (4)
J0020+0740	4.3 ± 1.3	1.5 ± 0.4	2.9 ± 0.5
J0034−0326	5 ± 1.7	1.3 ± 0.5	3.8 ± 1.1
J0037−0238	3.8 ± 1.1	1.7 ± 0.5	2.3 ± 0.4
J0103−1104	5.4 ± 1.7	1.4 ± 0.4	3.9 ± 0.8
J0106−0855	5.7 ± 1.8	2.8 ± 0.9	2 ± 0.4
J0123+0329	7.3 ± 2.2	3.8 ± 1.2	1.9 ± 0.3
J0210−0823	4 ± 1.6	1.6 ± 0.6	2.6 ± 0.9
J0827+0306	5.6 ± 2.2	1.4 ± 0.5	4 ± 1.5
J0829+0801	6 ± 1.7	2.4 ± 0.7	2.5 ± 0.3
J0836+0548	4.1 ± 1.3	2.1 ± 0.7	1.9 ± 0.4
J0845+0722	5.7 ± 1.7	2.5 ± 0.8	2.3 ± 0.4
J0847+0943	4.6 ± 1.4	2.4 ± 0.7	1.9 ± 0.3
J0858+0152	5.6 ± 1.4	2.5 ± 0.6	2.2 ± 0.2
J0903+0708	5 ± 1.7	1.8 ± 0.6	2.8 ± 0.8
J0915−0202	4.3 ± 1.4	1.5 ± 0.5	2.9 ± 0.6
J0926+0135	5.3 ± 1.5	2.7 ± 0.8	1.9 ± 0.2
J0929+0333	6.8 ± 2.2	3.6 ± 1.2	1.9 ± 0.4
J0946−0124	3.2 ± 0.9	1.8 ± 0.5	1.8 ± 0.2
J1024+0245	4.9 ± 1.5	2.1 ± 0.6	2.3 ± 0.4
J1026+0114	6.7 ± 2	2.3 ± 0.7	2.9 ± 0.5
J1145+0800	6 ± 2.3	2.6 ± 1	2.3 ± 0.9
J1214+0242	5.9 ± 1.7	1.9 ± 0.5	3.2 ± 0.4
J1215+0326	4.2 ± 1.2	1 ± 0.3	4.4 ± 0.5
J1219+0254	3.2 ± 1	1 ± 0.3	3.2 ± 0.5
J1231+0725	3.1 ± 1	1.2 ± 0.4	2.5 ± 0.5
J1244+0821	4.6 ± 1.3	1.8 ± 0.5	2.6 ± 0.3
J1259+0752	4.9 ± 1.7	1.4 ± 0.5	3.5 ± 1
J1314+0927	6.5 ± 2.6	2.6 ± 1	2.5 ± 0.9
J1419+0749	4.2 ± 1.2	1.7 ± 0.5	2.5 ± 0.3
J1509+0744	6.4 ± 2	2.7 ± 0.9	2.3 ± 0.5
J1519+0723	5.4 ± 1.6	2.6 ± 0.8	2.1 ± 0.4
J1545+0156	6.7 ± 2.1	3.6 ± 1.2	1.9 ± 0.4
J1609+0654	6.6 ± 2	2.4 ± 0.7	2.8 ± 0.4
J1618+0704	10.1 ± 3.5	4.7 ± 1.6	2.2 ± 0.6
J2116+0441	2 ± 0.6	0.6 ± 0.2	3.4 ± 0.4
J2145−0758	2.9 ± 0.9	0.9 ± 0.3	3 ± 0.6
μ	5.2 ± 1.6	2.1 ± 0.7	2.6 ± 0.5
σ	1.5 ± 0.6	0.9 ± 0.3	0.7 ± 0.3
SIQR	0.9 ± 0.4	0.6 ± 0.1	0.4 ± 0.1

Notes.(1) SDSS name, (2-7) line ratios of the broad components, (8-10) line ratios of the BLUE components. The measurements of the six BALQ were excluded from this table.

Table B.3: Flux ratios dependent on metallicity of normalized intensities measurements

SDSS JCODE (1)	BC Al III/He II (2)	BC C IV/He II (3)	BC Si IV/He II (4)	BC C IV/Al III (5)	BC Si IV/C IV (6)	BC Si IV/Al III (7)
J0020+0740	2.62 ± 1.00	6.25 ± 2.72	5.83 ± 2.06	2.38 ± 1.54	1.07 ± 0.30	2.22 ± 0.43
J0034−0326	2.24 ± 1.13	3.78 ± 3.07	3.29 ± 1.53	1.69 ± 2.04	1.15 ± 0.86	1.47 ± 0.57
J0037−0238	1.96 ± 0.70	7.53 ± 2.49	6.29 ± 2.08	3.83 ± 1.48	1.20 ± 0.17	3.20 ± 0.63
J0103−1104	1.77 ± 0.98	4.43 ± 2.41	3.88 ± 2.15	2.50 ± 1.01	1.14 ± 0.28	2.19 ± 0.58
J0106−0855	3.59 ± 1.61	6.25 ± 3.05	8.14 ± 3.64	1.74 ± 0.81	0.77 ± 0.24	2.27 ± 0.57
J0123+0329	…	…	…	1.11 ± 0.46	0.66 ± 0.26	1.68 ± 0.43
J0210−0823	2.80 ± 2.34	2.63 ± 2.53	0.77 ± 1.04	0.94 ± 0.53	3.42 ± 4.15	0.27 ± 0.31
J0827+0306	5.07 ± 8.96	…	…	1.95 ± 1.08	1.08 ± 0.42	1.80 ± 0.79
J0829+0801	4.79 ± 2.48	5.78 ± 3.44	6.31 ± 3.29	1.21 ± 0.46	0.92 ± 0.30	1.32 ± 0.18
J0836+0548	4.64 ± 2.24	8.44 ± 4.26	10.22 ± 4.91	1.82 ± 0.66	0.83 ± 0.19	2.20 ± 0.40
J0845+0722	3.90 ± 2.90	7.37 ± 5.43	7.41 ± 5.56	1.89 ± 0.72	0.99 ± 0.31	1.90 ± 0.63
J0847+0943	3.63 ± 1.81	6.78 ± 3.56	6.79 ± 3.28	1.87 ± 0.97	1.00 ± 0.32	1.87 ± 0.52
J0858+0152	3.66 ± 1.57	7.87 ± 4.88	7.14 ± 3.22	2.15 ± 2.18	1.10 ± 0.56	1.95 ± 0.49
J0903+0708	3.80 ± 3.41	1.79 ± 4.27	3.53 ± 3.25	0.47 ± 0.52	0.51 ± 1.13	0.93 ± 0.30
J0915−0202	1.43 ± 0.80	4.40 ± 3.00	5.41 ± 2.48	3.09 ± 5.03	0.81 ± 0.44	3.79 ± 1.45
J0926+0135	1.96 ± 0.61	5.03 ± 1.71	4.41 ± 1.38	2.56 ± 1.10	1.14 ± 0.22	2.25 ± 0.31
J0929+0333	4.09 ± 2.73	9.45 ± 6.58	8.64 ± 5.59	2.31 ± 1.55	1.09 ± 0.34	2.11 ± 0.51
J0946−0124	1.77 ± 0.36	6.52 ± 1.27	5.23 ± 1.07	3.69 ± 1.67	1.25 ± 0.23	2.96 ± 0.58
J1024+0245	5.18 ± 4.35	7.17 ± 6.68	8.81 ± 7.34	1.38 ± 0.85	0.81 ± 0.37	1.70 ± 0.34
J1026+0114	4.77 ± 1.92	5.09 ± 2.31	5.96 ± 2.33	1.07 ± 0.33	0.85 ± 0.24	1.25 ± 0.23
J1145+0800	5.24 ± 3.67	2.47 ± 9.30	8.28 ± 5.68	0.47 ± 0.85	0.30 ± 1.11	1.58 ± 0.40
J1214+0242	4.22 ± 1.23	8.76 ± 2.92	7.20 ± 2.16	2.08 ± 0.79	1.22 ± 0.26	1.71 ± 0.24
J1215+0326	2.11 ± 0.52	6.52 ± 3.54	6.70 ± 1.47	3.09 ± 4.79	0.97 ± 0.49	3.17 ± 0.48
J1219+0254	1.56 ± 0.37	6.24 ± 1.32	3.90 ± 0.81	4.00 ± 1.20	1.60 ± 0.16	2.50 ± 0.38
J1231+0725	0.87 ± 0.21	6.06 ± 0.80	2.71 ± 0.40	6.96 ± 5.13	2.23 ± 0.36	3.12 ± 0.81
J1244+0821	3.63 ± 1.59	7.65 ± 3.01	6.92 ± 3.30	2.11 ± 0.68	1.11 ± 0.37	1.91 ± 0.74
J1259+0752	2.60 ± 1.83	2.65 ± 4.05	5.87 ± 4.86	1.02 ± 1.44	0.45 ± 0.66	2.26 ± 1.23
J1314+0927	3.55 ± 3.63	1.19 ± 2.21	2.07 ± 2.82	0.34 ± 0.28	0.58 ± 1.05	0.58 ± 0.56
J1419+0749	3.03 ± 3.16	6.81 ± 7.07	5.31 ± 5.50	2.25 ± 0.71	1.28 ± 0.23	1.75 ± 0.37
J1509+0744	3.40 ± 1.66	4.94 ± 2.74	5.63 ± 2.69	1.45 ± 0.66	0.88 ± 0.29	1.66 ± 0.32
J1519+0723	4.69 ± 2.78	6.76 ± 4.26	6.26 ± 5.74	1.44 ± 0.59	1.08 ± 0.83	1.34 ± 0.99
J1545+0156	5.66 ± 7.46	6.12 ± 8.14	5.65 ± 7.47	1.08 ± 0.29	1.08 ± 0.31	1.00 ± 0.21
J1609+0654	7.34 ± 7.28	…	…	1.30 ± 0.92	0.87 ± 0.48	1.50 ± 0.51
J1618+0704	…	…	…	0.97 ± 0.40	0.72 ± 0.29	1.36 ± 0.38
J2116+0441	3.01 ± 1.22	11.13 ± 4.21	6.33 ± 2.48	3.70 ± 1.20	1.76 ± 0.28	2.10 ± 0.46
J2145−0758	5.85 ± 9.23	…	…	2.81 ± 2.03	1.50 ± 0.51	1.87 ± 0.67
μ	3.54 ± 2.58	5.93 ± 3.78	5.84 ± 3.28	2.08 ± 1.30	1.10 ± 0.53	1.91 ± 0.53
σ	1.48 ± 2.36	2.27 ± 2.02	2.07 ± 1.91	1.28 ± 1.23	0.54 ± 0.67	0.73 ± 0.27
SIQR	1.17 ± 1.03	1.29 ± 0.88	1.10 ± 1.41	0.66 ± 0.42	0.17 ± 0.12	0.37 ± 0.11

Notes.(1) SDSS short name, (2-7) line ratios of the broad components. The measurements of the six BALQ were excluded from this table.

Table B.4: Flux ratios dependent on metallicity of normalized intensities measurements

SDSS JCODE (1)	BLUE CIV/HeII (2)	BLUE (SiIV+OIV])/HeII (3)	BLUE CIV/(SiIV+OIV]) (4)
J0020+0740	5.12 ± 2.00	2.72 ± 1.20	1.88 ± 0.46
J0034−0326	...	...	3.06 ± 3.21
J0037−0238	4.29 ± 1.09	2.55 ± 0.92	1.68 ± 0.56
J0103−1104	5.50 ± 4.00	2.09 ± 1.86	2.63 ± 1.59
J0106−0855	6.66 ± 4.49	3.56 ± 2.91	1.87 ± 0.90
J0123+0329	6.36 ± 3.53	3.01 ± 5.36	2.11 ± 3.58
J0210−0823	2.59 ± 1.74	2.07 ± 1.46	1.25 ± 0.87
J0827+0306	3.05 ± 2.18	1.84 ± 1.50	1.66 ± 1.08
J0829+0801	5.33 ± 1.65	2.42 ± 1.58	2.21 ± 1.30
J0836+0548	4.05 ± 2.63	2.95 ± 1.57	1.38 ± 0.75
J0845+0722	4.70 ± 1.74	3.14 ± 1.21	1.50 ± 0.26
J0847+0943	5.31 ± 1.62	3.12 ± 1.07	1.70 ± 0.33
J0858+0152	4.78 ± 3.36	1.60 ± 3.32	2.99 ± 6.48
J0903+0708	6.44 ± 4.88	4.23 ± 3.46	1.52 ± 0.52
J0915−0202	4.31 ± 1.49	2.59 ± 1.12	1.66 ± 0.50
J0926+0135	5.78 ± 1.12	2.53 ± 1.95	2.29 ± 1.73
J0929+0333	6.15 ± 2.72	3.41 ± 1.87	1.80 ± 0.71
J0946−0124	4.06 ± 1.18	1.59 ± 0.64	2.56 ± 1.05
J1024+0245	6.51 ± 2.32	3.67 ± 1.44	1.77 ± 0.37
J1026+0114	6.82 ± 3.32	4.29 ± 2.11	1.59 ± 0.24
J1145+0800	...	4.79 ± 6.75	1.57 ± 0.51
J1214+0242	2.43 ± 3.66	1.84 ± 2.79	1.32 ± 2.82
J1215+0326	5.06 ± 1.72	1.74 ± 0.94	2.90 ± 1.68
J1219+0254	3.36 ± 0.72	1.22 ± 0.67	2.76 ± 1.47
J1231+0725	4.19 ± 1.49	0.04 ± 1.18	...
J1244+0821	5.14 ± 1.32	2.89 ± 0.74	1.78 ± 0.36
J1259+0752	5.14 ± 1.84	4.03 ± 1.37	1.28 ± 0.29
J1314+0927	4.56 ± 3.71	3.14 ± 3.03	1.45 ± 0.92
J1419+0749	5.27 ± 1.22	2.86 ± 0.78	1.84 ± 0.38
J1509+0744	4.77 ± 2.36	3.31 ± 1.92	1.44 ± 0.50
J1519+0723	4.82 ± 2.00	3.14 ± 1.38	1.53 ± 0.32
J1545+0156	0.04 ± 5.37	2.52 ± 3.30	0.02 ± 2.13
J1609+0654	...	...	1.64 ± 0.22
J1618+0704	5.90 ± 5.79	3.75 ± 4.05	1.57 ± 0.79
J2116+0441	2.52 ± 1.24	0.92 ± 1.51	2.75 ± 4.60
J2145−0758	3.20 ± 1.26	0.31 ± 1.29	...
μ	4.66 ± 2.47	2.63 ± 1.91	1.80 ± 1.26
σ	1.47 ± 1.34	1.09 ± 1.37	0.62 ± 1.39
SIQR	0.72 ± 0.94	0.68 ± 0.72	0.33 ± 0.58

Notes.(1) SDSS short name, (2-4) line ratios of the BLUE components. The measurements of the six BALQ were excluded from this table.

List of Figures

1.1 M87 Images 2
1.2 Schematic representation of the spectral energy distribution of an unobscured AGN 4
1.3 Identification of redshifted spectral lines 6
1.4 Images of the Seyfert galaxy NGC 4151 8
1.5 Examples of morphology in radio galaxies 9
1.6 Main types of galactic spectra 12
1.7 Schematic representation of AGN in the unified model 14
1.8 Two-dimensional projections of the Eigenvector 1 20
1.9 Optical plane of the 4DE1 21
1.10 The early stages in the evolution of AGN and quasars 25

2.1 UV spectra of a Type 1 and BALQ sources 32
2.2 Redshift distribution of the sample as a function of the absolute $i-$band magnitude 37

3.1 1550 Å region input file extraction 44
3.2 1900 Å region fitting example of a regular type 1 spectra. 47
3.3 1900 Å region fitting example of a BALQ spectra with BLUE AlIII and FeII emissions. 48
3.4 1550 Å region fitting example. 49
3.5 1550 Å region fitting example. 50
3.6 1400 Å region fitting example. 51

3.7 Observed and synthetic spectra of J0929+0333 for error estimation on line fluxes. 53
3.8 Distributions from our error routine for the FWHM , flux and wavelength of AlIII. 54
3.9 1550 Å region profile measurements ranges. 58

4.1 Distribution and individual intensity ratios between prominent lines not used for metallicity estimates. 78
4.2 Distribution and individual BC intensity ratios used as metallicity diagnostic involving HeIIλ1640. 79
4.3 Distribution and individual BC intensity ratios used as metallicity diagnostic for non involving HeIIλ1640 ratios. 80
4.4 Distribution and individual BLUE intensity ratios used as metallicity diagnostic. 82
4.5 Relation between intensity ratios AlIII/SiIII] and CIII]/SiIII]. 83
4.6 Correlation matrix between diagnostic ratios for BC and BLUE and physical parameters. 85
4.7 Intensity ratios trend predicted by CLOUDY as a function of metallicity, for physical parameters U and n_{H} fixed. 87
4.8 Distribution and individual BC metallicity estimates involving HeII. . 88
4.9 Distribution and individual BC metallicity estimates involving HeII. . 89
4.10 The parameter space n_{H}, U, Z for BLUE component. 94
4.11 The plane $\log U$ vs $\log Z$ 95

5.1 Relation between intensity ratios CIV/HeIIλ1640, AlIII/HeIIλ1640 and CIV/HeIIλ1640 BLUE computed with `specfit` and with profile ratio technique. 100
5.2 Relation between intensity ratios CIV/HeII, AlIII/HeII, CIV/HeII BLUE, (SiIV+OIV]/)HeII, and (SiIV+OIV]/)HeII BLUE for the 13 objects in common with S21. 102
5.3 Metallicity comparison of our two fitting methods. 103
5.4 The parameter space n_{H}, U, Z. 108

5.5 Difference in the metallicity estimates from the Al III/He II intensity ratio and from the C IV/He II ratio, as a function of ionization parameter and density. 112

A.1 J0020+0740 123
A.2 J0034−0326 124
A.3 J0037−0238 124
A.4 J0103−1104 125
A.5 J0106−0855 125
A.6 J0123+0329 126
A.7 J0210−0823 126
A.8 J0216+0115 127
A.9 J0252−0420 127
A.10 J0827+0306 128
A.11 J0829+0801 128
A.12 J0836+0548 129
A.13 J0845+0722 129
A.14 J0847+0943 130
A.15 J0858+0152 130
A.16 J0903+0708 131
A.17 J0915−0202 131
A.18 J0926+0135 132
A.19 J0929+0333 132
A.20 J0932+0237 133
A.21 J0946−0124 133
A.22 J1013+0851 134
A.23 J1024+0245 134
A.24 J1026+0114 135
A.25 J1145+0800 135
A.26 J1205+0201 136
A.27 J1214+0242 136

A.28 J1215+0326 137
A.29 J1219+0254 137
A.30 J1231+0725 138
A.31 J1244+0821 138
A.32 J1259+0752 139
A.33 J1314+0927 139
A.34 J1419+0749 140
A.35 J1509+0744 140
A.36 J1516+0029 141
A.37 J1519+0723 141
A.38 J1545+0156 142
A.39 J1609+0654 142
A.40 J1618+0704 143
A.41 J2116+0441 143
A.42 J2145−0758 144

List of Tables

1.1 Main AGN classifications according to their optical and radio spectroscopic properties. 16

1.2 Main trends along the 4DE1 sequence 22

2.1 Source identification and basic properties 39

3.1 Internally defined functions in `specfit` 43

3.2 Error models for spectra with EW ∼23 and no additional components 55

3.3 Physical Parameters 64

4.1 Measurements in the 1900Å blend region: AlIII broad and blueshifted components. 69

4.2 Measurements in the 1900Å blend region: SiIII], CIII] and FeIII broad components. 70

4.3 Measurements in the λ1550 region: CIV and HeII broad components. 71

4.4 Measurements in the λ1550 region: CIV and HeII asymmetric components. 72

4.5 Measurements in the λ1400 region: SiIV broad component and SiIV + OIV] asymmetric component. 73

4.6 Normalized intensities of AlIII, SiIII], CIV, HeII and SiIV broad components. 75

4.7 Normalized intensities of BLUE CIV, BLUE HeII and BLUE SiIV+ OIV]. 76

4.8 Metallicity ($\log Z$) of the BC assuming fixed $\log(U)$=-2.5 and $\log(n_{\mathrm{H}})$=12 91

4.9 Metallicity ($\log Z$) of the BC assuming fixed $\log(U)$=-2.5 and $\log(n_{\mathrm{H}})$=13 92

4.10 Metallicity ($\log Z$) of BLUE assuming fixed U, n_{H} 93
4.11 Z, U, n_{H} of individual sources and median derived from the BC . . . 97
4.12 Z, U, n_{H} of individual sources and median derived from BLUE 98

5.1 Metallicity of normalized intensities measurements 105
5.2 Measurements of the CIV full profile. 107

B.1 `specfit` Flux ratios dependent on metallicity for BC emissions 146
B.2 `specfit` Flux ratios dependent on metallicity for BLUE emissions . . 147
B.3 Flux ratios dependent on metallicity of normalized intensities measurements 148
B.4 Flux ratios dependent on metallicity of normalized intensities measurements 149